Lighting up nanoclusters: Path to efficient quantum chemical approaches

by

Don Sulalith Nadun Dinuksha Samarasinghe

B.S., University of Colombo, 2020

AN ABSTRACT OF A DISSERTATION

submitted in partial fulfillment of the requirements for the degree

DOCTOR OF PHILOSOPHY

Department of Chemistry
College of Arts and Sciences

KANSAS STATE UNIVERSITY
Manhattan, Kansas

2026

Abstract

Noble metal nanomaterials represent one of the most actively pursued research areas in modern science, driven by their wide range of applications in medicine, catalysis, sensing, and optoelectronics. The intriguing optical features observed in these systems have sparked considerable interest, motivating investigations from both experimental and theoretical perspectives. This dissertation focuses on the theoretical front of this endeavor.

In theoretical chemistry, the choice of computational method is a critical decision, one that must carefully balance the desired level of accuracy with the computational cost involved. In this dissertation, we center our approach around density functional theory (DFT), one of the most widely adopted and powerful methods for modeling noble metal nanoclusters, which we employ for ground-state calculations. From there, we take a step further into the excited-state regime through time-dependent density functional theory (TDDFT), a natural and elegant extension of DFT that opens a window into the absorption and photoluminescent properties of these systems. Together, these two complementary frameworks allow us to explore and understand light-matter interactions at their fundamental level.

This dissertation is built around two central objectives, the first of which is addressed in Chapters 3 and 4, where we explore how surrounding environmental factors influence the optical properties of noble metal nanomaterials. In Chapter 3, we investigate the effect of static electric fields on three geometrically distinct Ag_{10} dimer configurations: end-to-end, parallel, and 90° angled arrangements, using TDDFT. We systematically explore how the direction of the applied electric field affects the optical response of these systems, as well as the resulting changes in their molecular orbital characteristics. Building on this theme, Chapter 4 extends our investigation to the electronic structure and excitation characteristics of the $Au_{42}(SCH_3)_{32}$

nanorod, examined across different solvation media. This nanorod is of particular interest due to its experimentally and theoretically validated near-infrared (NIR) absorption peak and dual emission character in its photoluminescence spectra. In this chapter, we further probe its molecular orbital characteristics and investigate the sensitivity of this NIR absorption peak to changes in the surrounding environment, deepening our understanding of how solvation conditions modulate the optical behavior of this system.

The second objective of this dissertation shifts focus towards reducing the computational cost of conventional theoretical frameworks without compromising their accuracy, addressed in Chapters 5 and 6. In Chapter 5, we introduce a machine learning force field (MLFF) for gold hydride nanoclusters, capable of efficiently predicting relative potential energies across diverse cluster configurations at DFT-level accuracy, offering a computationally tractable alternative where exhaustive configurational sampling would otherwise be expensive. Chapter 6 extends the TDDFT plus tight binding (TDDFT+TB) method, which is an approximation to TDDFT, to explore the excited-state potential energy surfaces of open-shell molecular systems, through the derivations and implementation of unrestricted analytical excited-state gradients. A key advantage of TDDFT+TB is its computational efficiency; by introducing approximations at the level of the two-electron integrals, which is the primary computational bottleneck, the method achieves a dramatic reduction in cost compared to conventional TDDFT, while retaining accuracy.

Overall, this dissertation explores light-matter interactions from a theoretical perspective, investigating the influence of external environmental factors on the optical properties, while advancing efficient computational approaches that push the boundaries of theoretical chemistry without sacrificing accuracy.

Lighting up nanoclusters: Path to efficient quantum chemical approaches

by

Don Sulalith Nadun Dinuksha Samarasinghe

B.S., University of Colombo, 2020

A DISSERTATION

submitted in partial fulfillment of the requirements for the degree

DOCTOR OF PHILOSOPHY

Department of Chemistry
College of Art and Sciences

KANSAS STATE UNIVERSITY
Manhattan, Kansas

2026

Approved by:

Major Professor
Christine M. Aikens

Copyright

© Don Sulalith Nadun Dinuksha Samarasinghe 2026.

Abstract

Noble metal nanomaterials represent one of the most actively pursued research areas in modern science, driven by their wide range of applications in medicine, catalysis, sensing, and optoelectronics. The intriguing optical features observed in these systems have sparked considerable interest, motivating investigations from both experimental and theoretical perspectives. This dissertation focuses on the theoretical front of this endeavor.

In theoretical chemistry, the choice of computational method is a critical decision, one that must carefully balance the desired level of accuracy with the computational cost involved. In this dissertation, we center our approach around density functional theory (DFT), one of the most widely adopted and powerful methods for modeling noble metal nanoclusters, which we employ for ground-state calculations. From there, we take a step further into the excited-state regime through time-dependent density functional theory (TDDFT), a natural and elegant extension of DFT that opens a window into the absorption and photoluminescent properties of these systems. Together, these two complementary frameworks allow us to explore and understand light-matter interactions at their fundamental level.

This dissertation is built around two central objectives, the first of which is addressed in Chapters 3 and 4, where we explore how surrounding environmental factors influence the optical properties of noble metal nanomaterials. In Chapter 3, we investigate the effect of static electric fields on three geometrically distinct Ag_{10} dimer configurations: end-to-end, parallel, and 90° angled arrangements, using TDDFT. We systematically explore how the direction of the applied electric field affects the optical response of these systems, as well as the resulting changes in their molecular orbital characteristics. Building on this theme, Chapter 4 extends our investigation to the electronic structure and excitation characteristics of the $Au_{42}(SCH_3)_{32}$

nanorod, examined across different solvation media. This nanorod is of particular interest due to its experimentally and theoretically validated near-infrared (NIR) absorption peak and dual emission character in its photoluminescence spectra. In this chapter, we further probe its molecular orbital characteristics and investigate the sensitivity of this NIR absorption peak to changes in the surrounding environment, deepening our understanding of how solvation conditions modulate the optical behavior of this system.

The second objective of this dissertation shifts focus towards reducing the computational cost of conventional theoretical frameworks without compromising their accuracy, addressed in Chapters 5 and 6. In Chapter 5, we introduce a machine learning force field (MLFF) for gold hydride nanoclusters, capable of efficiently predicting relative potential energies across diverse cluster configurations at DFT-level accuracy, offering a computationally tractable alternative where exhaustive configurational sampling would otherwise be expensive. Chapter 6 extends the TDDFT plus tight binding (TDDFT+TB) method, which is an approximation to TDDFT, to explore the excited-state potential energy surfaces of open-shell molecular systems, through the derivations and implementation of unrestricted analytical excited-state gradients. A key advantage of TDDFT+TB is its computational efficiency; by introducing approximations at the level of the two-electron integrals, which is the primary computational bottleneck, the method achieves a dramatic reduction in cost compared to conventional TDDFT, while retaining accuracy.

Overall, this dissertation explores light-matter interactions from a theoretical perspective, investigating the influence of external environmental factors on the optical properties, while advancing efficient computational approaches that push the boundaries of theoretical chemistry without sacrificing accuracy.

Table of Contents

List of Figures xii
List of Tables xvii
Acknowledgements xxi
Dedication xxiv
Preface xxv
Chapter 1 - Introduction 1
1.1 Light and matter: What? Why? And how? 2
1.2 Potential energy surface (PES) 4
1.3 Atomically precise metal nanoclusters 6
1.4 From experimental to theoretical understanding 9
1.5 Objectives of the dissertation 9
1.6 References 10
Chapter 2 - Theory and methods 14
2.1 Schrödinger and electronic structure theory 14
2.2 Basis sets: A representation of molecular orbitals 17
2.3 Density functional theory 20
2.4 Types of exchange-correlation (xc) functionals 22
2.5 Time-dependent density functional theory (TDDFT) 24
2.5.1 Linear-response time-dependent density functional theory (LR-TDDFT) 25
2.5.2 Approximation methods to time-dependent density functional theory 27
2.6 Implicit and explicit solvent models 28
2.7 Machine learning approaches and quantum chemistry 31
2.8 References 34
Chapter 3 - Effects of static electric fields on the excitations of silver nanowire dimers 40
3.1 Abstract 40
3.2 Introduction 41
3.3 Theory and computations 42
3.4 Results and discussion 44
3.4.1 Ag_{10} end-to-end dimer system 44

3.4.2 Monomer vs. dimer systems 49
3.4.3 Ag_{10} parallel dimer system within a static electric field 50
3.4.4 Ag_{10} 90° dimer system within a static electric field 53
3.4.5 Transverse excitations in Ag_{10} dimer systems within a static electric field 56
3.5 Conclusion 57
3.6 Appendix A - Supporting information 58
3.7 Acknowledgements 59
3.8 References 59
Chapter 4 - Theoretical insights into the excitation characteristics of the $Au_{42}(SCH_3)_{32}$ nanorod in the near-infrared region 64
4.1 Abstract 64
4.2 Introduction 65
4.3 Theory 68
4.4 Results and discussion 70
4.4.1 Gas phase studies 70
4.4.2 Solvation effects on the structure geometry and the excitation characteristics 76
4.5 Conclusion 83
4.6 Appendix B - Supporting Information 84
4.7 Acknowledgments 84
4.8 References 84
Chapter 5 - Development of a machine learning force field for gold hydride nanoclusters that predicts potential energy with quantum-level precision 89
5.1 Abstract 89
5.2 Introduction 90
5.3 Theory 93
5.3.1 Sparse Gaussian process (SGP) to model the machine learning force field 93
5.3.2 Training procedure and structure selection 97
5.3.3 Testing and validation of the machine learning force field 100
5.4 Results and Discussion 103
5.4.1 MLFF vs. DFT potential energy prediction at 300 K 103
5.4.2 Structural landscape analysis 107

5.5 Conclusion 114
5.6 Data availability 115
5.7 Appendix C – Supporting Information 116
5.8 Acknowledgments 117
5.9 References 117
Chapter 6 - Implementation of analytical excited state gradients for open-shell systems in time-dependent density functional theory plus tight binding (TDDFT+TB) method 122
6.1 Abstract 122
6.2 Introduction 123
6.3 Theory 127
6.3.1 Excited state properties 127
6.3.2 Derivative of the excitation energy 129
6.4 Computational approach 135
6.4.1 Numerical vs. analytical excited state gradient comparison 137
6.4.2 Excited state geometry optimization 141
6.4.3 Total runtime for excited state geometry optimization 144
6.5 Discussion 149
6.6 Conclusion 150
6.7 Appendix D – Supporting Information 151
6.8 Acknowledgments 151
6.9 References 152
Chapter 7 - Conclusion and next steps 157
Appendix A - Supporting information for: Effects of static electric fields on the excitations of silver nanowire dimers 160
Appendix B - Supporting information for: Theoretical insights into the excitation characteristics of the $Au_{42}(SCH_3)_{32}$ nanorod in the near-infrared region 177
Appendix C - Supporting information for: Development of a machine learning force field for gold hydride nanoclusters that predicts potential energy with quantum-level precision 184
Appendix D - Supporting information for: Implementation of analytical excited state gradients for open-shell systems in time-dependent density functional theory plus tight binding (TDDFT+TB) method 189

Appendix E - Copyright Permissions 221

List of Figures

Figure 1.1. Jablonski diagram summarizing radiative (absorption, fluorescence, and phosphorescence) and nonradiative (vibrational relaxation, internal conversion, and intersystem crossing) transitions. Reprinted with permission from J. Chem. Educ. 2024, 101 (11), 5097–5104. Copyright 2024, American Chemical Society..... 5

Figure 1.2. Selected luminescent homogold NCs and their PL properties (QY and peak position). The ligands on the NCs are omitted for clarity. NIR = near-infrared, I: 700–1000 nm, II: 1000–1700 nm. Reprinted from the permission from *Adv. Mater.* 2024, *36* (8), 2309073. Copyright 2023 The Authors. Advanced Materials published by Wiley-VCH GmbH..... 7

Figure 1.3. (A) Chemical structure of the mixed phosphine–stibine ligand (SbP_3); (B) total structure of $[Au_6(SbP_3)_2]^{2+}$ cluster; (C) structure of the Au_6 core comprised of two Au_4 tetrahedra which assemble together by sharing a common Au_2 edge (highlighted in green) (colour labels: brown/green = Au; orange = P; blue = Sb, grey = C; H atoms are not shown for clarity). Reprinted with permission from *Nanoscale* 2023, *15* (15), 6934–6940. Copyright 2023, Royal Society of Chemistry..... 8

Figure 2.1. Example GTO and cGTOs intended to represent the hydrogenic 1s atomic orbital, overlayed with an STO for comparison. The GTO uses one Gaussian function to reproduce the shape of the 1s function; cGTO(2) and cGTO(3) are linear combinations of two and three Gaussian functions to better represent the cusp and exponential decay for longer distances. Reprinted with permission from *Mathematical Physics in Theoretical Chemistry*; Elsevier, 2019; pp 31–61. Copyright 2019, Elsevier Inc..... 19

Figure 2.2. Schematic representation of solvent models. Reprinted with permission from *Top. Catal.* 2022, *65*, 118–140. Copyright 2021, The Author(s), Springer Nature..... 30

Figure 2.3. Evolution of the research workflow in computational chemistry. The standard paradigm spanning from first-generation to third-generation computational approaches is shown alongside the four stages of machine learning model training, with common methodological choices listed in the bottom panel. Reprinted with permission from *Nature* 2018, *559*, 547–555. Copyright 2018, Macmillan Publishers Ltd., part of Springer Nature.32

Figure 3.1. Geometries and orientations of the dimer systems..... 43

Figure 3.2. (a) Calculated absorption spectra for Ag_{10} end-to-end dimer system with and without the static electric field applied in the z-direction. (b) Allowed transitions of the excitations: without an electric field (left) and with the application of a static electric field in the z-direction (right). 45
Figure 3.3. Illustrations of major molecular orbitals of Ag_{10} end-to-end dimer system, with and without the static electric field of 0.1 V/Å. Two views (with different iso-surface values) are provided for the z-direction field. Respective iso-surface values are denoted within the parentheses. 46
Figure 3.4. (a) Calculated absorption spectra for Ag_{10} end-to-end dimer system with and without the static electric field applied in the y-direction. (b) Allowed transitions of the excitations with the y-directional static electric field. 47
Figure 3.5. Graphical interpretation of the static electric field effect on the HOMO-4 molecular orbital of the end-to-end Ag_{10} dimer system; (a) without the electric field, (b) within the z-directional electric field, and (c) with the y-directional electric field (the yz plane shows the nanowires' geometric orientation). The iso-surface values are the same as in Figure 3.3. However, to appropriately demonstrate the effect, the molecular orbitals in the z-directional electric field is shown as a composite of multiple iso-surface values (with 0.015 for the left nanowire and 0.0009 for the right nanowire). 48
Figure 3.6. Calculated absorption spectra for Ag_{10} parallel dimer system with and without the static electric field (a) applied in the z-direction and (b) applied in the y-direction. 51
Figure 3.7. Illustrations of major molecular orbitals of Ag_{10} parallel dimer system, with and without the static electric field of 0.1 V/Å. 52
Figure 3.8. Calculated absorption spectra for the Ag_{10} 90° dimer system with and without the static electric field (a) applied in the z-direction and (b) applied in the y-direction. 54
Figure 3.9. Illustrations of major molecular orbitals of the Ag_{10} 90° dimer system, with and without the static electric field of 0.1 V/Å. Orbitals from HOMO-2 to HOMO-5 are given in Figure A.8. 55
Figure 3.10. Calculated absorption spectra indicating the transverse excitation for (a) Ag_{10} end-to-end dimer system (b) Ag_{10} parallel dimer system (c) Ag_{10} 90° dimer system, with and without the static electric field applied in the z- and y-directions. 57

Figure 4.1. Structure of the $Au_{42}(SR)_{32}$ nanorod (color labels: gold = core Au; dark green = Au from $Au_4(SR)_5$ motifs; light green = Au from $Au(SR)_2$ motifs; yellow = S). R groups of the staple motifs are omitted for clarity. 67
Figure 4.2. Atom definitions for $Au_{42}(SR)_{32}$. 71
Figure 4.3. (a) HOMO and LUMO orbitals (Iso-surface = 0.01) and (b) energy level diagram for $Au_{42}(SCH_3)_{32}$ at the BP86-D3/TZP level of theory. 72
Figure 4.4. (a) NIR region of the theoretical absorption spectrum at the BP86-D3/TZP level of theory, (b) energy level diagram of the molecular orbitals showing atomic orbital character and the corresponding electronic transitions of the two excitations, and (c) HOMO-1 of the $Au_{42}(SCH_3)_{32}$ nanorod (Iso-surface = 0.01). 74
Figure 4.5. Jablonski diagram depicting photophysical processes in $Au_{42}(SCH_3)_{32}$ nanorod: absorption (A1 and A2), fluorescence (F1), and phosphorescence (P1) with calculated energies at the BP86-D3/TZP level of theory. 76
Figure 4.6. Theoretical NIR absorption spectra at the BP86-D3/TZP level of theory for toluene and DMAc compared with the gas phase absorption spectrum. 78
Figure 4.7. Solvent dependent excitation properties of the $Au_{42}(SCH_3)_{32}$ nanorod as a function of dielectric constant: (a) excitation energies, (b) oscillator strengths, (c) HOMO → LUMO electronic transition contribution, and (d) HOMO-1 → LUMO electronic transition contribution for both $\boldsymbol{\alpha}$ and $\boldsymbol{\beta}$ excitations. 80
Figure 5.1. Gold hydride nanocluster systems used in the active learning phase (color labels: orange = Au and teal = H). 99
Figure 5.2. Gold hydride nanocluster systems used for validation and testing that are not included in the training database (color labels: orange = Au and teal = H). 102
Figure 5.3. MLFF-predicted vs. DFT reference potential energies throughout the MD simulations for (a) $Au_{13}H_5$ edge, (b) $Au_{13}H_5$ bridge I, (c) $Au_{13}H_5$ bridge II, (d) $Au_{18}H_{14}$, (e) $Au_{20}H_{16}$, (f) $Au_{24}H_{16}$, (g) $Au_{28}H_{20}$, (h) $Au_{30}H_{18}$, (i) $Au_{36}H_{24}$, and (j) $Au_{38}H_{24}$ clusters. 107
Figure 5.4. Prediction accuracy per atom for structures (a) included in the training set and (b) outside the training set, after applying constant energy offsets (Figure C.1 shows energies before offset correction). Data points correspond to the systems presented in Figure 5.3. 107
Figure 5.5. Box plots showing RMSDs for (a) gold atoms and (b) hydrogen atoms across all tested systems during 300 K MD simulations. 109

Figure 5.6. Box plots showing total RMSDs for (a) $Au_{24}H_{16}$, (b) $Au_{30}H_{18}$, and (c) $Au_{36}H_{24}$ clusters during the MD simulations at respective temperatures. 111
Figure 5.7. MLFF-predicted vs. DFT reference potential energies throughout the MD simulations for (a) $Au_{24}H_{16}$ at 200 K, (b) $Au_{24}H_{16}$ at 400 K, (c) $Au_{30}H_{18}$ at 200 K, (d) $Au_{30}H_{18}$ at 400 K, (e) $Au_{36}H_{24}$ at 200 K, and (f) $Au_{36}H_{24}$ at 400 K. 113

Appendix Figure A.1. Calculated absorption spectra for Ag_{10} end-to-end dimer system with and without the static electric field applied in z-direction using (a) BP86 and (b) long-range corrected (LC) CAMY-B3LYP functionals. 160
Appendix Figure A.2. Calculated absorption spectra for Ag_{10} parallel dimer system with and without the static electric field applied in z-direction using (a) BP86 and (b) long-range corrected (LC) CAMY-B3LYP functionals. 161
Appendix Figure A.3. Calculated absorption spectra for Ag_{10} 90° dimer system with and without the static electric field applied in z-direction using (a) BP86 and (b) long-range corrected (LC) CAMY-B3LYP functionals. 162
Appendix Figure A.4. Calculated absorption spectra for Ag_{10} monomer with and without the static electric field applied in the z-direction and y-direction. 163
Appendix Figure A.5. Calculated absorption spectra for Ag_{20} monomer with and without the static electric field applied in the z-direction and y-direction. 164
Appendix Figure A.6. Illustrations of the molecular orbitals of Ag_{10} monomer, with and without the static electric field of 0.1 V/Å. 165
Appendix Figure A.7. Illustrations of the molecular orbitals of Ag_{20} monomer, with and without the static electric field of 0.1 V/Å. 166
Appendix Figure A.8. Illustrations of additional molecular orbitals of the Ag_{10} 90° dimer system, with and without the static electric field of 0.1 V/Å in the y-direction. 167
Appendix Figure B.1. The theoretical absorption spectrum at the BP86-D3/TZP level of theory (in gas phase) of the $Au_{42}(SCH_3)_{32}$ nanorod. 178
Appendix Figure B.2. Atomic orbital character for each molecular orbital for the respective electronic states at the BP86-D3/TZP level of theory (in gas phase). 179
Appendix Figure C.1. Prediction accuracy per atom for structures outside the training set before offset corrections. 186

Appendix Figure C.2. Box plots showing total RMSDs across all tested systems during 300 K MD simulations. 187
Appendix Figure C.3. Box plots showing RMSDs at different temperatures for (a,c,e) gold atoms and (b,d,f) hydrogen atoms in $Au_{24}H_{16}$, $Au_{30}H_{18}$, and $Au_{36}H_{24}$, respectively. 188
Appendix Figure D.1. Different valence electronic configurations and how the "SPINPOLARIZATION" keyword is used based on the number of unpaired electrons. .. 201
Appendix Figure D.2. Relative energy of the HHe molecule in ground and excited states respect to the H-He bond length (at the PW92/DZP level of theory). The excited state potential energy surface represents the energy difference between D_1 and D_0 depending on the computational method used: TDDFT or TDDFT+TB. 212

List of Tables

Table 4.1. The comparison of average bond lengths between the experimental crystal structure and gas-phase optimized geometry (at the BP86-D3/TZP level of theory). Percent deviations (Δ) are calculated relative to the crystal structure values. Bond lengths are reported in Å. 71

Table 4.2. Excitation properties of the $Au_{42}(SCH_3)_{32}$ nanorod obtained from TDDFT calculations at the BP86-D3/TZP level of theory, including excitation energies, oscillator strengths, and the corresponding electronic transitions with their orbital contribution weights. 75

Table 4.3. Average bond lengths for ground state optimized geometries using toluene and DMAc phases (at the BP86-D3/TZP level of theory). Bond lengths are reported in Å. 77

Table 4.4. Excitation properties of the $Au_{42}(SCH_3)_{32}$ nanorod within toluene and DMAc solvation media obtained from TDDFT calculations at the BP86-D3/TZP level of theory, including excitation energies, oscillator strengths, and the corresponding electronic transitions with their orbital contribution weights. 78

Table 5.1. $\boldsymbol{Nrad}$ and $\boldsymbol{lmax}$ values employed in each training cycle. 95

Table 5.2. Tolerance factors and the optimized hyperparameters for each training cycle. 96

Table 5.3. Structural database composition for each training cycle by cluster type. 100

Table 5.4. Energy offsets, MAD, and RMSE values for tested gold hydride clusters. 104

Table 5.5. Energy offsets, MAD, and RMSE values for selected gold hydride clusters in different temperatures. 112

Table 6.1. Numerical vs. analytical gradient differences for excited states (D_1/T_1) of open-shell diatomic molecules (Hartree/Å). 139

Table 6.2. Numerical vs. analytical gradient differences for excited states (D_1/T_1) of small open-shell organic radical and charged species (Hartree/Å). 139

Table 6.3. Emission energy differences between TDDFT and TDDFT+TB for open-shell diatomic molecules. 143

Table 6.4. Emission energy differences between TDDFT and TDDFT+TB for open-shell small organic radical and charged species. 143

Table 6.5. Computational runtime required for excited state geometry optimization of open-shell diatomic molecules using TDDFT and TDDFT+TB methods. 146
Table 6.6. Computational runtime required for excited state geometry optimization of small open-shell organic radical and charged species using TDDFT and TDDFT+TB methods. 147

Appendix Table A.1. Longitudinal excitation energies for Ag_{10} end-to-end dimer system with and without the static electric field applied in z-direction using different functionals. 167
Appendix Table A.2. . Longitudinal excitation energies for Ag_{10} parallel dimer system with and without the static electric field applied in z-direction using different functionals. 168
Appendix Table A.3. Longitudinal excitation energies for Ag_{10} 90° dimer system with and without the static electric field applied in z-direction using different functionals. 169
Appendix Table A.4. Excitation energies for Ag_{10} monomer with and without the static electric field (with LC BP86 functional). 170
Appendix Table A.5. Excitation energies for Ag_{20} monomer with and without the static electric field (with LC BP86 functional). 171
Appendix Table A.6. Comparison of the transverse excitations and their orbital representations for the dimer systems with and without the static electric field applied in the z- and y-directions. 172
Appendix Table A.7. Ag_{10} end-to-end dimer coordinates. 173
Appendix Table A.8. Ag_{10} parallel dimer coordinates. 174
Appendix Table A.9. Ag_{10} 90° dimer coordinates. 175
Appendix Table B.1 Molecular orbital characteristics for $Au_{42}(SCH_3)_{32}$ at the BP86-D3/TZP level of theory (in gas phase). 179
Appendix Table B.2. Excitation properties of the $Au_{42}(SCH_3)_{32}$ nanorod in DCM, acetone, DMBA, and DMFA solvation media obtained from TDDFT calculations at the BP86-D3/TZP level of theory, including excitation energies, oscillator strengths, and the corresponding electronic transitions with their orbital contribution weights. 180
Appendix Table B.3. Relative ground and excited state energies. Note: S_1/S_2 ordering reverses between gas phase and polar solvents due to differential stabilization. States are labeled $\mathbf{E\alpha}$ and $\mathbf{E\beta}$ ($\mathbf{E\alpha}$: excited state corresponding to $\boldsymbol{\alpha}$ excitation and $\mathbf{E\beta}$: excited state corresponding to $\boldsymbol{\beta}$ excitation) for consistency across all media (energies are reported in eV). 181

Appendix Table B.4. Total transition dipole moments (in *x*, *y*, and *z* directions) for each excitation in different solvation media. 181
Appendix Table B.5. Transition dipole moment contributions (in *x*, *y*, and *z* direction) for each electronic transition, corresponding to the excitations in different solvation media. 182
Appendix Table C.1. Relative energies of the three $Au_{13}H_5$ nanocluster conformers considered in this work at the BP86/TZP level of theory. 185
Appendix Table D.1. Literature sources for the molecules used in this study. 202
Appendix Table D.2. Numerical vs. analytical gradient differences for excited state (D_1/T_1) of open-shell molecules at different numerical displacement values (at the PW92/DZP level of theory with "Very Good" numerical quality). MAD values are in Hartree/Å. 205
Appendix Table D.3. Excited state geometry optimization for the T_1 state of O_2 using various exchange-correlation functionals (XC), basis set, and numerical quality..... 207
Appendix Table D.4. Excited state geometry optimization for the T_1 state of O_2 using different numbers of compute cores. It should be noted that the O_2 molecule is a very small test case, and thus very little gain in speedup is achieved for more than 4 cores..... 208
Appendix Table D.5. Excited state geometry optimization for the D_1 state of pyrazine radical cation using various exchange-correlation functionals (XC), basis set, and numerical quality. 209
Appendix Table D.6. Excited state geometry optimization for the D_1 state of pyrazine radical cation using different number of compute cores..... 210
Appendix Table D.7. Numerical vs. analytical gradient differences for excited states of closed-shell diatomic molecules (Hartree/Å). 211
Appendix Table D.8. Spin-contaminations for excited states (D_1/T_1) of open-shell diatomic molecules using TDDFT and TDDFT+TB. 213
Appendix Table D.9. Spin-contaminations for excited states (D_1/T_1) of small open-shell organic radical and charged species using TDDFT and TDDFT+TB methods..... 213
Appendix Table D.10. Comparison of spin-contaminations for the excited states (D_1) of selected open-shell diatomic molecules with previously reported values by Ipatov et al.[19] Spin-contamination values are reported with respect to the method employed. 215
Appendix Table D.11. Comparison of excitation energies ($E_{TDDFT+TB}$) of selected open-shell diatomic molecules and small open-shell organic radical and charged species with

experimental and/or theoretical excitation energies ($E_{Reference}$). Excitation energies are provided in eV..... 216

Acknowledgements

I would like to begin by expressing my heartfelt and deepest gratitude to my advisor, Prof. Christine Aikens, without whom none of this would exist. When I first joined her group, I could not have imagined that I would one day produce a body of work like this. Yet, through her patient guidance, expectations, and genuine investment in my research development, here we are. She guided me into the depths of theoretical chemistry, shaped my ability to manage multiple projects with clarity and focus, and introduced me to the computational tools that become central to my research. She also connected me with wonderful experimental collaborators, each who enriched this work in their own way. I am forever grateful not just for the science she taught me, but for the confidence, resilience, and intellectual independence she helped me build. Prof. Christine thank you for everything.

I would like to extend my sincere gratitude to my committee members: Prof. Paul Smith, Prof. Daniel Higgins, and Prof. Bin Liu, for the continuous support and thoughtful guidance throughout this journey. I am truly grateful for your time and expertise.

Some of the most exciting moments of my doctoral years came through collaborations, and for that I am truly grateful. Working with Prof. Stefan Bossmann, Prof. Anindita Das, Prof. Rongchao Jin, Prof. Kenneth Knappenberger Jr., Prof. Hui Shen, Prof. Noelia Barrabés, and Dr. Elizabeth Ploetz broadened my scientific horizons. Each project we undertook together uncovered something new and unexpected, and I am richer as a scientist for every one of those experiences. I would also like to extend my heartfelt thanks to the SCM team, and especially to Dr. Erik van Lenthe and Dr. Robert Rüger, whose unwavering support and deep expertise were central to the analytical gradients project.

I am equally grateful to have been surrounded by such a wonderful group of colleagues in the Aikens Group. To every member: Dr. Gowri Udayangani Kuda-Singappulige, Dr. Pratima Pandeya, Dr. Zhen Liu, Dr. Olivia Hull, Dr. Shana Havenridge, Dr. Yuchen Wang, Paul Javed, Gayathri Habarakadage, Dmitri Leenatali, Jonathan Bvunzawabaya, Damith Aluthge, Dushmanthi Wasala Mudiyanselage, Peter Gorges, and Brie Little, thank you for five years of scientific discussions, shared laughter, and fond memories. I will never forget your support. I would also like to thank Prof. Bin Liu, Prof. Saswata Dasgupta, and all their group members for the enriching joint group meeting we shared.

My academic roots trace back to the Department of Chemistry at the University of Colombo, Sri Lanka, and I am forever grateful for the education and mentorship I received there. I would like to especially thank my undergraduate research advisor, Prof. Neranga Abeyasinghe, for sparking my passion for theoretical chemistry research, and Prof. Samantha Weerasinghe, whose vision and dedication have been the backbone of computational chemistry at the university, inspiring generations of students, me included. I am also sincerely thankful to Prof. Hasini Perera for her support and guidance throughout my undergraduate years. To all the faculty members at the University of Colombo who taught, mentored, and encouraged me along the way, this work carries a piece of your effort too. Thank you!

Moving thousands of miles from home is never simple, but the warmth of the people around me made every difficult moment bearable. The K-State Sri Lankan community and my wonderful friends embraced me in a way I will always cherish, giving me a sense of belonging far from home. My friends from school and university, though spread across the world, remained as close as ever, meeting whenever and wherever life allowed. You have always been more than friends to me, you are my brothers and sisters.

Lastly, I want to express my love and gratitude to my family. To my mother, father, and sister, thank you for your boundless love and support. To my uncle, aunt, father-in-law, mother-in-law, and brother-in-law, you are such wonderful souls, always checking in on me, and I am at a loss for words to express how much that meant. And finally, to my wife, Sahani. You are walking this same difficult path as a Ph.D. candidate yourself, yet you gave more support than I could have ever asked for. I do not know how I will ever repay you. I love you with all my heart.

Dedication

Every journey is shaped by countless invisible hands. People whose paths briefly crossed mine, whose words, actions, or presence left a mark I may not have fully recognized at the time. To each and every one of you, known and unknown, near and far, you are a part of this work too, and this is for you!

Preface

The following peer-reviewed journal articles have been published as part of the research conducted during this doctoral program at Kansas State University:

1. Samarasinghe, D. S. N. D.; Aikens, C. M. Effects of Static Electric Fields on the Excitations of Silver Nanowire Dimers. *J. Phys. Chem. A* **2024**, *128* (18), 3548–3556. (This work is presented in Chapter 3 of this dissertation)

2. Wang, Y.; Samarasinghe, D. S. N. D.; Deng, H.; Liu, B.; Aikens, C. M. Gaussian Process Approach to Constructing Transferable Force Fields for Thiolate-Protected Gold Nanoclusters. *J. Chem. Inf. Model.* **2025**, *65* (8), 3892–3902.

3. Seal, N.; Samarasinghe, D. S. N. D.; Siegler, M. A.; Vodnala, N.; Aikens, C. M.; Das, A. Distibine versus Diphosphine Ligands: Modulating the Properties of Isostructural $Au_{13}Cu_2$ Nanoclusters. *Chem. Mater.* **2025**, *37* (24), 9908–9918.

4. Sardar, A.; Wang, Y.; He, G.; Gianopoulos, C. G.; Samarasinghe, D. S. N. D.; Liu, Z.; Kirschbaum, K.; Aikens, C. M.; Jin, R. $Au_{20}Ag_{32}$ Nanocluster Emitting Bright Near-Infrared-II Photoluminescence with Quantum Yield of 30% in Aerated Solution. *ACS Nano* **2026**, *20* (10), 8827–8837.

5. Yan, B.; Samarasinghe, D. S. N. D.; Sun, J.; Deng, H.; Li, L.; Qi, M.; Zhao, F.; Xu, Q.; Guo, H.; Sun, X.; Gong, X.; Huo, R.; Zhu, M.; Wu, Q.; Xie, Z.; Xin, C.; Wang, Y.; Jiang, X.; Li, S.; Li, F.; Zhou, M.; Aikens, C. M.; Zheng, N.; Shen, H. Engineering Molecular Rotor-Stator Ligand Architectures on Copper Nanoclusters for Efficient Photothermal Conversion. *Nat. Commun.* **2026**, *17* (1), 3388.

Chapter 1 - Introduction

It all began with a “Big Bang”! Tracing back in time, our universe is estimated to be 13.8 billion years old (or 12.5 billion, depending on which technique you use to calculate the time).[1-3] At the very beginning, the fundamental forces governing nature existed as a unified entity. Within approximately ~10^{-10} seconds, the electromagnetic force split to become independent.[1,2] In this brief instant, quarks combined to create protons and neutrons, the fundamental constituents of atomic nuclei.[1,2,4] Minutes later, simple nuclei had emerged. However, it took considerably longer time (approximately 380,000 years) for an atom to form, with electrons bound to a central nucleus.[1,2,4] Through the cosmic expansion and the passage of time, a branch of science known as chemistry emerged with the dedication to understanding these various atoms and their culminations (e.g., molecules and clusters), exploring not only their remarkable properties but also transforming this understanding into practical applications that shape our daily lives.

In the modern era, the field is no longer a singular discipline but has evolved through countless discoveries to branch into numerous specialized subsections, from understanding simple reaction coordinates to synthesizing complex nanoclusters applicable to diverse medicinal applications such as cancer therapy. Yet throughout this evolution, two fundamental concepts have remained intertwined and central to scientific investigations from the very beginning: matter and light. Therefore, in the following section, we will delve deeper into the nature of matter and light and explore why their relationship is so fundamentally important.

1.1 Light and matter: What? Why? And how?

Since ancient times, philosophers have been intrigued by the question of how we see. To explain this phenomenon, they developed various theories. Some of these theories proposed that vision results from light emitted by both objects and the eyes themselves. However, philosophers such as Epicurus suggested that light originates from sources other than the eye and that vision occurs when light reflected from objects enters the eye.[5] In the late 17th century, Sir Isaac Newton demonstrated that white light can be separated into its component colors using a prism. When light passes through a prism, it bends due to refraction as it transitions from one medium to another.[5,6] In 1905, Albert Einstein explained the photoelectric effect, which elucidated the interaction of light with matter at the atomic level, for which he was awarded the Nobel Prize in Physics.[5,7]

In the modern era, we understand visible light as a form of electromagnetic radiation, an energy flow characterized by oscillating electric and magnetic fields that are mutually perpendicular and transverse to the direction of wave propagation.[8] This energy can travel through free space or through a material medium. From the classical perspective, electromagnetic radiation manifests as waves, with the electromagnetic spectrum spanning a broad range of frequencies that encompasses not only visible light but also microwaves, infrared radiation, ultraviolet radiation, X-rays, and gamma rays. With the advent of quantum mechanics, electromagnetic radiation came to be described through a fundamentally different lens. In quantum terms, electromagnetic radiation is understood as a stream of photons, which are discrete packets of energy known as quanta.[5] More importantly, quantum mechanics changes our understanding not only of light but also of matter, leading to theories that explain how the

electronic structure of atoms with quantized energy levels can exist.[5,9] In the next section, we will discuss how light interacts with electronic structure in more detail.

From an experimental standpoint, proper methods were needed to understand and study the interaction between matter and light (or electromagnetic radiation). This gave rise to spectroscopy, a suite of methods developed specifically to investigate the interaction of matter and light. Spectroscopic techniques are used to study the absorption, emission, or scattering phenomena of different materials, providing valuable information about their properties. Depending on which wavelengths of electromagnetic radiation and which type of phenomena are of interest, a vast variety of methods can be applicable. Among these numerous techniques, ultraviolet-visible spectroscopy measures absorption profiles in the ultraviolet and visible regime and is useful for understanding the optical properties and electronic transitions of materials, while the corresponding emission measurements are obtained through fluorescence spectroscopy. Infrared spectroscopy is primarily used for identifying vibrational modes and functional groups within systems, whereas X-ray diffraction methods provide information about crystal structures and atomic arrangement of materials.[5,10] To date, spectroscopic methods have been employed not only in chemistry but across most scientific disciplines, including physics, astronomy, biology, and many others.

As evident from these examples, the interaction between light and matter is fundamentally important for understanding the structure-property relationships of different materials. In the research field, knowledge of these fundamental aspects provides the foundation for addressing broader scientific challenges.

1.2 Potential energy surface (PES)

Energy is ubiquitous in nature, and molecular systems are no exception, as each atomic configuration of a molecule has an associated potential energy. Through the collective efforts of brilliant minds, methods have been developed to describe the energetic landscape of molecular systems. This is accomplished through a potential energy surface (PES), which defines molecular potential energy as a function of the relevant nuclear degrees of freedom. As discussed by Schlegel,[11] a PES can exhibit fascinating topological features that resemble mountainous terrain, complete with peaks, valleys, and saddle points. While a PES can span an enormous configurational space, the stationary points on this surface play unique roles in elucidating different physical aspects of the molecular system. These may include determining reaction energies, reaction rates, and vibrational spectra.

The ground state of a molecule represents its lowest possible energy state, where electrons occupy the orbitals closest to the nucleus in their most stable arrangement. But what happens when these molecules are exposed to an external energy source (electromagnetic radiation)? If the energetics are favorable, electrons in the ground state will absorb this energy and transition to higher electronic levels, resulting in less stable configurations compared to the ground state. Now we have transitioned from the ground state to an excited state. As with the ground state, each excited state possesses its own distinct PES, and the energy separation between electronic states gives rise to the system's electronic absorption spectrum. Similar to the ground state PES, excited state PESs provide valuable information about molecular properties in excited states, including excited state geometries, excitation energies, and emission energies (via fluorescence and phosphorescence).[11-13]

Figure 1.1 provides a clear depiction of the PES in the form of a Jablonski diagram for both ground and excited states, and understanding this general representation is fundamental to the discussion that follows. It is important to note that electronic transitions between energy levels can be categorized into two main types: radiative and non-radiative transitions. The key difference between these two types lies in whether photons are involved or not, where radiative transitions result due to the absorption or emission of photons, whereas non-radiative transitions occur without photon exchange. These transitions are further characterized according to the spin multiplicity of the electronic states participating in the process. Transitions between two electronic states of the same spin multiplicity include fluorescence, internal conversion, and vibrational relaxation, while transitions between different spin multiplicities include phosphorescence and intersystem crossing.[11-13]

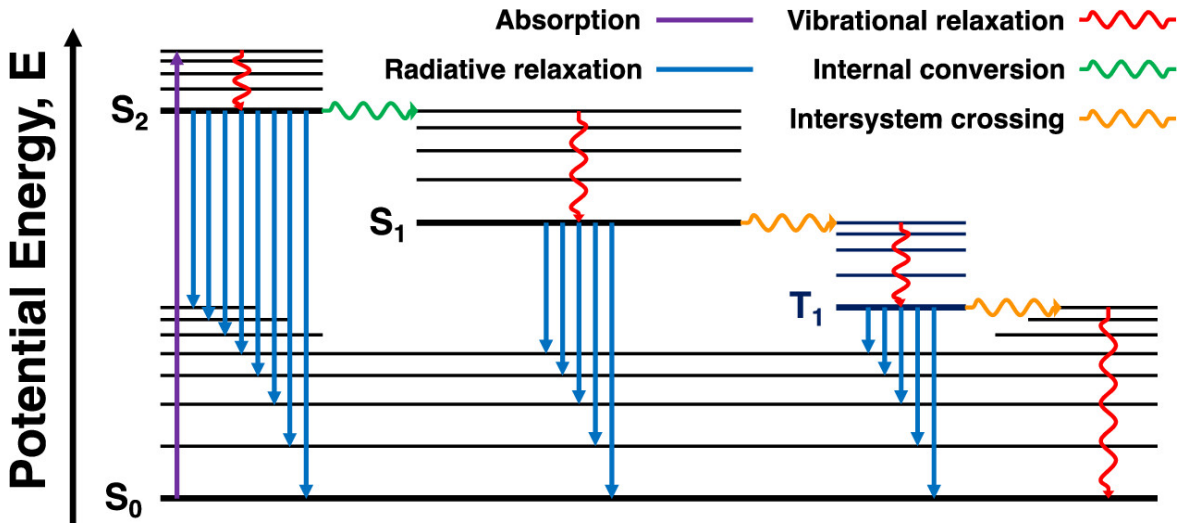


Figure 1.1. Jablonski diagram summarizing radiative (absorption, fluorescence, and phosphorescence) and nonradiative (vibrational relaxation, internal conversion, and intersystem crossing) transitions. Reprinted with permission from J. Chem. Educ. 2024, 101 (11), 5097–5104. Copyright 2024, American Chemical Society.

As Figure 1.1 illustrates, light-matter interactions are far from simple, as they can proceed through various pathways that ultimately yield different outcomes; outcomes that prove

significantly useful for applications across diverse fields. In this dissertation, we will focus on atomically precise metal nanoclusters and their corresponding light-matter interactions. Therefore, in the following section, we will discuss atomically precise nanochemistry and why it represents an important field for investigating light-matter interactions.

1.3 Atomically precise metal nanoclusters

Most methods of making nanomaterials create particles that vary in shape, size, and composition. These differences matter because they affect how the materials behave.[14-18] Therefore, making nanomaterials with exact atomic control is crucial. When we know exactly how structure relates to properties, we can design materials that works consistently and predictably for many different uses. Atomic-level control becomes essential when materials reach ultrasmall dimensions, typically in the range of 1 to 3 nm in diameter for nanoparticles (or nanoclusters).[15,16] As Yu et al. aptly stated, at this scale *"every atom counts"*.[14] In other words, changes in the number of atoms and even the changes in atom positions can lead to significant changes in materials behavior (for example, conformational changes of Au nanoclusters can lead to different optical and chiroptical measurements[19-21]), reflecting that achieving atomic precision is crucial when working at this scale.

Advances in nanochemistry over recent decades have made it possible to synthesize atomically precise nanomaterials, with metal nanoclusters being a prominent example.[14] Since the twentieth century, metal nanoparticles have attracted considerable interest owning to their distinctive optical phenomenon called localized surface plasmon resonance (LSPR), which arises from the collective oscillation of conduction band electrons when exposed to electromagnetic radiation.[16,22,23] But at the level of atomic precision, metal nanoclusters occupy an intermediate

position between atomistic and plasmonic nature, displaying characteristic molecular-like behavior.[16] Therefore, understanding the light-matter interactions of these atomically precise metal nanoclusters represents one of the forefronts of modern research. Figure 1.2 shows a selection of gold nanoclusters with emission wavelengths spanning from the visible to near-infrared regions.[15] These intriguing optical properties, combined with the enhanced stability and biocompatibility exhibited by metal nanoparticles, have led to proposed applications in medical diagnostics,[17,24,25] catalytic processes,[26,27] chemical sensing,[24,28] light harvesting,[29] and beyond.[15,16]

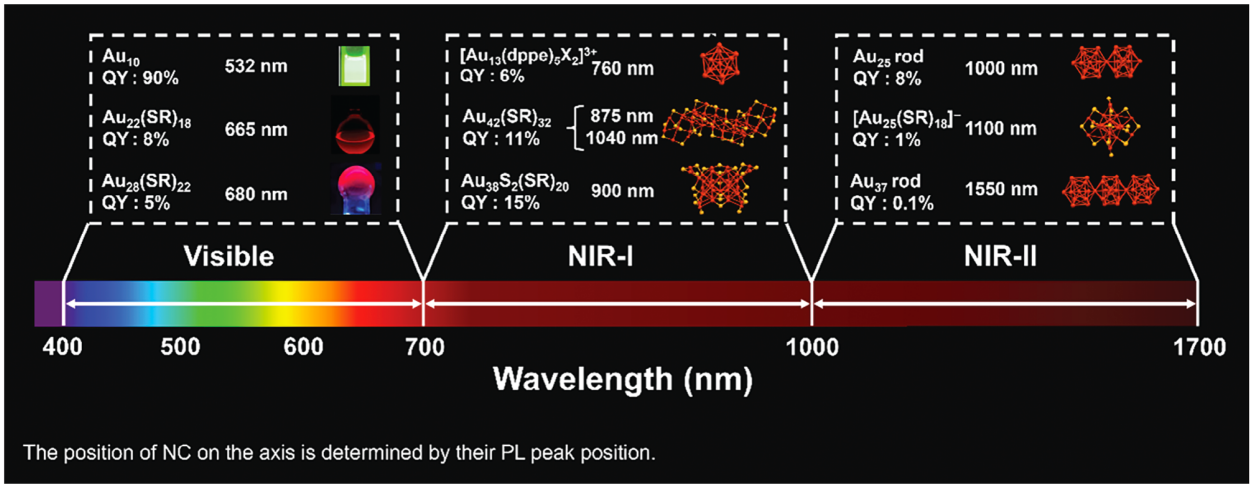


Figure 1.2. Selected luminescent homogold NCs and their PL properties (QY and peak position). The ligands on the NCs are omitted for clarity. NIR = near-infrared, I: 700–1000 nm, II: 1000–1700 nm. Reprinted from the permission from *Adv. Mater.* 2024, *36* (8), 2309073. Copyright 2023 The Authors. Advanced Materials published by Wiley-VCH GmbH.

Among these atomically precise nanoclusters, investigation of Au, Ag, and Cu based clusters are at the forefront. A key challenge with these metals is that their tendency to aggregate when unprotected, driven by their high surface energy.[18] To prevent this aggregation, protective ligands are essential for stabilizing the nanoclusters. Researchers have developed diverse synthetic strategies that utilize a wide range of stabilizing ligands, including mono- and

multidentate ligands (thiolates, phosphines, and stibines), as well as halides, alkynyls, and various other protecting groups.[18] Figure 1.3 illustrates the atomic structure of a gold nanocluster with mixed phosphine-stibine ligand shell protection.[30]

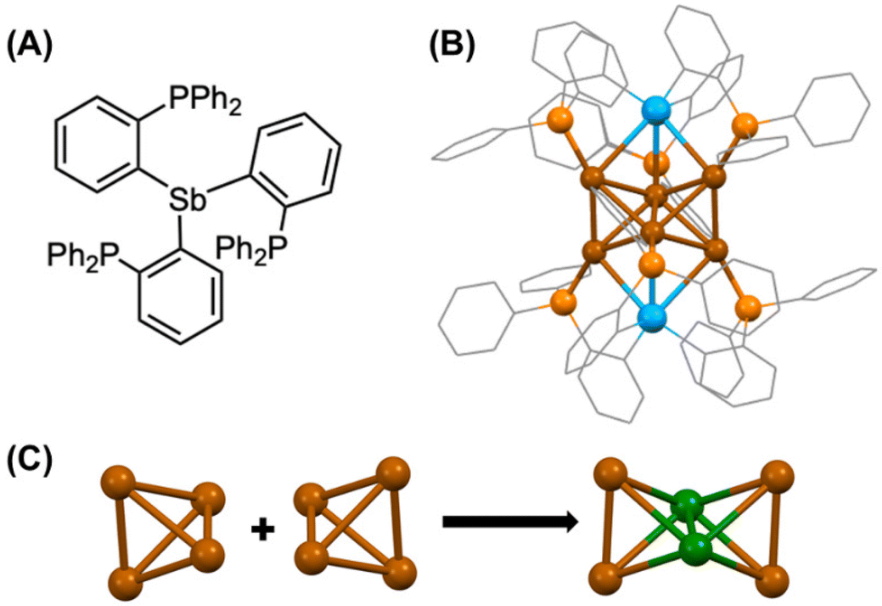


Figure 1.3. (A) Chemical structure of the mixed phosphine–stibine ligand (SbP_3); (B) total structure of $[Au_6(SbP_3)_2]^{2+}$ cluster; (C) structure of the Au_6 core comprised of two Au_4 tetrahedra which assemble together by sharing a common Au_2 edge (highlighted in green) (colour labels: brown/green = Au; orange = P; blue = Sb, grey = C; H atoms are not shown for clarity). Reprinted with permission from *Nanoscale* 2023, *15* (15), 6934–6940. Copyright 2023, Royal Society of Chemistry.

Thus far, we have examined the developments and discoveries that have brought atomically precise metal nanocluster systems to their current state in the research field. While experimental advances have been crucial, achieving atomic-level precision also enables profound theoretical insights into these systems. The following section describes how theoretical analysis bridges experimental observations with the underlying electronic structure of the metal nanoclusters.

1.4 From experimental to theoretical understanding

In any theoretical treatment of metal nanoclusters, the "Jellium model" stands as a cornerstone concept. This model provides crucial insights into why certain cluster sizes exhibit enhanced stability and distinct physicochemical characteristics. Put simply, the spherical jellium approximation treats valence electrons as delocalized throughout a uniformly charged sphere, rather than localized on individual metal atoms, resulting in discrete quantized energy levels.[18,31] This delocalization gives rise to electronic shell structures of metallic nanoclusters reminiscent of atomic orbitals (or "superatomic" orbitals).[18,32] Therefore, this approaches paved a path that connects between the metal nanoclusters with the atoms at the electronic structure level, which can be extensively applicable for theoretical understanding of these types of systems.[26,33,34]

Since the introduction of the first density functional theory (DFT) model for the $Au_{32}(SCH_3)_{24}$ nanocluster in 1999, computational techniques have evolved significantly.[35] Today, theoretical insights have become essential when new atomically precise nanoclusters are synthesized and characterized. With enhanced theoretical capabilities, we can now support experimental observations and substantially deepen our understanding of these systems. In this dissertation, we will employ and develop methods applicable to understanding and determining the properties of metal nanocluster systems, ultimately providing valuable insights that complement experimental investigations.

1.5 Objectives of the dissertation

In this dissertation, I present four main research projects that can be divided based on two primary objectives. The first objective, addressed in Chapter 3 and 4, focuses on elucidating the impact of external perturbations and environmental factors that influence the optical behavior of

nanowires and nanoclusters. Specifically, Chapter 3 investigates the impact of an external static electric field on the optical properties of silver nanowire dimers in different special arrangements. Chapter 4 explores how different solvent environments modulate near-infrared absorption and dual emission phenomena of an atomically precise gold thiolate protected nanorod. These investigations utilize a combination of computational approaches: DFT, linear-response time-dependent DFT (LR-TDDFT), complemented by detailed analysis of electronic structures, molecular orbitals, and characterization of optical properties (both absorption and emission). The second objective, pursued in Chapters 5 and 6, tackles computational challenges inherent in conventional theoretical frameworks by developing methods that enhance efficiency without sacrificing accuracy. Chapter 5 introduces a machine learning-based force field designed to gain quantum-level accuracy in predicting potential energies for gold hydride nanoclusters. Chapter 6 describes the implementation of analytical excited state gradients for open-shell systems using the time-dependent density functional theory plus tight binding (TDDFT+TB) approach, thereby facilitating efficient exploration of excited state potential energy surfaces in open-shell systems.

Before exploring the research landscape in detail, we establish the theoretical principles that guide our path. While numerous computational approaches could illuminate nanocluster properties, Chapter 2 examines the methods chosen for this work, their fundamental underpinnings, strengths in capturing the physics of these systems, and why they emerge as the most appropriate tools for the investigations ahead.

1.6 References

1. Tyson, Neil; Trefil, James. *Cosmic Queries: StarTalk's Guide to Who We Are, How We Got Here, and Where We're Going*; National Geographic, 2021.

2. Hawking, Stephen. *A Brief History of Time*; Bantam Books, 1998.

3. Balbi, Amedeo. *The Music of the Big Bang: The Cosmic Microwave Background and the New Cosmology*; Springer, 2008.

4. Borissov, Guennadi. *The Story of Antimatter: Matter's Vanished Twin*; World Scientific Publishing, 2018.

5. Prasad, R. D.; Sarvalkar, P. D.; Prasad, N.; Prasad, S. R.; Prasad, R. S.; Prasad, R. B.; Prasad, R. R.; Desai, C. B.; Vaidya, A. K.; Teli, Shivanand. B.; Saxena, M.; Kale, V. B.; Pande, R. S.; Charmode, N.; Deshmukh, R. N.; Patil, V. N.; Samant, A.; Chiplunkar, C.; Guo, Z.; Ramteke, A. A.; Ghosh, J. A Review on Spectroscopic Techniques for Analysis of Nanomaterials and Biomaterials. *ES Energy Environ.* **2024**, *27*, 1264.

6. Fara, P. Newton Shows the Light: A Commentary on Newton (1672) 'A Letter . . . Containing His New Theory about Light and Colours...'. *Phil. Trans. R. Soc. A* **2015**, *373* (2039), 20140213.

7. Niaz, M.; Klassen, S.; McMillan, B.; Metz, D. Reconstruction of the History of the Photoelectric Effect and Its Implications for General Physics Textbooks. *Science Education* **2010**, *94* (5), 903–931.

8. Gersten, A. Maxwell Equations – The One-Photon Quantum Equation. *Foundations of Physics.* **2001**, 31, 8, 1211-1231.

9. Ford, K. W. Niels Bohr's First 1913 Paper: Still Relevant, Still Exciting, Still Puzzling. *Phys. Teach.* **2018**, *56* (8), 500–502.

10. Micheals, A. D. Materials Analysis and Failure Analysis. In *Encyclopedia of Forensic Sciences*; Elsevier, 2013; pp 483–493.

11. Schlegel, H. B. Exploring Potential Energy Surfaces for Chemical Reactions: An Overview of Some Practical Methods. *J. Comput. Chem.* **2003**, *24* (12), 1514–1527.

12. Zimmermann, J.; Zeug, A.; Röder, B. A Generalization of the Jablonski Diagram to Account for Polarization and Anisotropy Effects in Time-Resolved Experiments. *Phys. Chem. Chem. Phys.* **2003**, *5* (14), 2964–2969.

13. Zheng, X.; Drummer, M. C.; Russell, T. A.; Gozem, S.; Glusac, K. D. Teaching Nonradiative Transitions with MATLAB and Python. *J. Chem. Educ.* **2024**, *101* (11), 5097–5104.

14. Antoine, R.; Yao, Q.; Yu, K. Looking for Atomic Precision in Nanochemistry. *Commun. Chem.* **2024**, *7* (1), 24, s42004-023-01057–3.

15. Liu, Z.; Luo, L.; Jin, R. Visible to NIR-II Photoluminescence of Atomically Precise Gold Nanoclusters. *Adv. Mater.* **2024**, *36* (8), 2309073.

16. Maity, S.; Kolay, S.; Chakraborty, S.; Devi, A.; Rashi; Patra, A. A Comprehensive Review of Atomically Precise Metal Nanoclusters with Emergent Photophysical Properties towards Diverse Applications. *Chem. Soc. Rev.* **2025**, *54* (4), 1785–1844.

17. Du, B.; Jiang, X.; Das, A.; Zhou, Q.; Yu, M.; Jin, R.; Zheng, J. Glomerular Barrier Behaves as an Atomically Precise Bandpass Filter in a Sub-Nanometre Regime. *Nat. Nanotechnol.* **2017**, *12* (11), 1096–1102.

18. Omoda, T.; Takano, S.; Tsukuda, T. Toward Controlling the Electronic Structures of Chemically Modified Superatoms of Gold and Silver. *Small* **2021**, *17* (27), 2001439.

19. Truttmann, V.; Loxha, A.; Banu, R.; Pittenauer, E.; Malola, S.; Matus, M. F.; Wang, Y.; Ploetz, E. A.; Rupprechter, G.; Bürgi, T.; Häkkinen, H.; Aikens, C.; Barrabés, N. Directing Intrinsic Chirality in Gold Nanoclusters: Preferential Formation of Stable Enantiopure Clusters in High Yield and Experimentally Unveiling the "Super" Chirality of Au_{144}. *ACS Nano* **2023**, *17* (20), 20376–20386.

20. Monti, M.; Brancolini, G.; Coccia, E.; Toffoli, D.; Fortunelli, A.; Corni, S.; Aschi, M.; Stener, M. The Conformational Dynamics of the Ligands Determines the Electronic Circular Dichroism of the Chiral $Au_{38}(SC_2H_4Ph)_{24}$ Cluster. *J. Phys. Chem. Lett.* **2023**, *14* (7), 1941–1948.

21. Shichibu, Y.; Ogawa, Y.; Sugiuchi, M.; Konishi, K. Chiroptical Activity of Au_{13} Clusters: Experimental and Theoretical Understanding of the Origin of Helical Charge Movements. *Nanoscale Adv.* **2021**, *3* (4), 1005–1011.

22. Kosuda, K. M.; Bingham, J. M.; Wustholz, K. L.; Van Duyne, R. P.; Groarke, R. J. Nanostructures and Surface-Enhanced Raman Spectroscopy. In *Comprehensive Nanoscience and Nanotechnology*; Elsevier, 2016; pp 117–152.

23. Mayer, K. M.; Hafner, J. H. Localized Surface Plasmon Resonance Sensors. *Chem. Rev.* **2011**, *111* (6), 3828–3857.

24. Xiao, Y.; Wu, Z.; Yao, Q.; Xie, J. Luminescent Metal Nanoclusters: Biosensing Strategies and Bioimaging Applications. *Aggregate* **2021**, *2* (1), 114–132.

25. Song, X.-R.; Goswami, N.; Yang, H.-H.; Xie, J. Functionalization of Metal Nanoclusters for Biomedical Applications. *Analyst* **2016**, *141* (11), 3126–3140.

26. Seal, N.; Samarasinghe, D. S. N. D.; Vodnala, N.; Siegler, M. A.; Aikens, C. M.; Das, A. Distibine versus Diphosphine Ligands: Modulating the Properties of Isostructural $Au_{13}Cu_2$ Nanoclusters. *Chem. Mater.* **2025**, *37* (24), 9908–9918.

27. Yuan, X.; Zhu, M. Recent Advances in Atomically Precise Metal Nanoclusters for Electrocatalytic Applications. *Inorg. Chem. Front.* **2023**, *10* (14), 3995–4007.

28. Zhang, L.; Wang, E. Metal Nanoclusters: New Fluorescent Probes for Sensors and Bioimaging. *Nano Today* **2014**, *9* (1), 132–157.

29. Galchenko, M.; Black, A.; Heymann, L.; Klinke, C. Field Effect and Photoconduction in Au_{25} Nanoclusters Films. *Adv. Mater.* **2019**, *31* (18), 1900684.

30. Singh, K. K.; Bhattacharyya, A.; Havenridge, S.; Ghabin, M.; Ausmann, H.; Siegler, M. A.; Aikens, C. M.; Das, A. A First Glance into Mixed Phosphine–Stibine Moieties as Protecting Ligands for Gold Clusters. *Nanoscale* **2023**, *15* (15), 6934–6940.

31. De Heer, W. A. The Physics of Simple Metal Clusters: Experimental Aspects and Simple Models. *Rev. Mod. Phys.* **1993**, *65* (3), 611–676.

32. Walter, M.; Akola, J.; Lopez-Acevedo, O.; Jadzinsky, P. D.; Calero, G.; Ackerson, C. J.; Whetten, R. L.; Grönbeck, H.; Häkkinen, H. A Unified View of Ligand-Protected Gold Clusters as Superatom Complexes. *Proc. Natl. Acad. Sci. U.S.A.* **2008**, *105* (27), 9157–9162.

33. Zhu, M.; Aikens, C. M.; Hendrich, M. P.; Gupta, R.; Qian, H.; Schatz, G. C.; Jin, R. Reversible Switching of Magnetism in Thiolate-Protected Au_{25} Superatoms. *J. Am. Chem. Soc.* **2009**, *131* (7), 2490–2492.

34. Aikens, C. M. Electronic and Geometric Structure, Optical Properties, and Excited State Behavior in Atomically Precise Thiolate-Stabilized Noble Metal Nanoclusters. *Acc. Chem. Res.* **2018**, *51* (12), 3065–3073.

35. Häkkinen, H.; Barnett, R. N.; Landman, U. Electronic Structure of Passivated $Au_{38}(SCH_3)_{24}$ Nanocrystal. *Phys. Rev. Lett.* **1999**, *82* (16), 3264–3267.

Chapter 2 - Theory and methods

Quantum mechanics is a fundamental formalism of modern science that describes the behavior of light (or energy) and matter at atomic scales. As briefly demonstrated in Chapter 1, computational and theoretical approaches based on quantum mechanics can both illuminate experimental observations and predict outcomes before experiments are performed. Given the wide variety of such approaches available, this chapter delves deeper into the specific concepts and methods employed throughout this dissertation, systematically answering: What are the methods? Why were they selected? And how are they applied?

At the heart of quantum mechanics lie two cornerstone concepts: wave-particle duality, demonstrating that matter at the quantum scale possess both particle and wave characteristics, and the Schrödinger equations, which provide the mathematical description of a system's quantum state. These principles provide the foundation for understanding matter at the microscopic level, from the electronic structure of atoms and molecules to the collective behavior of particles in complex environments.[1,2]

2.1 Schrödinger and electronic structure theory

In its most commonly encountered form, the time-independent Schrödinger equation for a single particle in one dimension is represented as (Equation 2.1):[2-4]

$$\widehat{H}\Psi(x) = E\Psi(x) = \frac{-\hbar^2}{2m}\frac{\partial^2}{\partial x^2}\Psi(x) + V(x)\Psi(x) \tag{2.1}$$

where m denotes the particle mass, $\hbar$ is the reduced Planck constant ($\hbar = h/2\pi$), and $\Psi(x)$ is the wavefunction describing the quantum state of the system. The time-independent Schrödinger equation applies the Hamiltonian operator ($\widehat{H}$) to the wavefunction to obtain the total energy of

the system, E, which is comprised of both the kinetic, $\frac{-\hbar^2}{2m}\frac{\partial^2}{\partial x^2}\Psi(x)$, and potential energy, $V(x)$, contributions.[2-4]

It is important to note that Equation 2.1 represents a simplest form of the Schrödinger equation, corresponding to a single particle in one dimension. However, for molecular systems, we must account for three spatial dimensions. Moreover, as systems grow larger, the number of electrons increases, and the Hamiltonian operator must account for all electrons and the nuclei along with their mutual interactions, which collectively contribute to the total energy. This increasing complexity makes the time-independent Schrödinger equation progressively more difficult to solve for larger systems. Accounting for all these factors, we can present a more general form of the Schrödinger equation from Equation 2.1:[5]

$$\left[\sum_i \frac{-\hbar^2}{2m_i}\nabla_i^2 - \sum_A \frac{\hbar^2}{2m_A}\nabla_A^2 + \sum_{i,j>i} \frac{e^2}{|r_i - r_j|} - \sum_{i,A} \frac{e^2 Z_A}{|r_i - R_A|} + \sum_{A,B>A} \frac{e^2 Z_A Z_B}{|R_A - R_B|}\right]\Psi(r,R) = E\Psi(r,R) \quad (2.2)$$

where r and R are vectors that represent the positions of the electronic and nuclear degrees of freedom, respectively; i and j index the electrons; A and B index the nuclei; and Z denotes the atomic charge. The first two terms describe the kinetic energy of the electrons and nuclei, respectively, while the third and the fifth terms account for electron-electron and nuclear-nuclear interactions. The fourth term represents the electron-nuclear interactions.

The complexity of this equation can be dramatically reduced through the Born-Oppenheimer approximation,[5,6] which addresses the large mass difference between electrons and nuclei and the consequences of this. Since electrons are much lighter than the nuclei, they move much faster. This vast difference in their respective motion allows us to treat the nuclei as stationary while electrons move. Under this framework, Equation 2.2 simplifies considerably,

where the nuclear kinetic energy term vanishes, and the nuclear-nuclear potential energy term can be treated as a constant.

While the Born-Oppenheimer approximation simplifies Equation 2.2, it does not solve our fundamental problem. We still do not know the exact form of the many-electron wavefunction itself. To address this issue, we can employ the orbital approximation and use a Slater determinant, which constructs the many-electron wavefunction from single-electron wavefunctions.[7] The Slater determinant elegantly addresses two requirements at once: it provides a practical mathematical framework for the wavefunction while ensuring antisymmetry, thereby satisfying the Pauli exclusion principle that governs electron behavior.[8] For an N-electron system, the wavefunction from the Slater determinant can be given as in Equation 2.3, where each χ represents a spin-orbital (or a single particle wavefunction).[7]

$$\Psi(x_1, \cdots, x_N) = \frac{1}{\sqrt{N!}} det[\chi_1(x_1), \cdots, \chi_N(x_N)] \tag{2.3}$$

This Slater determinant form is typically used to evaluate the Hartree-Fock equation, which employs a variational approach to solve the time-independent Schrödinger equation. Due to the variational principle, the energy obtained from Hartree-Fock calculations is always higher than the exact ground-state electronic energy.[3,9] We introduce an iterative refinement to the spin-orbitals (which can be represented as a linear combination of atomic orbitals, as described in the following section), to produce new spin-orbitals by adjusting specific parameters in the trial wavefunction (these are coefficients within the orbital representation and are optimized at each iterative step) and the calculations proceed until minimal (or no) changes are observed (i.e., the energy is converged at this point). This process is known as the self-consistent field (SCF) approach, and upon convergence, the resulting wavefunction will yield the minimum energy achievable within the chosen framework.[10] To enable this iterative optimization, we require a

flexible mathematical representation of the trial wavefunction. This is where basis sets come into the picture.

2.2 Basis sets: A representation of molecular orbitals

A basis set comprises a collection of mathematical functions that are linearly combined to approximate molecular orbitals. These basis functions often represent the atomic orbitals of constituent atoms and are introduced in quantum chemical calculations to overcome the inherent difficulty of solving the equations that define molecular orbitals analytically. Ideally, an infinite basis set would be employed to achieve the Hartree-Fock limit, defined as the solution to the Hartree-Fock equations with an infinitely large basis set. However, this is clearly impractical. The optimal approach is therefore to use as few basis functions as possible while still approaching the accuracy of the Hartree-Fock limit, thereby balancing computational efficiency with chemical accuracy.[11]

Over the years, basis sets have been formulated using different functional forms. Slater-type orbitals (STO) and Gaussian-type orbitals (GTO) are some of the most widely adopted in quantum chemical calculations. Beginning with the STO, their mathematical form is represented in Equation 2.4, where N is a normalization constant, r is the distance of the electron from the atomic nucleus, ζ (Zeta) represents the orbital exponent that controls the radial extent of the orbital, $Y_{l,m}(\theta, \phi)$ is the spherical harmonics term, while n, l, and m represent the principle, angular, and magnetic quantum numbers, respectively.[3,11-13]

$$\psi_{n,l,m}^{STO}(r, \theta, \phi) = Nr^{n-1}e^{-\zeta r}Y_{l,m}(\theta, \phi) \tag{2.4}$$

A key advantage of STOs is that they accurately reproduce the correct exponential decay of the orbital with increasing distance from the nucleus. However, the analytical evaluation of

integrals involving STOs is computationally challenging. To address this limitation, GTOs were introduced as a more tractable alternative, offering expressions that are easier to solve analytically. The functional form of a GTO is expressed in Equation 2.5:[3,11-13]

$$\psi_{i,j,k}^{GTO}(x,y,z) = Nx^i y^j z^k e^{-\alpha r^2} \tag{2.5}$$

When expressed in Cartesian coordinates, GTOs take the form of a Gaussian function multiplied by polynomial terms in x, y, and z, where the exponents i, j, and k on these variables collectively define the total angular momentum of the basis function, $L = i + j + k$. α represents the orbital exponent, while the remaining terms are analogues to those of STOs. It is important to note that GTOs also exhibit certain drawbacks. Most notably, these orbitals do not exhibit the correct behavior at the nucleus, where they fail to represent the characteristic cusp, and their radial decay is excessively rapid compared to the true orbital behavior.[3,11-13]

To better capture the correct behavior both at the nucleus and at larger distances, a linear combination of Gaussian functions was introduced. This combination of primitive GTOs, commonly referred to as contracted GTOs (cGTOs), is widely employed in electronic structure calculations.[11,13] Figure 2.1 illustrates this contrasting radial behavior of STOs, GTOs, and cGTOs.

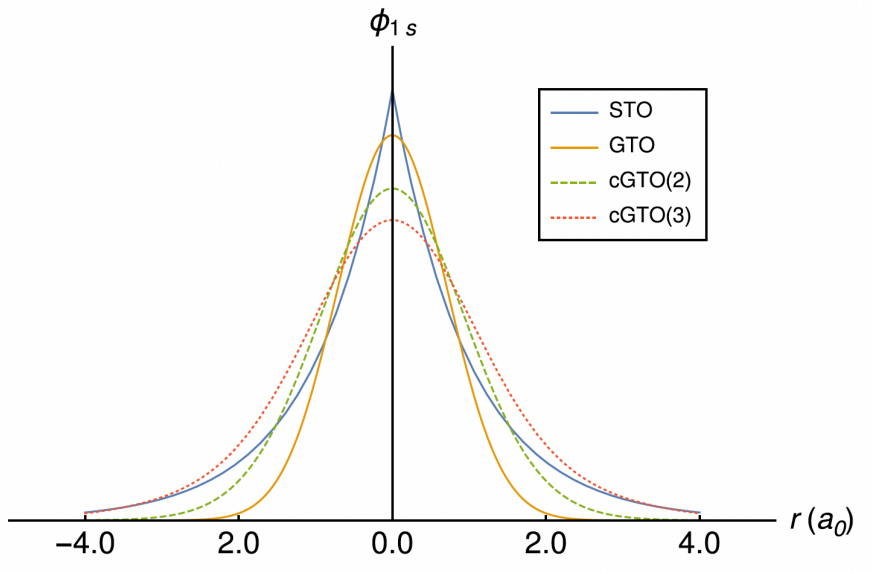


Figure 2.1. Example GTO and cGTOs intended to represent the hydrogenic 1s atomic orbital, overlayed with an STO for comparison. The GTO uses one Gaussian function to reproduce the shape of the 1s function; cGTO(2) and cGTO(3) are linear combinations of two and three Gaussian functions to better represent the cusp and exponential decay for longer distances. Reprinted with permission from *Mathematical Physics in Theoretical Chemistry*; Elsevier, 2019; pp 31–61. Copyright 2019, Elsevier Inc.

To incorporate greater flexibility into the wavefunction, the basis set can be systematically expanded (e.g., by increasing the ζ-level).[11,13] Up to this point we have talked about only single-ζ (SZ) basis sets, where a single basis function is used to represent each orbital. In a double-ζ (DZ) basis set, the number of basis functions for each orbital type is doubled relative to a minimal basis set. This expansion can be extended further: a triple-ζ (TZ) basis set employs three functions per orbital, quadruple-ζ (QZ) uses four, and so on to even higher levels. It is important to note, however, that each increase in ζ-level comes with a corresponding increase in computational cost, which becomes particularly significant as molecular systems grow larger in number of electrons.[11,13]

It is important to note that additional functions can be incorporated into basis sets to improve the description of the wavefunction. Two of the most commonly employed types are

polarization functions and diffuse functions. Polarization functions add higher angular momentum functions to the basis set, providing greater mathematical flexibility in describing molecular orbitals, which is particularly important for systems exhibiting hypervalent bonding or significant electron correlation effects (or, indeed, any bonding that distorts the orbitals away from their ideal spherical harmonic forms).[11,13] Diffuse functions, on the other hand, are essential for systems with weakly bound electrons that exhibit spatially extended electron densities, such as anions or excited states.[11,13]

Aside from STOs and GTOs, other types of basis sets are employed in quantum chemical calculations. One notable alternative is plane wave basis sets, which can be viewed as a grid basis in momentum space based on Bloch's theorem.[14,15] Because they span the entire real space, plane waves work especially well for systems with periodic boundary conditions. Another advantage is that plane wave basis sets can be improved step by step without creating redundant functions.[14,16] Similar to GTOs, plane waves also have the limitation of not accurately representing the electron-nuclear cusp. However, this issue is usually addressed by using special pseudopotentials.[14,17]

Through this dissertation, we employ both STO basis sets (using the Amsterdam Density Functional (ADF) package[18]) and plane wave basis sets (using the Vienna Ab initio Simulation Package (VASP)[19]). It is important to note that the choice of basis set for each study is guided by careful consideration of both accuracy and computational efficiency.

2.3 Density functional theory

Despite its simplicity and early promise, according to Becke,[20] the Hartree-Fock-Slater method remained fundamentally incomplete as a model rather than a rigorous theory, which

offered no explanation for dynamical correlation or the correlation contribution to the kinetic energy. These deficiencies were investigated in part through the landmark theoretical framework developed by Hohenberg and Kohn in 1964,[21] followed by Kohn and Sham in 1965,[22] which provided a rigorous mathematical foundation that validated the earlier intuitive work by Thomas, Fermi, Dirac, and Slater.[20] The pivotal 1964 Hohenberg-Kohn theorem demonstrated that the ground-state electronic density $\rho(r)$ alone completely and uniquely determines all properties of an *N*-electron system, establishing density as the fundamental variable in electronic structure calculations and giving birth to modern density functional theory.[20,21] This revelation emerges from two complementary theorems. The first Hohenberg-Kohn theorem states that a unique one-to-one mapping exists between the ground-state wavefunction and its electronic density, meaning that all properties of the system are functionals of the electronic density. The second theorem establishes that a ground-state density functional exists such that the energy of this functional reaches its minimum at the true ground-state density, effectively applying variational principles to density functional theory.[20,21] However, a critical challenge remains: the exact form of this ground-state density functional is unknown.[20]

The challenge of calculating the ground-state electron density for interacting many-electron systems motivated Kohn and Sham's insight to replace the complex interacting system with a non-interacting electronic system that produces an identical density.[22] This mapping converts the intractable many-body problem into a series of single-particle Schrödinger-like equations, where non-interacting electrons move through an effective potential that implicitly captures all interaction effects.[22-24] Therefore, the Kohn-Sham equation can be given as follows:

$$\hat{h}\phi_i^{KS}(r) = \left[-\frac{\nabla^2}{2} + v(r) + \int \frac{\rho(r')}{|r-r'|}dr' + v_{xc}(r)\right]\phi_i^{KS}(r) = \epsilon_i\phi_i^{KS}(r) \qquad (2.6)$$

where $v(r)$ is the external potential, $v_{xc}(r)$ denotes the exchange-correlation (xc) term, $-\frac{\nabla^2}{2}$ is the kinetic energy operator in atomic units, and ϵ_i corresponds to the orbital eigenvalue (i.e., the orbital energy). Therefore, the resulting ground-state density emerges as $\rho(r) = \sum_{i=1}^{occ.} \left|\phi_i^{KS}(r)\right|^2$, where the sum runs over all occupied orbitals.[20,22-24]

Equation 2.6 indicates that the Kohn-Sham orbital energy, ϵ_i, naturally decomposes into kinetic energy, external potential (Coulombic term), electron-electron repulsion ($\int \frac{\rho(r')}{|r-r'|} dr'$), and xc contribution terms. The xc term can be written as $v_{xc}(r) = \delta E_{xc} / \delta\rho(r)$, where E_{xc} denotes the xc potential. Herein lies a key challenge, where the exact form of the E_{xc} is unknown, requiring the development of various approximation approaches to solve this issue.[20,23-26]

2.4 Types of exchange-correlation (xc) functionals

The popularity of Kohn-Sham DFT has spurred the development of numerous approximations for the exchange-correlation functional. Notably, the first approximation was introduced by Kohn and Sham themselves in their original 1965 paper.[22] This simplest approximation is known as the local density approximation (LDA), and assumes that the exchange-correlation energy at each point in space equals that of a homogeneous electron gas with the same local density $\rho(r)$. Mathematically, this can be expressed as shown in Equation 2.7, where e_{xc}^{HEG} represents the exchange-correlation energy per electron of the homogeneous electron gas.[22,25]

$$E_{xc}^{LDA} = \int d^3r \rho(r) e_{xc}^{HEG}\big(\rho(r)\big) \tag{2.7}$$

This was only the beginning. As computational chemistry advanced, other exchange-correlation functionals were developed and systematically categorized into distinct families. These families differ in both their complexity and the predictive accuracy. In terms of accuracy itself, LDA functions occupy the lowest rung of Jacobs's ladder (introduced by John Perdew where the lowest rung represents the least accurate xc functionals and accuracy increases as one ascends the ladder).[27] The next level is represented by the generalized gradient approximation (GGA), which improves upon LDA by recognizing that real electron densities are inherently non-uniform. GGA functionals achieve this improvement by incorporating not only the local density $\rho(r)$, but also its gradient $\nabla\rho(r)$, thereby capturing spatial variations in the electron distribution (Equation 2.8).[25]

$$E_{xc}^{GGA} = \int d^3r\rho(r)e_{xc}^{GGA}\big(\rho(r), \nabla\rho(r)\big) \tag{2.8}$$

Ascending the ladder, we encounter meta-GGA functionals (mGGA), which extend GGA by incorporating the kinetic energy density $\tau(r)$ and/or the Laplacian of the density $\nabla^2\rho(r)$, as shown in Equation 2.9.[25]

$$E_{xc}^{mGGA} = \int d^3r\rho(r)e_{xc}^{GGA}\big(\rho(r), \nabla\rho(r), \nabla^2\rho(r), \tau(r)\big) \tag{2.9}$$

Climbing further, we reach hybrid functionals, which combine standard DFT functionals (E_{xc}^{DFT}; typically used with GGA as shown in Equation 2.10, but mGGA and LDA are also applicable) with a percent of exact exchange from the Hartree-Fock theory ($c_x E_x^{EXX}$, where c_x denotes the percentage). This mixing of DFT functionals and exact Hartree-Fock exchange significantly improves accuracy for many chemical systems.[25]

$$E_{xc}^{Hybrid} = c_x E_x^{EXX} + (1 - c_x)E_{xc}^{GGA} \tag{2.10}$$

At the summit of Jacob's ladder lies the random-phase approximation (RPA), which depends on empty Kohn-Sham orbitals. As it represents the highest rung, it reflects the greatest chemical accuracy among DFT approximations.[25] However, this enhanced accuracy comes at a significant computational cost. Therefore, selecting an appropriate functional requires balancing accuracy against computational feasibility for the system and the property of interest.

Beyond these traditional exchange-correlation functionals, additional corrections can be incorporated to enhance their accuracy. One important enhancement is introducing dispersion corrections (typically applied to LDA and GGA functionals), which accounts for long-range van der Waals (London dispersion) forces, enabling accurate modeling of non-covalent interactions.[28] Addressing similar long-range interaction deficiencies, long-range corrected functionals have been developed. These functionals employ 100% Hartree-Fock exchange at long-range while utilizing standard exchange-correlation functionals (such as GGA) for short-range electron interactions, providing a balanced treatment across all distance scales.[29]

Having established methods for calculating ground-state properties, the question naturally arises: how do we address excited-state properties? Since the main objectives of this dissertation involve the investigation of excited-state characteristics, particularly the optical properties of molecules and nanoclusters, the following section will explore how the theoretical framework of ground-state DFT can be extended to treat electronic excitations.

2.5 Time-dependent density functional theory (TDDFT)

Time-dependent density functional theory (TDDFT) emerged in 1984 through the pioneering work of Runge and Gross,[30] extending the ground-state DFT formalism developed by Hohenberg, Kohn, and Sham.[21,22,31] Since then, TDDFT has emerged as a thriving research

domain with an extensive global network of researchers and method developers, distinguished by continual innovation and progressively broader applications. Today, it stands as one of the most dynamic areas in computational chemistry.

The work of Runge and Gross established that a unique one-to-one mapping exists between the time-dependent external potential $v(r,t)$ and the time-depended electron density $\rho(r,t)$, analogous to the Hohenberg and Kohn theorems for ground-state DFT.[30,31] Consequently, the time-dependent density of an interacting system can be mapped to the time-dependent density of a non-interacting system. Following the Kohn-Sham formalism, this leads to the time-dependent Kohn-Sham equations, which can be expressed as follows (Equation 2.11):[30,31]

$$i\frac{\partial}{\partial t}\phi_i(r,t) = \left[-\frac{\nabla^2}{2} + v(r,t) + \int \frac{\rho(r',t)}{|r-r'|}dr' + v_{xc}(r,t)\right]\phi_i(r,t) \qquad (2.11)$$

The terms in Equation 2.11 are analogues to those in the ground-state Kohn-Sham equations, but now they are time-dependent. As with ground-state DFT, determining the exact form of the time-dependent exchange-correlation potential remains a challenge.

The next step involves calculating how the ground-state electron density responds to an electromagnetic field (such as light). This leads to the linear-response formalism, where the poles of the response function correspond to excitation energies. By solving the linear-response equations, one can determine the excitation energies and oscillator strengths that characterize the optical properties of the system.

2.5.1 Linear-response time-dependent density functional theory (LR-TDDFT)

The Casida approach (introduced by Mark Casida) provides a practical framework for solving the TDDFT eigenvalue problem to obtain excitation energies.[32] A key feature of this

approach is that the linear-response equations can be reformulated as a matrix eigenvalue problem, as shown in Equation 2.12:[32]

$$\begin{pmatrix} A & B \\ B^* & A^* \end{pmatrix}\begin{pmatrix} X \\ Y \end{pmatrix} = \omega \begin{pmatrix} 1 & 0 \\ 0 & -1 \end{pmatrix}\begin{pmatrix} X \\ Y \end{pmatrix} \tag{2.12}$$

where A and B are the Hessians of orbital rotation, X and Y denote the transition density vectors for single particle transitions, and ω denotes the excitation energy. The Casida equation can be transformed into a more compact form (for pure functionals), $\Omega F = \omega^2 F$, where Ω and F are represented as,[33]

$$\Omega = (A-B)^{\frac{1}{2}}(A+B)(A-B)^{\frac{1}{2}} \tag{2.13}$$

$$F = (A-B)^{-\frac{1}{2}}(X+Y) \tag{2.14}$$

To solve these equations, we must evaluate the elements of $(A+B)$ and $(A-B)$. Within the LR-TDDFT framework, they take the following forms:[34]

$$(A+B)_{ia\sigma,jb\sigma'} = \left(\epsilon_{a\sigma} - \epsilon_{j\sigma}\right)\delta_{ij}\delta_{ab}\delta_{\sigma\sigma'} + 2(ia\sigma|jb\sigma') + 2\left(ia|f^{xc}_{\sigma\sigma'}|jb\right) - c_x\delta_{\sigma\sigma'}[(ja\sigma|ib\sigma) + (ab\sigma|ij\sigma)] \tag{2.15}$$

$$(A-B)_{ia\sigma,jb\sigma'} = \left(\epsilon_{a\sigma} - \epsilon_{j\sigma}\right)\delta_{ij}\delta_{ab}\delta_{\sigma\sigma'} + c_x\delta_{\sigma\sigma'}[(ja\sigma|ib\sigma) - (ab\sigma|ij\sigma)] \tag{2.16}$$

where i and j denote the occupied molecular orbitals in the ground state, a and b denote virtual (unoccupied) molecular orbitals in the ground state, and σ and σ' represent spin indices. The term $\epsilon_{p\sigma}$ represents the orbital energy of a general orbital p with its respective spin, while c_x denotes the Hartree-Fock exchange percentage. The two-electron integrals are represented as $(ia\sigma|jb\sigma')$ and $\left(ia|f^{xc}_{\sigma\sigma'}|jb\right)$, where the exchange-correlation kernel is given by $f^{xc}_{\sigma\sigma'}$.[34] It is important to note that evaluating these two-electron integrals represents the primary computational bottleneck in the LR-TDDFT formalism due to their steep scaling with system size. However, once the Casida equations are solved, the resulting excitation energies and their

corresponding oscillator strengths can be used to construct theoretical absorption spectra. These calculated spectra enable direct comparison with experimental measurements and provide detailed insights into the electronic structure of the system.[35,36]

As discussed earlier in this chapter, a major limitation of TDDFT is its computational cost, which scales significantly with system size and the level of theory employed. However, this limitation presents an opportunity to explore alternative approaches that are less computationally demanding than TDDFT while still maintaining the accuracy. Therefore, the following section of this chapter focuses on these approximation methods and how they can be applied to our target computations.

2.5.2 Approximation methods to time-dependent density functional theory

As theorists began tackling larger systems, such as nanoclusters, the need arose to move beyond traditional TDDFT toward new approaches. Some approximation methods targeted not only excited states but also ground states, such as the density functional tight-binding (DFTB) approach. DFTB was introduced as an approximation to DFT calculations and subsequently extended to excited states, yielding time-dependent density functional tight-binding (TDDFTB). While this method proved computationally efficient, it had limitations in its accuracy. The approximations introduced at the ground state led to large errors compared to standard TDDFT, with deviations reaching 1.0 eV.[37] Furthermore, the method's applicability was substantially constrained by its reliance on its parameterization.[38-40]

A shift in perspective emerged. What if the approximations were restricted to the excited states? This is precisely what Grimme et al. accomplished when they developed the simplified time-dependent density functional theory (sTDDFT) and simplified Tamm-Dancoff

approximation (sTDA) methods,[41-43] retaining the DFT ground state while employing a TDDFTB-type approximation for the excited states. Importantly, however, these methods were only applicable when using hybrid functionals. To address this for pure functionals, Rüger et al. introduced an alternative approximation method known as time-dependent density functional theory plus tight binding (TDDFT+TB).[39] Notably, the distinction in the use of xc functionals among sTDDFT, sTDA, and TDDFT+TB is significant, as TDDFT+TB still yields less computationally expensive calculations. While computational efficiency was the driving force behind these developments, the accuracy of these methods cannot be overlooked. It has been demonstrated that the TDDFT+TB method requires only a fraction of the computational time demanded by a standard TDDFT calculation, with approximation errors in excitation energies not exceeding 0.15 eV.[37] This achievement can be attributed to the retention of the DFT ground state, with approximations only introduced at the primary computational bottleneck of TDDFT calculations. This is accomplished by applying a first-order monopole approximation to the transition density, $\phi_{i\sigma}(\boldsymbol{r})\phi_{a\sigma}(\boldsymbol{r}) \approx \sum_A q_{ia\sigma,A}\zeta_A(\boldsymbol{r})$, where the atomic transition charges ($q_{ia\sigma,A}$) and a spherically symmetric function ($\zeta_A(\boldsymbol{r})$) on atom A are utilized within the linear response framework.[39,40,44] Chapter 6 examines TDDFT+TB in comprehensive detail, walking through the derivation and implementation of analytical excited state gradients for open-shell systems, a methodological extension that enhances the capabilities of the ADF software package.

2.6 Implicit and explicit solvent models

The surrounding environment plays a crucial role in determining how molecular systems behave. As such, accounting for solvent effects is essential, especially given that accurate prediction of solution-phase properties underpins numerous applications. Therefore, two primary

modeling strategies have been developed to capture these effects: implicit and explicit solvation approaches.

Implicit solvent models, often called continuum models, treat the solvent as a uniform medium defined by macroscopic properties like dielectric constraint and surface tension, thereby eliminating the need for explicit solvent coordinates. Explicit solvent models take a fundamentally different approach by representing individual solvent molecules, which can include over thousands of molecules that surround the solute. This molecular-level representation captures the spatial arrangement and dynamic fluctuations of the solvent environment.[45-48]

Several implicit solvent models are widely used in quantum chemical calculations, including the conductor-like screening model (COSMO),[49-51] polarizable continuum model (PCM),[52,53] and solvent model based on density (SMD),[54] among others.[48] Throughout this dissertation, the COSMO model serves as our primary solvation approach. The COSMO model operates as a dielectric continuum model wherein a solute molecule occupies a cavity shaped to its molecular geometry, where this cavity is immersed in a dielectric medium defined by the solvent's dielectric constant.[49-51] In contrast, explicit solvation is typically handled through molecular dynamics or Monte Carlo simulations, as well as by hybrid quantum mechanics/ molecular mechanics (QM/MM) methods.

Both explicit and implicit solvent models present direct advantages and limitations. Explicit solvent simulations provide a highly detailed, physical picture of the solvent structure and dynamics surrounding the solute, capturing specific interactions such as hydrogen bonding, ion pairing, and local density fluctuations.[45,48] Conversely, implicit models inherently lack these microscopic structural details. However, accurately modeling bulk behavior with an explicit solvent requires simulating thousands of solvent molecules. When applied within a quantum

chemical framework, such calculations become computationally very expensive. Implicit solvent models resolve this by removing discrete solvent atoms, significantly reducing the system size and computational cost while still capturing the bulk macroscopic electrostatics.[45,47,48] A schematic representation of these approaches is provided in Figure 2.2. The figure illustrates a gas-phase model (in vacuum), alongside implicit, explicit, and a hybrid implicit-explicit model, arranged in order of increasing computational demand.[48,55]

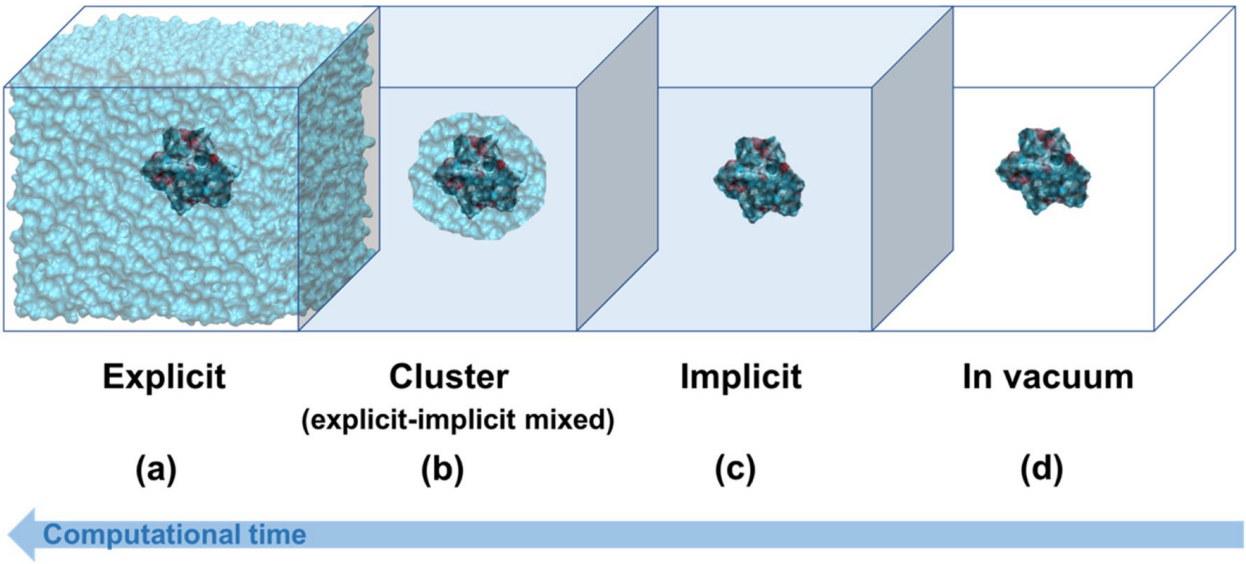


Figure 2.2. Schematic representation of solvent models. Reprinted with permission from *Top. Catal.* 2022, *65*, 118–140. Copyright 2021, The Author(s), Springer Nature.

Therefore, choosing between solvent models inevitably involves balancing accuracy against computational cost, with the optimal choice dictated by the nature of the problem under investigation. Chapter 4 explores the influence of solvent environment through the use of an implicit solvation model, revealing systematic trends in optical properties while illuminating pathways toward explicit solvation treatment that reflect deeper insights into both structural and optoelectronic behavior of atomically precise metal nanoclusters.

2.7 Machine learning approaches and quantum chemistry

The rise of modern artificial intelligence methods has the potential to transform how computers are used in science. According to Choudhary et al., the convergence of big data and artificial intelligence represents the fourth paradigm of science,[56-58] evidenced by the remarkable expansion of applications with chemistry, including models that predict interatomic potential energies,[59,60] molecular forces,[61] molecular polarizabilities,[62] and many other properties.[63] Among the various artificial intelligence approaches, machine learning occupies a particularly interesting position as a technique that employs statistical algorithms capable of improving through training. Importantly, machine learning tools are especially effective for tackling complex problems that traditional methods cannot solve efficiently, if at all.[56] Figure 2.3 illustrates the evolution of computational chemistry research workflows leading to the integration of machine learning approaches.

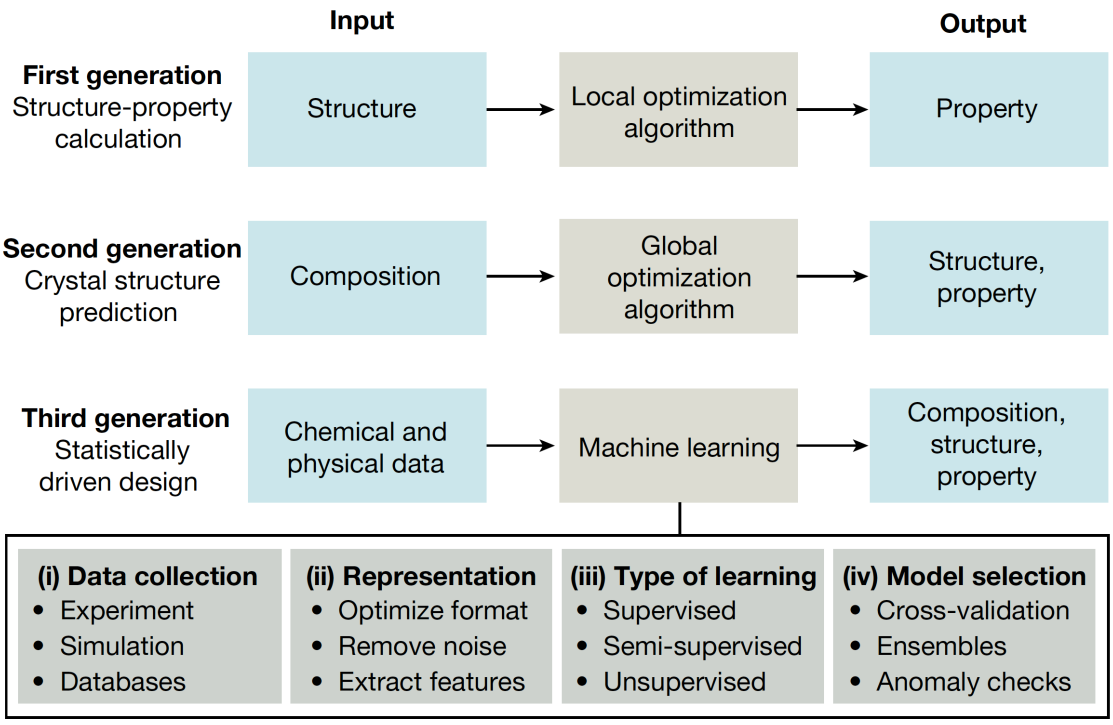


Figure 2.3. Evolution of the research workflow in computational chemistry. The standard paradigm spanning from first-generation to third-generation computational approaches is shown alongside the four stages of machine learning model training, with common methodological choices listed in the bottom panel. Reprinted with permission from *Nature* 2018, *559*, 547–555. Copyright 2018, Macmillan Publishers Ltd., part of Springer Nature.

As noted above, machine learning centers on algorithms that learn to solve problems through training. This learning process begins with data, the essential raw material from which patterns emerge. The workflow starts by collecting and preprocessing a dataset tailored to the problem at hand. With the data prepared, the next step is selecting an algorithm suited to the specific task, as different algorithms excel at different types of problems. Once chosen, the algorithm ingests the training data and begins building a predictive model. After training completes, rigorous evaluation determines whether the model has truly learned to perform as intended.[64]

The learning process itself mirrors human development. Consider how children acquire language: they begin by uttering single words, then gradually expand their vocabulary and comprehension as they encounter more examples. Machine learning follows the same trajectory. Given sufficient high-quality data and appropriate configuration, these models progressively refine their predictions, moving from crude approximations toward increasingly accurate results.

A critical decision in applying machine learning is choosing the right learning approach for the problem. While many methods exist, two fundamental approaches dominate the field: supervised and unsupervised learning. Supervised learning operates when labeled data is available (i.e., datasets where the correct answers are already known). The algorithm studies these examples, learning to recognize patterns that connect inputs to their corresponding labels. Once trained, it can then predict outcomes for new, previously unseen data. This approach excels when you want to replicate human judgment or known relationships at scale. On the other hand, unsupervised learning takes a fundamentally different path. Here, no labels exist to guide the algorithm, Instead, the system explores the data independently, discovering hidden structures, grouping, and relationships that may not be immediately apparent. This approach proves invaluable when you want the algorithm to reveal patterns you did not know to look for.[64]

As datasets expand, so does the computational cost of training machine learning models. Traditional passive learning approaches experience this challenge as the algorithm must process every data point in a predefined dataset, regardless of how informative each of them actually is. Therefore, this approach becomes considerably impractical as data volumes increase. In contrast, active learning offers a more intelligent alternative. Rather than passively training through all available data, the algorithm actively participates by selecting which data points will be most valuable for learning. This selective strategy dramatically reduces computational costs by

focusing training on the most informative data points, often achieving comparable or superior performance with only a fraction of the data.[64,65]

Chapter 5 of this dissertation adopts a supervised learning strategy that integrates both active and passive training approaches. The core methodology relies on Gaussian process regression, (GPR), a flexible probabilistic technique applicable to diverse machine learning challenges.[66,67] What distinguishes GPR from conventional models is its capacity to deliver not just predictions, but full probability distributions that capture inherent uncertainty.[66,68] While standard deterministic approaches yield fixed outcomes, GPR provides a spectrum of possible results weighted by likelihood, an attribute that proves indispensable in domains like autonomous navigation and computational sciences where gauging confidence matters as much as accuracy. This capability arises from GPR's kernel-based architecture, which allows tailored adaptation to specific problem characteristics.[66] For our purpose, we utilize this probabilistic method to characterize potential energy surfaces in nanocluster systems, where both energy predictions and confidence bounds illuminate the complex energetic landscape governing chemical phenomena.

2.8 References

1. Schrödinger, E. An Undulatory Theory of the Mechanics of Atoms and Molecules. *Phys. Rev.* **1926**, *28* (6), 1049–1070.
2. Gorard, J. Deriving the Time-Independent Schrödinger Equation. *Phys. Educ.* **2016**, *51* (6), 063003.
3. Szabo, A.; Ostlund, N. S. *Modern Quantum Chemistry: Introduction to Advanced Electronic Structure Theory*; Dover Publications, Inc: Mineola, New York, 2012.
4. Vlasov, A. D. The Schrödinger Atom. *Phys.-Usp.* **1993**, *36* (2), 94–99.
5. Born, M.; Oppenheimer, R. Zur Quantentheorie Der Molekeln. *Annalen der Physik* **1927**, *389* (20), 457–484.

6. Jecko, T. On the Mathematical Treatment of the Born-Oppenheimer Approximation. *J. Math. Phys.* **2014**, *55* (5), 053504.

7. Slater, J. C. The Theory of Complex Spectra. *Phys. Rev.* **1929**, *34* (10), 1293–1322.

8. Pauli, W. On the Connexion between the Completion of Electron Groups in an Atom with the Complex Structure of Spectra. In *The Old Quantum Theory*; Elsevier, 1967; pp 184–203.

9. Fock, V. Naherungsmethode zur Losung des quantenmechanischen Mehrkorperproblems. *Z. Physik* **1930**, *61* (1–2), 126–148.

10. Mayer, I.; Vibók, Á. SCF Equations in the Chemical Hamiltonian Approach. *Chem. Phys. Lett.* **1988**, *148* (1), 68–72.

11. Jensen, F. *Introduction to Computational Chemistry*, 1st ed.; New York Academy of Sciences Series; John Wiley & Sons, Incorporated: Newark, 2017.

12. Magalhães, A. L. Gaussian-Type Orbitals versus Slater-Type Orbitals: A Comparison. *J. Chem. Educ.* **2014**, *91* (12), 2124–2127.

13. Ulusoy, I. S.; Wilson, A. K. Slater and Gaussian Basis Functions and Computation of Molecular Integrals. In *Mathematical Physics in Theoretical Chemistry*; Elsevier, 2019; pp 31–61.

14. Bischoff, F. A. Computing Accurate Molecular Properties in Real Space Using Multiresolution Analysis. In *Advances in Quantum Chemistry*; Elsevier, 2019; Vol. 79, pp 3–52.

15. Ireta, J.; Galván, M. Plane Waves Basis Sets in the Description of Diatomic Anions and Valence Charge Density. *J. Chem. Phys.* **1996**, *105* (18), 8231–8236.

16. Shepherd, J. J.; Grüneis, A.; Booth, G. H.; Kresse, G.; Alavi, A. Convergence of Many-Body Wave-Function Expansions Using a Plane-Wave Basis: From Homogeneous Electron Gas to Solid State Systems. *Phys. Rev. B* **2012**, *86* (3), 035111.

17. Blöchl, P. E. Projector Augmented-Wave Method. *Phys. Rev. B* **1994**, *50* (24), 17953–17979.

18. Te Velde, G.; Bickelhaupt, F. M.; Baerends, E. J.; Fonseca Guerra, C.; Van Gisbergen, S. J. A.; Snijders, J. G.; Ziegler, T. Chemistry with ADF. *J. Comput. Chem.* **2001**, *22* (9), 931–967.

19. Hafner, J.; Kresse, G. The Vienna AB-Initio Simulation Program VASP: An Efficient and Versatile Tool for Studying the Structural, Dynamic, and Electronic Properties of Materials. In *Properties of Complex Inorganic Solids*; Gonis, A., Meike, A., Turchi, P. E. A., Eds.; Springer US: Boston, MA, 1997; pp 69–82.

20. Becke, A. D. Perspective: Fifty Years of Density-Functional Theory in Chemical Physics. *J. Chem. Phys.* **2014**, *140* (18), 18A301.

21. Hohenberg, P.; Kohn, W. Inhomogeneous Electron Gas. *Phys. Rev.* **1964**, *136* (3B), B864–B871.

22. Kohn, W.; Sham, L. J. Self-Consistent Equations Including Exchange and Correlation Effects. *Phys. Rev.* **1965**, *140* (4A), A1133–A1138.

23. Aouina, A.; Borlido, P.; Marques, M. A. L.; Botti, S. Assessing Exchange-Correlation Functionals for Accurate Densities of Solids. *J. Chem. Theory Comput.* **2024**, *20* (24), 10852–10860.

24. Kohn, W.; Becke, A. D.; Parr, R. G. Density Functional Theory of Electronic Structure. *J. Phys. Chem.* **1996**, *100* (31), 12974–12980.

25. Marques, M. A. L.; Oliveira, M. J. T.; Burnus, T. Libxc: A Library of Exchange and Correlation Functionals for Density Functional Theory. *Comput. Phys. Commun.* **2012**, *183* (10), 2272–2281.

26. Lehtola, S.; Steigemann, C.; Oliveira, M. J. T.; Marques, M. A. L. Recent Developments in Libxc — A Comprehensive Library of Functionals for Density Functional Theory. *SoftwareX* **2018**, *7*, 1–5.

27. Perdew, J. P. Jacob's Ladder of Density Functional Approximations for the Exchange-Correlation Energy. In *AIP Conference Proceedings*; AIP: Antwerp (Belgium), 2001; Vol. 577, pp 1–20.

28. Grimme, S.; Antony, J.; Ehrlich, S.; Krieg, H. A Consistent and Accurate *Ab Initio* Parametrization of Density Functional Dispersion Correction (DFT-D) for the 94 Elements H-Pu. *J. Chem. Phys.* **2010**, *132* (15), 154104.

29. Lin, Y.-S.; Li, G.-D.; Mao, S.-P.; Chai, J.-D. Long-Range Corrected Hybrid Density Functionals with Improved Dispersion Corrections. *J. Chem. Theory Comput.* **2013**, *9* (1), 263–272.

30. Runge, E.; Gross, E. K. U. Density-Functional Theory for Time-Dependent Systems. *Phys. Rev. Lett.* **1984**, *52* (12), 997–1000.

31. Ullrich, C. A. A Snapshot of Time-Dependent Density-Functional Theory. *APL Comput. Phys.* **2025**, *1* (2), 020901.

32. Casida, M. E.; Huix-Rotllant, M. Progress in Time-Dependent Density-Functional Theory. *Annu. Rev. Phys. Chem.* **2012**, *63* (1), 287–323.

33. Niehaus, T. A.; Suhai, S.; Della Sala, F.; Lugli, P.; Elstner, M.; Seifert, G.; Frauenheim, Th. Tight-Binding Approach to Time-Dependent Density-Functional Response Theory. *Phys. Rev. B* **2001**, *63* (8), 085108.

34. Furche, F.; Ahlrichs, R. Adiabatic Time-Dependent Density Functional Methods for Excited State Properties. *J. Chem. Phys.* **2002**, *117* (16), 7433–7447.

35. Zeng, Y.; Havenridge, S.; Gharib, M.; Baksi, A.; Weerawardene, K. L. D. M.; Ziefuß, A. R.; Strelow, C.; Rehbock, C.; Mews, A.; Barcikowski, S.; Kappes, M. M.; Parak, W. J.; Aikens, C. M.; Chakraborty, I. Impact of Ligands on Structural and Optical Properties of Ag_{29} Nanoclusters. *J. Am. Chem. Soc.* **2021**, *143* (25), 9405–9414.

36. Muniz-Miranda, F.; Menziani, M. C.; Pedone, A. Influence of Silver Doping on the Photoluminescence of Protected Ag_nAu_{25-n} Nanoclusters: A Time-Dependent Density Functional Theory Investigation. *J. Phys. Chem. C* **2015**, *119* (19), 10766–10775.

37. Asadi-Aghbolaghi, N.; Rüger, R.; Jamshidi, Z.; Visscher, L. TD-DFT+TB: An Efficient and Fast Approach for Quantum Plasmonic Excitations. *J. Phys. Chem. C* **2020**, *124* (14), 7946–7955.

38. Kumawat, R. L.; Schatz, G. C. Efficient Modeling of Structural, Electronic, and Optical Properties of Silver and Gold Metal Nanoclusters and Alloys Using Optimized SCC-DFTB Parameters. *J. Phys. Chem. C* **2025**, *129* (2), 1348–1361.

39. Rüger, R.; Van Lenthe, E.; Heine, T.; Visscher, L. Tight-Binding Approximations to Time-Dependent Density Functional Theory — A Fast Approach for the Calculation of Electronically Excited States. *J. Chem. Phys.* **2016**, *144* (18), 184103.

40. Havenridge, S.; Rüger, R.; Aikens, C. M. Analytical Excited State Gradients for Time-Dependent Density Functional Theory plus Tight Binding (TDDFT + TB). *J. Chem. Phys.* **2023**, *158* (22), 224103.

41. Grimme, S. A Simplified Tamm-Dancoff Density Functional Approach for the Electronic Excitation Spectra of Very Large Molecules. *J. Chem. Phys.* **2013**, *138* (24), 244104.

42. Risthaus, T.; Hansen, A.; Grimme, S. Excited States Using the Simplified Tamm–Dancoff-Approach for Range-Separated Hybrid Density Functionals: Development and Application. *Phys. Chem. Chem. Phys.* **2014**, *16* (28), 14408–14419.

43. Bannwarth, C.; Grimme, S. A Simplified Time-Dependent Density Functional Theory Approach for Electronic Ultraviolet and Circular Dichroism Spectra of Very Large Molecules. *Comput. Theor. Chem.* **2014**, *1040–1041*, 45–53.

44. Wang, Y.; Havenridge, S.; Aikens, C. M. Implementation of Energy and Gradient for the TDDFT-Approximate Auxiliary Function (Aas) Method. *J. Chem. Phys.* **2024**, *161* (2), 024101.

45. Zhang, J.; Zhang, H.; Wu, T.; Wang, Q.; Van Der Spoel, D. Comparison of Implicit and Explicit Solvent Models for the Calculation of Solvation Free Energy in Organic Solvents. *J. Chem. Theory Comput.* **2017**, *13* (3), 1034–1043.

46. Godschalk, F.; Genheden, S.; Söderhjelm, P.; Ryde, U. Comparison of MM/GBSA Calculations Based on Explicit and Implicit Solvent Simulations. *Phys. Chem. Chem. Phys.* **2013**, *15* (20), 7731.

47. Norjmaa, G.; Ujaque, G.; Lledós, A. Beyond Continuum Solvent Models in Computational Homogeneous Catalysis. *Top. Catal.* **2022**, *65* (1–4), 118–140.

48. Huang, K.; Duan, L.; Zhang, J. Z. H. From Implicit to Explicit: An Interaction-Reorganization Approach to Molecular Solvation Energy. *J. Chem. Theory Comput.* **2024**, *20* (24), 10961–10971.

49. Klamt, A.; Schüürmann, G. COSMO: A New Approach to Dielectric Screening in Solvents with Explicit Expressions for the Screening Energy and Its Gradient. *J. Chem. Soc., Perkin Trans. 2* **1993**, No. 5, 799–805.

50. Klamt, A. Conductor-like Screening Model for Real Solvents: A New Approach to the Quantitative Calculation of Solvation Phenomena. *J. Phys. Chem.* **1995**, *99* (7), 2224–2235.

51. Klamt, A.; Jonas, V. Treatment of the Outlying Charge in Continuum Solvation Models. *J. Chem. Phys.* **1996**, *105* (22), 9972–9981.

52. Miertuš, S.; Scrocco, E.; Tomasi, J. Electrostatic Interaction of a Solute with a Continuum. A Direct Utilizaion of AB Initio Molecular Potentials for the Prevision of Solvent Effects. *Chem. Phys.* **1981**, *55* (1), 117–129.

53. Miertuš, S.; Tomasi, J. Approximate Evaluations of the Electrostatic Free Energy and Internal Energy Changes in Solution Processes. *Chem. Phys.* **1982**, *65* (2), 239–245.

54. Marenich, A. V.; Cramer, C. J.; Truhlar, D. G. Universal Solvation Model Based on Solute Electron Density and on a Continuum Model of the Solvent Defined by the Bulk Dielectric Constant and Atomic Surface Tensions. *J. Phys. Chem. B* **2009**, *113* (18), 6378–6396.

55. Rajpal, S.; Mishra, P.; Mizaikoff, B. Rational In Silico Design of Molecularly Imprinted Polymers: Current Challenges and Future Potential. *Int. J. Mol. Sci.* **2023**, *24* (7), 6785.

56. Butler, K. T.; Davies, D. W.; Cartwright, H.; Isayev, O.; Walsh, A. Machine Learning for Molecular and Materials Science. *Nature* **2018**, *559* (7715), 547–555.

57. Tkatchenko, A. Machine Learning for Chemical Discovery. *Nat. Commun.* **2020**, *11* (1), 4125.

58. Agrawal, A.; Choudhary, A. Perspective: Materials Informatics and Big Data: Realization of the "Fourth Paradigm" of Science in Materials Science. *APL Mater.* **2016**, *4* (5), 053208.

59. Behler, J.; Parrinello, M. Generalized Neural-Network Representation of High-Dimensional Potential-Energy Surfaces. *Phys. Rev. Lett.* **2007**, *98* (14), 146401.

60. Podryabinkin, E. V.; Shapeev, A. V. Active Learning of Linearly Parametrized Interatomic Potentials. *Comput. Mater. Sci.* **2017**, *140*, 171–180.

61. Chmiela, S.; Sauceda, H. E.; Müller, K.-R.; Tkatchenko, A. Towards Exact Molecular Dynamics Simulations with Machine-Learned Force Fields. *Nat. Commun.* **2018**, *9* (1), 3887.

62. Wilkins, D. M.; Grisafi, A.; Yang, Y.; Lao, K. U.; DiStasio, R. A.; Ceriotti, M. Accurate Molecular Polarizabilities with Coupled Cluster Theory and Machine Learning. *Proc. Natl. Acad. Sci. U.S.A.* **2019**, *116* (9), 3401–3406.

63. Schütt, K. T.; Gastegger, M.; Tkatchenko, A.; Müller, K.-R.; Maurer, R. J. Unifying Machine Learning and Quantum Chemistry with a Deep Neural Network for Molecular Wavefunctions. *Nat. Commun.* **2019**, *10* (1), 5024.

64. Du, K.-L.; Zhang, R.; Jiang, B.; Zeng, J.; Lu, J. Understanding Machine Learning Principles: Learning, Inference, Generalization, and Computational Learning Theory. *Math.* **2025**, *13* (3), 451.

65. Jordan, M. I.; Mitchell, T. M. Machine Learning: Trends, Perspectives, and Prospects. *Science* **2015**, *349* (6245), 255–260.

66. Esmaeilbeigi, M.; Chatrabgoun, O.; Cavoretto, R.; De Rossi, A.; Shafa, M. Sparse Gaussian Process Regression via Compactly Supported Kernels: A Trade-off between Accuracy and Computational Efficiency. *Inf. Sci.* **2025**, *717*, 122306.

67. Yang, K.; Lu, J.; Wan, W.; Zhang, G.; Hou, L. Transfer Learning Based on Sparse Gaussian Process for Regression. *Inf. Sci.* **2022**, *605*, 286–300.

68. Deisenroth, M. P.; Fox, D.; Rasmussen, C. E. Gaussian Processes for Data-Efficient Learning in Robotics and Control. *IEEE Trans. Pattern Anal. Mach. Intell.* **2015**, *37* (2), 408–423.

Chapter 3 - Effects of static electric fields on the excitations of silver nanowire dimers

Reprinted with permission from *J. Phys. Chem. A* 2024, 128, 18, 3548–3556.

Copyright 2024 American Chemical Society

D. Sulalith N. D. Samarasinghe and Christine M. Aikens*

Department of Chemistry, Kansas State University, Manhattan, KS 66506, USA

*Email: cmaikens@ksu.edu

3.1 Abstract

We theoretically studied the introduction of static electric fields to Ag_{10} nanowire dimer systems, including the effects of this field on optical absorption characteristics and the orbitals responsible for these excitations. Linear-response time-dependent density functional theory (TDDFT) computations were performed on three distinct dimer systems: end-to-end, parallel, and 90° angle dimer systems separated by a closest interparticle distance of 7.0 Å. The calculations were performed in the presence of a 0.1 V/Å electric field strength applied in the z and y directions. The orientation of the dimer system and the direction of the applied static electric field each play a significant role in the resulting absorption spectra and the electronic structure of the nanowires. As a result, a dimer system can exhibit a blue shift for the longitudinal excitation and a red shift for the transverse excitation in the presence of one direction of the static electric field, but not for the other direction. Notably, electron density shifts from one nanowire to the other in the presence of the static electric field. Changes in optical characteristics and electronic structure suggest that usage of a static electric field with a particular spatial configuration of nanowires provides a way to tune the optical properties of the system.

3.2 Introduction

Interest in nanowires has sparked both theoretical and experimental research during the last few decades. These one-dimensional nanostructures have many applications due to the structures' unique properties. Due to their flexibility and stretchability in addition to their electrical properties, metallic nanowires have become extremely desirable.[1,2] Flexible light-emitting diodes (LED),[3,4] flexible solar cell devices,[5] bendable screens,[6-8] wearable articular thermotherapy,[9,10] and antibacterial and medicinal applications[11,12] are just a few of the many applications that are currently in use.

Another essential attribute of nanoparticles is their unique optical properties, which have been discovered to be a key feature that can be fine-tuned depending on the structural, geometrical, and environmental parameters of the nanoparticles.[13,14] These unique optical characteristics arise from their surface plasmon resonances, which is a collective oscillation of conduction band electrons in metal nanoparticles in response to an electromagnetic field.[15-17] Research on nanowires and their optical properties includes both linear[18,19] and nonlinear[18-20] optical characteristics, from both experimental[20,21] and theoretical[18,19] perspectives.

Plasmonic coupling is a phenomenon that occurs when two or more plasmonic nanoparticles come into close proximity, greatly affecting the optical characteristics of the nanoparticles.[22-29] A nanoparticle dimer system is the simplest situation in which to witness this effect. Silver nanowire dimer systems exhibit absorption spectra with coupled longitudinal and transverse mode excitations.[25-28] Recent research in this field has employed time-dependent density functional theory (TDDFT)[24,27,28,30-32] and approximate TDDFT approaches[27,29,33] in dimer systems to examine their optical properties from a theoretical perspective.

Research on the optical properties of nanoparticles under applied external static electric fields is in its infancy. Even so, Farain et al.[34,35] made two important experimental contributions in one of the few investigations in the literature that used silver nanowires and an external static electric field. In the initial experiment, they investigated the rotational dynamics of silver nanowires in viscous dielectric liquids under the influence of a static uniform electric field.[34] This study demonstrated that the dimensions and electrical characteristics of the nanowires have no bearing on the rotational dynamics under the influence of the static electric field. As a result, this has a significant impact on controlling how well nanowires align in devices.[34] Their second study focused on the fast mobility of silver nanowires within a similar environment as the initial work. This investigation has potential applications on thin membrane piercings using nanowires.[35] In addition to silver nanowires, rotational dynamics and alignment modifications with AC electric fields have been considered for gold,[36-38] platinum,[38] and nickel[38] nanowires.

In this study, we use TDDFT computations to examine the impact of an external static electric field on several silver nanowire dimer systems. Our main goal is to analyze how the electric field affects these systems' optical properties, which includes understanding how the electric field impacts the molecular orbitals and how the field affects which orbitals are responsible for the excitations of interest. Therefore, we compare the results of the nanowire systems with and without an applied static electric field. In addition, we assess how the properties vary in response to the direction of the electric field.

3.3 Theory and computations

All linear-response TDDFT calculations were conducted using the ADF2021 software package.[39,40] For the systems of interest, we have used three different Ag_{10} nanowire dimer

systems. Optimized geometries of the monomers were obtained from a previous study in our group.[28] The Ag_{10} dimer systems include end-to-end, parallel, and 90° angle dimers, with a closest interparticle distance of 7.0 Å. As for the symmetry point groups of these systems, the end-to-end dimer is $D_{\infty h}$, the parallel dimer is D_{2h}, and the 90° dimer is C_{2v}. Figure 3.1 indicates these three different dimers and the spatial orientation used in this work; the coordinates are given in the Appendix A.

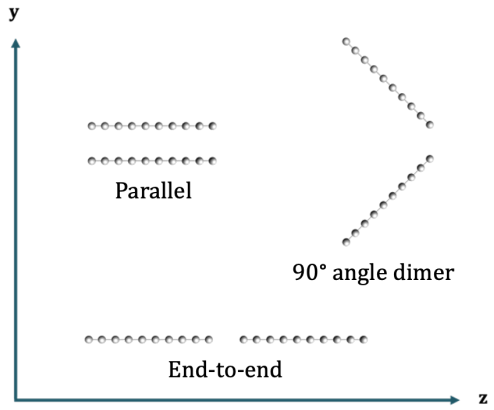


Figure 3.1. Geometries and orientations of the dimer systems.

Linear-response TDDFT calculations for all systems were performed using a double-zeta (DZ) basis set with three different functionals: BP86,[41,42] a long-range corrected (LC) version of BP86,[41,42] and LC CAMY-B3LYP.[43-45] Both LC functionals used a range separation parameter (gamma) of 0.75; it should be noted that the CAMY-B3LYP functional does not include 100% of the correct exchange at long-range. It should also be noted that the CAMY-B3LYP functional has a different form than the CAM-B3LYP functional due to a different switching function.[43-45] The selection of LC functionals was based on their previously reported success with silver nanoparticle systems.[46-49]

These calculations were conducted with and without a static electric field, which is applied with a 0.1 V/Å strength in the z and y directions. Because a static electric field in the x direction would be perpendicular to the nanowire chains in all configurations and thus the effects of this field would be expected to be small, it is not considered for this study. The absorption spectra were obtained from these calculations using a 0.08 eV full-width-half-maximum Gaussian broadening. In this work, we will describe the results acquired from the LC-BP86/DZ level of theory, with results from additional levels of theory included in the Appendix A (Figures A.1-A.3, Tables A.1-A.3). Previous work has shown that inclusion of long-range correction helps with charge transfer issues present in nanowire dimers when using functionals such as BP86.[28]

3.4 Results and discussion

3.4.1 Ag_{10} end-to-end dimer system

Effects of a static electric field in the z-direction

The absorption spectra obtained for the end-to-end dimer system with the z-polarized static electric field reveal a surprising difference when compared to the one without the static electric field. As shown in Figure 3.2a, the maximum of the absorption peak without the electric field is calculated to lie at 1.1932 eV, whereas the maximum changed to 1.2070 eV when the electric field is applied in the z-direction. This results in a blue shift of 0.0138 eV with the presence of a z-directional electric field.

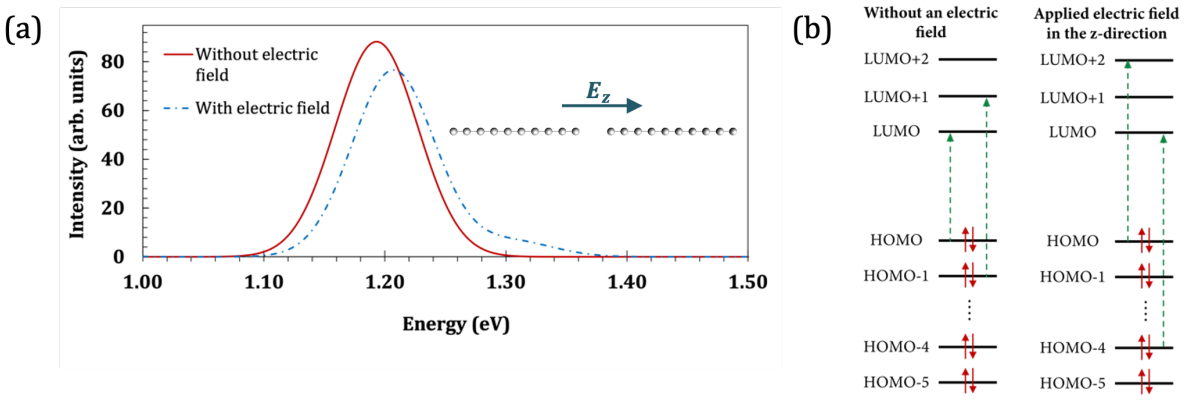


Figure 3.2. (a) Calculated absorption spectra for Ag_{10} end-to-end dimer system with and without the static electric field applied in the z-direction. (b) Allowed transitions of the excitations: without an electric field (left) and with the application of a static electric field in the z-direction (right).

Further analysis of the orbital contributions to these excitations generates novel findings. The major contributions for the strong excitation in this dimer without the electric field arise from HOMO→LUMO and HOMO-1→LUMO+1 transitions. However, with the presence of the z-directional electric field, this changes to HOMO→LUMO+2 and HOMO-4→LUMO (Figure 3.2b).

In the presence of the z-directional electric field, electron density on nanowires ultimately shifts from one nanowire to the other. As shown in Figure 3.3, upon application of the electric field, the molecular orbitals of the dimer system significantly change. Examining the number of nodes on these orbitals reveals that, while their appearance has changed, the number of nodes in their respective orbitals is similar both with and without the static electric field. For example, the HOMO orbital has nine nodes without the electric field, and even with the shifts due to the presence of the z-direction electric field, we can distinguish the nine nodes within the molecular orbitals. However, in the presence of a y-directional electric field, the orbitals of the nanowires are similar to the orbitals when no electric field is applied. “Effects of the static electric field on

orbitals" section will go through the changes in the "one-electron" densities arising from the molecular orbitals in detail.

Depending on the molecular orbital interactions between the monomeric levels, the orbitals can be considered as either bonding or antibonding, where bonding orbitals have the same phase in the lobes between the wires and antibonding orbitals have different phases in these lobes.[28] Therefore, the HOMO→LUMO transition in the field-free case is considered to be antibonding→bonding, while HOMO-1→LUMO+1 is considered to be bonding→antibonding. As previously stated, these orbital contributions alter in the presence of the z-directional electric field. However, investigating them in terms of bonding and antibonding orbitals reveals that transitions from antibonding to bonding orbitals continue to occur for both HOMO→LUMO+2 and HOMO-4→LUMO transitions.

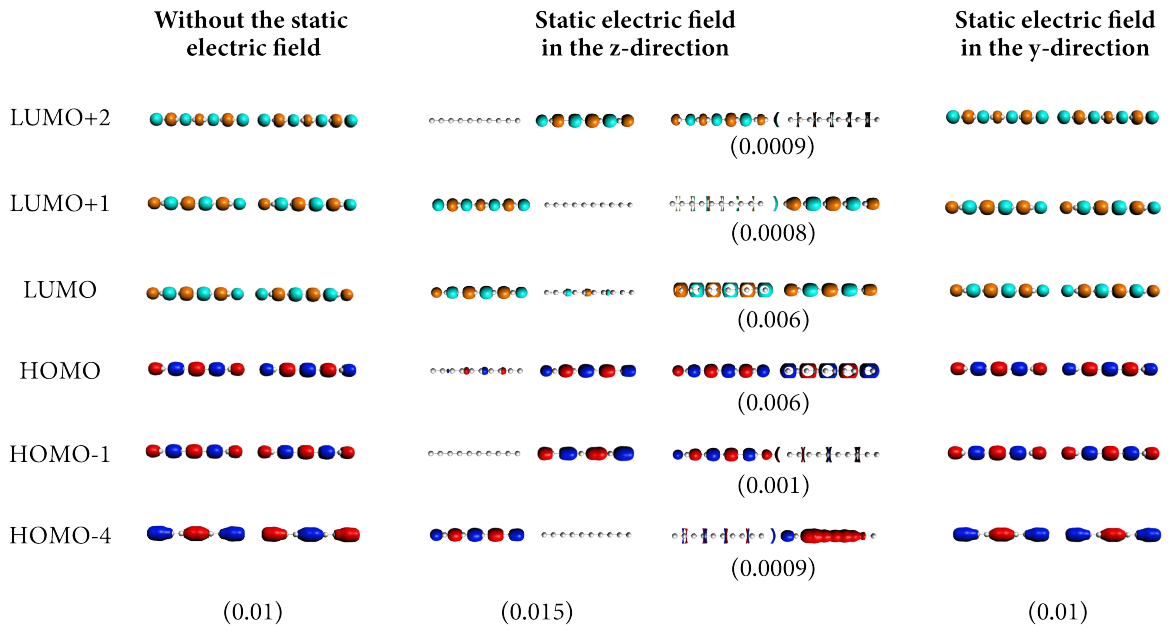


Figure 3.3. Illustrations of major molecular orbitals of Ag_{10} end-to-end dimer system, with and without the static electric field of 0.1 V/Å. Two views (with different iso-surface values) are provided for the z-direction field. Respective iso-surface values are denoted within the parentheses.

Effects of a static electric field in the y-direction

When the static electric field is changed to the y-direction, the change in the absorption spectrum of the end-to-end system (Figure 3.4a) is substantially smaller than when the static electric field is applied in the z-direction. The longitudinal absorption peak lies at 1.1933 eV, with a 0.0001 eV blueshift compared to the one without the electric field. Analyzing the orbital contributions to the excitations also reveals identical transitions to those observed in the absence of the electric field: HOMO→LUMO and HOMO-1→LUMO+1.

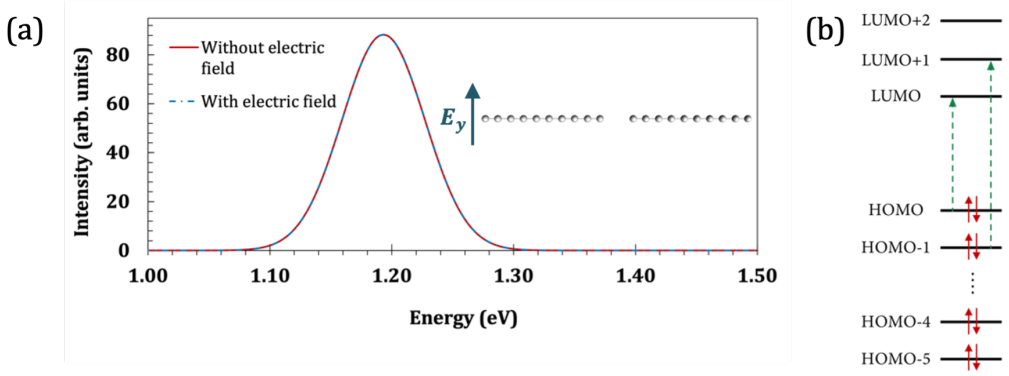


Figure 3.4. (a) Calculated absorption spectra for Ag_{10} end-to-end dimer system with and without the static electric field applied in the y-direction. (b) Allowed transitions of the excitations with the y-directional static electric field.

The analysis of the molecular orbitals reveals that they are identical to the orbitals found in the absence of an electric field (Figure 3.3). In contrast to the molecular orbitals of the end-to-end dimer in the z-directional electric field, no orbital alterations are seen with the y-directional field. This means that the y-directional static electric field has less of an influence on the end-to-end dimer system than the z-directional field.

Effect of the static electric fields on orbitals

Without the presence of the static electric field (Figure 3.5a), the one-electron density for each orbital is evenly spread through the dimer. When the z-directional electric field is present, it will affect the electron density of the two nanowires and shift the electron density from one wire to the other (Figure 3.5b). Therefore, in the presence of the z-directional electric field, most of the electron density for this orbital can be found in the left nanowire rather than being evenly spread through the dimer (as in Figure 3.5a). Further considering the nodal structure of the two nanowires indicates five nodes for each case, whether with or without the presence of the electric field. It should be noted that Figure 3.5b uses a much smaller iso-surface value for the right nanowire, which indicates that this orbital has significantly less electron density on the right nanowire.

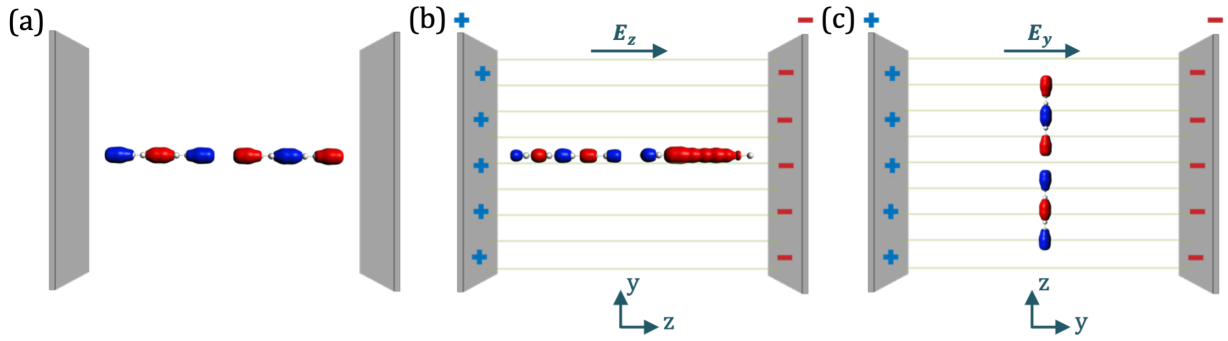


Figure 3.5. Graphical interpretation of the static electric field effect on the HOMO-4 molecular orbital of the end-to-end Ag_{10} dimer system; (a) without the electric field, (b) within the z-directional electric field, and (c) with the y-directional electric field (the yz plane shows the nanowires' geometric orientation). The iso-surface values are the same as in Figure 3.3. However, to appropriately demonstrate the effect, the molecular orbitals in the z-directional electric field is shown as a composite of multiple iso-surface values (with 0.015 for the left nanowire and 0.0009 for the right nanowire).

This can be described as the electric field affecting the delocalized orbitals in the direction of the delocalization. As a result, it is evident that no changes in the molecular orbitals

are observed when the y-directional field is present (Figure 3.5c) because the pull of the electron density is perpendicular to the nanowires. This suggests that the simple presence of an electric field is not sufficient to change the electronic structure, as the relative orientation of the field and the dimer system are important components.

3.4.2 Monomer vs. dimer systems

When the z-directional static electric field is applied only to a single Ag_{10} monomer, its longitudinal peak shifts to 1.2539 eV from 1.2500 eV (Figure A.4, Table A.4), resulting a smaller 0.0039 eV blue shift compared to the shift observed in the Ag_{10} end-to-end dimer system (0.0138 eV blue shift). The blue shift for the y-direction field is only 0.0001 eV, which matches with the blue shift experienced by the dimer with this field, so both the monomer and dimer experience greater blue shifts with z-direction fields.

The Ag_{10} end-to-end dimer system with 7.0 Å separation between the monomers behaves very differently from a single longer silver nanowire monomer, Ag_{20}. In the presence of the z-directional static electric field, the longitudinal peak of Ag_{20} shifts from 0.7622 eV to 0.7718 eV, indicating a 0.0096 eV blue shift (Figure A.5, Table A.5). This blue shift is over twice the blue shift experienced by the Ag_{10} monomer itself but is not as large as the blue shift experienced by the Ag_{10} end-to-end dimer system, so the magnitude of the blue shift is not directly proportional to the number of silver atoms in the system. Regardless, compared to the Ag_{10} monomer, the Ag_{20} monomer results clearly suggest that the blue shift of the longitudinal peak becomes more significant in the presence of the z-directional electric field, similar to the Ag_{10} end-to-end dimer system. Figure A.6 and Figure A.7 indicate the molecular orbital changes occurring for Ag_{10} and Ag_{20} monomers, respectively, in the presence of the static electric field, and reflect the fact that

the longer systems exhibit more noticeable changes in electronic structure. Distortion of the molecular orbitals in the direction of the applied field can be observed, especially in the presence of a field that aligns along the long axis of the system. These results suggest that the electric field effect on absorption peak energies becomes stronger as the length of the nanowire increases, when the electric field peak direction is the same as the elongation direction of the system. In contrast, a y-directional static electric field results in 0.0001 eV blue shifts in the longitudinal peaks for both Ag_{10} and Ag_{20} monomers, which is identical to the Ag_{10} end-to-end dimer system with the y-directional static electric field.

3.4.3 Ag_{10} parallel dimer system within a static electric field

For the Ag_{10} parallel dimer system (Figure 3.1), comparable absorption spectra are produced upon the application of static electric fields in both y- and z-directions compared to no applied field (Figure 3.6). The results show that the absorption peak without an electric field is centered at 1.3792 eV and shifts to 1.3800 eV with a z-directional static electric field. This results in a significantly smaller blue shift of 0.0008 eV with the presence of the z-directional electric field. Furthermore, if the field direction is changed to y, the absorption peak appears at 1.3793 eV, which results in a significantly lower blue shift of 0.0001 eV. When compared to the end-to-end dimer system in the z-directional electric field, the parallel dimer system in the presence of either z-directional or y-directional static electric fields does not exhibit a considerable effect on the longitudinal absorption peak.

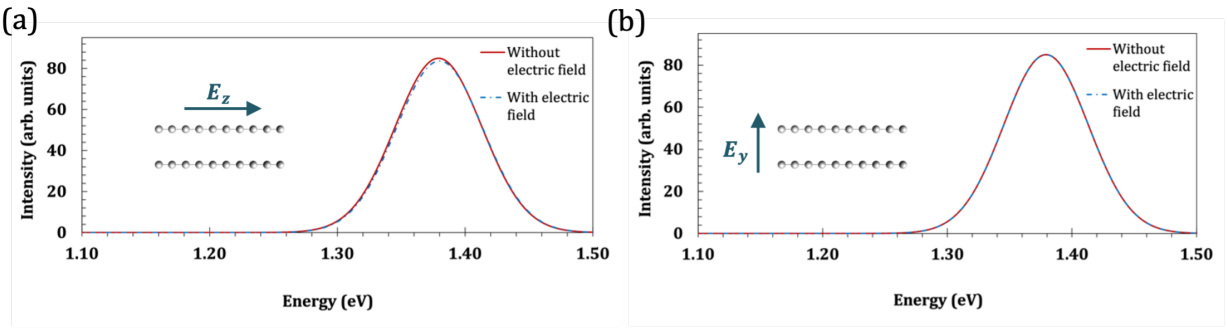


Figure 3.6. Calculated absorption spectra for Ag_{10} parallel dimer system with and without the static electric field (a) applied in the z-direction and (b) applied in the y-direction.

For the molecular orbitals (Figure 3.7), the presence of the y-directional electric field results in significant effects in the one-electron density compared to the case without the electric field. As the y-directional field induces changes in the electron density of the two nanowires, the one-electron density for each orbital eventually shifts from one nanowire to the other; the parallel alignment of the Ag_{10} dimer system demonstrates this effect as the y-directional electric field induces the electron density to move across the short axis of the system. However, in all cases, the monomers have the same number of lobes and nodes in the orbitals. For the electric field in the z-direction, changes in the electron density will still be induced and the field will pull the electron density parallel to the system. As a result, fewer changes occur in this case because the one-electron density remains on the same nanowire. The distortion in the orbitals of the parallel system with the z-direction field are minor compared to the end-to-end case.

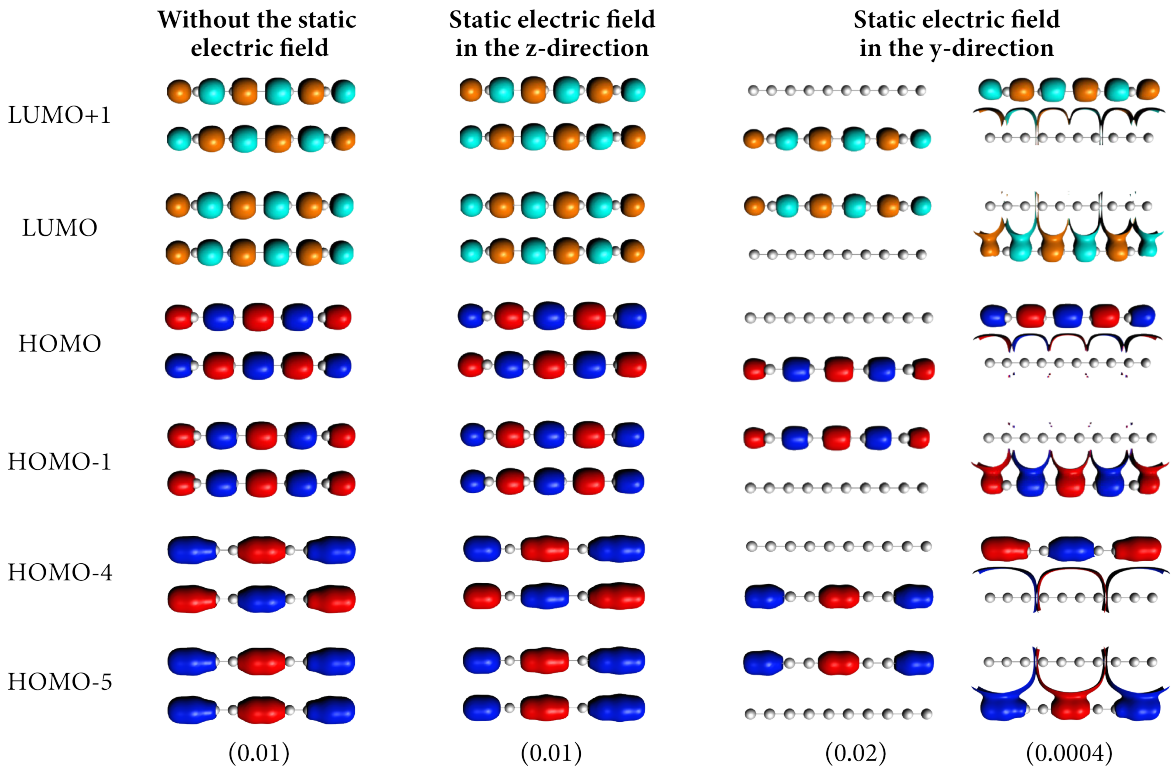


Figure 3.7. Illustrations of major molecular orbitals of Ag_{10} parallel dimer system, with and without the static electric field of 0.1 V/Å.

The orbital contributions in the excitations with the applied static electric fields are also identical to the case where there is no electric field present. The excitations involve transitions from HOMO→LUMO+1 and HOMO-1→LUMO. Considering the monomeric interactions, these transitions occur from antibonding→antibonding and bonding→bonding orbitals, respectively. In the case of the z-direction field, the minor distortions in the orbitals result in a very small (0.0008 eV) shift in the absorption spectrum, as discussed above. Although the y-directional field affects the orbitals more in the parallel dimer, very little change is observed in the absorption spectrum because the one-electron densities for the HOMO and LUMO+1 are located on the same wire, and the one-electron densities for the HOMO-1 and LUMO are located

on the other wire, so the HOMO→LUMO+1 and HOMO-1→LUMO transitions are essentially similar to HOMO→LUMO transitions on a single monomer.

3.4.4 Ag_{10} 90° dimer system within a static electric field

In the case of the 90° dimer system, no major changes are seen in the presence of the z-directional static electric field (Figure 3.8a). Without the electric field, two prominent absorption peaks of 1.1892 eV and 1.2994 eV are observed. In the presence of the z-directional electric field, the absorption energies are calculated at 1.1904 eV and 1.3003 eV, which correspond to 0.0012 eV and 0.0009 eV blue shifts, respectively. The peak shifts are significantly less compared to the shifts observed with the end-to-end dimer system with the z-directional electric field.

The changes observed when the static electric field is considered in the y-direction (Figure 3.8b) are reminiscent of results obtained previously for the end-to-end dimer with the z-directional electric field, as the shifts in the absorption are more pronounced in this case compared to the 90° dimer system with the z-directional electric field. In this case, the absorptions occur at 1.2019 eV and 1.3043 eV, resulting in 0.0127 eV and 0.0049 eV blue shifts, respectively. The results indicate that with the y-directional static electric field, we can observe a prominent blue shift in the 90° dimer. The y-direction field can be thought of as the field that affects the end-to-end coupling of the two nanowires for this configuration.

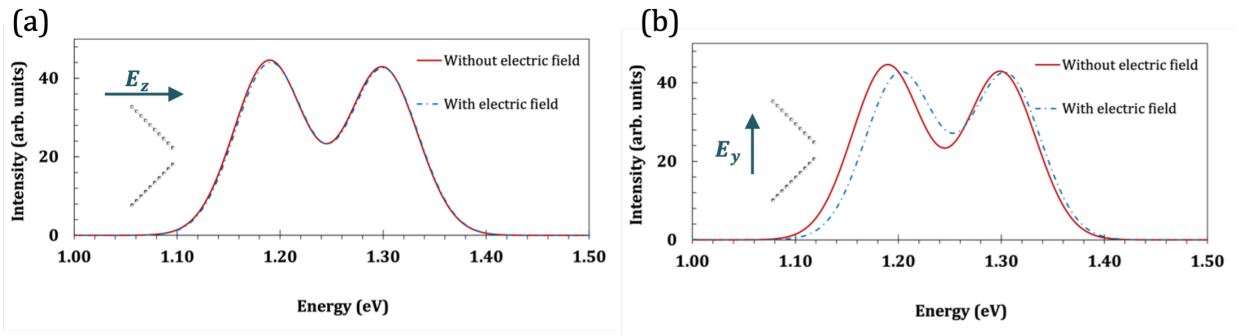


Figure 3.8. Calculated absorption spectra for the Ag_{10} 90° dimer system with and without the static electric field (a) applied in the z-direction and (b) applied in the y-direction.

As shown in Figure 3.9, there are no notable differences between the molecular orbitals of the Ag_{10} 90° dimer within the z-directional static electric field compared to the one without the electric field. However, adjusting the electric field direction to y has a considerable effect since noticeable electron density shifts are seen (Figure 3.9). These observations can be interpreted as the z-direction field inducing shifts in the electron density of the nanowires toward or away from the interaction point between the two nanowires, whereas the y-direction field induces the electron density to shift from one wire to the other.

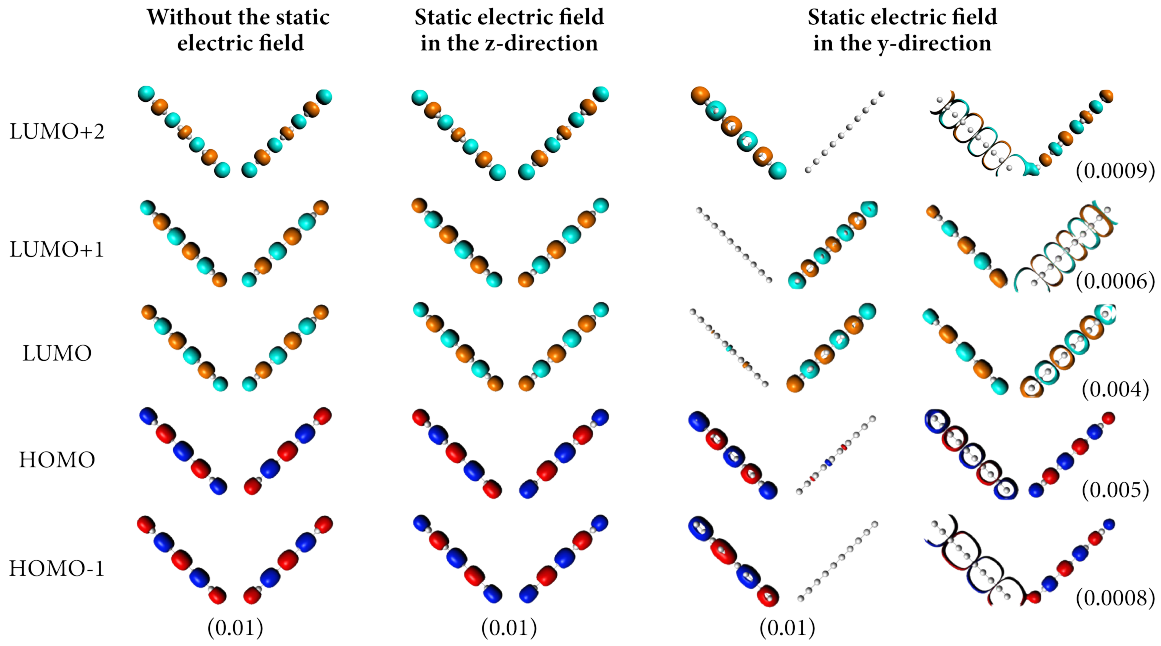


Figure 3.9. Illustrations of major molecular orbitals of the Ag_{10} 90° dimer system, with and without the static electric field of 0.1 V/Å. Orbitals from HOMO-2 to HOMO-5 are given in Figure A.8.

For the orbital contributions responsible for the excitations, the 90° dimer system without any electric field exhibits HOMO→LUMO and HOMO-1→LUMO+1 transitions for the ~1.1904 eV absorption peak and HOMO-1→LUMO and HOMO→LUMO+1 transitions for ~1.3003 eV absorption. Considering the monomer levels and their interactions, these transitions occur through antibonding→bonding and bonding→antibonding for the initial absorption peak and bonding→bonding and antibonding→antibonding for the second peak. Further investigation of the excitations in the presence of a z-directional electric field reveals that they are identical to the excitations in the absence of an electric field.

With the presence of the y-directional static electric field, the transitions involved in the excitations changed dramatically compared to the results without the field. In this case, the reported transitions involve HOMO→LUMO+2 for ~1.2019 eV and HOMO-5→LUMO for

~1.3043 eV absorptions. Furthermore, this indicates that these transitions are from antibonding→bonding and bonding→bonding respectively, which is the same as the character of the transitions in the absence of an applied field, although the orbitals have changed.

3.4.5 Transverse excitations in Ag_{10} dimer systems within a static electric field

Up to this point, we have investigated the impact of the external static electric field on the longitudinal excitations of the Ag_{10} dimer systems. We now shift our attention to the transverse excitations and observe a significant impact from the presence of a static electric field. One main distinction between longitudinal and transverse excitations is that the transverse excitations red shift in the presence of a static electric field.

In this work, we find that transverse peak shifts are prominent in systems where a static electric field has a significant effect on longitudinal peaks. As a result, the presence of a z-polarized static electric field results in a significant red shift on the transverse peak when compared to the presence of a y-polarized static electric field on the end-to-end dimer system, as shown in Figure 3.10a. Without any static electric field, the transverse peak occurs at 5.7914 eV, but this peak is shifted to 5.7612 eV when an electric field is introduced in the z-direction, resulting in a red shift of 0.0302 eV. This can also be seen in the 90° dimer system, as shown in Figure 3.10c, where the system exhibits a strong red shift (0.0132 eV) when the y-directional static electric field is applied, which shifts the transverse peak from 5.7927 eV to 5.7795 eV. Similar to the previously observed results for the parallel dimer system longitudinal absorption peak, the presence of both z- and y-directional static electric fields has no significant influence on the transverse absorption peak (Figure 3.10b). Table A.6 in the Appendix A contains an

extensive comparison of the transverse peak energies with their orbital contributions for the excitations of the dimer systems.

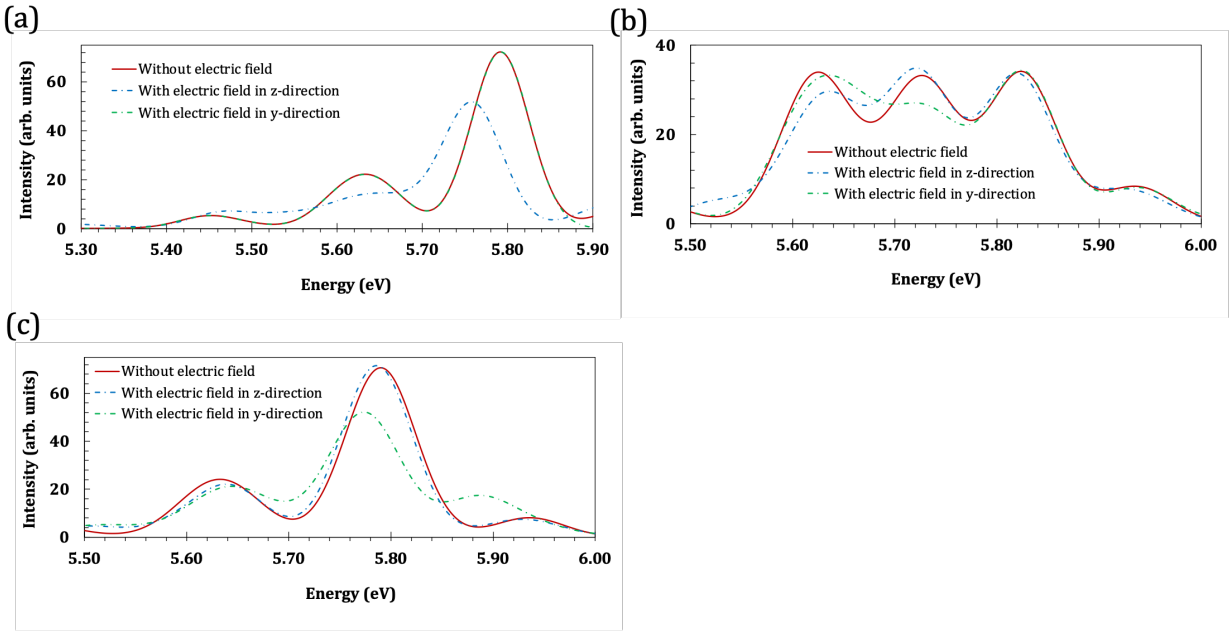


Figure 3.10. Calculated absorption spectra indicating the transverse excitation for (a) Ag_{10} end-to-end dimer system (b) Ag_{10} parallel dimer system (c) Ag_{10} 90° dimer system, with and without the static electric field applied in the z- and y-directions.

3.5 Conclusion

In summary, we investigated the effect of static electric fields on three distinct Ag_{10} dimer systems (end-to-end, parallel, or with a 90° angle) using linear response TDDFT simulations. The results show that different applied static electric fields (applied in the z-direction or in the y-direction) will alter the excitations and the molecular orbitals in these different arrangements of Ag_{10} nanowires. Significantly, depending on the arrangement of the dimers and the direction of the electric field, the electron density of the delocalized orbitals will shift in the direction of the delocalization. The Ag_{10} end-to-end dimer with the z-directional electric field exhibits a noticeable shift in its longitudinal and transverse absorption peaks due to

changes in its electronic structure. On the other hand, in some cases the absorption spectrum stays quite similar to the results obtained without the electric field, as in the case of the Ag_{10} end-to-end dimer with the y-directional electric field. In this case, although the orbitals are affected by the electric field, offsetting effects decrease the shifts in the excited states responsible for the absorption spectrum. Furthermore, the electron density on the nanowires is similar to the density without the static electric field in this case. For the 90° system, the observations depend on the relative orientation of the nanowires and the applied electric field. With the geometry used in this system, the z-directional electric field causes minor effects on the electronic structure, whereas the y-directional electric field causes more noticeable effects on the electronic structure, which shifts its absorption spectrum.

Overall, the effects on the longitudinal and transverse excitations resulting from the presence of a static electric field indicate blue shifts for the longitudinal and red shifts for the transverse peaks. In dimer systems, the specific configuration of monomers and the applied direction of the static electric field play crucial roles in orbital shifts and excitations.

3.6 Appendix A - Supporting information

Absorption spectra and excitation information from BP86 and (LC) CAMY-B3LYP functionals; absorption spectra, excitation information, and orbitals for Ag_{10} and Ag_{20} monomer calculations; additional orbitals for the Ag_{10} 90° dimer system; excitation information for transverse excitations; and coordinates used in this work.

3.7 Acknowledgements

This material is based on work supported by the Department of Energy under grant DE-SC0012273. The computing for this work was performed on the Beocat Research Cluster at Kansas State University, which is in part funded by the NSF (Grant Nos. CHE-1726332, CNS-1006860, EPS-1006860, and EPS-0919443). The authors thank Prof. Ken Knappenberger for interesting discussions that inspired this research.

3.8 References

1. Jiu, J.; Suganuma, K. Metallic Nanowires and Their Application. *IEEE Trans. Compon., Packag., Manuf. Technol.* **2016**, *6* (12), 1733−1751.

2. Dresselhaus, M. S.; Lin, Y. M.; Rabin, O.; Jorio, A.; Souza Filho, A. G.; Pimenta, M. A.; Saito, R.; Samsonidze, G.; Dresselhaus, G. Nanowires and Nanotubes. *Mater. Sci. Eng. C* **2003**, *23* (1−2), 129−140.

3. Jun, S.; Ju, B. K.; Kim, J. W. Fabrication of Substrate-Free Double-Side Emitting Flexible Device Based on Silver Nanowire-Polymer Composite Electrode. *Curr. Appl. Phys.* **2017**, *17* (1), 6−10.

4. Hui, Z.; Liu, Y.; Guo, W.; Li, L.; Mu, N.; Jin, C.; Zhu, Y.; Peng, P. Chemical Sintering of Direct-Written Silver Nanowire Flexible Electrodes under Room Temperature. *Nanotechnology* **2017**, *28* (28), 285703.

5. Tsai, W. C.; Thomas, S. R.; Hsu, C. H.; Huang, Y. C.; Tseng, J. Y.; Wu, T. T.; Chang, C. H.; Wang, Z. M.; Shieh, J. M.; Shen, C. H.; et al. Flexible High Performance Hybrid AZO/Ag-Nanowire/AZO Sandwich Structured Transparent Conductors for Flexible Cu-(In,Ga)Se_2 Solar Cell Applications. *J. Mater. Chem. A* **2016**, *4* (18), 6980−6988.

6. Ma, F.; Lin, Y.; Yuan, W.; Ding, C.; Su, W.; Meng, X.; Cui, Z. Fully Printed, Large-Size Alternating Current Electroluminescent Device on Fabric for Wearable Textile Display. *ACS Appl. Electron. Mater.* **2021,** *3* (4), 1747−1757.

7. Zhou, Y.; Zhao, C.; Wang, J.; Li, Y.; Li, C.; Zhu, H.; Feng, S.; Cao, S.; Kong, D. Stretchable High-Permittivity Nanocomposites for Epidermal Alternating-Current Electroluminescent Displays. *ACS Mater. Lett.* **2019**, *1* (5), 511−518.

8. Zhou, Y.; Cao, S.; Wang, J.; Zhu, H.; Wang, J.; Yang, S.; Wang, X.; Kong, D. Bright Stretchable Electroluminescent Devices Based on Silver Nanowire Electrodes and High-k Thermoplastic Elastomers. *ACS Appl. Mater. Interfaces* **2018**, *10* (51), 44760−44767.

9. Choi, S.; Park, J.; Hyun, W.; Kim, J.; Kim, J.; Lee, Y. B.; Song, C.; Hwang, H. J.; Kim, J. H.; Hyeon, T.; et al. Stretchable Heater Using Ligand-Exchanged Silver Nanowire Nanocomposite for Wearable Articular Thermotherapy. *ACS Nano* **2015**, *9* (6), 6626−6633.

10. Lan, W.; Chen, Y.; Yang, Z.; Han, W.; Zhou, J.; Zhang, Y.; Wang, J.; Tang, G.; Wei, Y.; Dou, W.; et al. Ultraflexible Transparent Film Heater Made of Ag Nanowire/PVA Composite for Rapid-Response Thermotherapy Pads. *ACS Appl. Mater. Interfaces* **2017**, *9* (7), 6644−6651.

11. Jones, R.; Draheim, R.; Roldo, M. Silver Nanowires: Synthesis, Antibacterial Activity and Biomedical Applications. *Appl. Sci.* **2018**, *8* (5), 673.

12. Hong, X.; Wen, J.; Xiong, X.; Hu, Y. Shape Effect on the Antibacterial Activity of Silver Nanoparticles Synthesized via a Microwave-Assisted Method. *Environ. Sci. Pollut. Res.* **2016**, *23* (5), 4489−4497.

13. Kelly, K. L.; Coronado, E.; Zhao, L. L.; Schatz, G. C. The Optical Properties of Metal Nanoparticles: The Influence of Size, Shape, and Dielectric Environment. *J. Phys. Chem. B* **2003**, *107* (3), 668−677.

14. Goyal, M.; Singh, M. Size and Shape Dependence of Optical Properties of Nanostructures. *Appl. Phys. A: Mater. Sci. Process.* **2020**, *126* (3), 176.

15. Link, S.; El-Sayed, M. A. Spectral Properties and Relaxation Dynamics of Surface Plasmon Electronic Oscillations in Gold and Silver Nanodots and Nanorods. *J. Phys. Chem. B* **1999**, *103* (40), 8410−8426.

16. Azarian, A.; Babaei, F. Surface Plasmon Resonance of Cu Nanowires in Polycarbonate Template. *Opt. Commun.* **2013**, *289*, 1−5.

17. Zhu, J. Surface Plasmon Resonance from Bimetallic Interface in Au-Ag Core-Shell Structure Nanowires. *Nanoscale Res. Lett.* **2009**, *4* (9), 977−981.

18. Singh, S.; Srivastava, P. Linear and Non-Linear Optical Properties of GaAs Nanowires. *Appl. Nanosci.* **2015**, *5* (3), 273−279.

19. Zhang, L.; Guo, K. X.; Xie, H. J. Linear and Nonlinear Optical Absorption of Excitonic States in a Wurtzite ZnO Nanowire: Quantum Size Effect. *Phys. Status Solidi B* **2013**, *250* (9), 1898−1906.

20. Cai, S.; Xiao, X.; Ye, X.; Li, W.; Zheng, C. Nonlinear Optical and Optical Limiting Properties of Ultra-Long Gold Nanowires. *Mater. Lett.* **2016**, *166*, 51−54.

21. Ji, X.; Zou, T.; Gong, H.; Wu, Q.; Qiao, Z.; Wu, W.; Wang, H. Cobalt Phthalocyanine Nanowires: Growth, Crystal Structure, and Optical Properties. *Cryst. Res. Technol.* **2016**, *51* (2), 154−159.

22. Aćimović, S. S.; Kreuzer, M. P.; Gonz.lez, M. U.; Quidant, R. Plasmon Near-Field Coupling in Metal Dimers as a Step toward Single-Molecule Sensing. *ACS Nano* **2009**, *3* (5), 1231−1237.

23. Yadav, P. R.; Rizvi, M. H.; Kuttich, B.; Mishra, S. R.; Chapman, B. S.; Lynch, B. B.; Kraus, T.; Oldenburg, A. L.; Tracy, J. B. Plasmon-Coupled Gold Nanoparticles in Stretched Shape-Memory Polymers for Mechanical/Thermal Sensing. *ACS Appl. Nano Mater.* **2021**, *4* (4), 3911−3921.

24. Alkan, F.; Aikens, C. M. Understanding Plasmon Coupling in Nanoparticle Dimers Using Molecular Orbitals and Configuration Interaction. *Phys. Chem. Chem. Phys.* **2019**, *21* (41), 23065−23075.

25. N'Gom, M.; Ringnalda, J.; Mansfield, J. F.; Agarwal, A.; Kotov, N.; Zaluzec, N. J.; Norris, T. B. Single Particle Plasmon Spectroscopy of Silver Nanowires and Gold Nanorods. *Nano Lett.* **2008**, *8* (10), 3200−3204.

26. Qin, Y.; Cao, W.; Zhang, Z. Surface Plasmon Polariton Coupling between a Metal Nanowire and a Metal Helix. *Optik* **2013**, *124* (22), 5363−5365.

27. Alkan, F.; Aikens, C. M. TD-DFT and TD-DFTB Investigation of the Optical Properties and Electronic Structure of Silver Nanorods and Nanorod Dimers. *J. Phys. Chem. C* **2018**, *122* (41), 23639−23650.

28. Alkan, F.; Aikens, C. M. Understanding the Effect of Symmetry Breaking on Plasmon Coupling from TDDFT. *J. Phys. Chem. C* **2021**, *125* (22), 12198−12206.

29. Liu, Z.; Alkan, F.; Aikens, C. M. TD-DFTB Study of Optical Properties of Silver Nanoparticle Homodimers and Heterodimers. *J. Chem. Phys.* **2020**, *153* (14), 144711.

30. Zhang, K.; Zhang, H. Plasmon Coupling in Gold Nanotube Assemblies: Insight from a Time-Dependent Density Functional Theory (TDDFT) Calculation. *J. Phys. Chem. C* **2014**, *118* (1), 635−641.

31. Pandeya, P.; Aikens, C. M. Theoretical Analysis of Optical Absorption Spectra of Parallel Nanowire Dimers and Dolmen Trimers. *J. Phys. Chem. C* **2020**, *124* (24), 13495−13507.

32. Bae, G. T.; Aikens, C. M. TDDFT and CIS Studies of Optical Properties of Dimers of Silver Tetrahedra. *J. Phys. Chem. A* **2012**, *116* (31), 8260−8269.

33. Liu, Z.; Oviedo, M. B.; Wong, B. M.; Aikens, C. M. Plasmon-Induced Excitation Energy Transfer in Silver Nanoparticle Dimers: A Real-Time TDDFTB Investigation. *J. Chem. Phys.* **2022**, *156* (15), 154705.

34. Farain, K.; Esfandiar, A.; Moshfegh, A. Z. Universal Rotation of Nanowires in Static Uniform Electric Fields in Viscous Dielectric Liquids. *Appl. Phys. Lett.* **2018**, *113* (6), 063101.

35. Farain, K.; Esfandiar, A.; Moshfegh, A. Z. Shooting at the Nanoscale: Collection and Acceleration of Nanowires with an External Electric Field. *Appl. Phys. Lett.* **2019**, *114* (1), 013102.

36. Smith, P. A.; Nordquist, C. D.; Jackson, T. N.; Mayer, T. S.; Martin, B. R.; Mbindyo, J.; Mallouk, T. E. Electric-Field Assisted Assembly and Alignment of Metallic Nanowires. *Appl. Phys. Lett.* **2000**, *77* (9), 1399−1401.

37. Fan, D. L.; Zhu, F. Q.; Cammarata, R. C.; Chien, C. L. Manipulation of Nanowires in Suspension by AC Electric Fields. *Appl. Phys. Lett.* **2004**, *85* (18), 4175−4177.

38. Fan, D. L.; Zhu, F. Q.; Cammarata, R. C.; Chien, C. L. Controllable High-Speed Rotation of Nanowires. *Phys. Rev. Lett.* **2005**, *94* (24), 247208.

39. te Velde, G.; Bickelhaupt, F. M.; Baerends, E. J.; Fonseca Guerra, C.; van Gisbergen, S. J. A.; Snijders, J. G.; Ziegler, T. Chemistry with ADF. *J. Comput. Chem.* **2001**, *22* (9), 931−967.

40. ADF2021, SCM. Theoretical Chemistry; Vrije Universities: Amsterdam, 2021. http://www.scm.com (accessed 20 December 2021).

41. Becke, A. D. Density-Functional Exchange-Energy Approximation with Correct Asymptotic Behavior. *Phys. Rev. A* **1988**, *38* (6), 3098−3100.

42. Perdew, J. P. Density-Functional Approximation for the Correlation Energy of the Inhomogeneous Electron Gas. *Phys. Rev. B: Condens. Matter Mater. Phys.* **1986**, *33* (12), 8822−8824.

43. Yanai, T.; Tew, D. P.; Handy, N. C. A New Hybrid Exchange-Correlation Functional Using the Coulomb-Attenuating Method (CAM-B3LYP). *Chem. Phys. Lett.* **2004**, *393* (1−3), 51−57.

44. Akinaga, Y.; Ten-no, S. Range-Separation by the Yukawa Potential in Long-Range Corrected Density Functional Theory with Gaussian-Type Basis Functions. *Chem. Phys. Lett.* **2008**, *462* (4−6), 348−351.

45. Seth, M.; Ziegler, T. Range-Separated Exchange Functionals with Slater-Type Functions. *J. Chem. Theory Comput.* **2012**, *8* (3), 901−907.

46. Rabilloud, F. Assessment of the Performance of Long-Range-Corrected Density Functionals for Calculating the Absorption Spectra of Silver Clusters. *J. Phys. Chem. A* **2013**, *117* (20), 4267−4278.

47. Rabilloud, F. Description of Plasmon-like Band in Silver Clusters: The Importance of the Long-Range Hartree-Fock Exchange in Time-Dependent Density-Functional Theory Simulations. *J. Chem. Phys.* **2014**, *141* (14), 144302.

48. Anak, B.; Bencharif, M.; Rabilloud, F. Time-Dependent Density Functional Study of UV-Visible Absorption Spectra of Small Noble Metal Clusters (Cu_n, Ag_n, Au_n, n = 2−9, 20). *RSC Adv.* **2014**, *4* (25), 13001−13011.

49. Hull, O. A.; Lingerfelt, D. B.; Li, X.; Aikens, C. M. Electronic Structure and Nonadiabatic Dynamics of Atomic Silver Nanowire-N_2 Systems. *J. Phys. Chem. C* **2020**, *124* (38), 20834−20845.

Chapter 4 - Theoretical insights into the excitation characteristics of the $Au_{42}(SCH_3)_{32}$ nanorod in the near-infrared region

D. Sulalith N. D. Samarasinghe[†], Christine M. Aikens[†*]

[†] Department of Chemistry, Kansas State University, Manhattan, KS 66506, United States

*Email: cmaikens@ksu.edu

4.1 Abstract

Gold nanoclusters with atomically precise structures exhibit tunable optical properties, with certain systems demonstrating efficient near-infrared (NIR) absorption and photothermal conversion. These characteristics make them particularly promising for cancer and photothermal therapy. We investigate the NIR excitation characteristics and electronic structure of the $Au_{42}(SCH_3)_{32}$ nanorod in different solvation media using density functional theory (DFT) and time-dependent density functional theory (TDDFT) methods. Starting from the $Au_{42}(SCH_2Ph)_{32}$ crystal structure and simplifying the ligands to SCH_3, we performed geometry optimization and optical property calculations at the BP86-D3/TZP level of theory. Analysis of the NIR absorption in gas phase reveals two closely spaced excitations at 1.35 eV and 1.40 eV, both arising from coupled HOMO → LUMO and HOMO-1 → LUMO transitions with varying weights. The HOMO and LUMO display superatomic character localized in the metal core with distinct nodal structures, whereas the HOMO-1 exhibits ligand-centered character with dominant sulfur contributions. Solvent effects were examined using the COSMO implicit solvation model in six solvents spanning a range of dielectric constants (toluene, dichloromethane, acetone, N,N-dimethylbenzamide, N,N-dimethylformamide, and N,N-dimethylacetamide). Increasing solvent polarity preferentially red shifts the HOMO → LUMO dominated excitation while leaving the HOMO-1 → LUMO transition nearly unchanged. This differential solvent response

demonstrates that the NIR absorption wavelength can be tuned through solvent selection without structural modification, offering a route to optimize photothermal performance for specific applications.

4.2 Introduction

Localized surface plasmon resonance (LSPR) arises in gold nanoparticles when incident light drives collective oscillations of surface conduction electrons.[1–4] In elongated nanostructures like nanorods, this produces two resonance modes: the transverse mode polarized along the short axis and a longitudinal mode along the long axis, appearing in the visible to near-infrared (NIR) spectral range.[5] It is important to note that this absorbed energy can be converted into heat through electron-phonon and phonon-phonon processes.[6,7] This efficient photothermal effect, combined with the known biocompatibility of gold nanoparticles, has enabled medical applications where targeted irradiation at the LSPR wavelength generates localized heating for cancer therapy and diagnostics.[8–13] Clinical photothermal therapy typically employs 808 nm lasers, which operates within the NIR biological transparency window where tissue absorption and scattering are minimized.[9,11,13] Consequently, gold nanostructures must be designed (or tuned) with LSPR absorption near 808 nm to maximize the therapeutic efficiency.

As nanoparticle size decreases to the ultrasmall regime, typically 1-3 nm in diameter, they transition into the nanocluster regime where atomic precision becomes achievable.[14,15] Note that this size reduction fundamentally alters their electronic structure, where the continuum of plasmonic states in larger nanoparticles collapses into discrete molecular-like energy levels.[16,17] Consequently, the LSPR absorption is replaced by discrete electronic transitions resembling those of molecules.[18] Elucidating optical properties at this atomic scale constitutes an active

research frontier. While NIR LSPR is absent in this ultrasmall size regime, a critical advantage of nanoclusters is that they can be atomically precise and therefore these structures enable deterministic control over properties. This atomic-level control opens pathways for rational design: by systematically varying composition, structure, and ligand environment, optical responses that can be tailored for specific applications. Therefore, these insights have enabled applications of gold nanoclusters in diverse fields such as medical,[19,20] catalytic,[21,22] sensing,[23,24] opto-electronic,[17,25] and beyond. For example, Liu et al.[14] highlighted gold nanoclusters designed to exhibit photoluminescence properties in both NIR-I (700 – 1000 nm) and NIR-II (1000 – 1700 nm) windows. Interestingly, these clusters can also display NIR absorption characteristics similar to the LSPR observations in nanoparticles, highlighting that atomically precise nanoclusters are capable of exhibiting NIR excitation behavior comparable to larger nanoparticle systems.

Among the gold nanoclusters that exhibit NIR absorption character, $Au_{42}(SR)_{32}$ occupies a unique position and serves as the focus of this study. Jin and coworkers first reported the synthesis of this cluster with R = CH_2Ph ligands in 2022.[6] Structurally, $Au_{42}(SR)_{32}$ features an Au_{20} kernel at its cluster core, arranged in a hexagonal closed-packed structure with two terminal gold atoms, yielding an elongated geometry with an aspect ratio of 6.2. The protecting ligand shell is comprised of two types of staple motifs: (1) two pairs of $Au_4(SR)_5$ units at both ends of the core, and (2) six monometallic $Au(SR)_2$ units encircling the body (Figure 4.1). A key finding from this work is the intriguing optical properties that make this cluster relevant for photothermal applications. In toluene, the cluster displays a strong NIR absorption centered at 815 nm with a molar absorption coefficient exceeding 1×10^5 M^{-1} cm^{-1}.[6] Thus, this absorption is close to the therapeutic 808 nm laser wavelength. Therefore, photothermal measurements under 808 nm irradiation demonstrated rapid heating, where a 50 μg/mL cluster solution (in toluene) reached a

temperature rise of approximately ~27 °C in just 5 minutes, confirming efficient light-to-heat conversion.[6] To elucidate the origin of this NIR feature, Li et al.[6] performed density functional theory (DFT) and time-dependent density functional theory (TDDFT) calculations, which revealed that the NIR absorption corresponds to a longitudinal excitation. Building on this foundation, several other studies have explored additional properties of this system.

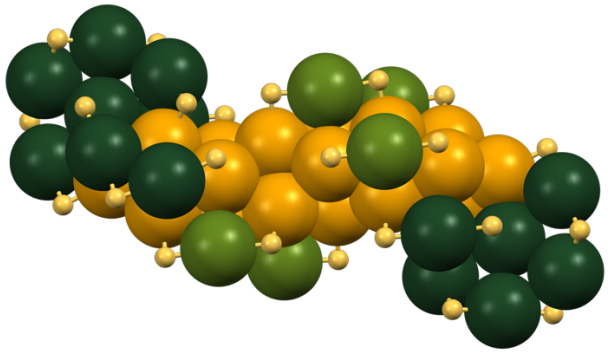


Figure 4.1. Structure of the $Au_{42}(SR)_{32}$ nanorod (color labels: gold = core Au; dark green = Au from $Au_4(SR)_5$ motifs; light green = Au from $Au(SR)_2$ motifs; yellow = S). R groups of the staple motifs are omitted for clarity.

Building on this initial work, Jin and coworkers later investigated[26] the photoluminescence properties of $Au_{42}(SR)_{32}$ with R = CH_2CH_2Ph groups in dichloromethane (DCM) and discovered a dual emission phenomenon in the NIR region, in which they observed a fluorescence peak at 875 nm and phosphorescence peak at 1040 nm. The NIR absorption peak for this system was observed at 806 nm.[26,27] Theoretical calculations by the Pei group[28] complemented these experimental findings as well as the proposed mechanisms of the photoluminescence pathway, further revealing that structural flexibility significantly influences the emission behavior of nanorod shaped clusters.[28,29] To understand how cluster size affects the optical properties, Jin and coworkers then examined a periodically elongated nanorod series (with R = CH_2CH_2Ph): $Au_{42}(SR)_{32}$ (Au_{20} core), $Au_{60}(SR)_{44}$ (Au_{32} core), $Au_{78}(SR)_{56}$ (Au_{44} core),

$Au_{96}(SR)_{68}$ (Au_{56} core), and $Au_{114}(SR)_{80}$ (Au_{68} core).[30] As the core aspect ratio increases with rod length, the HOMO – LUMO gap systematically decreases, accompanied by progressive red shifting of the NIR absorption peak. These trends are confirmed by DFT and TDDFT calculations. Notably, $Au_{42}(SR)_{32}$ exhibited the longest excited-state lifetime (2122 ns) among the series, suggesting potential for applications requiring long-lived charge carriers.[30]

Recent work by Knappenberger and coworkers[31] examined the electronic relaxation dynamics of $Au_{42}(SR)_{32}$ (with R = CH_2CH_2Ph) and demonstrated that the NIR longitudinal excitation is molecular rather than in plasmonic in origin. As part of an ongoing collaboration between us and the Jin and Knappenberger groups, the present computational study investigates the NIR absorption characteristics in greater depth, with particular focus on solvent dependent effects. Given the established significance of the $Au_{42}(SR)_{32}$ system, we employ DFT and TDDFT to elucidate the fundamental nature of its structure and optical transitions. This study addresses two key objectives: (1) characterization of the molecular orbital contributions governing the NIR excitations, and (2) systematic investigation of solvent effects on NIR absorption properties. These computational insights reveal the potential for environmental tuning to impact the NIR peak, enabling wavelength control through solvent selection without structural modification.

4.3 Theory

We examined the electronic structure and optical properties of the $Au_{42}(SCH_3)_{32}$ nanorod using DFT and TDDFT methods. Starting from the experimentally determined crystal structure of $Au_{42}(SCH_2Ph)_{32}$ reported by Li et al.,[6] we simplified the ligands by replacing the phenyl (Ph) groups with hydrogen atoms using a visualization tool (MacMolPlt),[32] yielding $Au_{42}(SCH_3)_{32}$.

Ground-state geometry optimizations employed the BP86 generalized gradient approximation (GGA) exchange-correlation functional[33,34] with a triple-ζ (TZP) basis set. Dispersion corrections were incorporated via Grimme's D3 method,[35] and scalar relativistic effects were treated using the zeroth-order regular approximation (ZORA).[36,37] We applied a tight convergence criterion: 1×10^{-8} for the self-consistent field procedure, 1×10^{-4} Hartree for energy, and 1×10^{-3} Hartree/Å for gradients. Following ground-state geometry optimization, linear-response TDDFT calculations were performed to obtain the optical absorption spectrum using the same level of theory. Then, vertical excitation energies were computed and broadened with Gaussian functions using a full-width half-maximum (FWHM) of 0.08 eV to simulate the absorption spectrum. Subsequently, excited-state geometries were optimized using analytical excited-state gradients within the TDDFT framework.[38]

All calculations described above were initially performed in the gas phase. To assess solvent effects on the electronic structure and optical properties, we extended the study by incorporating implicit solvation through the conductor like screening model (COSMO).[39–41] Ground-state geometry optimizations and excited-state calculations were performed in six different solvents: toluene, DCM, acetone, N,N-dimethylbenzamide (DMBA), N,N-dimethylformamide (DMFA), and N,N-dimethylacetamide (DMAc). These solvents were selected to span a range of dielectric constants and assess the influence of solvent polarity on the cluster's properties. All calculations were carried out using the Amsterdam Density Functional (ADF2021) software package.[42,43]

4.4 Results and discussion

4.4.1 Gas phase studies

Table 4.1 compares the average bond lengths between the experimental crystal structure and the BP86-D3/TZP gas-phase optimized ground state (S_0), with atomic labels shown in Figure 4.2. These calculated bond lengths show good agreement with experimental values. Within the Au_{20} core, the calculated average Au-Au bond length (2.852 Å) exceeds the experimental value (2.812 Å) by just 1.42%. Across all bond types examined, deviations remain modest, with the maximum discrepancy of 2.95% appearing in the Au (core) - S (edge) bonds of the $Au(SR)_2$ staple motifs (average bond length calculated: 2.387 Å; experimental: 2.319 Å). It is important to note that our computational model employs methylthiolate (SCH_3) groups, whereas the experimental crystal structure contains phenylmethanethiolate (SCH_2Ph) ligands. The absence of phenyl groups in our model may contribute to the slight bond elongations observed, as the aromatic substituents can influence packing and sterics in the experimental structure. Additionally, Häberlen et al.[44] demonstrated that GGA functionals tend to overestimate Au-Au bond lengths in gold clusters. Nevertheless, all calculated bond lengths deviated by less than 3.00% from experimental values, demonstrating that the simplified ligand model captures the essential structural features of the nanorod.

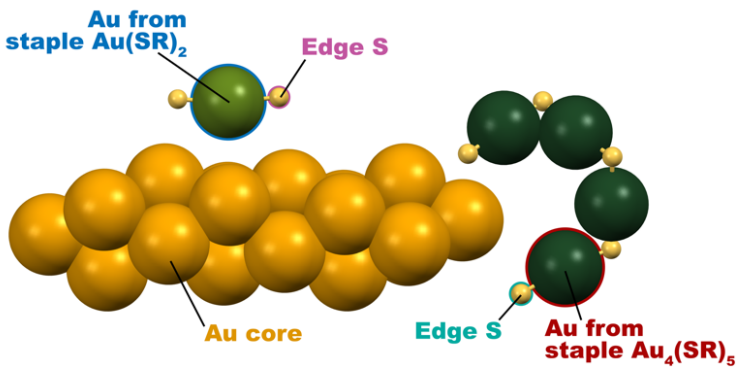


Figure 4.2. Atom definitions for $Au_{42}(SR)_{32}$.

Table 4.1. The comparison of average bond lengths between the experimental crystal structure and gas-phase optimized geometry (at the BP86-D3/TZP level of theory). Percent deviations (Δ) are calculated relative to the crystal structure values. Bond lengths are reported in Å.

Bond	Crystal structure	Gas phase (S_0)	Δ(%)
Au core – Au core	2.812 ± 0.016	2.852 ± 0.016	1.42
Au core – edge S from $Au_4(SR)_5$ motif	2.353 ± 0.013	2.401 ± 0.005	2.03
Au from $Au_4(SR)_5$ motif – S from $Au_4(SR)_5$ motif	2.301 ± 0.004	2.344 ± 0.002	1.86
Au core – edge S from $Au(SR)_2$ motif	2.319 ± 0.008	2.387 ± 0.003	2.95
Au from $Au(SR)_2$ motif – S from $Au(SR)_2$ motif	2.289 ± 0.009	2.347 ± 0.001	2.51

Electronic structure analysis of $Au_{42}(SCH_3)_{32}$ nanorod indicates a HOMO-LUMO energy separation of 1.14 eV (Figure 4.3a). Visualization of the frontier molecular orbitals (Figure 4.3b)

shows that electron density is primarily located on the central Au_{20} core in both HOMO and LUMO, although with distinct nodal patterns. The HOMO contains four nodal planes creating five lobes with overall σ_g symmetry, whereas the LUMO features five nodal planes producing six lobes with σ_u symmetry. To understand the origin of these molecular orbitals, we investigated the individual atomic orbital contributions. Gold s orbitals dominate in both HOMO and LUMO. However, a key distinction emerges in that the LUMO incorporates considerably higher gold p character than the HOMO. These observations indicate that both the HOMO and LUMO are metal-centered molecular orbitals. Complete atomic orbital contributions are provided in the Appendix B (Table B.1).

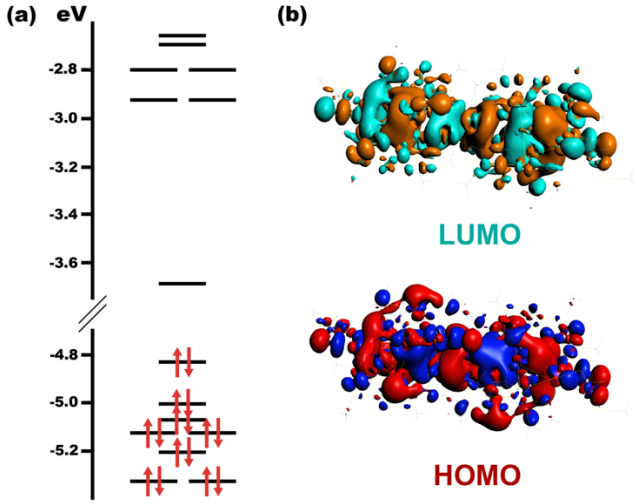


Figure 4.3. (a) HOMO and LUMO orbitals (Iso-surface = 0.01) and (b) energy level diagram for $Au_{42}(SCH_3)_{32}$ at the BP86-D3/TZP level of theory.

To elucidate the electronic origins of the experimentally observed NIR absorption band, we perform TDDFT calculations on the $Au_{42}(SCH_3)_{32}$ nanorod system. As mentioned earlier, the experimental absorption spectrum exhibits a characteristic NIR peak at 1.54 eV (806 nm), which is a primary focus of our theoretical investigations.[6,26,27,30] The calculated absorption spectrum,

shown in Figure 4.4a, successfully captures this NIR absorption feature (the overall theoretical absorption spectrum in Figure B.1 and its agreement with the experimental spectrum are presented in the Appendix B). Our TDDFT analysis reveals that this NIR peak arises from two closely spaced excitations at 1.35 eV (918 nm) and 1.40 eV (885 nm). Both transitions are red-shifted relative to experiment by 0.19 eV and 0.14 eV, respectively. This systematic underestimation of excitation energies is characteristic of GGA functionals and has been observed in previous studies as well.[45–47] To further characterize the nature of these excitations and understand the specific contributions to the NIR absorption, we have analyzed the electronic transition characters of each excitation (Figure 4.4b and Table 4.2). Previous theoretical studies by Li et al.,[6] and Luo et al.[28] have investigated the electronic structure and optical properties of this system. Li et al.,[6] employed the B3LYP/def2-SV(P) level of theory and reported the lowest excitation at 1.68 eV (738 nm; blue-shifted relative to experiment), attributed to a HOMO → LUMO electronic transition. Luo et al.[28], using the B3LYP/DZ level of theory, calculated this excitation at 1.35 eV (920 nm, red-shifted relative to experiment), also with dominant HOMO → LUMO character. Both studies confirmed that these frontier orbitals are localized on the gold core, consistent with our findings.

Our BP86-D3/TZP level of theory calculations yield two closely spaced excitations with HOMO → LUMO character, separated by only 0.05 eV. However, the ground state (S_0) → first excited state (S_1) excitation at 1.35 eV (918 nm) has a higher electronic transition contribution from HOMO-1 → LUMO compared to the S_0 → second excited state (S_2) excitation at 1.40 eV (885 nm). Comparison of oscillator strengths reveals that the excitation at 1.40 eV dominates the optical intensity in this spectral region, making it the primary contributor to the observed NIR absorption peak. Analysis of HOMO-1 shows that it has a different character than HOMO and

LUMO, where this orbital consists mainly of sulfur *p* atomic orbitals from the thiolate ligands, with some contributions from gold *d* orbitals (see Figure 4.4c and Table B.1 for detailed atomic orbital contributions). Therefore, unlike HOMO and LUMO which are located on the gold core, HOMO-1 is localized at the metal-ligand shell. As a result, the two excitations have different dominant electronic transition character. The excitation at 1.35 eV ($S_0 \rightarrow S_1$) involves electronic transition from the metal-ligand shell → metal core, while the excitation at 1.40 eV ($S_0 \rightarrow S_2$) involves electronic transition within metal core → metal core. Inclusion of scalar relativistic effects via ZORA decreases the splitting between the orbitals arising primarily from s electrons (such as the HOMO) and those with significant d character (such as HOMO-1), which enables the efficient coupling of transitions arising from these orbitals.

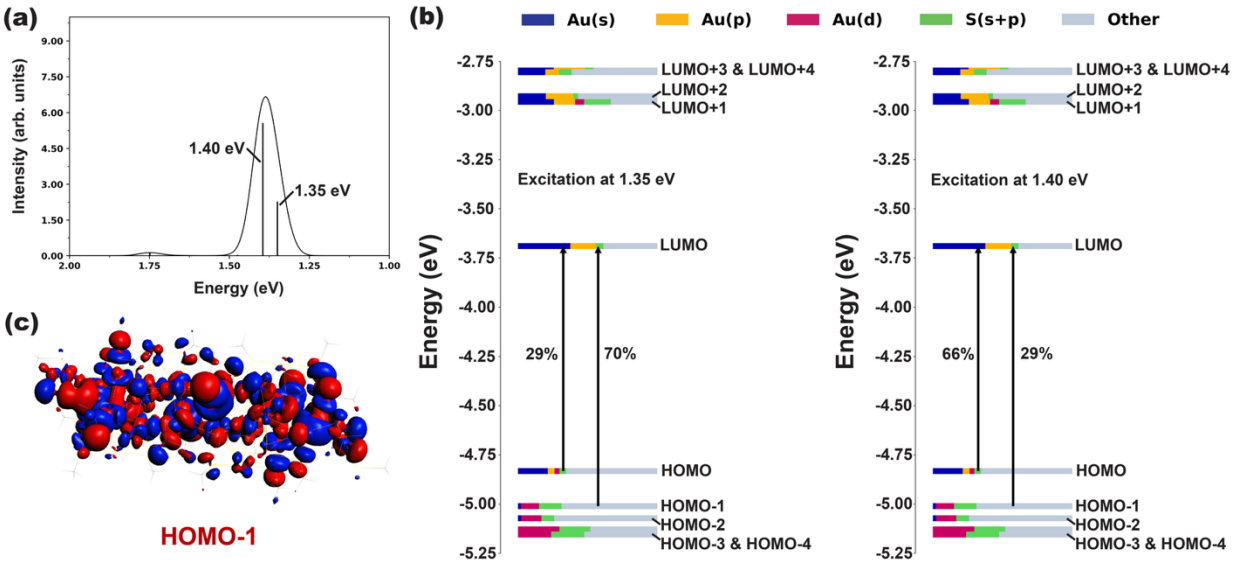


Figure 4.4. (a) NIR region of the theoretical absorption spectrum at the BP86-D3/TZP level of theory, (b) energy level diagram of the molecular orbitals showing atomic orbital character and the corresponding electronic transitions of the two excitations, and (c) HOMO-1 of the $Au_{42}(SCH_3)_{32}$ nanorod (Iso-surface = 0.01).

Table 4.2. Excitation properties of the $Au_{42}(SCH_3)_{32}$ nanorod obtained from TDDFT calculations at the BP86-D3/TZP level of theory, including excitation energies, oscillator strengths, and the corresponding electronic transitions with their orbital contribution weights.

Excitation energy	Oscillator strength (a.u.)	Transitions	Weight
1.35 eV (918 nm)	0.194	HOMO-1 → LUMO	0.70
		HOMO → LUMO	0.29
1.40 eV (885 nm)	0.475	HOMO → LUMO	0.66
		HOMO-1 → LUMO	0.29

To investigate the dual emission properties, we optimized the geometries of the S_1 state and first triplet excited state (T_1) to obtain theoretical fluorescence and phosphorescence emission energies (Figure 4.5). The calculated fluorescence energy is 1.24 eV (1000 nm), underestimating the experimental value of 1.42 eV (875 nm) by 0.18 eV. Similarly, the computed phosphorescence energy of 1.02 eV (1215 nm) lies below the experimental value of 1.19 eV (1040 nm) by 0.17 eV. Importantly, both emission energies exhibit red shifts of approximately ~0.18 eV, matching the systematic offset observed in our absorption calculations. This consistent deviation across both absorption and emission suggests that our BP86-D3 level of theory systematically underestimates electronic transition energies by a nearly constant amount, while correctly reproducing the relative energetics and Stokes shifts. Specifically, the calculated energy separation between fluorescence and phosphorescence matches the experimentally observed gap between the dual emission peaks (~0.23 eV).[26,27] Luo et al.[28] reported emission energies (1.43 eV for fluorescence and 1.11 eV for phosphorescence) using the hybrid B3LYP functional in closer agreement with experimental energies albeit with an energy separation that is too large. However, our GGA results correctly capture the

photophysical behavior and provide accurate relative energy spacings. Analysis of molecular orbitals in the optimized excited-state structures reveals characteristics similar to those in the ground state (detailed comparison is provided in Figure B.2).

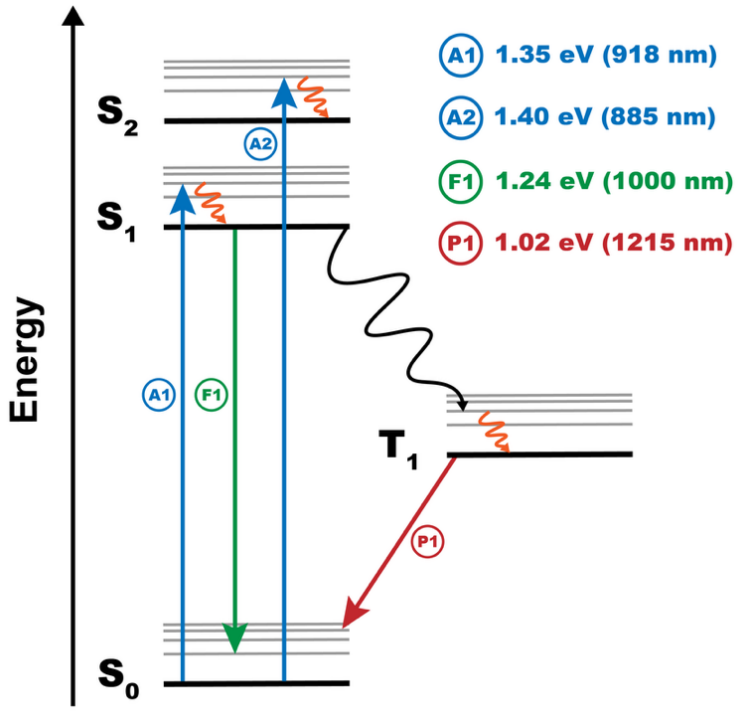


Figure 4.5. Jablonski diagram depicting photophysical processes in $Au_{42}(SCH_3)_{32}$ nanorod: absorption (A1 and A2), fluorescence (F1), and phosphorescence (P1) with calculated energies at the BP86-D3/TZP level of theory.

4.4.2 Solvation effects on the structure geometry and the excitation characteristics

To examine how solvent environment influences the NIR absorption features, we performed further theoretical calculations using the COSMO implicit solvation model with room-temperature dielectric constants to represent the solvent medium. Initial investigations focused on two solvents: toluene and DMAc, representing low and high polarity environments. Following the same computational protocol as for the gas phase, we first optimized the ground-state geometry in each solvent. The results reveal no structural deviations, where all calculated

bond lengths in solvation media are as same as from the gas-phase values (Table 4.3), indicating that implicit solvation exerts negligible influence on the cluster's equilibrium geometry. This lack of structural change suggests that solvent effects on the optical properties, if present, arise primarily from electronic rather than geometric changes.

Table 4.3. Average bond lengths for ground state optimized geometries using toluene and DMAc phases (at the BP86-D3/TZP level of theory). Bond lengths are reported in Å.

Bond	Toluene (S_0)	DMAc (S_0)
Au core – Au core	2.851 ± 0.015	2.852 ± 0.015
Au core – edge S from $Au_4(SR)_5$ motif	2.401 ± 0.006	2.401 ± 0.005
Au from $Au_4(SR)_5$ motif – S from $Au_4(SR)_5$ motif	2.344 ± 0.002	2.344 ± 0.002
Au core – edge S from $Au(SR)_2$ motif	2.387 ± 0.003	2.387 ± 0.003
Au from $Au(SR)_2$ motif – S from $Au(SR)_2$ motif	2.347 ± 0.001	2.347 ± 0.001

Next, we examined how solvent affects the absorption spectrum. Figure 4.6 shows that solvation causes a clear red shift in the NIR absorption peak. Analysis of the underlying excitations (Table 4.4) reveals systematic changes in energy, electronic transition character, and the oscillator strength. Recall that in the gas phase, the NIR absorption peak contains two closely spaced excitations, both having mixed HOMO → LUMO and HOMO-1 → LUMO character. In solution, these two excitations shift differently: the excitation with stronger HOMO → LUMO character (labeled as α) red shifts significantly compared to the gas-phase results. In contrast, the other excitation (labeled as β) with strong HOMO-1 → LUMO character shows much smaller shifts: its energy is 1.37 eV in toluene and 1.36 eV in DMAc, both very close to the gas-phase

excitation energy (1.35 eV). This differential shift causes α to be the lowest energy excitation ($S_0 \rightarrow S_1$) in both toluene (1.32 eV) and DMAc (1.26 eV). The red shift is larger in DMAc than in toluene due to its higher polarity.

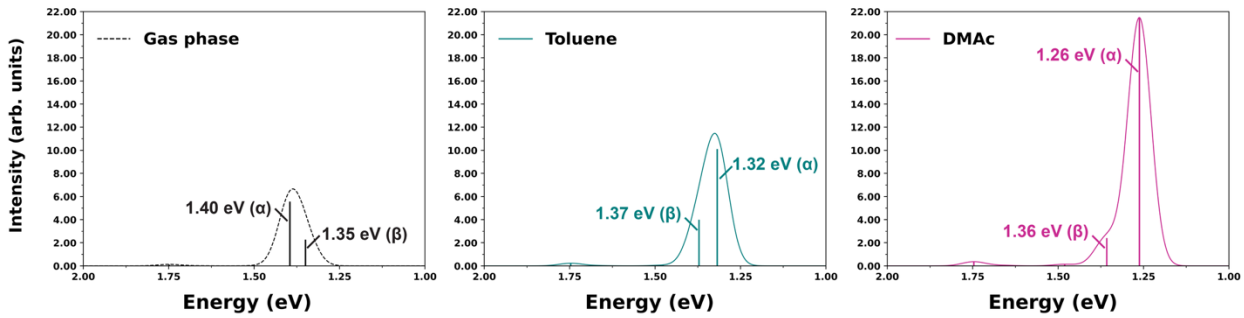


Figure 4.6. Theoretical NIR absorption spectra at the BP86-D3/TZP level of theory for toluene and DMAc compared with the gas phase absorption spectrum.

Table 4.4. Excitation properties of the $Au_{42}(SCH_3)_{32}$ nanorod within toluene and DMAc solvation media obtained from TDDFT calculations at the BP86-D3/TZP level of theory, including excitation energies, oscillator strengths, and the corresponding electronic transitions with their orbital contribution weights.

Excitation energy	Oscillator strength (a.u.)	Transitions	Weight
Toluene			
1.32 eV (939 nm)	0.861	HOMO → LUMO	0.74
		HOMO-1 → LUMO	0.24
1.37 eV (905 nm)	0.340	HOMO-1 → LUMO	0.75
		HOMO → LUMO	0.23
DMAc			
1.26 eV (984 nm)	1.826	HOMO → LUMO	0.94
		HOMO-1 → LUMO	0.05
1.36 eV (912 nm)	0.206	HOMO-1 → LUMO	0.95
		HOMO → LUMO	0.04

The solvation medium also affects how these transitions behave. As mentioned earlier, in the gas phase, both α and β involve mixed electronic transition character. When the continuum solvation medium is introduced, this mixed transition character simplifies as the excitation tends to become dominated by a single electronic transition. For example, the α excitation HOMO → LUMO contribution grows from 66% in the gas phase to 74% in toluene and further increases to 94% in DMAc. As this transition becomes more purely HOMO → LUMO, it simultaneously becomes stronger, with its oscillator strength increasing in the same progression from gas phase to toluene to DMAc (Tables 4.2, 4.4). The β excitation follows a similar pattern for the HOMO-1 → LUMO transition contribution but shows much smaller changes in its oscillator strengths (Tables 4.2, 4.4).

These observations demonstrate that the α and β excitations respond differently to the solvent environment. To examine whether these changes correlate with solvent polarity, we extended the study to include four additional solvents spanning a range of dielectric constants: DCM, acetone, DMBA, and DMFA. The results are shown in Figure 4.7, with detailed excitation energies, oscillator strengths, and orbital contributions provided in Table B.2.

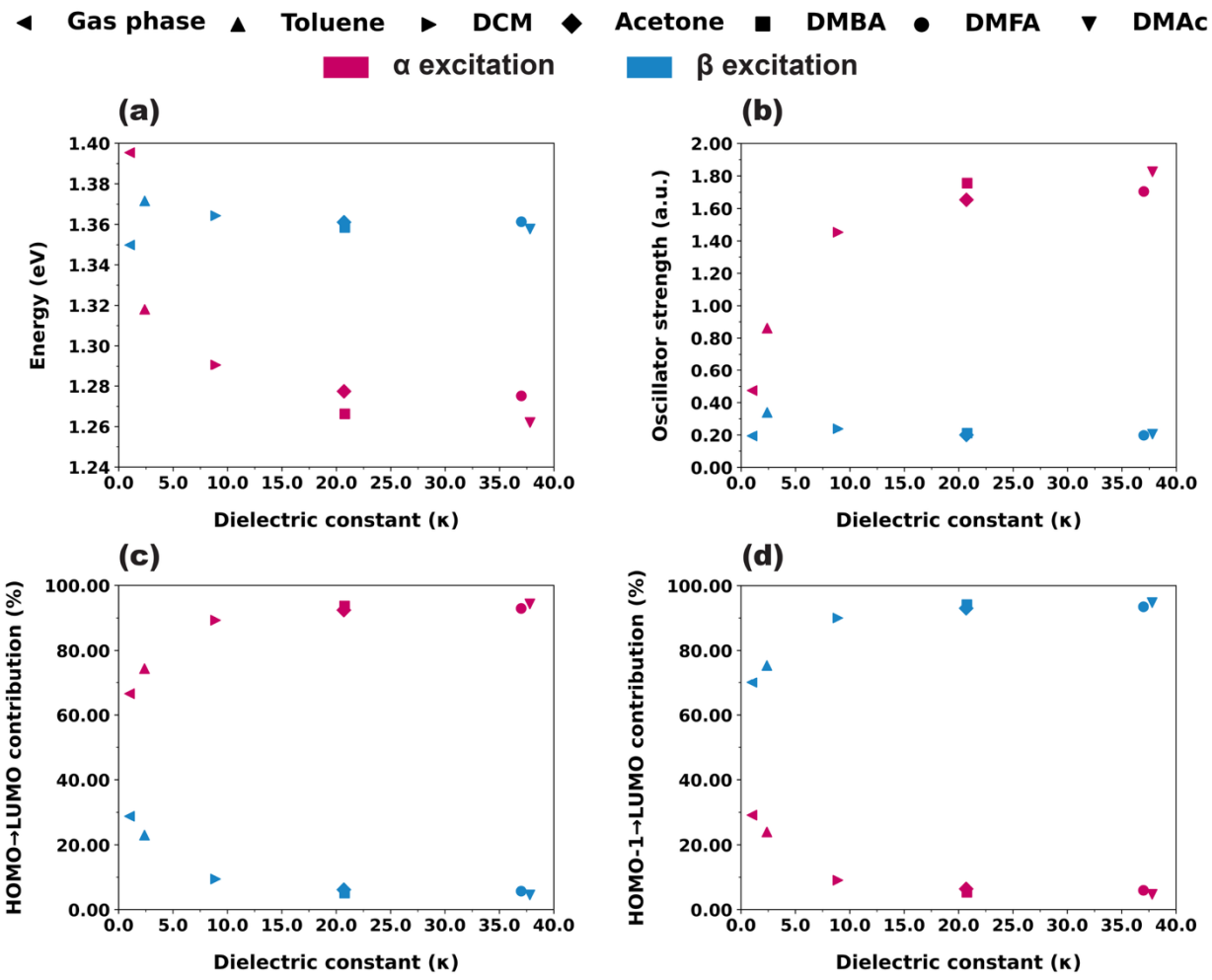


Figure 4.7. Solvent dependent excitation properties of the $Au_{42}(SCH_3)_{32}$ nanorod as a function of dielectric constant: (a) excitation energies, (b) oscillator strengths, (c) HOMO → LUMO electronic transition contribution, and (d) HOMO-1 → LUMO electronic transition contribution for both α and β excitations.

Figure 4.7 demonstrates that the NIR absorption properties depend strongly on solvent dielectric constant (i.e., solvent polarity). The trends across all seven media reveal clear systematic relationships between each spectroscopic parameter and the dielectric environment. Figure 4.7a shows that the α excitation energy decreases markedly with increasing polarity: from 1.40 eV in the gas phase to 1.26 eV in DMAc, representing a 0.14 eV red shift. In contrast, the β excitation remains nearly constant at ~1.36 eV across all solvents, indicating minimal solvent

sensitivity. To understand this differential solvent response, we examined the energies of the ground and excited states separately in each environment (Table B.3). This analysis reveals that the excited state corresponding to the α excitation is preferentially stabilized by polar solvents; as the dielectric constant increases, the excited state energy decreases relative to the ground state, reducing the energy gap between the two states (reflecting solvatochromism). Therefore, the resulting red shift (bathochromic shift) follows from the decreased energy gap between the two states.[48,49] The excited state corresponding to β excitation (i.e., has dominant HOMO-1 → LUMO character) experiences little solvent stabilization, which explains why its excitation energy remains constant.

To understand the oscillator strength variations in Figure 4.7b, we must examine the underlying total transition dipole moments. The transition dipole moment is a vector quantity that determines both the intensity and transition dipole direction of an electronic transition.[50] Li et al.[6] previously showed that the α excitation exhibits a strong transition dipole moment along the x-axis (the long axis of the metal core), characteristic of a longitudinal metal core → metal core transition. Our calculations confirm this finding, in which the transition dipole moment in the x-axis (which is along the long axis of the cluster in the coordinates used in our work) dominates in all environments (Table B.4). Since oscillator strength scales as the square of the transition dipole moment magnitude, changes in the dipole strength directly affect absorption intensity.[50] For the α excitation, the transition dipole moment increases systematically with solvent polarity (as shown in Table B.4), causing the oscillator strength to rise correspondingly. The β excitation's transition dipole moment, by contrast, remains essentially less varied across all solvents, explaining why its oscillator strength shows minimal variation in Figure 4.7b.

For elucidating the electronic transition contribution changes in Figure 4.7c and 4.7d, we must examine the transition dipole moments for each individual orbital transitions. Table B.5 provides the complete breakdown of these individual transition dipole moment components for HOMO → LUMO and HOMO-1 → LUMO contributions in each solvent and excitation. As we observed earlier, the total transition dipole moment is stronger for the α excitation, and their individual contributions indicates that it is mainly governed by the HOMO → LUMO electronic transition. Investigating this α excitation (Figure 4.7c and 4.7d) reveals that the HOMO → LUMO contribution increases from 66% in gas phase to 94% in DMAc as solvent polarity increases, while the HOMO-1 → LUMO contribution decreases accordingly. Examining the underlying transition dipole moments explains this shift: the HOMO → LUMO transition dipole moment contribution strengthens with increasing dielectric constant, thereby increasing its effect on the overall oscillator strength of the excitation. Conversely, the HOMO-1 → LUMO transition dipole moment weakens, reducing its contribution. The β excitation shows systematic but opposite behavior. With increasing solvent polarity, the HOMO-1 → LUMO transition dipole moment increases in its weight in the β excitation while the HOMO → LUMO weight weakens, causing their transition dipole moment contributions to reflect this shift.

These results demonstrate that the NIR absorption peak is highly tunable: systematic variation of solvent polarity enables control over excitation energy, oscillator strength, and orbital character. This tunability has potential implications for applications requiring wavelength-specific optical responses in gold nanocluster systems. It is important to note that the present analysis employs implicit solvation, which treats the solvent as a continuum dielectric medium. A potential extension of this work would be to incorporate explicit solvation, where individual solvent molecules are included in the calculation. Therefore, the explicit solvation

would capture specific solute-solvent interactions, local solvation shell structure, and dynamic effects that implicit models cannot describe, providing a more complete picture of how solvent interactions influence the optical properties of these nanoclusters.

4.5 Conclusion

We have investigated the electronic structure and excitation characteristics of the $Au_{42}(SCH_3)_{32}$ nanorod across a range of solvent polarities. Gas-phase absorption calculations reveal that the NIR peak is comprised of two closely spaced excitations separated by only 0.05 eV. Both transitions arise from coupled HOMO → LUMO and HOMO-1 → LUMO transition contributions with different weights. Similar dual transition contributions have been observed in other NIR absorbing nanoclusters, such as $Au_{20}Ag_{32}(^tBuPA)_{24}Cl_{12}$ (PA – phenylacetylene).[51] Despite the systematic underestimation of absolute energies, a known GGA characteristic, our approach correctly captures relative photophysical properties, including the dual emission behavior and the experimentally observed gap between the dual emission peaks (~0.23 eV).

Solvent effects were examined using an implicit solvation model (COSMO). While geometry remains essentially unchanged across all media, the optical properties show pronounced sensitivity to dielectric environments. The excitation dominated by HOMO → LUMO red shifts systematically with increasing solvent polarity, whereas the HOMO-1 → LUMO transition remains nearly invariant. These excitation energy shifts are accompanied by systematic changes in oscillator strength and orbital character, reflecting solvent-induced variations in transition dipole moments. The strong polarity dependence demonstrates that the NIR absorption wavelength can be tuned through solvent selection, which is potentially a useful

strategy for optimizing photothermal applications. Therefore, this study establishes a foundation for understanding environmental control of NIR optical properties in $Au_{42}(SCH_3)_{32}$.

4.6 Appendix B - Supporting Information

Full theoretical absorption spectrum, molecular orbital characteristics of the nanorod, excitation properties observed within different solvation media, relative ground and excited state energies, total and individual contributions of transition dipole moments for the respective excitation.

4.7 Acknowledgments

D.S.N.D.S. and C.M.A. were supported by the National Science Foundation (CHE-2404212) of the United States. The computing for this work was performed on the Beocat Research Cluster at Kansas State University, which is funded in part by NSF grants CHE-1726332, CNS-1006860, EPS-1006860, and EPS-0919443.

4.8 References

1. Kelly, K. L.; Coronado, E.; Zhao, L. L.; Schatz, G. C. The Optical Properties of Metal Nanoparticles: The Influence of Size, Shape, and Dielectric Environment. *J. Phys. Chem. B* **2003**, *107* (3), 668–677.

2. Murphy, C. J.; Chang, H.-H.; Falagan-Lotsch, P.; Gole, M. T.; Hofmann, D. M.; Hoang, K. N. L.; McClain, S. M.; Meyer, S. M.; Turner, J. G.; Unnikrishnan, M.; Wu, M.; Zhang, X.; Zhang, Y. Virus-Sized Gold Nanorods: Plasmonic Particles for Biology. *Acc. Chem. Res.* **2019**, *52* (8), 2124–2135.

3. Jain, P. K.; Lee, K. S.; El-Sayed, I. H.; El-Sayed, M. A. Calculated Absorption and Scattering Properties of Gold Nanoparticles of Different Size, Shape, and Composition: Applications in Biological Imaging and Biomedicine. *J. Phys. Chem. B* **2006**, *110* (14), 7238–7248.

4. Martinez, A. J.; Wang, A.; Khvichia, M.; Zhang, J. Z.; Zou, S. Coupling and Energy Transfer between an Exciton in a Semiconductor Quantum Dot and a Surface Plasmon in a Metal Nanoparticle. *J. Phys. Chem. Lett.* **2025**, *16* (4), 985–990.

5. Hinman, J. G.; Stork, A. J.; Varnell, J. A.; Gewirth, A. A.; Murphy, C. J. Seed Mediated Growth of Gold Nanorods: Towards Nanorod Matryoshkas. *Faraday Discuss.* **2016**, *191*, 9–33.

6. Li, Y.; Song, Y.; Zhang, X.; Liu, T.; Xu, T.; Wang, H.; Jiang, D.; Jin, R. Atomically Precise Au_{42} Nanorods with Longitudinal Excitons for an Intense Photothermal Effect. *J. Am. Chem. Soc.* **2022**, *144* (27), 12381–12389.

7. Link, S.; El-Sayed, M. A. Shape and Size Dependence of Radiative, Non-Radiative and Photothermal Properties of Gold Nanocrystals. *Int. Rev. Phys. Chem.* **2000**, *19* (3), 409–453.

8. Vines, J. B.; Yoon, J.-H.; Ryu, N.-E.; Lim, D.-J.; Park, H. Gold Nanoparticles for Photothermal Cancer Therapy. *Front. Chem.* **2019**, *7*, 167.

9. Amaral, M. N.; Kumar, P.; Faísca, P.; Ferreira, H. A.; Coelho, J. M. P.; Gaspar, M. M.; Reis, C. P. Gold Nanoparticle-Mediated Photothermal Therapy: Expanding the Frontiers of Cancer Treatment and Theragnostics. *Biomed. Pharmacother.* **2025**, *190*, 118399.

10. Broadbent, M.; Chadwick, S. J.; Brust, M.; Volk, M. Gold Nanoparticles for Photothermal and Photodynamic Therapy. *ACS Omega* **2024**, *9* (44), 44846–44859.

11. Li, Z.; Huang, H.; Tang, S.; Li, Y.; Yu, X.-F.; Wang, H.; Li, P.; Sun, Z.; Zhang, H.; Liu, C.; Chu, P. K. Small Gold Nanorods Laden Macrophages for Enhanced Tumor Coverage in Photothermal Therapy. *Biomaterials* **2016**, *74*, 144–154.

12. Li, B.; Yakufu, M.; Xie, R.; Peng, H.; Mi, X.; Tuxun, H. Functional Gold Nanoparticles in Diagnosis and Treatment of Cancer: A Systematic Review. *APL Mater.* **2025**, *13* (5), 050602.

13. Bianchi, L.; Mooney, R.; Cornejo, Y. R.; Schena, E.; Berlin, J. M.; Aboody, K. S.; Saccomandi, P. Thermal Analysis of Laser Irradiation-Gold Nanorod Combinations at 808 nm, 940 nm, 975 nm and 1064 nm Wavelengths in Breast Cancer Model. *Int. J. Hyperthermia* **2021**, *38* (1), 1099–1110.

14. Liu, Z.; Luo, L.; Jin, R. Visible to NIR-II Photoluminescence of Atomically Precise Gold Nanoclusters. *Adv. Mater.* **2024**, *36* (8), 2309073.

15. Park, H.; Shin, D. J.; Yu, J. Categorization of Quantum Dots, Clusters, Nanoclusters, and Nanodots. *J. Chem. Educ.* **2021**, *98* (3), 703–709.

16. Maity, S.; Kolay, S.; Chakraborty, S.; Devi, A.; Rashi; Patra, A. A Comprehensive Review of Atomically Precise Metal Nanoclusters with Emergent Photophysical Properties towards Diverse Applications. *Chem. Soc. Rev.* **2025**, *54* (4), 1785–1844.

17. Galchenko, M.; Black, A.; Heymann, L.; Klinke, C. Field Effect and Photoconduction in Au_{25} Nanoclusters Films. *Adv. Mater.* **2019**, *31* (18), 1900684.

18. López-Lozano, X.; Barron, H.; Mottet, C.; Weissker, H.-C. Aspect-Ratio- and Size-Dependent Emergence of the Surface-Plasmon Resonance in Gold Nanorods – an Ab Initio TDDFT Study. *Phys. Chem. Chem. Phys.* **2014**, *16* (5), 1820–1823.

19. Du, B.; Jiang, X.; Das, A.; Zhou, Q.; Yu, M.; Jin, R.; Zheng, J. Glomerular Barrier Behaves as an Atomically Precise Bandpass Filter in a Sub-Nanometre Regime. *Nat. Nanotechnol.* **2017**, *12* (11), 1096–1102.

20. Xiao, Y.; Wu, Z.; Yao, Q.; Xie, J. Luminescent Metal Nanoclusters: Biosensing Strategies and Bioimaging Applications. *Aggregate* **2021**, *2* (1), 114–132.

21. Li, S.; Alfonso, D.; Nagarajan, A. V.; House, S. D.; Yang, J. C.; Kauffman, D. R.; Mpourmpakis, G.; Jin, R. Monopalladium Substitution in Gold Nanoclusters Enhances CO_2 Electroreduction Activity and Selectivity. *ACS Catal.* **2020**, *10* (20), 12011–12016.

22. Seal, N.; Samarasinghe, D. S. N. D.; Vodnala, N.; Siegler, M. A.; Aikens, C. M.; Das, A. Distibine versus Diphosphine Ligands: Modulating the Properties of Isostructural $Au_{13}Cu_2$ Nanoclusters. *Chem. Mater.* **2025**, *37* (24), 9908–9918.

23. Zhang, L.; Wang, E. Metal Nanoclusters: New Fluorescent Probes for Sensors and Bioimaging. *Nano Today* **2014**, *9* (1), 132–157.

24. Nasrollahpour, H.; Sánchez, B. J.; Sillanpää, M.; Moradi, R. Metal Nanoclusters in Point-of-Care Sensing and Biosensing Applications. *ACS Appl. Nano Mater.* **2023**, *6* (14), 12609–12672.

25. Niesen, B.; Rand, B. P. Thin Film Metal Nanocluster Light-Emitting Devices. *Adv. Mater.* **2014**, *26* (9), 1446–1449.

26. Luo, L.; Liu, Z.; Du, X.; Jin, R. Near-Infrared Dual Emission from the $Au_{42}(SR)_{32}$ Nanocluster and Tailoring of Intersystem Crossing. *J. Am. Chem. Soc.* **2022**, *144* (42), 19243–19247.

27. Luo, L.; Liu, Z.; Mazumder, A.; Jin, R. Raising Near-Infrared Photoluminescence Quantum Yield of Au_{42} Quantum Rod to 50% in Solutions and 75% in Films. *J. Am. Chem. Soc.* **2024**, *146* (41), 27993-27997.

28. Luo, Y.; Li, K.; Wang, P.; Pei, Y. Structural Flexibility-Driven Dual Emission Switching in Ultrathin Gold Nanorod Clusters. *JACS Au* **2025**, *5* (9), 4593–4603.

29. He, G.; Chen, S.; Jin, R. Manipulating the Intersystem Crossing Process in Atomically Precise Gold Nanoclusters. *J. Phys. Chem. Lett.* **2025**, *16* (51), 13118–13131.

30. Luo, L.; Liu, Z.; Kong, J.; Gianopoulos, C. G.; Coburn, I.; Kirschbaum, K.; Zhou, M.; Jin, R. Three-Atom-Wide Gold Quantum Rods with Periodic Elongation and Strongly Polarized Excitons. *Proc. Natl. Acad. Sci. U.S.A.* **2024**, *121* (10), e2318537121.

31. Heintzelman, D. J.; Smith, N. L.; Miller, N. J.; Luo, L.; Jin, R.; Knappenberger, K. L. Electronic Relaxation Dynamics of the $Au_{42}(SC_8H_9)_{32}$ Cluster Nanorod Studied Using 2D Electronic Spectroscopy. *J. Phys. Chem. Lett.* **2026**, *17* (1), 54–60.

32. Bode, B. M.; Gordon, M. S. Macmolplt: A Graphical User Interface for GAMESS. *J. Mol. Graph. Model.* **1998**, *16* (3), 133–138.

33. Becke, A. D. Density-Functional Exchange-Energy Approximation with Correct Asymptotic Behavior. *Phys. Rev. A* **1988**, *38* (6), 3098–3100.

34. Perdew, J. P. Density-Functional Approximation for the Correlation Energy of the Inhomogeneous Electron Gas. *Phys. Rev. B* **1986**, *33* (12), 8822–8824.

35. Grimme, S.; Ehrlich, S.; Goerigk, L. Effect of the Damping Function in Dispersion Corrected Density Functional Theory. *J. Comput. Chem.* **2011**, *32* (7), 1456–1465.

36. Lenthe, E. V.; Baerends, E. J.; Snijders, J. G. Relativistic Regular Two-Component Hamiltonians. *J. Chem. Phys.* **1993**, *99* (6), 4597–4610.

37. Van Lenthe, E.; Ehlers, A.; Baerends, E.-J. Geometry Optimizations in the Zero Order Regular Approximation for Relativistic Effects. *J. Chem. Phys.* **1999**, *110* (18), 8943–8953.

38. Seth, M.; Mazur, G.; Ziegler, T. Time-Dependent Density Functional Theory Gradients in the Amsterdam Density Functional Package: Geometry Optimizations of Spin-Flip Excitations. *Theor. Chem. Acc.* **2011**, *129* (3–5), 331–342.

39. Klamt, A.; Schüürmann, G. COSMO: A New Approach to Dielectric Screening in Solvents with Explicit Expressions for the Screening Energy and Its Gradient. *J. Chem. Soc., Perkin Trans. 2* **1993**, No. 5, 799–805.

40. Klamt, A. Conductor-like Screening Model for Real Solvents: A New Approach to the Quantitative Calculation of Solvation Phenomena. *J. Phys. Chem.* **1995**, *99* (7), 2224–2235.

41. Klamt, A.; Jonas, V. Treatment of the Outlying Charge in Continuum Solvation Models. *J. Chem. Phys.* **1996**, *105* (22), 9972–9981.

42. Te Velde, G.; Bickelhaupt, F. M.; Baerends, E. J.; Fonseca Guerra, C.; Van Gisbergen, S. J. A.; Snijders, J. G.; Ziegler, T. Chemistry with ADF. *J. Comput. Chem.* **2001**, *22* (9), 931–967.

43. *ADF2021, SCM. Theoretical Chemistry; Vrije Universities: Amsterdam, 2021.* http://www.scm.com (accessed 2026-03-13).

44. Häberlen, O. D.; Chung, S.-C.; Stener, M.; Rösch, N. From Clusters to Bulk: A Relativistic Density Functional Investigation on a Series of Gold Clusters Aun, N=6,…,147. *J. Chem. Phys.* **1997**, *106* (12), 5189–5201.

45. Weerawardene, K. L. D. M.; Aikens, C. M. Theoretical Insights into the Origin of Photoluminescence of $Au_{25}(SR)_{18}^-$ Nanoparticles. *J. Am. Chem. Soc.* **2016**, *138* (35), 11202–11210.

46. Aikens, C. M. Effects of Core Distances, Solvent, Ligand, and Level of Theory on the TDDFT Optical Absorption Spectrum of the Thiolate-Protected Au_{25} Nanoparticle. *J. Phys. Chem. A* **2009**, *113* (40), 10811–10817.

47. Marques, M. A. L.; Castro, A.; Rubio, A. Assessment of Exchange-Correlation Functionals for the Calculation of Dynamical Properties of Small Clusters in Time-Dependent Density Functional Theory. *J. Chem. Phys.* **2001**, *115* (7), 3006–3014.

48. Obstarczyk, P.; Kundu, S.; Bürgi, T.; Olesiak-Bańska, J. Solvatochromism of Amphiphilic $Au_{25}(SR)_{18}$ Nanoclusters Based on Supramolecular Ligand–Thiolated Crown Ether. *J. Phys. Chem. Lett.* **2025**, *16* (29), 7331–7336.

49. Deng, H.-H.; Huang, K.-Y.; Zhong, Y.; Li, Y.; Huang, H.-X.; Fang, X.-Y.; Sun, W.-M.; Yao, Q.; Chen, W.; Xie, J. Enzyme-Activatable Charge Transfer in Gold Nanoclusters. *Chem. Sci.* **2024**, *15* (23), 8922–8933.

50. Bhattacharya, D.; Vaval, N.; Pal, S. Electronic Transition Dipole Moments and Dipole Oscillator Strengths within Fock-Space Multi-Reference Coupled Cluster Framework: An Efficient and Novel Approach. *J. Chem. Phys.* **2013**, *138* (9), 094108.

51. Sardar, A.; Wang, Y.; He, G.; Gianopoulos, C. G.; Samarasinghe, D. S. N. D.; Liu, Z.; Kirschbaum, K.; Aikens, C. M.; Jin, R. $Au_{20}Ag_{32}$ Nanocluster Emitting Bright Near-Infrared-II Photoluminescence with Quantum Yield of 30% in Aerated Solution. *ACS Nano* **2026**, acsnano.5c22362.

Chapter 5 - Development of a machine learning force field for gold hydride nanoclusters that predicts potential energy with quantum-level precision

D. Sulalith N. D. Samarasinghe[†], Yuchen Wang[†], Christine M. Aikens[†*]

[†] Department of Chemistry, Kansas State University, Manhattan, KS 66506, United States

*Email: cmaikens@ksu.edu

5.1 Abstract

Achieving quantum-mechanically accurate molecular dynamics (MD) simulations for large molecular systems remains challenging due to the computational cost of density functional theory (DFT). Gold-hydride clusters (which have important applications in sensing and catalysis) can have a size and complexity that necessitate efficient computational methods, especially if dynamical properties are of interest. In this study, we developed a machine learning force field (MLFF) with DFT level accuracy for gold-hydride nanoclusters using the FLARE++ framework. We first employed active learning on $Au_{13}H_5$ and $Au_{18}H_{14}$ nanoclusters to generate the initial training data. The model was then refined through four passive learning iterations, which involved combining databases, retraining, validating predictions from LAMMPS MD against VASP DFT, and incorporating structures with large prediction errors. The final MLFF is trained on 647 structures (447 $Au_{13}H_5$ and 200 $Au_{18}H_{14}$) and accurately predicts relative energies for the training clusters as well as for larger clusters that are not included in the training set. While the model captures relative energy landscapes accurately, absolute energies require systematic offset corrections. Further validations at 200 K and 400 K show that the model works well with the expanded structural landscape even though it was only trained using structures sampled from 300

K simulations. This MLFF provides a computationally efficient tool for exploring gold-hydride nanocluster dynamics and establishes a foundation for future reactive force field development.

5.2 Introduction

Atomically precise metal nanoclusters (NCs) have emerged as a rapidly growing area of chemistry research. These systems have attracted considerable attention owing to their promising applications in catalysis, photothermal therapy, cancer diagnostics, and optoelectronic devices.[1–5] The atomic-level understanding of these clusters enables rational design strategies to optimize their performance for targeted applications. A metal NC is typically comprised of a metal core (e.g., Au, Ag, and Cu) and protecting ligands (e.g., thiolates and phosphines), resulting in a diverse family of systems with distinct properties. Among these, metal hydride nanoclusters have recently attracted particular interest due to the unique influence of hydrides on cluster properties.[6,7] For instance, Sun et al. demonstrated that hydride incorporation enhances both structural stability and versatility in copper NCs.[8] Moreover, these hydrides can participate directly in catalytic mechanisms, adding another dimension to their utility.[8–10] To date, the majority of well-characterized metal hydride NCs are copper-based systems, typically stabilized by a combination of hydride and other protecting ligands.[6,8–12] In contrast, this study focuses on gold hydride NCs, which represent a less explored area.

Similar to the copper-based systems, gold hydride nanoclusters are typically stabilized by a combination of hydride and other protecting ligands. These gold-hydrides are most commonly observed as heterometallic complexes, with Pt, Pd, or Cu as the secondary metal within the metal cluster.[13–15] It is important to note that gold's chemical inertness has long obscured our understanding of Au-H bond formation.[16] Spectroscopic observations have revealed the

existence of gold-hydride diatomic molecules, yet questions about their stability persisted. This uncertainty was resolved by Wang et al., who employed both experimental and theoretical modeling to establish that mono-gold hydride molecules can indeed be produced under controlled conditions.[17] Beyond molecular and nanocluster-scale, gold-hydride investigations extend into nanoparticle-scale, where interest centers on exploiting their potential for sensing and catalytic applications enhanced by the local surface plasmon resonance.[18–20] Further evidence indicates that hydrogen present in these larger nanoparticle systems plays a critical role, simultaneously enhancing structural robustness and boosting catalytic performance.[21,22]

Given their importance, gold-hydride clusters have been studied through both experimental and theoretical approaches.[22] Computational methods such as density functional theory (DFT) have become increasingly powerful tools for understanding not only hydride-containing nanoclusters but the entire family of metallic cluster systems. These calculations provide insights into electronic structure, optical properties, structural configurations, and numerous other characteristics.[22–27] However, a major challenge remains, as these calculations become exponentially more expensive as system size increases. This scaling problem is particularly acute for gold clusters, where adding just a few atoms can dramatically increase computational demands. As noted previously, gold-hydride clusters are particularly relevant for catalytic applications. Consequently, characterizing the dynamics and interatomic potentials for a wide array of different hydride positions within these systems is essential for understanding and optimizing their catalytic performance. Therefore, selecting appropriate theoretical methods which reflect this information requires careful consideration of both the desired accuracy and available computational resources. This trade-off has spawned an active research area dedicated to applying and developing other methods that achieve near-equivalent accuracy to DFT at

significantly reduced computational cost. Alternative approaches for exploring the structural dynamics of these systems include classical molecular dynamics (MD) and *ab initio* molecular dynamics (AIMD). These methods have been successfully applied to metal clusters, enabling investigation of structural behavior and exploration of potential energy surfaces.[22,25,28–31] However, it is important to note that these methods have their own limitations. Classical MD simulations require carefully parameterized force fields tailored to the specific systems under study, which can be challenging at the development stage (and the accuracy may still not be comparable with AIMD). Although AIMD simulations offer high accuracy, their considerable computational cost confines them to relatively shorter time scales. Therefore, opportunities remain for further innovation. In particular, machine learning approaches offer promising avenues for enhancing computational efficiency while maintaining chemical accuracy.

The application of machine learning to nanocluster systems has emerged as a dynamic and rapidly evolving field. Recent work in this domain includes several notable studies. Jäger et al. applied machine learning to predict hydrogen adsorption patterns on molybdenum disulfide and copper-gold clusters,[32] while Vandermause et al. introduced a Bayesian active learning strategy to study hydrogen dynamics on platinum surfaces.[33] Pihlajamäki et al. developed distance-based approaches for Monte Carlo simulations for gold-thiolate nanoclusters,[34] and both Wang et al.[35] and McCandler et al.[36] constructed machine learning force fields (MLFFs) specifically designed to capture potential energy landscapes in gold-thiolate systems. Meanwhile, Fang et al. took a different approach, using kernel ridge regression methods to model cystine-protected gold nanoclusters.[37] Collectively, these studies showcase the breadth and adaptability of machine learning tools for tackling complex nanoscale systems.

Having established both the importance of studying gold-hydride cluster systems and current applications of machine learning approaches, this study combines these elements to develop an MLFF capable of predicting potential energies for diverse gold-hydride clusters with quantum-level accuracy. We employ an active learning methodology using sparse Gaussian process regression to generate the initial structural database along with the initial training, followed by interactive model training that incorporates passive learning for refinement. Therefore, this study will elaborate on: (1) the theoretical background of the machine learning approaches employed, (2) the training and testing procedures, and (3) computational validation of the trained MLFF. These validations assess the accuracy of predicted potential energies for both structures within the training set and those outside it, ultimately addressing a key question: can a model trained on smaller gold-hydride nanoclusters accurately predict potential energies for larger clusters?

5.3 Theory

5.3.1 Sparse Gaussian process (SGP) to model the machine learning force field

In this study, we employ sparse Gaussian processes (SGP) to develop our machine learning force field. Standard Gaussian processes (GP) are powerful non-parametric Bayesian methods that provide not only predictions, but also quantitative uncertainty estimates for those predictions.[38] However, the major limitation of standard GPs is their poor scalability with dataset size. SGP addresses this challenge by using variational inference methods to significantly reduce computational cost while maintaining predictive accuracy.[39] For our modeling, we employ the FLARE++ package, an efficient framework for SGP based force field training that has been

successfully applied to develop MLFFs for predicting potential energies across diverse chemical systems.[33,35]

Following the framework established by Vandermause et al.,[33,40] the SGP based force field is constructed through three interconnected components. First, we define the energy model by expressing the total potential energy as a sum of local contributions from individual atomic environments. Second, each local atomic environment is mapped onto a descriptor vector, specifically using the atomic cluster expansion (ACE) descriptors of Drautz[35,41] that serves as the model's input, capturing the essential geometric and chemical information. Third, we select a kernel function that quantifies the similarity between any two local environments, enabling the model to make predictions based on learned patterns from the training data.

Accurate representation of the local atomic environment requires symmetry preserving descriptors. ACE accomplishes this by efficient computations of many-body descriptors that respect the fundamental symmetries of the potential energy surface. In practice, each atom's descriptor is constructed by examining its local neighborhood and encoding the geometric relationships using a basis set composed of radial functions and spherical harmonics. The resulting equivariant descriptors undergo transformation to ensure rotational invariance.[33] The final descriptor dimensionality (n_{desc}) is determined by three factors: the types of atomic species present ($N_{species}$), the number of radial basis functions employed (N_{rad}), and the highest order of spherical harmonics included (l_{max}), given by, $n_{desc} = N_{species}N_{rad}\left(N_{species}N_{rad}+1\right)(l_{max}+1)/2$. The specific values of N_{rad} and l_{max} employed in each training cycle are listed in Table 5.1.

Table 5.1. N_{rad} and l_{max} values employed in each training cycle.

Training model	N_{rad}	l_{max}
OTF	8	3
OTC-1	8	3
OTC-2	8	3
OTC-3	14	6
OTC-4	14	6

For predictions, the SGP model evaluates the local energy of each atomic environment by computing a weighted sum of kernel functions between that environment and representative sparse environments from the training set. Therefore, the kernel-based similarity metric determines how strongly each sparse environment influences the final energy prediction. For a local environment (ρ_i), the predicted energy (ε) emerges from evaluating kernels between ρ_i and representative sparse environments S, as expressed in Eq. 5.1:[33]

$$\varepsilon(\rho_i) = \sum_{t \in S}^{N_s} k(\boldsymbol{d_i}, \boldsymbol{d_t}) \alpha_t \tag{5.1}$$

where d_i represents the descriptor vector, k is the kernel function that quantifies similarity between two local environments, N_s denotes the number of sparse environments, and α is the training coefficients vector. The kernel function takes the form shown in Eq. 5.2, where ξ is an integer power applied to the normalized dot product, and σ represents a hyperparameter controlling the kernel scale.[33]

$$k(\boldsymbol{d_1}, \boldsymbol{d_2}) = \sigma^2 \left(\frac{\boldsymbol{d_1} . \boldsymbol{d_2}}{d_1 d_2} \right)^{\xi} \tag{5.2}$$

Note that the training coefficients (α) in Eq. 5.1 depend on a diagonal noise matrix that accounts for the expected errors in the training data, encompassing noise components for energy (σ_E), force (σ_F), and stress (σ_S).[33,40] In our training process, these values were set to 96 meV, 0.05 meV/Å, and 0.001 meV/Å^3, respectively (a detailed description is provided in the Appendix C). Additionally, the σ term in Eq. 5.2 characterizes the variation in local energy and was set to 2.00 eV at the beginning of the training process, consistent with the thiolate protected nanocluster MLFF reported by Wang et al.[35] Importantly, both the noise terms and σ are treated as hyperparameters and optimized during the training (optimized values are provided in Table 5.2). The cutoff radius for local atomic environments represents another critical parameter. To balance computational cost against adequate environment sampling, we chose a cutoff of 5.0 Å.

Table 5.2. Tolerance factors and the optimized hyperparameters for each training cycle.

Training model	Tolerance factor	σ	σ_E	σ_F	σ_S
OTF for $Au_{13}H_5$ edge	5.00×10^{-2}	2.13	5.94×10^{-2}	-3.07×10^{-2}	1.03×10^{-5}
OTF for $Au_{13}H_5$ bridge I	5.00×10^{-2}	1.48	5.81×10^{-2}	-6.50×10^{-2}	9.64×10^{-6}
OTF for $Au_{13}H_5$ bridge II	5.00×10^{-2}	1.99	8.19×10^{-2}	-1.47×10^{-3}	-1.31×10^{-5}
OTF for $Au_{18}H_{14}$	5.00×10^{-2}	1.21	8.16×10^{-2}	1.95×10^{-3}	-1.90×10^{-5}
OTC-1	1.00×10^{-2}	2.30×10^{1}	2.33×10^{2}	-6.46	-4.19×10^{4}
OTC-2	1.00×10^{-2}	2.04	9.66×10^{-2}	3.74×10^{-1}	2.13×10^{-5}
OTC-3	5.00×10^{-3}	9.00×10^{-1}	-1.01×10^{-1}	4.45×10^{-1}	2.13×10^{-5}
OTC-4	5.00×10^{-3}	8.97×10^{-1}	1.01×10^{-1}	4.26×10^{-1}	-2.18×10^{-5}

5.3.2 Training procedure and structure selection

Our approach combines two complementary strategies: active learning (on-the-fly or OTF), where training and data generation occur simultaneously without requiring an initial dataset, and passive learning (offline training or OTC), which trains on a pre-existing database. Our training procedure initiates with an active learning cycle that builds the model dynamically. The process starts by performing a DFT calculation of the initial gold-hydride structure, establishing both the first training point and the starting geometry for the MD exploration of the potential energy surface. As the MD simulation progresses, the SGP model evaluates each new configuration, predicting energies, forces, and stresses while simultaneously computing Bayesian uncertainties for its predictions.[33] These uncertainties reflect how unfamiliar the current atomic environments are compared to those already captured in the sparse training set. The model's confidence determines the next action: low uncertainty (if below the tolerance factor) signals reliable predictions, allowing the simulations to continue using the SGP forces to sample new regions of configuration space, while higher uncertainty (if above the tolerance factor) triggers a different mechanism, where the MD simulation is stopped at that point and moved to a DFT calculation to provide accurate potential energy predictions (i.e., a label for the current structure) for the new configuration. This new information then augments the training set, improving the model before simulation resumes. This active learning cycle continues until DFT calculations are called less frequently, indicating that the model has learned to accurately predict most configurations.[33,35] In this study, the FLARE++ framework is coupled with the VASP package to perform DFT calculations,[42] using the PBE[43] exchange-correlation functional with a plane-wave basis set and an energy cutoff of 450 eV.[44,45]

Upon completion of the active learning cycles, the accumulated training dataset becomes available for the next phase. In the passive learning stage, we combine datasets generated across multiple active learning cycles into a unified database. This passive training also requires several iterations to converge to the final MLFF. Unlike active learning, passive (offline) training does not explore new configurations during the training process itself. Therefore, structures that exhibit large prediction errors during MLFF validation represent previously unsampled regions of configuration space and are candidates for inclusion in the training database to improve model accuracy. The testing and validation procedures are discussed in detail in section c. The training and testing procedures cannot be clearly separated, as they function as complementary components of an iterative refinement process.

Having established the training procedure, the next critical consideration is structure selection. For the initial active learning cycles, we employed two gold hydride nanocluster systems: $Au_{13}H_5$ and $Au_{18}H_{14}$ (these structures are depicted in Figure 5.1). For $Au_{13}H_5$, we prepared three conformers distinguished by their hydride arrangements: two featuring bridging hydrides between gold atoms ("bridge I" and "bridge II") and one with only terminal hydrides ("edge"). Table C.1 provides the relative energies of the three $Au_{13}H_5$ conformers, indicating that bridge I is energetically most favorable. Importantly, the icosahedral Au_{13}^{+5}, unit appears frequently as a structural building block in ligand-protected nanoclusters, particularly in gold-thiolate systems,[24,26–28,30,47] and therefore the Au_{13}^{+5} unit was adopted with three different hydride arrangements to generate these conformers. The $Au_{18}H_{14}$ initial geometry was constructed by adapting previously optimized gold chloride nanoclusters from Kuda-Singappulige et al.,[46] systematically replacing chlorides with hydrogens. Following hydrogen substitution, all four configurations underwent geometry optimization to ensure reasonable

starting points for the active learning procedure. The optimizations were performed at the BP86/TZP level of theory[48,49] in the gas phase using the Amsterdam Modeling Suite (AMS) 2021.1 package.[50,51] The convergence criteria employed were: an SCF convergence of 1×10^{-8}, an energy convergence of 5×10^{-5} Hartree, and a gradient convergence of 1×10^{-4} Hartree/Å. Upon completion of these optimizations, we adopted Wang et al.'s multi-conformer approach,[33] initiating separate active learning cycles for each configuration. This parallel training yielded four independent MLFFs with their respective databases (OTF training models).

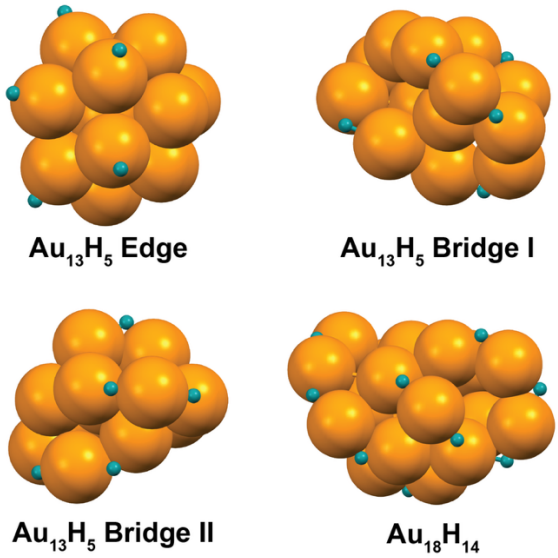


Figure 5.1. Gold hydride nanocluster systems used in the active learning phase (color labels: orange = Au and teal = H).

As previously mentioned, upon completion of the active learning phase, we combined all four databases into a single unified database for passive learning. Before initiating the passive training, we tested the current MLFFs and identified structures with large prediction errors for addition to the database, thereby expanding the database beyond the original active learning configurations. The passive learning phase then proceeded through four iterative cycles (labeled

OTC-V, where V denotes the cycle number), each involving model testing, identification of structures with less accurately predicted potential energies, database augmentation, and retraining. By the fourth cycle (OTC-4), the training database comprised 647 total configurations: 447 $Au_{13}H_5$ and 200 $Au_{18}H_{14}$ structures. This database captures extensive configurational sampling across the potential energy surfaces of these two cluster systems. A detailed breakdown of the number of structures in each training cycle is provided in Table 5.3. Having established a model trained on only $Au_{13}H_5$ and $Au_{18}H_{14}$ systems, the critical question becomes how well it predicts energies for different gold hydride clusters.

Table 5.3. Structural database composition for each training cycle by cluster type.

Training model	$Au_{13}H_5$ edge	$Au_{13}H_5$ bridge I	$Au_{13}H_5$ bridge II	$Au_{18}H_{14}$	Total structures
OTF for $Au_{13}H_5$ edge	82	-	-	-	82
OTF for $Au_{13}H_5$ bridge I	-	43	-	-	43
OTF for $Au_{13}H_5$ bridge II	-	-	105	-	105
OTF for $Au_{18}H_{14}$	-	-	-	81	81
OTC-1	91	59	114	119	383
OTC-2	108	79	134	138	459
OTC-3	135	91	160	160	546
OTC-4	164	91	192	200	647

5.3.3 Testing and validation of the machine learning force field

For the testing phase, we employed LAMMPS[52] to perform molecular dynamics simulations using the trained MLFF, enabling evaluation of the model's potential energy

predictions at each timestep. All MD simulations utilized an NVT ensemble with a Nosé-Hoover thermostat,[53–55] running for 100 ps with a 1 fs time step in a cubic simulation box of 30 Å × 30 Å × 30 Å. From each production run, we extracted structural snapshots at 5 ps intervals. These configurations were then subjected to single-point DFT calculations using VASP to obtain reference potential energies. Comparing the MLFF-predicted energies from the MD trajectories with the corresponding VASP reference values provides a quantitative assessment of model accuracy. All VASP calculations used the same computational settings and convergence criteria as the active learning phase to maintain consistency. Finally, mean absolute deviation (MAD) and root mean square error (RMSE) of the MLFF-predicted potential energies were calculated to quantify model accuracy. The equations for these metrics are provided in Eq. C.1 and C.2 in the Appendix C.

A critical aspect of validation is determining which structures are used to assess model performance. Therefore, we conducted the validation in two distinct ways: (1) evaluating prediction accuracy for structures included in the training set, and (2) evaluating prediction accuracy for structures outside the training set. This dual approach allows us to assess both the model's ability to reproduce energies within its training domain (interpolation) and its capacity to generalize to novel structures (extrapolation). Importantly, this analysis reveals whether an MLFF trained on a limited set of initial structures can accurately predict energies for significantly larger or structurally distinct systems. To assess model transferability beyond the training set, we tested the MLFF on six additional gold hydride nanoclusters: $Au_{20}H_{16}$, $Au_{24}H_{16}$, $Au_{28}H_{20}$, $Au_{30}H_{18}$, $Au_{36}H_{24}$, and $Au_{38}H_{24}$. Following the same protocol used for the $Au_{18}H_{14}$ structure, these geometries were derived from previously optimized gold chloride nanoclusters reported by Kuda-Singappulige et al.,[46] with chlorides systematically replaced by hydrogens,

followed by geometry optimization. The nanoclusters used for the testing phase are visualized in Figure 5.2.

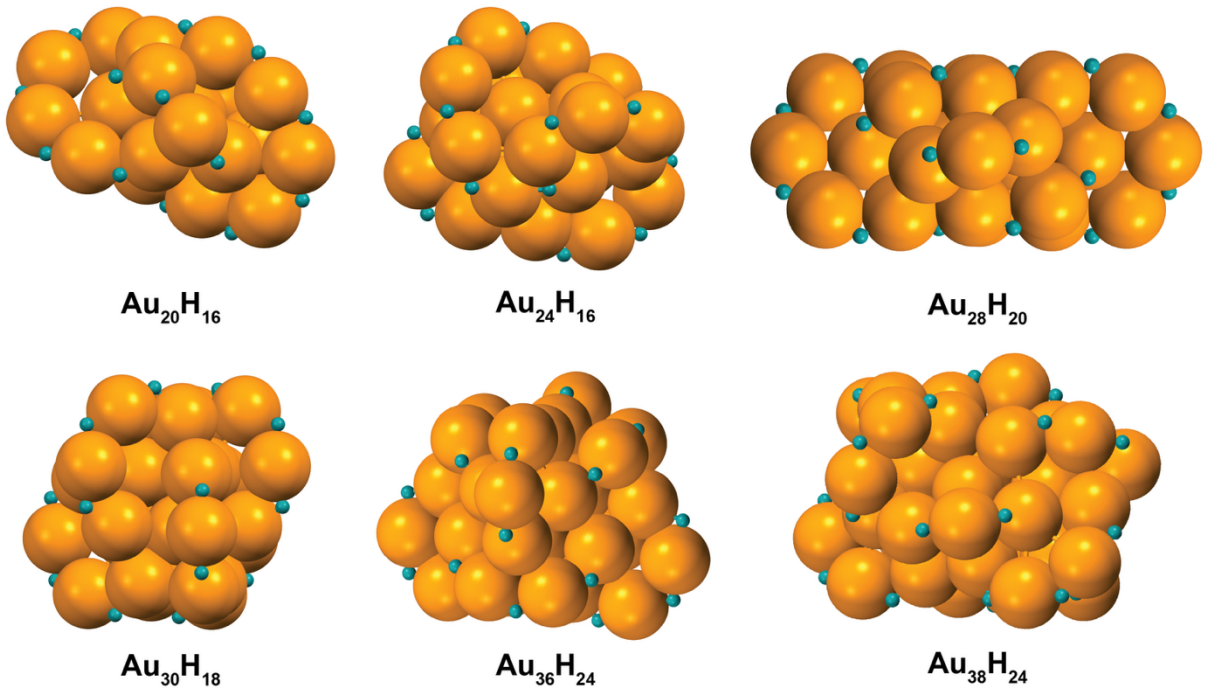


Figure 5.2. Gold hydride nanocluster systems used for validation and testing that are not included in the training database (color labels: orange = Au and teal = H).

Our active learning phase employed MD simulations at 300 K, establishing this temperature as the reference for initial model validation. However, practical applications often require predictions across different temperatures. We therefore tested the model's predictive capability at both lower (200 K) and higher (400 K) temperatures using selected gold hydride systems. Since the training database lacks any configurations sampled outside 300 K, testing at different temperatures (particularly higher temperatures), enables exploration of configurational regions typically not sampled during standard 300 K simulations. This provides insight into the breadth of the configurational landscape the trained MLFF can accurately predict.

5.4 Results and Discussion

5.4.1 MLFF vs. DFT potential energy prediction at 300 K

To evaluate the MLFF performance, we conducted MD simulations of various gold hydride nanoclusters at 300 K using LAMMPS. We first assessed prediction accuracy for structures included in the training set by performing simulations on the three $Au_{13}H_5$ conformers and on $Au_{18}H_{14}$, and computed the respective MAD and RMSE values. The resulting MAD values were 5.90 meV/atom for the edge conformer, 18.07 meV/atom for bridge I, and 12.69 meV/atom for bridge II. In contrast, $Au_{18}H_{14}$ exhibited a notably lower MAD value of 2.76 meV/atom. Extending validation to six larger clusters absent from the training data revealed an intriguing pattern. While MLFF predictions consistently overestimated absolute energies relative to DFT, in most cases they accurately align with the shape and relative features of the DFT energy landscapes. Therefore, applying a constant energy offset to the MLFF predictions substantially reduced discrepancies, following the approach employed by Wang et al. for a gold-thiolate nanocluster MLFF.[35] This indicates that while the MLFF accurately captures relative energies, which are crucial for understanding structural dynamics, achieving quantitative accuracy in absolute energies requires further refinements. Notably, these systems that are outside the training database yielded MAD and RMSE values below 10.00 meV/atom, with the largest cluster, $Au_{38}H_{24}$, achieving an exceptionally low MAD of 3.54 meV/atom despite containing 62 atoms, nearly double the size of the largest trained cluster ($Au_{18}H_{14}$ with 32 atoms in total). Table 5.4 summarizes the tested systems along with their applied energy offsets and corresponding MAD and RMSE values.

Table 5.4. Energy offsets, MAD, and RMSE values for tested gold hydride clusters.

Gold hydride cluster	Offset (meV/ atom)	MAD (meV/ atom)	RMSE (meV/ atom)
$Au_{13}H_5$ edge	-	5.90	7.56
$Au_{13}H_5$ bridge I	-	18.07	19.87
$Au_{13}H_5$ bridge II	-	12.69	15.14
$Au_{18}H_{14}$	-	2.76	3.22
$Au_{20}H_{16}$	8.45	5.52	7.24
$Au_{24}H_{16}$	24.26	3.51	4.25
$Au_{28}H_{20}$	21.81	8.40	9.84
$Au_{30}H_{18}$	53.47	2.69	3.66
$Au_{36}H_{24}$	47.27	3.34	4.00
$Au_{38}H_{24}$	60.45	3.60	4.18

Notably, the test systems outside the training set generally achieved lower MAD and RMSE values than the training structures themselves, with the $Au_{13}H_5$ conformers showing particularly large disparities. This counterintuitive phenomenon, where out-of-sample predictions surpass in in-sample accuracy, mirrors findings by McCandler et al. in their MLFF for gold-thiolate protected nanoclusters.[36] Yet this overall accuracy improvement masks an important nuance. While training clusters require minimal shifts to match DFT values, the necessary offset grows systematically with cluster size for the test systems (Table 5.4). This reveals the MLFF's dual nature, where it has learned transferable local atomic environment descriptors that are enough to reproduce the potential energy landscapes and relative stabilities across a broad size range, but exhibit a systematic energy bias that scales with system size. Therefore, the model is

successful in capturing relative energetics, which is a key requirement for predicting structural evolution and dynamics; this demonstrates effective knowledge transfer from the compact training set, although the absolute energy quantification remains a challenge. Figure 5.3 illustrates the comparison of MLFF and DFT potential energy predictions for all gold hydride structures tested during the validation process, while Figure 5.4 shows the per atom prediction accuracy for these systems.

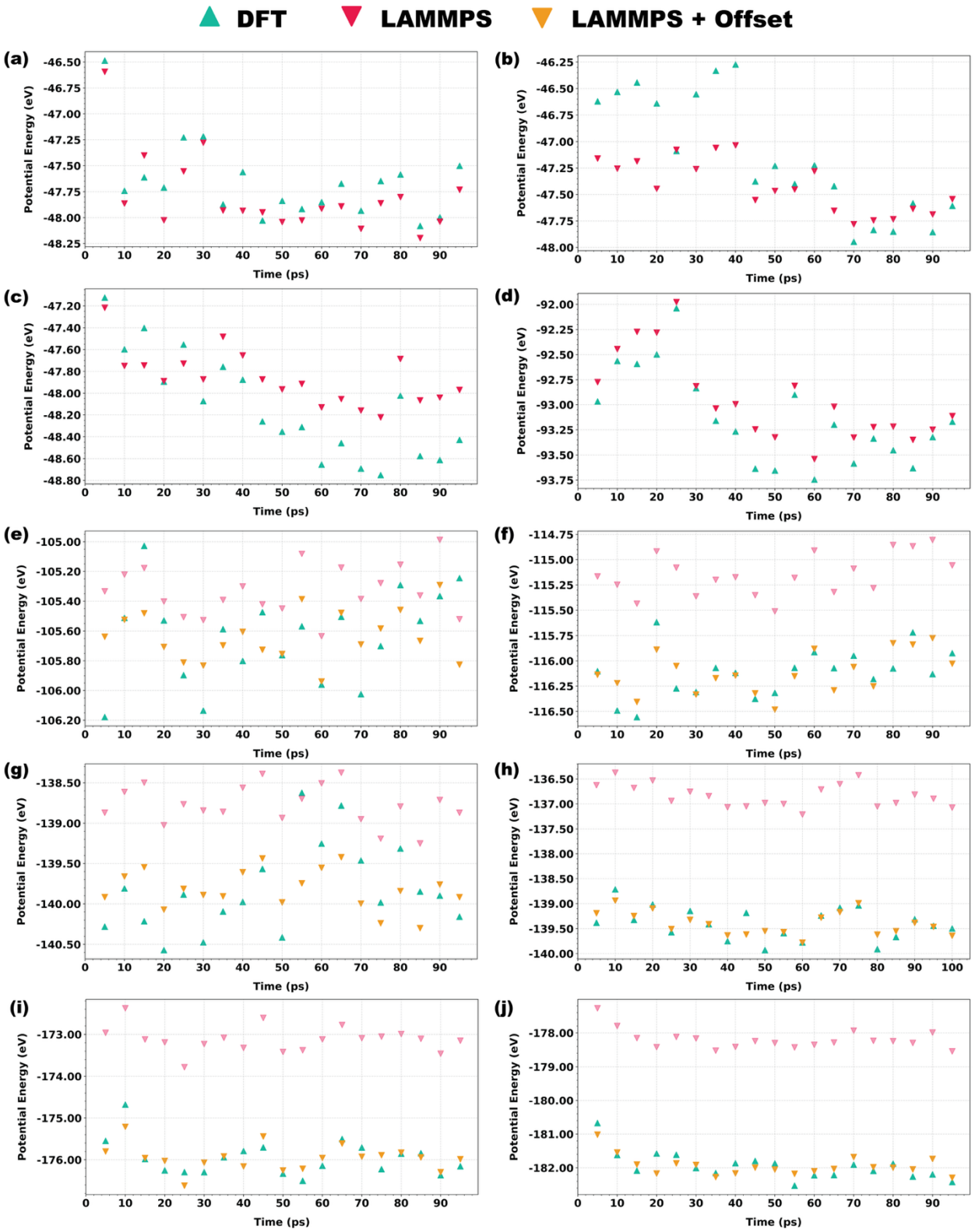

DFT
LAMMPS
LAMMPS + Offset
(a)
(b)
(c)
(d)
(e)
(f)
(g)
(h)
(i)
(j)
Potential Energy (eV)
Time (ps)

Figure 5.3. MLFF-predicted vs. DFT reference potential energies throughout the MD simulations for (a) $Au_{13}H_5$ edge, (b) $Au_{13}H_5$ bridge I, (c) $Au_{13}H_5$ bridge II, (d) $Au_{18}H_{14}$, (e) $Au_{20}H_{16}$, (f) $Au_{24}H_{16}$, (g) $Au_{28}H_{20}$, (h) $Au_{30}H_{18}$, (i) $Au_{36}H_{24}$, and (j) $Au_{38}H_{24}$ clusters.

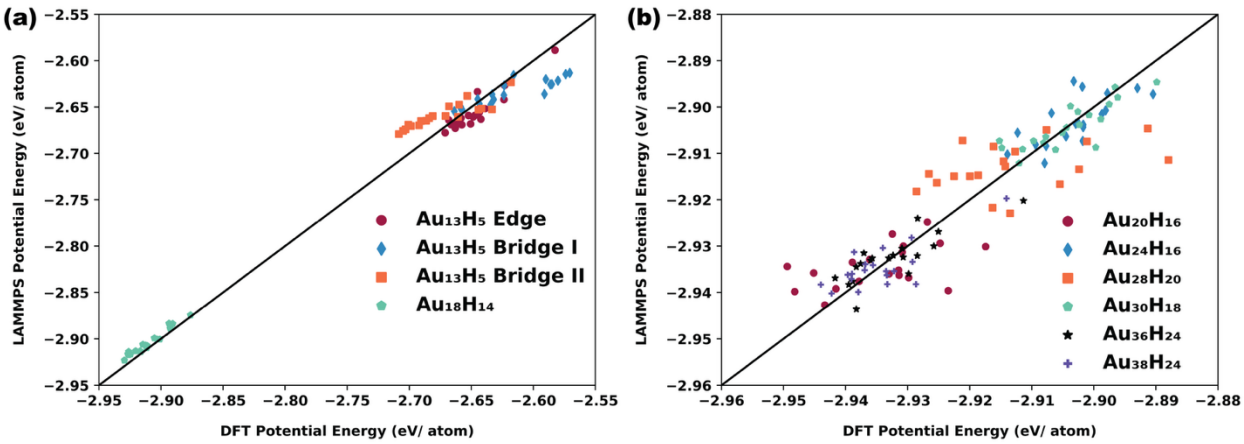


Figure 5.4. Prediction accuracy per atom for structures (a) included in the training set and (b) outside the training set, after applying constant energy offsets (Figure C.1 shows energies before offset correction). Data points correspond to the systems presented in Figure 5.3.

5.4.2 Structural landscape analysis

To quantify the structural diversity explored during the MD testing simulations, we calculate the root-mean-square deviation (RMSD) between each sampled configuration (structural snapshots at 1 ps intervals) and the initial structure used to start the simulation. RMSD is defined by Eq. 5.3:

$$MSD = \sqrt{\frac{1}{N}\sum_{i}^{N}[(x_i - x_i')^2 + (y_i - y_i')^2 + (z_i - z_i')^2]} \tag{5.3}$$

where N is the number of atoms in the system, and x_i, y_i, z_i and x_i', y_i', z_i' represent the Cartesian coordinates of atom i in the initial (reference structure) and sampled structures, respectively (note that to minimize RMSD between configurations, we account for center-of-

mass shifts and apply the Kabsch algorithm[56] to optimize rotational alignment for best overlap). To decompose structural changes by component, we calculated the RMSD independently for gold atoms (Figure 5.5a) and hydrogen atoms (Figure 5.5b). Corresponding total RMSD variation for all atoms is provided in Figure C.2. As shown in Figure 5.5, $Au_{18}H_{14}$ and $Au_{13}H_5$ bridge I sampled a wide range of configurations during the testing. For the other two $Au_{13}H_5$ conformers (edge and bridge II), gold atom positions remained relatively stable while hydrogen positions exhibited relatively greater variation. Among the larger test systems, $Au_{28}H_{20}$ explored diverse structural configurations, whereas $Au_{24}H_{16}$ (median total RMSD: 1.06 Å) and $Au_{30}H_{18}$ (median total RMSD: 1.78 Å) showed more limited RMSD for both gold and hydrogen. This sampling suggested that 300 K simulations may not adequately explore the configurational landscape for certain systems. To address this, we conducted additional simulations at 200 K and 400 K to enhance configurational sampling and assess model performance across a selected set of structures ($Au_{24}H_{16}$, $Au_{30}H_{18}$, and $Au_{36}H_{24}$), including those with smaller structural deviations from the initial geometry.

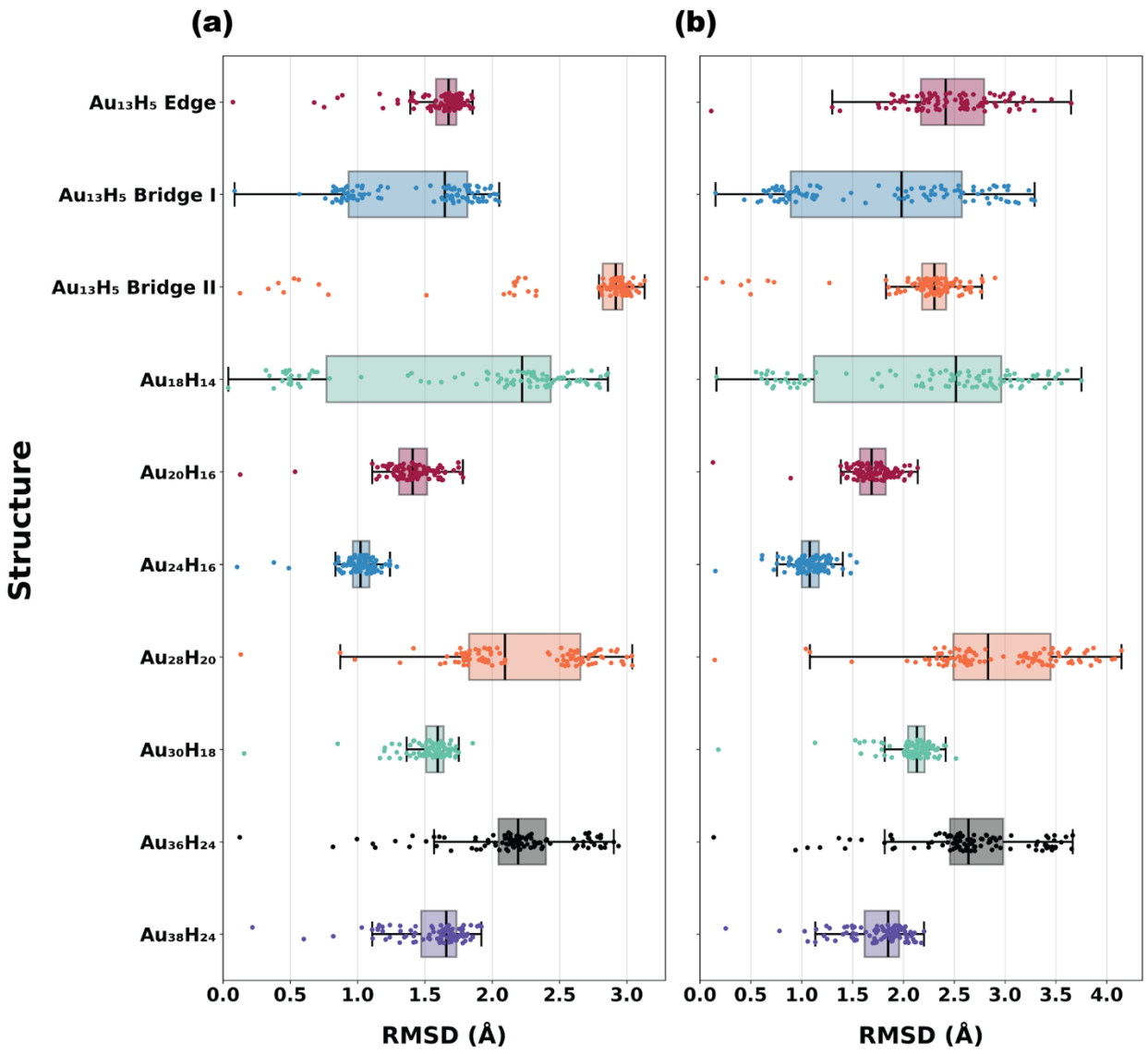


Figure 5.5. Box plots showing RMSDs for (a) gold atoms and (b) hydrogen atoms across all tested systems during 300 K MD simulations.

As shown in Figure 5.6, the simulations beyond 300 K benefited by exploring further deviations in the structural landscape for $Au_{24}H_{16}$, $Au_{30}H_{18}$, and $Au_{36}H_{24}$ systems. This is especially true for the 400 K simulations, as the RMSD span is wider compared to both the 200 K and 300 K simulations. Note that all simulations were initiated using the same structure, so comparisons between respective systems are feasible. Overall, at 400 K, all clusters exhibited a

higher median total RMSD compared to 300 K: $Au_{24}H_{16}$ with 1.54 Å, $Au_{30}H_{18}$ with 1.99 Å, and $Au_{36}H_{24}$ with 2.66 Å. At 200 K, the clusters shifted toward a lower median total RMSD compared to 300 K for $Au_{30}H_{18}$ with 1.25 Å, and $Au_{36}H_{24}$ with 1.74 Å, although $Au_{24}H_{16}$ shifted towards a slightly higher RMSD, with a median of 1.14 Å. A further breakdown on the gold atom and hydrogen atom RMSDs is provided in Figure C.3 for the respective systems.

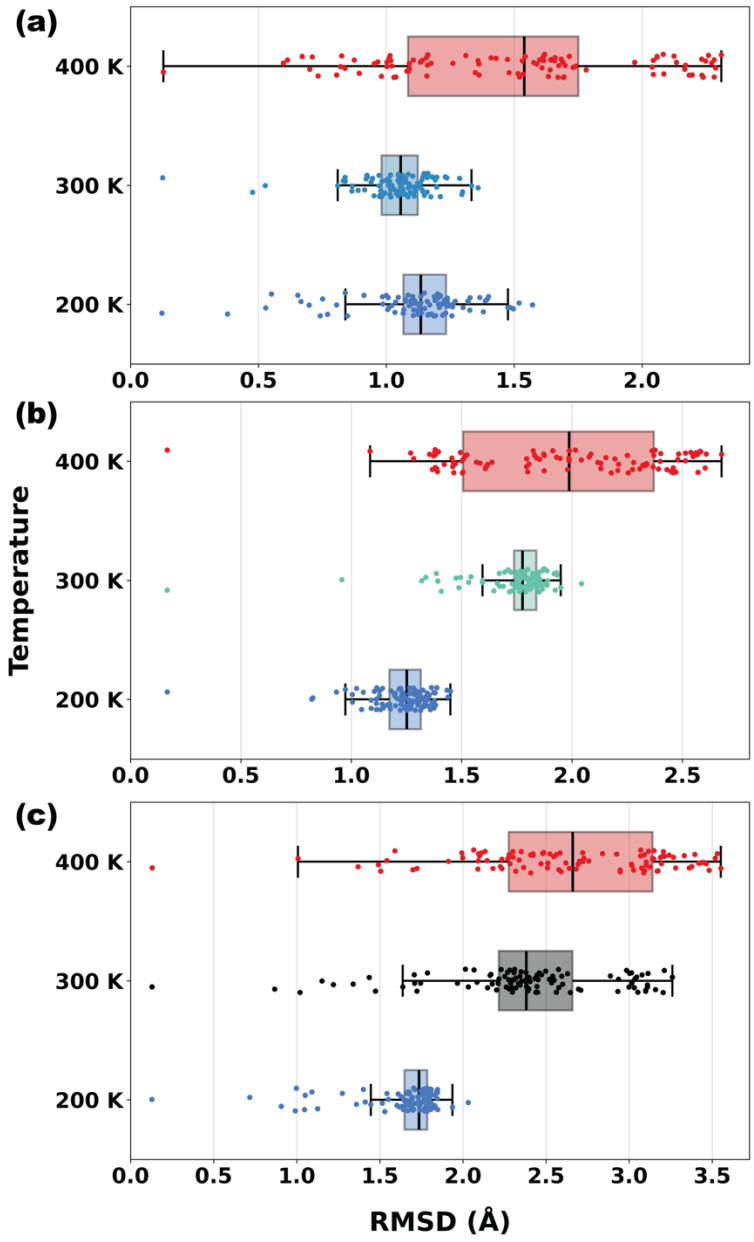


Figure 5.6. Box plots showing total RMSDs for (a) $Au_{24}H_{16}$, (b) $Au_{30}H_{18}$, and (c) $Au_{36}H_{24}$ clusters during the MD simulations at respective temperatures.

Application of the trained MLFF on this extended landscape would further shed light on the applicability of the MLFF to diverse cluster systems. To determine the accuracy of the predicted potential energies, we employed the same strategy to compute the MAD and RMSE values corresponding to the energy differences between MLFF and DFT predicted potential

energies. It is interesting to note that the overall MAD values across all systems at both 200 K and 400 K exhibited a MAD value of less than ~4.00 meV/ atom (less than ~5.00 meV/ atom for RMSE), which is comparable to the previously reported accuracy. As shown in Table 5.5, with the exception of $Au_{24}H_{16}$ at 200 K, all other systems at their respective temperatures yielded MAD values slightly higher than those obtained at 300 K. Overall, these results indicate that the trained MLFF remains applicable throughout the structural landscape sampled due to varying kinetic energy (reflecting the different temperature used), with both higher- and lower-energy structures predicted with relative accuracy by the model. Table 5.5 summarizes the prediction accuracies and Figure 5.7 illustrates the comparison of MLFF and DFT potential energy predictions for the gold hydride structures sampled during 200 K and 400 K MD simulations.

Table 5.5. Energy offsets, MAD, and RMSE values for selected gold hydride clusters in different temperatures.

Gold hydride cluster	Temperature (K)	Offset (meV/ atom)	MAD (meV/ atom)	RMSE (meV/ atom)
$Au_{24}H_{16}$	200	27.77	2.99	3.54
	400	31.42	4.09	5.04
$Au_{30}H_{18}$	200	54.17	3.37	4.19
	400	49.92	4.09	4.73
$Au_{36}H_{24}$	200	56.38	3.72	4.86
	400	48.06	3.77	4.72

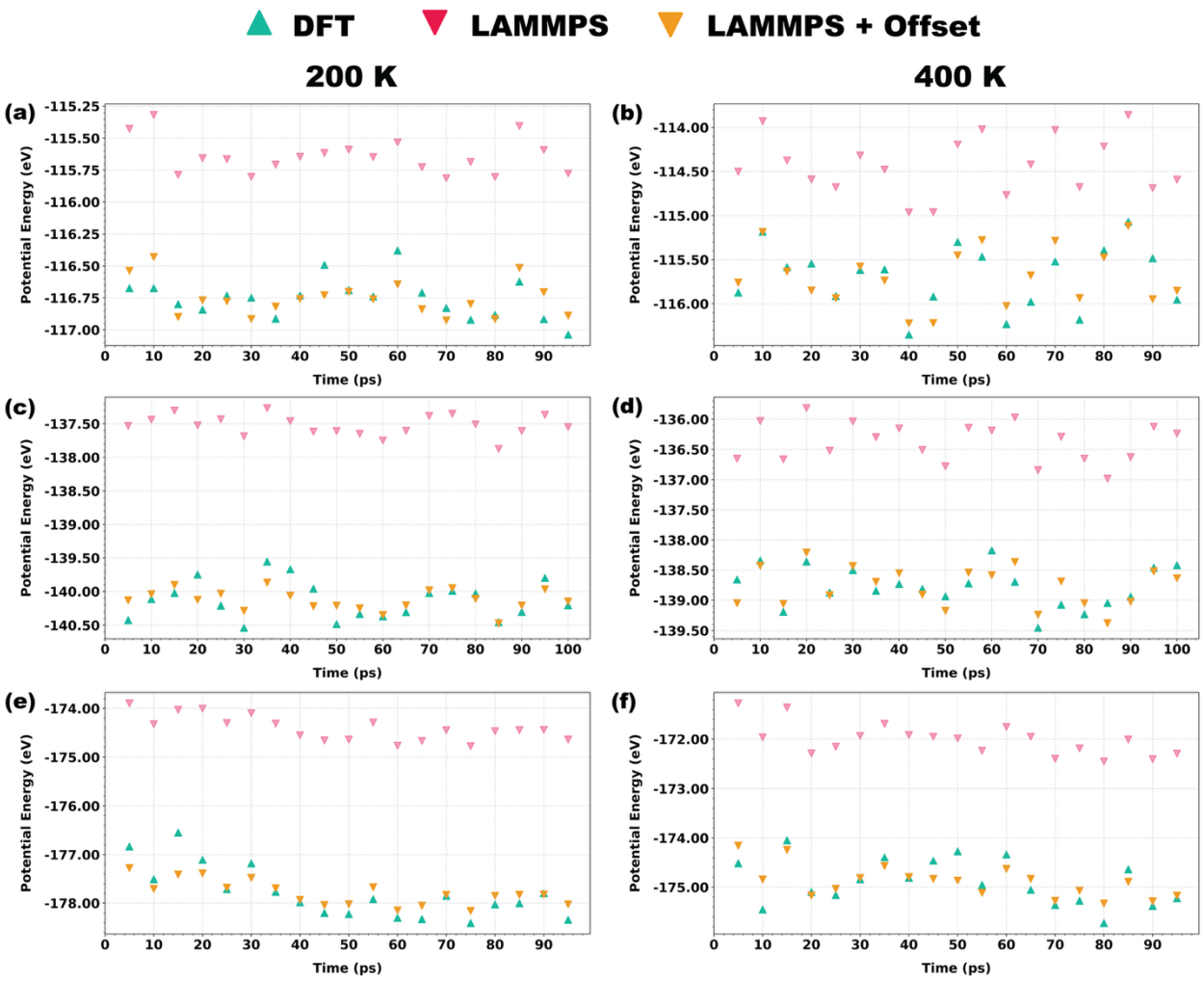


Figure 5.7. MLFF-predicted vs. DFT reference potential energies throughout the MD simulations for (a) $Au_{24}H_{16}$ at 200 K, (b) $Au_{24}H_{16}$ at 400 K, (c) $Au_{30}H_{18}$ at 200 K, (d) $Au_{30}H_{18}$ at 400 K, (e) $Au_{36}H_{24}$ at 200 K, and (f) $Au_{36}H_{24}$ at 400 K.

Overall, the MLFF based MD simulations offer significant computational speedup compared to AIMD. It should be noted that this MLFF is trained on Au_xH_y and is therefore applicable to capturing the potential energies of similar gold hydride nanoclusters. A key future direction for this MLFF would be to extend it towards capturing hydrogen (H_2) bond breaking and formation processes on gold surfaces. The current MLFF cannot capture these effects, as it lacks any knowledge of this phenomenon. Nevertheless, with these future modifications, it

would potentially be possible to apply this MLFF to understand gold-hydrogen interactions on gold surfaces.

5.5 Conclusion

A MLFF for gold hydride nanoclusters was developed by training on the configurational space of $Au_{13}H_5$ and $Au_{18}H_{14}$, achieving DFT level accuracy in predicting relative potential energies across larger gold hydride cluster systems. The workflow initially employed active learning approaches to efficiently sample the potential energy surface and construct the databases used in the training process. This was carried out starting from three different conformers of $Au_{13}H_5$ and one $Au_{18}H_{14}$ configuration. Upon completion of the active learning stage, it was coupled with a passive training approach that combined all initial databases with additional structures that exhibited considerable discrepancies during initial model testing, and all of which were configurations of $Au_{13}H_5$ and $Au_{18}H_{14}$. This iterative testing and training cycle was carried out over 4 cycles, with the final trained model (OTC-4) comprising 647 total structures (447 $Au_{13}H_5$: 200 $Au_{18}H_{14}$). The model was then evaluated not only on structures within the training set, but also on structures outside of it, thereby validating both the applicability and predictive capabilities of the MLFF across diverse gold hydride cluster configurations. To further extend the structural landscape sampled throughout the MD simulations at 300 K, we initiated calculations at 200 K and 400 K on selected structures and validated the model performance to assess its capability of capturing correct energetics not only for structures sampled at 300 K, but beyond that scope as well.

The OTC-4 MLFF model demonstrated considerable agreement between MLFF and DFT predicted potential energies, with MAD values below 19.00 meV/atom for structures within the

database and below 8.50 meV/atom for structures outside the database, while performing accelerated MD simulations. Comparable accuracy was observed in testing performed on configurations sampled during MD simulations conducted at different temperatures. However, it should be noted that although the model predicts relative energies with good agreement, an offset must be applied to achieve absolute energies, which varies with the system size tested. Therefore, while the model predicts relative energetics of larger gold hydride clusters with reasonable accuracy, indicating that the local atomic environments sampled using 447 $Au_{13}H_5$ and 200 $Au_{18}H_{14}$ are sufficient to reflect the relative energetics, there remains room for improvement in obtaining absolute energies. This model holds strong potential as a foundation for further developments such as extending this model to a force field that can examine H_2 bond dissociation/formation processes on gold.

5.6 Data availability

All input files, initial geometries, and results corresponding to the MLFF training and testing procedures are available across two platforms. The final trained MLFF model (MLFF-OTC-4-Model), including three component files (*lmp.flare*, *L_inv_lmp.flare*, and *sparse_desc_lmp.flare*), is archived on Open Science Framework (OSF) at https://osf.io/58emp/overview?view_only=8a98b807cf5742a1a25b44badea07e1a. The remaining directories: (1) Initial-Optimized-Geometries – ADF optimization input files and optimized structures for all gold-hydride nanoclusters; (2) Training – All files related to the training process; and (3) Testing – all files related to the testing procedures, are available on GitHub at https://github.com/sulalith99/gold-hydride-nanoclusters-MLFF.git.

The *Training/* directory contains three subdirectories: (1) Starting-Files-For-OTF – initial files for on-the-fly (active learning) training, including POSCAR files (initial geometries) and *otf_train.yaml* (FLARE++ configuration file); (2) Starting-Files-For-OTC: initial files for offline (passive learning) training, including *offline.yaml* (FLARE++ input) and *all_otf_dft.xyz* (training databases with geometries and corresponding labels) for each training cycles; and (3) Databases – individual training databases used or generated during each training cycle.

The *Testing/* directory contains two subdirectories: (1) LAMMPS-Testing – input files for MLFF-based MD simulations, including *lammps.in* (LAMMPS input script) and initial structure files. Note that LAMMPS simulations also require the three MLFF model files (*lmp.flare*, *L_inv_lmp.flare*, and *sparse_desc_lmp.flare*) to be preset in the same directory. This subdirectory also includes representative output files: *log.lammps* (MLFF predicted energies at each timestep) and *output.dump* (trajectory coordinates, which can be visualized and analyzed using OVITO software package); and (2) VASP-Testing – DFT calculation inputs including INCAR, KPOINTS and POTCAR files. To run VASP calculations on trajectory snapshots, POSCAR files must be extracted from the LAMMPS *output.dump* files.

Together, these materials ensure reproducibility of our results and provide a computational framework adaptable to other ligand-protected metal nanocluster systems.

5.7 Appendix C – Supporting Information

Appendix C provides additional details on hyperparameters, $Au_{13}H_5$ conformer energetics, MAD and RMSE calculations, pre-atom energy prediction accuracy for structures outside the training set, R^2 values for the per atom prediction accuracy, and extended structural landscape analysis.

5.8 Acknowledgments

D.S.N.D.S. would like to thank Jonathan Bvunzawabaya for the helpful discussions during this project. The computing for this work was performed on the Beocat Research Cluster at Kansas State University, which is funded in part by NSF grants CHE-1726332, CNS-1006860, EPS-1006860, and EPS-0919443. The authors thank Kansas State University for support of this research.

5.9 References

1. Du, B.; Jiang, X.; Das, A.; Zhou, Q.; Yu, M.; Jin, R.; Zheng, J. Glomerular Barrier Behaves as an Atomically Precise Bandpass Filter in a Sub-Nanometre Regime. *Nature Nanotech* **2017**, *12* (11), 1096–1102.

2. Galchenko, M.; Black, A.; Heymann, L.; Klinke, C. Field Effect and Photoconduction in Au_{25} Nanoclusters Films. *Adv. Mater.* **2019**, *31* (18), 1900684.

3. Zhang, L.; Wang, E. Metal Nanoclusters: New Fluorescent Probes for Sensors and Bioimaging. *Nano Today* **2014**, *9* (1), 132–157.

4. Yuan, X.; Zhu, M. Recent Advances in Atomically Precise Metal Nanoclusters for Electrocatalytic Applications. *Inorg. Chem. Front.* **2023**, *10* (14), 3995–4007.

5. Liu, Z.; Luo, L.; Jin, R. Visible to NIR-II Photoluminescence of Atomically Precise Gold Nanoclusters. *Advanced Materials* **2024**, *36* (8), 2309073.

6. Sun, C.; Teo, B. K.; Deng, C.; Lin, J.; Luo, G.-G.; Tung, C.-H.; Sun, D. Hydrido-Coinage-Metal Clusters: Rational Design, Synthetic Protocols and Structural Characteristics. *Coord. Chem. Rev.* **2021**, *427*, 213576.

7. Cesari, C.; Femoni, C.; Forti, F.; Carmela Iapalucci, M.; Scorzoni, G.; Zacchini, S. Molecular Hydride Carbonyl Clusters and Nanoclusters. *Inorg. Chim. Acta* **2025**, *574*, 122394.

8. Sun, C.; Mammen, N.; Kaappa, S.; Yuan, P.; Deng, G.; Zhao, C.; Yan, J.; Malola, S.; Honkala, K.; Häkkinen, H.; Teo, B. K.; Zheng, N. Atomically Precise, Thiolated Copper–Hydride Nanoclusters as Single-Site Hydrogenation Catalysts for Ketones in Mild Conditions. *ACS Nano* **2019**, *13* (5), 5975–5986.

9. Brocha Silalahi, R. P.; Liang, H.; Jo, Y.; Liao, J.; Chiu, T.; Wu, Y.; Wang, X.; Kahlal, S.; Wang, Q.; Choi, W.; Lee, D.; Saillard, J.; Liu, C. W. Hydride-Containing Pt-doped Cu-rich Nanoclusters: Synthesis, Structure, and Electrocatalytic Hydrogen Evolution. *Chem. Eur. J.* **2024**, *30* (13), e202303755.

10. Dhayal, R. S.; Van Zyl, W. E.; Liu, C. W. Polyhydrido Copper Clusters: Synthetic Advances, Structural Diversity, and Nanocluster-to-Nanoparticle Conversion. *Acc. Chem. Res.* **2016**, *49* (1), 86–95.

11. Liu, S.; Eberhart, M. S.; Norton, J. R.; Yin, X.; Neary, M. C.; Paley, D. W. Cationic Copper Hydride Clusters Arising from Oxidation of $(Ph_3P)_6Cu_6H_6$. *J. Am. Chem. Soc.* **2017**, *139* (23), 7685–7688.

12. Bezman, S. A.; Churchill, M. R.; Osborn, J. A.; Wormald, J. Preparation and Crystallographic Characterization of a Hexameric Triphenylphosphinecopper Hydride Cluster. *J. Am. Chem. Soc.* **1971**, *93* (8), 2063–2065.

13. Kanters, R. P. F.; Bour, J. J.; Schlebos, P. P. J.; Bosman, W. P.; Behm, H.; Steggerda, J. J.; Ito, L. N.; Pignolet, L. H. Structure and Properties of the Hydride-Containing Cluster Ion Hydrido(Triphenylphosphine)Heptakis[(Triphenylphosphine)Gold]Platinum(2+). *Inorg. Chem.* **1989**, *28* (13), 2591–2594.

14. Takano, S.; Hirai, H.; Muramatsu, S.; Tsukuda, T. Hydride-Mediated Controlled Growth of a Bimetallic $(Pd@Au_8)^{2+}$ Superatom to a Hydride-Doped $(HPd@Au_{10})^{3+}$ Superatom. *J. Am. Chem. Soc.* **2018**, *140* (39), 12314–12317.

15. Chen, A.; Kang, X.; Jin, S.; Du, W.; Wang, S.; Zhu, M. Gram-Scale Preparation of Stable Hydride $M@Cu_{24}$ (M = Au/Cu) Nanoclusters. *J. Phys. Chem. Lett.* **2019**, *10* (20), 6124–6128.

16. Sil, D.; Lane, C.; Glor, E.; Gilroy, K. D.; Sylla, S.; Barbiellini, B.; Markiewicz, R.; Hajfathalian, M.; Neretina, S.; Bansil, A.; Fakhraai, Z.; Borguet, E. Synthesis and Properties of Au Hydride. *ChemistrySelect* **2019**, *4* (14), 4287–4292.

17. Wang, X.; Andrews, L. Infrared Spectra and DFT Calculations for the Gold Hydrides AuH, $(H_2)AuH$, and the AuH_3 Transition State Stabilized in $(H_2)AuH_3$. *J. Phys. Chem. A* **2002**, *106* (15), 3744–3748.

18. Giangregorio, M. M.; Losurdo, M.; Bianco, G. V.; Operamolla, A.; Dilonardo, E.; Sacchetti, A.; Capezzuto, P.; Babudri, F.; Bruno, G. Insight into Gold Nanoparticle–Hydrogen Interaction: A Way To Tailor Nanoparticle Surface Charge and Self-Assembled Monolayer Chemisorption. *J. Phys. Chem. C* **2011**, *115* (40), 19520–19528.

19. Ishida, R.; Yamazoe, S.; Koyasu, K.; Tsukuda, T. Repeated Appearance and Disappearance of Localized Surface Plasmon Resonance in 1.2 nm Gold Clusters Induced by Adsorption and Desorption of Hydrogen Atoms. *Nanoscale* **2016**, *8* (5), 2544–2547.

20. Mukherjee, S.; Libisch, F.; Large, N.; Neumann, O.; Brown, L. V.; Cheng, J.; Lassiter, J. B.; Carter, E. A.; Nordlander, P.; Halas, N. J. Hot Electrons Do the Impossible: Plasmon-Induced Dissociation of H_2 on Au. *Nano Lett.* **2013**, *13* (1), 240–247.

21. Oliveira, R. L.; Zanchet, D.; Kiyohara, P. K.; Rossi, L. M. On the Stabilization of Gold Nanoparticles over Silica-Based Magnetic Supports Modified with Organosilanes. *Chem. Eur. J.* **2011**, *17* (16), 4626–4631.

22. Wang, Q.; Nassereddine, A.; Loffreda, D.; Ricolleau, C.; Alloyeau, D.; Louis, C.; Delannoy, L.; Nelayah, J.; Guesmi, H. Cu Segregation in Au–Cu Nanoparticles Exposed to Hydrogen Atmospheric Pressure: How Is Fcc Symmetry Maintained? *Faraday Discuss.* **2023**, *242*, 375–388.

23. Li, Y.; Song, Y.; Zhang, X.; Liu, T.; Xu, T.; Wang, H.; Jiang, D.; Jin, R. Atomically Precise Au_{42} Nanorods with Longitudinal Excitons for an Intense Photothermal Effect. *J. Am. Chem. Soc.* **2022**, *144* (27), 12381–12389.

24. Patty, J. B.; Havenridge, S.; Tietje-Mckinney, D.; Siegler, M. A.; Singh, K. K.; Hajy Hosseini, R.; Ghabin, M.; Aikens, C. M.; Das, A. Crystal Structure and Optical Properties of a Chiral Mixed Thiolate/Stibine-Protected Au_{18} Cluster. *J. Am. Chem. Soc.* **2022**, *144* (1), 478–484.

25. Truttmann, V.; Loxha, A.; Banu, R.; Pittenauer, E.; Malola, S.; Matus, M. F.; Wang, Y.; Ploetz, E. A.; Rupprechter, G.; Bürgi, T.; Häkkinen, H.; Aikens, C.; Barrabés, N. Directing Intrinsic Chirality in Gold Nanoclusters: Preferential Formation of Stable Enantiopure Clusters in High Yield and Experimentally Unveiling the "Super" Chirality of Au_{144}. *ACS Nano* **2023**, *17* (20), 20376–20386.

26. Seal, N.; Samarasinghe, D. S. N. D.; Vodnala, N.; Siegler, M. A.; Aikens, C. M.; Das, A. Distibine versus Diphosphine Ligands: Modulating the Properties of Isostructural $Au_{13}Cu_2$ Nanoclusters. *Chem. Mater.* **2025**, *37* (24), 9908–9918.

27. Monti, M.; Brancolini, G.; Coccia, E.; Toffoli, D.; Fortunelli, A.; Corni, S.; Aschi, M.; Stener, M. The Conformational Dynamics of the Ligands Determines the Electronic Circular Dichroism of the Chiral Au_{38} $(SC_2H_4Ph)_{24}$ Cluster. *J. Phys. Chem. Lett.* **2023**, *14* (7), 1941–1948.

28. Juarez-Mosqueda, R.; Malola, S.; Häkkinen, H. Ab Initio Molecular Dynamics Studies of Au38(SR)24 Isomers under Heating. *Eur. Phys. J. D* **2019**, *73* (3), 62.

29. Sabooni Asre Hazer, M.; Malola, S.; Häkkinen, H. Isomer Dynamics of the $[Au_6(NHC\text{-}S)_4]^{2+}$ Nanocluster. *Chem. Commun.* **2022**, *58* (19), 3218–3221.

30. Guberman-Pfeffer, M. J.; Ulcickas, J.; Gascón, J. A. Connectivity-Based Biocompatible Force Field for Thiolated Gold Nanoclusters. *J. Phys. Chem. C* **2015**, *119* (49), 27804–27812.

31. Pohjolainen, E.; Chen, X.; Malola, S.; Groenhof, G.; Häkkinen, H. A Unified AMBER-Compatible Molecular Mechanics Force Field for Thiolate-Protected Gold Nanoclusters. *J. Chem. Theory Comput.* **2016**, *12* (3), 1342–1350.

32. Jäger, M. O. J.; Morooka, E. V.; Federici Canova, F.; Himanen, L.; Foster, A. S. Machine Learning Hydrogen Adsorption on Nanoclusters through Structural Descriptors. *npj Comput. Mater.* **2018**, *4* (1), 37.

33. Vandermause, J.; Xie, Y.; Lim, J. S.; Owen, C. J.; Kozinsky, B. Active Learning of Reactive Bayesian Force Fields Applied to Heterogeneous Catalysis Dynamics of H/Pt. *Nat. Commun.* **2022**, *13* (1), 5183.

34. Pihlajamäki, A.; Hämäläinen, J.; Linja, J.; Nieminen, P.; Malola, S.; Kärkkäinen, T.; Häkkinen, H. Monte Carlo Simulations of $Au_{38}(SCH_3)_{24}$ Nanocluster Using Distance-Based Machine Learning Methods. *J. Phys. Chem. A* **2020**, *124* (23), 4827–4836.

35. Wang, Y.; Samarasinghe, D. S. N. D.; Deng, H.; Liu, B.; Aikens, C. M. Gaussian Process Approach to Constructing Transferable Force Fields for Thiolate-Protected Gold Nanoclusters. *J. Chem. Inf. Model.* **2025**, *65* (8), 3892–3902.

36. McCandler, C. A.; Pihlajamäki, A.; Malola, S.; Häkkinen, H.; Persson, K. A. Gold–Thiolate Nanocluster Dynamics and Intercluster Reactions Enabled by a Machine Learned Interatomic Potential. *ACS Nano* **2024**, *18* (29), 19014–19023.

37. Fang, L.; Laakso, J.; Rinke, P.; Chen, X. Machine-Learning Accelerated Structure Search for Ligand-Protected Clusters. *J. Chem. Phys.* **2024**, *160* (9), 094106.

38. Titsias, M. K. New Bounds for Sparse Variational Gaussian Processes. arXiv June 26, 2025.

39. Rochussen, T.; Fortuin, V. Sparse Gaussian Neural Processes. arXiv April 24, 2025.

40. Vandermause, J.; Torrisi, S. B.; Batzner, S.; Xie, Y.; Sun, L.; Kolpak, A. M.; Kozinsky, B. On-the-Fly Active Learning of Interpretable Bayesian Force Fields for Atomistic Rare Events. *npj Comput. Mater.* **2020**, *6* (1), 20.

41. Drautz, R. Atomic Cluster Expansion for Accurate and Transferable Interatomic Potentials. *Phys. Rev. B* **2019**, *99* (1), 014104.

42. Hafner, J.; Kresse, G. The Vienna AB-Initio Simulation Program VASP: An Efficient and Versatile Tool for Studying the Structural, Dynamic, and Electronic Properties of Materials. In *Properties of Complex Inorganic Solids*; Gonis, A., Meike, A., Turchi, P. E. A., Eds.; Springer US: Boston, MA, 1997; pp 69–82.

43. Perdew, J. P.; Burke, K.; Ernzerhof, M. Generalized Gradient Approximation Made Simple. *Phys. Rev. Lett.* **1996**, *77* (18), 3865–3868.

44. Kresse, G.; Furthmüller, J. Efficiency of Ab-Initio Total Energy Calculations for Metals and Semiconductors Using a Plane-Wave Basis Set. *Comput. Mater. Sci.* **1996**, *6* (1), 15–50.

45. Kresse, G.; Furthmüller, J. Efficient Iterative Schemes for *Ab Initio* Total-Energy Calculations Using a Plane-Wave Basis Set. *Phys. Rev. B* **1996**, *54* (16), 11169–11186.

46. Kuda-Singappulige, G. U.; Aikens, C. M. Geometrical and Electronic Structure, Stability, and Optical Absorption Spectra Comparisons between Thiolate- and Chloride-Stabilized Gold Nanoclusters. *J. Phys. Chem. A* **2019**, *123* (45), 9712–9720.

47. Kong, J.; Zhang, W.; Wu, Y.; Zhou, M. Optical Properties of Gold Nanoclusters Constructed from Au_{13} Units: Special Issue: Emerging Investigators. *Aggregate* **2022**, *3* (6), e207.

48. Becke, A. D. Density-Functional Exchange-Energy Approximation with Correct Asymptotic Behavior. *Phys. Rev. A* **1988**, *38* (6), 3098–3100.

49. Perdew, J. P. Density-Functional Approximation for the Correlation Energy of the Inhomogeneous Electron Gas. *Phys. Rev. B* **1986**, *33* (12), 8822–8824.

50. Te Velde, G.; Bickelhaupt, F. M.; Baerends, E. J.; Fonseca Guerra, C.; Van Gisbergen, S. J. A.; Snijders, J. G.; Ziegler, T. Chemistry with ADF. *J. Comput. Chem.* **2001**, *22* (9), 931–967.

51. *ADF2021, SCM. Theoretical Chemistry; Vrije Universities*. http://www.scm.com (accessed 2026-02-27).

52. Thompson, A. P.; Aktulga, H. M.; Berger, R.; Bolintineanu, D. S.; Brown, W. M.; Crozier, P. S.; In 'T Veld, P. J.; Kohlmeyer, A.; Moore, S. G.; Nguyen, T. D.; Shan, R.; Stevens, M. J.; Tranchida, J.; Trott, C.; Plimpton, S. J. LAMMPS - a Flexible Simulation Tool for Particle-Based Materials Modeling at the Atomic, Meso, and Continuum Scales. *Comput. Phys. Commun.* **2022**, *271*, 108171.

53. Nosé, S. Constant Temperature Molecular Dynamics Methods. *Prog. Theor. Phys. Suppl.* **1991**, *103*, 1–46.

54. Nosé, S. A Unified Formulation of the Constant Temperature Molecular Dynamics Methods. *J. Chem. Phys.* **1984**, *81* (1), 511–519.

55. Hoover, W. G. Canonical Dynamics: Equilibrium Phase-Space Distributions. *Phys. Rev. A* **1985**, *31* (3), 1695–1697.

56. Kabsch, W. A Solution for the Best Rotation to Relate Two Sets of Vectors. *Acta. Cryst. A* **1976**, *32* (5), 922–923.

Chapter 6 - Implementation of analytical excited state gradients for open-shell systems in time-dependent density functional theory plus tight binding (TDDFT+TB) method

Reprinted with permission from *J. Chem. Phys.* of API Publishing, accepted for publication.

Unpublished work copyright 2026

D. Sulalith N. D. Samarasinghe[†], Shana Havenridge[†], Christine M. Aikens[†*]

[†] Department of Chemistry, Kansas State University, Manhattan, KS 66506, United States

*Email: cmaikens@ksu.edu

6.1 Abstract

Excited state potential energy surfaces are essential for understanding molecular behavior in excited states, including electronic transitions, reaction dynamics, and other photochemical and photophysical properties. When excited state minima or reaction dynamics are of interest, the gradients of the total excited state energy are required. Time-dependent density functional theory (TDDFT) is a widely used method as it provides reasonably accurate excited state energies compared to experiment; however, its computational cost scales unfavorably with molecule size. To address this limitation, methods that maintain TDDFT accuracy while reducing the computational cost are needed. The time-dependent density functional theory plus tight binding (TDDFT+TB) method offers comparable accuracy to TDDFT with significantly improved efficiency. Previously, Havenridge et al. implemented TDDFT+TB analytical excited state gradients for closed-shell molecules. This was achieved using a Lagrangian-based approach by taking analytical derivatives of the excitation energies with respect to nuclear coordinates. In this study, we extend this implementation to handle open-shell molecular systems. Our

unrestricted TDDFT+TB analytical gradient implementation follows the framework of the unrestricted TDDFT analytical gradient code in the Amsterdam Density Functional engine within the Amsterdam Modeling Suite. Building on the existing closed-shell implementation, we focus on key modifications to the coupling matrix and the incorporation of spin indices in the gradient expressions required for open-shell systems. We validate the method through calculations on various molecular systems, comparing gradient accuracy, emission energies, and computational cost to demonstrate that it delivers reliable results for open-shell molecular excited states with improved efficiency compared to the standard TDDFT method.

6.2 Introduction

Similar to ground state potential energy surface (PES) analysis, physical insights into molecular properties and reactivity in excited states can be determined at stationary points on their excited state surface (i.e., excited state geometries, transition states, and emission energies) or from dynamics on these surfaces.[1] Therefore, understanding excited state PESs is essential for numerous applications, including the enhancement of photocatalytic performance,[2,3] the design of optoelectronic devices,[4,5] the elucidation of biochemical processes,[6] and the interpretation of spectroscopic measurements.[7]

Experimental characterization of the PESs is limited to simple systems, essentially diatomic molecules and single internal modes in small polyatomic molecules.[1,8,9] Therefore, theoretical and computational chemistry has emerged as an essential tool for mapping these complex energy landscapes. Among the various methods developed over time, accuracy and computational efficiency can vary significantly between approaches. The selection of an appropriate method depends on the specific requirements of the system of interest and the

desired balance between computational cost and accuracy. Among these numerous methods, time-dependent density functional theory (TDDFT) has emerged as one of the most popular approaches for investigating excited state PESs. This method has been extensively used to investigate the excited state optimized geometries, optical properties, molecular orbital distribution, etc., for molecular systems.[10-18] It is important to note that benchmark studies comparing TDDFT excitation energies with experimental absorption data for molecular chromophores have consistently demonstrated accuracies within 0.3 - 0.5 eV.[19,20] This performance has been observed across various density functionals, including pure, hybrid, and range-separated functionals, when benchmarked against both experimental measurements and correlated ab initio methods.[19,20] However, a major limitation of TDDFT is its computational cost, which scales significantly with system size and the level of theory employed in the calculations. For example, even with the same level of theory, the computational cost of TDDFT is exponentially higher for nanoclusters (e.g., thiolate protected Au/Cd nanoclusters[10]) compared to smaller systems such as diatomic molecules. This has motivated the investigation of alternative approaches that are less computationally expensive than TDDFT. Consequently, time-dependent density functional theory based tight binding (TDDFTB) was developed.[21-23] This method is built upon the density functional tight-binding (DFTB) approach,[24-27] which serves as an approximation to the traditional density functional theory (DFT). As expected, TDDFTB can calculate excited state energies at a significantly reduced computational cost compared to TDDFT. Therefore, this method is well suited for systems that are computationally expensive for TDDFT calculations[28-32] such as nanoclusters.[31-33] However, there are major limitations associated with TDDFTB usage. The reduced computational cost comes at the expense of accuracy, as TDDFTB relies on the approximate ground state electronic structure from DFTB

rather than full DFT calculations. Additionally, the applicability of the method is constrained by the limited availability and quality of the parameterization for the elements and element combinations in the system.[34-36] Therefore, previous studies have demonstrated that while TDDFTB is considerably faster than TDDFT, the calculated excitation energies can exhibit considerable deviations from the corresponding TDDFT results.[30,31]

Building upon these insights, Grimme et al. developed the simplified time-dependent density functional theory (sTDDFT) and simplified Tamm-Dancoff approximation (sTDA) methods[37-39] that incorporate full DFT for the ground state calculations and TDDFTB-style approximations for the excited states. Subsequently, Rüger et al. introduced another approximation method known as time-dependent density functional theory plus tight binding (TDDFT+TB).[35] Notably, both sTDDFT and sTDA methods require hybrid exchange-correlation functionals, while TDDFT+TB can be employed with pure exchange-correlation functionals, which are computationally more efficient than hybrid functionals. The TDDFT+TB method has shown the ability to reproduce TDDFT excitation energies with errors within 0.15 eV with just one tenth of the total time required by TDDFT, while comparatively larger errors of 1.0 eV are observed with TDDFTB.[31] This substantial improvement in the TDDFT+TB method can be attributed to two key factors: (1) the use of full DFT for the ground state, which improves the accuracy compared to TDDFTB, and (2) the introduction of approximations in the computational bottleneck of TDDFT calculations by applying a first-order monopole approximation to the transition density in the linear response approach.[35,36] Beyond TDDFTB based approaches, other approximate TDDFT methods have been developed based on minimal auxiliary basis sets. The time-dependent density functional theory with minimal auxiliary basis model (TDDFT-as) employs a single s-type Gaussian auxiliary function per atoms and was initially formulated for

pure functionals.[40] This approach was subsequently extended to hybrid functionals, resulting in the time-dependent density functional theory with resolution of identity method (TDDFT-ris).[41,42] Both variants serve as computationally efficient approximations to standard TDDFT calculations.

Up to this point, the novel TDDFT+TB method has been shown to be a useful approach that can investigate excited state energies, particularly for larger molecular systems.[10,30,31] In 2023, Havenridge et al.[36] extended the method to obtain analytical excited state gradients, enabling the determination of optimized geometries in excited states and thereby facilitating more efficient exploration of excited state PESs. Importantly, this implementation was conducted for closed-shell molecular systems. Therefore, in this study, we extend the method developed by Havenridge et al.[36] to apply to open-shell molecules. A Lagrangian-based approach is employed for the gradient derivation. Notably, this implementation incorporates an additional dimension for the spin component, following the framework of TDDFT analytical excited state gradient methodology, while introducing necessary modifications to the coupling matrix. Following the approach established by Havenridge et al.,[36] this study will elaborate on: (1) the open-shell analytical excited state gradient derivation, (2) implementation in the Amsterdam Modeling Suite (AMS),[43] and (3) computational validation using various molecular systems to compare results with standard TDDFT calculations. These validations were conducted to assess both accuracy (via gradients and emission energies) and computational efficiency (via total calculation time) of the new analytical excited state gradient implementation for open-shell systems in TDDFT+TB with the standard TDDFT method.

6.3 Theory

To characterize excited state properties, a robust technique for exploring the excited state PESs is required. For example, analytical excited state gradients are used to find stationary points, where the energy gradient is zero, which represent potentially emissive molecular species. Hence, these gradients must be derived for excited state PESs. In 2002, Furche and Ahlrichs introduced a Lagrangian-based approach for deriving analytical excited state gradients in the TDDFT method by taking the derivative of the excitation energy expression.[44] This approach was later adapted by Havenridge et al.[36] to obtain analytical excited state gradients in the TDDFT+TB method for closed-shell molecular systems. For the extension of this method to open-shell systems, our approach begins by deriving the expression for TDDFT+TB vertical excitation energies with respect to nuclear coordinates. Subsequently, we introduce the Lagrangian approach to overcome the costly derivative of the expression obtained at the first step and solve for the Lagrange multipliers. Finally, the complete derivative of the TDDFT+TB excitation energy expression with respect to nuclear coordinates is obtained.

6.3.1 Excited state properties

The vertical excitation energies of TDDFT+TB can be expressed using a variational approach (Eq. (6.1)).[36] The excited state energies (Ω) correspond to the stationary points of the functional,

$$G[X,Y,\Omega] = \frac{1}{2}\left\langle \begin{matrix} X+Y \\ X-Y \end{matrix} \middle| \Lambda \middle| \begin{matrix} X+Y \\ X-Y \end{matrix} \right\rangle - \frac{1}{2}\Omega\left(\left\langle \begin{matrix} X+Y \\ X-Y \end{matrix} \middle| \Delta \middle| \begin{matrix} X+Y \\ X-Y \end{matrix} \right\rangle - 2\right) \tag{6.1}$$

Transition density vectors of single particle transitions are represented as X and Y in the Hilbert space $N_{virt} \times N_{occ} \oplus N_{occ} \times N_{virt}$, where N_{occ} denotes the Hilbert space of occupied molecular orbitals and N_{virt} denotes the Hilbert space of virtual molecular orbitals. These molecular

orbitals ($\phi_{p\sigma}(\boldsymbol{r})$) arise from solving the static Kohn-Sham (KS) equations, with their respective orbital energies, $\varepsilon_{p\sigma}$.[44-46] In this work, $p, q, ...$ denote general molecular orbitals, which can be either (1) occupied molecular orbitals in the ground state, denoted by $i, j, ...$, or (2) unoccupied molecular orbitals in the ground state, denoted by $a, b, ...$ Furthermore, different atoms are denoted by $A, B, ...$, while their atomic basis functions are denoted as $\mu, \nu, ...$ In the previous analytical excited state gradient implementation for TDDFT+TB,[36] spin indices were neglected as only singlet ground state systems were considered. In contrast, the current study considers spin, as it needs to treat doublet, triplet, and other multiplet ground state electronic configurations. Therefore, spin is denoted by σ and σ', which may represent a or b spin, while the angular momentum is denoted by l and l'.

The super-operators in Eq. (6.1) can be elaborated as follows: $\Lambda = \begin{pmatrix} A+B & 0 \\ 0 & A-B \end{pmatrix}$ and $\Delta = \begin{pmatrix} 0 & 1 \\ 1 & 0 \end{pmatrix}$, where A and B are the Hessians of orbital rotation. Solving Eq. (6.1) requires evaluating both $A+B$ and $A-B$ matrices (for pure functionals):[44]

$$(A+B)_{ia\sigma,jb\sigma'} = \left(\epsilon_{a\sigma} - \epsilon_{j\sigma}\right)\delta_{ij}\delta_{ab}\delta_{\sigma\sigma'} + 2(ia\sigma|jb\sigma') + 2\left(ia|f^{xc}_{\sigma\sigma'}|jb\right) \tag{6.2}$$

$$(A-B)_{ia\sigma,jb\sigma'} = \left(\epsilon_{a\sigma} - \epsilon_{j\sigma}\right)\delta_{ij}\delta_{ab}\delta_{\sigma\sigma'} \tag{6.3}$$

The TDDFT+TB approach tackles the bottleneck of computing the two-electron integrals, i.e., $(ia\sigma|jb\sigma')$ and $\left(ia|f^{xc}_{\sigma\sigma'}|jb\right)$ (see Appendix D for formulas) in the linear response TDDFT formalism via a monopole approximation.[21,22,35] Therefore, rather than computing the integrals in Eq. (6.2) explicitly, the transition densities are approximated as $\phi_{i\sigma}(\boldsymbol{r})\phi_{a\sigma}(\boldsymbol{r}) \approx \sum_{Al} q_{ia\sigma,Al}\zeta_{Al}(\boldsymbol{r})$, where $q_{ia\sigma,Al}$ represents the atomic transition charges and $\zeta_{Al}(\boldsymbol{r})$ is a spherically symmetric function on atom A (see Appendix D). In TDDFT+TB, atomic transition

charges are evaluated through a Löwdin population analysis instead of a Mulliken analysis.[35,36,47] Once these changes are applied to Eq. (6.2), it will have the following form:

$$(A+B)_{ia\sigma,jb\sigma'} = \left(\epsilon_{a\sigma} - \epsilon_{j\sigma}\right)\delta_{ij}\delta_{ab}\delta_{\sigma\sigma'} + 4K_{ia\sigma,jb\sigma'} \tag{6.4}$$

where $K_{ia\sigma,jb\sigma'} = \sum_{ABll'}\left[q_{ia\sigma,Al}\gamma_{Al,Bl'}q_{jb\sigma',Bl'} + q_{ia\sigma,Al}\delta_{\sigma}\delta_{\sigma'}\delta_{AB}W_{Al,l'}q_{jb\sigma',Bl'}\right]$ represents the modified coupling matrix term that now accounts for spin, and $\delta_{\sigma} = 2\delta_{\uparrow\sigma} - 1$ determines the sign of the function.[21,22] The gamma function ($\gamma_{Al,Bl'}$) is determined by the chemical hardness and interatomic distance between atoms *A* and *B*, whereas $W_{Al,l'}$ refers to the magnetic Hubbard parameter.[21,22,35,36,48] It is important to note that the magnetic Hubbard parameter becomes particularly significant for open-shell systems, where it enters as a second-order energy contribution controlling the charge populations and spin polarization on each atom or shell.[48] Therefore, the coupling matrix term can also take the form, $K_{ia\sigma,jb\sigma'} = K^{S}_{ia\sigma,jb\sigma'} + K^{T}_{ia\sigma,jb\sigma'}$, where the superscripts *S* and *T* are used historically to indicate singlet and triplet excitations, respectively. Here, $K^{S}_{ia\sigma,jb\sigma'}$ is applicable for the closed-shell systems, while $K^{T}_{ia\sigma,jb\sigma'}$ is also included for open-shell systems (not only triplet states). Notably, both the chemical hardness and magnetic Hubbard parameters are obtained from atomic DFT calculations. Within the new implementation, these parameters are retrieved directly from the preceding ground state DFT step rather than being recalculated. A step-by-step evolution of the TDDFT terms to the TDDFT+TB approach is provided in the Appendix D [Eq. (D.1)-(D.20)].

6.3.2 Derivative of the excitation energy

Taking the derivative of Eq. (6.1) is the primary computational challenge in this work because calculating the derivatives of the molecular orbital coefficients at each geometric step is very costly. This issue has been previously tackled through the use of Lagrangian-based methods

in analytical excited state gradient derivations for TDDFT,[44] TDDFTB,[46] and restricted TDDFT+TB[36] methods. Following these established approaches, we introduce canonical KS molecular orbitals as a constraint, exploiting the fact that all physical properties remain invariant under unitary transformations of molecular orbitals. This constraint thereby maintains the invariance of the excited state formalism with respect to these transformations.[44] In the basis of canonical KS molecular orbitals, the Fock operator ($F_{pq\sigma}$) and its eigenvalue entries ($\epsilon_{p\sigma}$) are diagonal. Therefore, the diagonal components of Eq. (6.3) and (6.4) can be replaced by $\left(F_{ab\sigma}\delta_{ij} - F_{ij\sigma}\delta_{ab}\right)\delta_{\sigma\sigma'}$,

$$(A+B)_{ia\sigma,jb\sigma'} = \left(F_{ab\sigma}\delta_{ij} - F_{ij\sigma}\delta_{ab}\right)\delta_{\sigma\sigma'} + 4K_{ia\sigma,jb\sigma'} \tag{6.5}$$

$$(A-B)_{ia\sigma,jb\sigma'} = \left(F_{ab\sigma}\delta_{ij} - F_{ij\sigma}\delta_{ab}\right)\delta_{\sigma\sigma'} \tag{6.6}$$

where $F_{pq\sigma}$ includes the core Hamiltonian ($h_{pq\sigma}$), Coulomb integrals ($pq\sigma|ii\sigma'$) and the exchange-correlation potential ($V_{pq\sigma}^{xc}$):

$$F_{pq\sigma} = h_{pq\sigma} + \sum_{i\sigma'}(pq\sigma|ii\sigma') + V_{pq\sigma}^{xc} \tag{6.7}$$

Therefore, an auxiliary function is defined, which equals the excitation energies and incorporates the molecular orbital constraints:

$$L[X,Y,\Omega,C,Z,W] = G[X,Y,\Omega] + \sum_{ia\sigma} Z_{ia\sigma}\,F_{ia\sigma} - \sum_{pq\sigma,p\leq q} W_{pq\sigma}\left(S_{pq\sigma} - \delta_{pq}\right) \tag{6.8}$$

Here, the Lagrangian L serves as a fully variational treatment of the excited state energy functional. Notably, the Lagrange multipliers Z and W are employed to constrain the molecular orbitals, and to be orthonormal, with the following restriction criteria: $\frac{\partial L}{\partial Z_{ia\sigma}} = F_{ia\sigma} = 0$ and $\frac{\partial L}{\partial W_{pq\sigma}} = S_{pq\sigma} - \delta_{pq} = 0$. Since these criteria fix the molecular orbital coefficients (C), determining the Lagrange multipliers (Z and W) requires an additional condition:

$$\frac{\partial L}{\partial C_{\mu p\sigma}} = 0 \tag{6.9}$$

We then proceed to determine the Lagrange multipliers with respect to the constraints. Consequently, to simplify $L[X, Y, \Omega, C, Z, W]$ into a more workable form, both sides are multiplied by the coefficient matrix ($C_{\mu q\sigma}$) and summed over μ via the relation given in Eq. (6.9), resulting in Eq. (6.10),[44]

$$Q_{pq\sigma} + \sum_{ia\sigma'} Z_{ia\sigma'} \sum_{\mu} \frac{\partial F_{ia\sigma'}}{\partial C_{\mu p\sigma}} C_{\mu q\sigma} = \sum_{rs\sigma', r\leq s} W_{rs\sigma'} \sum_{\mu} \frac{\partial S_{rs\sigma'}}{\partial C_{\mu p\sigma}} C_{\mu q\sigma} \tag{6.10}$$

where $Q_{pq\sigma}$ is,

$$Q_{pq\sigma} = \sum_{\mu} \frac{\partial G[X, Y, \Omega]}{\partial C_{\mu p\sigma}} C_{\mu q\sigma} \tag{6.11}$$

Notably, four distinct conditions emerge from the molecular orbital constraints for Z and for components of W: occupied-occupied, virtual-virtual, occupied-virtual, and virtual-occupied. To simplify these expressions, we utilize the unrelaxed difference density matrix T and the linear transformation definitions from TDDFT.[44] After applying these constraints, we obtain the expressions presented in Eq. (6.12) through (6.19). A complete derivation of the resulting equations is given in the Appendix D [Eq. (D.21-D.29)].

When p and q are both occupied, Eq. (6.10) transforms to:

$$Q_{ij\sigma} + H^{+}_{ij\sigma}[Z] = W_{ij\sigma} + W_{ij\sigma}\delta_{ij} \tag{6.12}$$

where,

$$Q_{ij\sigma} = \Omega \sum_{a} \{(X+Y)_{ia\sigma}(X-Y)_{ja\sigma} + (X-Y)_{ia\sigma}(X+Y)_{ja\sigma}\}$$

$$- \sum_{a} \varepsilon_{a\sigma} \{(X+Y)_{ia\sigma}(X+Y)_{ja\sigma} + (X-Y)_{ia\sigma}(X-Y)_{ja\sigma}\} + H^{+}_{ij\sigma}[T] \tag{6.13}$$

For p and q both virtual,

$$Q_{ab\sigma} = W_{ab\sigma} + W_{ab\sigma}\delta_{ab} \tag{6.14}$$

where,

$$Q_{ab\sigma} = \Omega \sum_{i} \{(X+Y)_{ia\sigma}(X-Y)_{ib\sigma} + (X-Y)_{ia\sigma}(X+Y)_{ib\sigma}\}$$

$$+ \sum_{i} \varepsilon_{i\sigma}\{(X+Y)_{ia\sigma}(X+Y)_{ib\sigma} + (X-Y)_{ia\sigma}(X-Y)_{ib\sigma}\} \tag{6.15}$$

For p occupied and q virtual,

$$Q_{ia\sigma} + \varepsilon_{a\sigma}Z_{ia\sigma} + H^{+}_{ia\sigma}[Z] = W_{ia\sigma} \tag{6.16}$$

where,

$$Q_{ia\sigma} = 2\sum_{b}(X+Y)_{ib\sigma}\sum_{jc\sigma'} K_{ab\sigma,jc\sigma'}\,(X+Y)_{jc\sigma} + H^{+}_{ia\sigma}[T] \tag{6.17}$$

For p virtual and q occupied,

$$Q_{ai\sigma} + \varepsilon_{i\sigma}Z_{ia\sigma} = W_{ia\sigma} \tag{6.18}$$

where,

$$Q_{ai\sigma} = 2\sum_{j}(X+Y)_{ja\sigma}\sum_{kb\sigma'} K_{ji\sigma,kb\sigma'}\,(X+Y)_{kb\sigma} \tag{6.19}$$

It is important to note that setting up an energy functional that is stationary with respect to the molecular orbital coefficients imposes the symmetry constraint relation of $W_{ia\sigma} = W_{ai\sigma}$.[36,44] We can exploit this relation to obtain an equation for Z:

$$-(Q_{ia\sigma} - Q_{ai\sigma}) = -R_{ia\sigma} = (\varepsilon_{a\sigma} - \varepsilon_{i\sigma})Z_{ia\sigma} + H^{+}_{ia\sigma}[Z] \tag{6.20}$$

Here, Eq. (6.20) resembles the Z vector equation, $-R_{ia\sigma} = \sum_{jb\sigma'}(A+B)^{TDDFT}_{ia\sigma,jb\sigma'}Z_{jb\sigma'}$, and therefore, solving this equation can yield the solution for the vector Z. Once the Z vector is known, we proceed to determine W. A detailed derivation is provided in the Appendix D [Eq. (D.30) to (D.39)].

For p and q both occupied,

$$W_{ij\sigma} = \frac{1}{1+\delta_{ij}}\Bigg(\Omega\sum_{a}\{(X+Y)_{ia\sigma}(X-Y)_{ja\sigma} + (X-Y)_{ia\sigma}(X+Y)_{ja\sigma}\}$$

$$-\sum_{a}\varepsilon_{a\sigma}\{(X+Y)_{ia\sigma}(X+Y)_{ja\sigma} + (X-Y)_{ia\sigma}(X-Y)_{ja\sigma}\} + H^{+}_{ij\sigma}[P]\Bigg) \tag{6.21}$$

When p and q are both virtual,

$$W_{ab\sigma} = \frac{1}{1+\delta_{ab}}\Bigg(\Omega\sum_{i}\{(X+Y)_{ia\sigma}(X-Y)_{ib\sigma} + (X-Y)_{ia\sigma}(X+Y)_{ib\sigma}\}$$

$$+\sum_{i}\varepsilon_{i\sigma}\{(X+Y)_{ia\sigma}(X+Y)_{ib\sigma} + (X-Y)_{ia\sigma}(X-Y)_{ib\sigma}\}\Bigg) \tag{6.22}$$

For p occupied and q virtual, as well as for p virtual and q occupied,

$$W_{ia\sigma} = W_{ai\sigma} = 2\sum_{j}(X+Y)_{ja\sigma}\sum_{kb\sigma'}K_{ji\sigma,kb\sigma'}\,(X+Y)_{kb\sigma} + \varepsilon_{i\sigma}Z_{ia\sigma} \tag{6.23}$$

After obtaining the Lagrange multipliers (Z and W), we evaluate the derivative of the auxiliary functional (L) with respect to the nuclear coordinates (R_A). We adopt the notation used by Furche et al.,[44] using superscript ξ to indicate the derivatives, i.e., $F^{\xi}_{ia\sigma} = \frac{dF_{ia\sigma}}{dR_A}$:

$$L^{\xi}[X,Y,\Omega,C,Z,W] = G^{\xi}[X,Y,\Omega] + \sum_{ia\sigma}Z_{ia\sigma}\,F^{\xi}_{ia\sigma} - \sum_{pq\sigma,p\leq q}W_{pq\sigma}\,S^{\xi}_{pq\sigma} \tag{6.24}$$

With the definitions established throughout this work, Eq. (6.24) can be rewritten as:

$$L^{\xi}[X,Y,\Omega,C,Z,W] = \sum_{pq\sigma}F^{\xi}_{pq\sigma}\,P_{pq\sigma} + 2\sum_{ia\sigma}\sum_{jb\sigma'}(X+Y)_{ia\sigma}\,K^{\xi}_{ia\sigma,jb\sigma'}(X+Y)_{jb\sigma'}$$

$$-\sum_{pq\sigma,p\leq q}W_{pq\sigma}\,S^{\xi}_{pq\sigma} \tag{6.25}$$

It should be noted that Eq. (6.25) resembles the form of the restricted TDDFT+TB gradient implementation.[36] The three terms represent, respectively, the Fock matrix derivative (excluding Hartree-Fock exchange), the coupling matrix derivative, and the contributions from the Lagrange multiplier W. A step-by-step derivation is provided in the Supporting Information [Eq. (D.40) to (D.53)], which presents the expanded derivative form of the coupling matrix. Therefore, the final form of the gradient can be given by:

$$
\begin{aligned}
&L^{\xi}[X, Y, \Omega, C, Z, W] \\
&\quad = \sum_{\mu \in A, \nu \notin A, \sigma} h^{\xi}_{\mu\nu\sigma} P_{\mu\nu\sigma} + \sum_{\mu\nu\sigma} \sum_{\kappa \in A, \lambda \notin A, \sigma'} (\mu\nu\sigma|\kappa\lambda\sigma')^{\xi} P_{\mu\nu\sigma} + \sum_{\mu \in A, \nu \notin A, \sigma} V^{xc\,\xi}_{\mu\nu\sigma} P_{\mu\nu\sigma} \\
&+2 \sum_{\mu \in A, \nu \notin A, \sigma} S^{1/2}_{\mu\nu\sigma} \left[S^{1/2}_{\mu\nu\sigma}\right]^{\xi} (\Xi_A + \Xi_B) U_{\mu\nu\sigma} + 4 \sum_{\mu \in A, \nu \notin A, \sigma} \gamma^{\xi}_{Al,Bl'} U_A U_B + \\
&\quad + \delta_{\sigma}\delta_{\sigma'} 2 \sum_{\mu \in A} S^{1/2}_{\mu\nu\sigma} \left[S^{1/2}_{\mu\nu\sigma}\right]^{\xi} \Theta_A U_{\mu\nu\sigma} - \sum_{\mu \in A, \nu \notin A, \sigma} W_{\mu\nu\sigma} S^{\xi}_{\mu\nu\sigma}
\end{aligned}
\tag{6.26}
$$

where the corresponding definitions for $U_{\mu\nu\sigma}$, U_A, Ξ_A, and Θ_A are shown in the Appendix D.

We have implemented the unrestricted TDDFT+TB excited state gradient code in the Amsterdam Modeling Suite (AMS).[43] Notably, this new implementation was built based on the existing unrestricted TDDFT analytical gradients in AMS.[44] Similar to the restricted TDDFT+TB analytical excited state gradients, the first three terms in Eq. (6.26) are identical to the corresponding terms of the TDDFT analytical excited state gradients, while the fourth, fifth, and seventh terms likewise reflect the restricted TDDFT+TB analytical excited state gradients. Since the restricted TDDFT+TB analytical excited state gradients[36] are already implemented in AMS, the new implementation introduces two key modifications: an updated coupling matrix (introducing the sixth term involving the magnetic Hubbard parameter) and the incorporation of spin indices into the gradient terms.

6.4 Computational approach

To validate the accuracy and efficiency of the TDDFT+TB analytical excited state gradient implementation for open-shell molecules, three approaches were employed: (1) analytical gradients were benchmarked against numerical gradients computed using finite difference methods; (2) excited state geometry optimizations were performed, with the resulting optimized excited state geometries and emission energies compared to those obtained from standard TDDFT calculations; and (3) computational efficiency was assessed by comparing the total runtime required for excited state geometry optimizations using both TDDFT and TDDFT+TB methods. The TDDFT+TB method represents an approximation to the conventional TDDFT; therefore, this study focuses on comparing these two computational approaches rather than validation against experimental data. All calculations were performed using a development version of the Amsterdam Density Functional (ADF) engine within the AMS.[43]

Validation of the new implementation was performed using a test set of 38 molecules: 9 open-shell diatomic molecules, 6 closed-shell diatomic molecules, and 23 open-shell organic radicals and charged species. These 23 organic molecules are derivatives of the Thiel test set,[49] which originally includes closed-shell molecules. Since our primary objective is to validate the performance of the new implementation for open-shell molecules, we identified the corresponding open-shell counterparts from the literature. For instance, naphthalene (a closed-shell molecule in the Thiel test set) was replaced by the naphthalene radical cation (an open-shell molecule). The resulting set of 23 molecules includes free radicals, radical cations, and radical anions. All relevant literature references for these open-shell species are listed in Table D.1 of the Appendix D. The validation results reported in the manuscript used the PW92/DZP level of

theory, where PW92[50] is a local density approximation (LDA) exchange-correlation functional with a double-ζ polarized (DZP) basis set. All the calculations were performed without considering symmetry, which is essential for TDDFT+TB calculations. Given that ADF employs numerical integrations on a grid-based system, the numerical integration quality was set to "Very Good" for all test cases (the Appendix D includes a detailed description of the numerical quality parameters). Since this study involved testing the new implementation, additional keywords must be specified in the input file, as discussed in detail in the Appendix D (Figure D.1). All calculations were executed on a single compute node using 6 cores to maintain consistency across the validation studies. Finally, mean absolute deviation (MAD) and root mean square (rms) values were calculated to determine the accuracy of each individual analysis. The equations used for these calculations are provided in Eq. (D.54) and (D.55) in the Appendix D.

To investigate the numerical vs. analytical excited state gradients, a finite difference calculation was performed to compute numerical gradients using a displacement of 0.001 Å, with the aid of the Python Library for Automating Molecular Simulations (PLAMS) code in ADF.[43,51] This approach systematically offsets the atom coordinates along the x, y, and z directions, and single point calculations were executed for each displaced geometry. Finally, it computes the numerical gradient as a $3N$ dimensional vector, where N represents the number of total atoms in the system. The analytical excited state gradient was calculated at the initial geometry (prior to displacements), and then deviations between analytical and numerical gradients were evaluated. Additionally, we investigated the effect of various displacement values on the numerical gradient calculations, as shown in Table D.2. It should be noted that at this stage we do not compute full excited state geometry optimization; rather, we are comparing the excited state gradient accuracy from a single geometric step on the excited state PES.

For the second and third validation approaches, complete excited state geometry optimizations were performed on each molecule. As this is a geometry optimization process, convergence criteria were specified using energy and gradient convergence criteria of 1×10^{-5} Hartree and 1×10^{-4} Hartree/Å for diatomic molecules and 1×10^{-5} Hartree and 1×10^{-3} Hartree/Å for polyatomic molecules, respectively. Comparisons of the emission energy and computational runtime were conducted between both unrestricted TDDFT+TB and TDDFT calculated results. Therefore, both calculations used completely identical input parameters, aside from selecting TDDFT+TB calculations by including the "TD-DFTB" keyword in the excitation block.

It is important to note that all the calculations presented in the manuscript employed a single level of theory (PW92/DZP with "Very Good" numerical quality) executed on 6-cores on a single processor performed on identical nodes. However, different exchange-correlation functionals, basis sets, numerical quality levels, and computational architectures can be incorporated into these calculations. To assess the robustness of our findings, we investigated the influence of these parameters by systematically varying exchange-correlation functionals, basis sets, numerical quality levels, and number of compute cores for both O_2 and pyrazine radical cation. A detailed analysis of these results is provided in Tables D.3 – D.6 in the Appendix D.

6.4.1 Numerical vs. analytical excited state gradient comparison

Initially, we compared numerical gradients computed at different geometries for each test molecule and assessed the deviation from the corresponding analytical gradient values. The comparison between numerical and analytical excited state gradients for the first excited state (D_1 or T_1 depending on the molecule) are reported in Table 6.1 for open-shell diatomic molecules and in Table 6.2 for open-shell organic radicals and charged species. The reported

MAD and rms values correspond to the differences between numerical and analytical excited state gradients across all atoms in all cartesian directions. Overall, these results demonstrate good agreement between numerical and analytical excited state gradients, with test cases exhibiting MAD values below 5.00×10^{-4} Hartree/Å, comparable to the accuracy previously achieved for restricted TDDFT+TB excited state gradients in closed-shell systems.[36] In our work, we demonstrate that the unrestricted TDDFT+TB method also exhibits similar accuracy for closed-shell molecules, as shown in Table D.7, mirroring the performance observed with open-shell systems.

Among these test molecules, the HHe molecule represents a notable case, as the optimized ground state geometry exhibited a large H-He bond distance of 4.85 Å, exceeding distances expected for covalent bonds (Table 6.1 provides the results for this structure). To assess this behavior, we evaluated the PESs of the HHe molecule for both the ground state (D_0) and first excited state (D_1) using TDDFT and TDDFT+TB methods (Figure D.2). The results reveal relatively shallow PESs, which often represents weak binding or minima that are not very stable kinetically. When the bond distance is fixed at a shorter distance (2.75 Å), comparatively larger MAD and rms values are obtained (4.65×10^{-5} Hartree/Å and 8.06×10^{-5} Hartree/Å, respectively). Similar observations for diatomic molecular systems have been previously reported by Havenridge et al.[36] and Wang et al.[47] It should be noted that the numerical gradient calculations are computed using finite difference methods, which can introduce numerical inaccuracies. Similar differences between numerical and analytical results for the existing unrestricted TDDFT gradients are also observed. Therefore, given the possible numerical errors in the finite difference calculations and the negligible differences observed between various

displacement values (Table D.2), these deviations fall within acceptable limits and do not compromise the overall accuracy of the approach.

Table 6.1. Numerical vs. analytical gradient differences for excited states (D_1/T_1) of open-shell diatomic molecules (Hartree/Å).

Molecule	State	MAD	rms
O_2	T_1	2.89×10^{-5}	5.01×10^{-5}
SO	T_1	1.64×10^{-5}	2.05×10^{-5}
S_2	T_1	5.17×10^{-6}	6.41×10^{-6}
NH (Imidogen)	T_1	2.13×10^{-5}	3.68×10^{-5}
NF	T_1	1.66×10^{-4}	2.88×10^{-4}
HHe	D_1	1.64×10^{-6}	2.82×10^{-6}
CN	D_1	1.07×10^{-4}	1.74×10^{-4}
BeH	D_1	2.58×10^{-7}	4.47×10^{-7}
BeF	D_1	1.71×10^{-5}	2.96×10^{-5}

Table 6.2. Numerical vs. analytical gradient differences for excited states (D_1/T_1) of small open-shell organic radical and charged species (Hartree/Å).

Molecule	State	MAD	rms
Acetyl free radical	D_1	3.50×10^{-5}	6.08×10^{-5}
Adenine radical cation	D_1	4.25×10^{-5}	6.29×10^{-5}
Benzyl free radical	D_1	2.41×10^{-5}	3.35×10^{-5}
p-benzoquinone radical anion	D_1	1.50×10^{-4}	4.57×10^{-4}
cis-Butadiene radical cation	D_1	3.04×10^{-5}	5.07×10^{-5}
trans-Butadiene radical cation	D_1	2.13×10^{-5}	3.12×10^{-5}

Cyclopentadienyl cation	T_1	3.64×10^{-5}	5.58×10^{-5}
Cyclopentadienyl free radical	D_1	3.80×10^{-5}	4.90×10^{-5}
Cyclopropene radical cation	D_1	2.80×10^{-5}	6.44×10^{-5}
2-dehydroimidazolyl free radical	D_1	4.25×10^{-5}	6.43×10^{-5}
4-dehydroimidazolyl free radical	D_1	4.19×10^{-5}	6.69×10^{-5}
5-dehydroimidazolyl free radical	D_1	4.22×10^{-5}	6.73×10^{-5}
Ethene radical cation	D_1	2.33×10^{-5}	4.52×10^{-5}
1-furanyl free radical	D_1	3.95×10^{-5}	6.95×10^{-5}
2-furanyl free radical	D_1	3.85×10^{-5}	6.74×10^{-5}
Formyl free radical	D_1	5.16×10^{-5}	9.00×10^{-5}
Naphthalene radical cation	D_1	1.77×10^{-4}	2.49×10^{-4}
Pyrazine radical cation	D_1	3.32×10^{-5}	5.31×10^{-5}
Pyridazine radical cation	D_1	3.13×10^{-5}	5.26×10^{-5}
Pyridine radical cation	D_1	2.85×10^{-5}	5.71×10^{-5}
Pyrimidine radical cation	D_1	3.66×10^{-5}	5.76×10^{-5}
Pyrrole radical cation	D_1	5.05×10^{-5}	7.57×10^{-5}
Tetrazine radical cation	D_1	5.84×10^{-5}	8.79×10^{-5}

6.4.2 Excited state geometry optimization

A main goal of this implementation is to enable geometry optimization of a specified excited state in order to accurately represent the optimized structures on the excited-state potential energy surface. Accordingly, excited state geometry optimizations were performed and emission energy differences between respective excited states were calculated for the TDDFT and TDDFT+TB methods (via $\Delta\text{E_Emission} = \text{E_Emission}_{\text{TDDFT}} - \text{E_Emission}_{\text{TDDFT+TB}}$). The comparative analysis includes open-shell diatomic molecules (in Table 6.3) and small open-shell organic radicals and charged species (in Table 6.4). As open-shell systems, the selected test cases include systems with ground-state doublet (D_0) and triplet (T_0) configurations. We initially aimed to analyze the respective first excited states; however, it was not possible with some states. Additionally, certain excited states failed to optimize during the geometry optimization, requiring analysis of states beyond the first excited state. This limitation is not an issue of the new implementation, and it affects both TDDFT and TDDFT+TB calculations equally. This can be due to conical intersections with the ground state, dissociative potential energy surfaces, or triplet instabilities.[36] Furthermore, open-shell systems are numerically more challenging to solve than closed-shell cases, leading to convergence issues that frequently caused geometry optimization failures during the testing phase. Moreover, unrestricted TDDFT is well established to exhibit substantial spin contamination for single transitions, arising from the incomplete excited-state configurational space. (Tables D.8 and D.9 reports the spin-contaminations observed across all testcases, along with a comparison of spin-contaminations of selected diatomic molecules against values reported in the literature, in Table D.10.) This spin-contamination likely carries over into the TDDFT+TB formalism and may be a contributing factor to the discrepancies noted herein.[22,52,53] For example, the D_1 excited state geometry

optimization of the pyridine radical cation failed to converge in both TDDFT and TDDFT+TB methods while the D_2 state successfully optimized in both approaches. Several other molecules exhibited similar behavior, requiring investigation of higher excited state PES. It should be noted that the cyclopentadienyl free radical exhibited the same issues across the excited states examined (D_1 to D_8). However, TDDFT+TB was able to obtain an optimized geometry only for the D_2 state. When this TDDFT+TB optimized D_2 state geometry was subsequently used as the initial coordinates for the TDDFT excited state geometry optimization, TDDFT was also able to converge to the optimized structure at the same excited state.

The emission energy differences between TDDFT and TDDFT+TB exhibit MAD and rms deviations of 0.085 eV and 0.125 eV, respectively, for the open-shell diatomic molecules, and 0.035 eV and 0.052 eV, respectively, for the small open-shell organic radicals and charged species. The emission energy deviations for diatomic molecules are notably higher than those observed for organic molecules. This trend has been previously reported by Havenridge et al.,[36] who attributed these deviations to approximations inherent in the coupling matrix. In general, the TDDFT+TB approach works better on polyatomic molecules than on diatomic molecules. Overall, the TDDFT+TB emission energies obtained through this implementation agree well with TDDFT results, with deviations typically within 0.10 eV. To assess the applicability of the computed excitation energies, Table D.11 presents a comparison of TDDFT+TB results against experimental values and previously reported higher-level theoretical data for selected test cases, demonstrating good overall agreement.

Table 6.3. Emission energy differences between TDDFT and TDDFT+TB for open-shell diatomic molecules.

Molecule	State	Energy difference (eV)
O_2	T_1	-0.05
SO	T_1	-0.01
S_2	T_1	0.00
NH (Imidogen)	T_1	0.01
NF	T_1	0.01
HHe	D_1	-0.15
CN	D_1	-0.06
BeH	D_1	0.10
BeF	D_1	0.32

Table 6.4. Emission energy differences between TDDFT and TDDFT+TB for open-shell small organic radical and charged species.

Molecule	State	Energy difference (eV)
Acetyl free radical	D_3	-0.05
Adenine radical cation	D_5	-0.02
Benzyl free radical	D_2	-0.07
p-Benzoquinone radical anion	D_1	0.02
cis-Butadiene radical cation	D_1	-0.03
trans-Butadiene radical cation	D_1	-0.02
Cyclopentadienyl cation	T_1	-0.08
Cyclopentadienyl free radical*	D_2	0.00

Cyclopropene radical cation	D_3	0.14
2-Dehydroimidazolyl free radical	D_1	-0.10
4-Dehydroimidazolyl free radical	D_1	-0.04
5-Dehydroimidazolyl free radical	D_2	0.01
Ethene radical cation	D_2	-0.05
1-Furanyl free radical	D_2	0.00
2-Furanyl free radical	D_2	-0.06
Formyl free radical	D_2	0.03
Naphthalene radical cation	D_1	0.00
Pyrazine radical cation	D_1	-0.01
Pyridazine radical cation	D_1	-0.01
Pyridine radical cation	D_2	-0.02
Pyrimidine radical cation	D_1	-0.01
Pyrrole radical cation	D_1	-0.08
Tetrazine radical cation	D_1	0.04

*TDDFT geometry optimization was started from the optimized TDDFT+TB D_2 state geometry.

6.4.3 Total runtime for excited state geometry optimization

The previous analysis demonstrates that analytical excited state gradients for open-shell systems in TDDFT+TB achieve accuracy comparable to TDDFT emission energies and calculated numerical gradients. In this section, we evaluate another critical aspect of TDDFT+TB performance: the computational efficiency of excited state geometry optimizations. A key advantage of TDDFT+TB is its ability to maintain TDDFT level accuracy while significantly

reducing the computational cost. Table 6.5 and Table 6.6 present the computational run times required for excited state geometry optimization using both TDDFT and TDDFT+TB methods for open-shell diatomic molecules and small open-shell organic radicals and charged species, respectively. The data also includes the number of optimization steps required to achieve a fully converged structure.

Overall, the results indicate that the TDDFT+TB method requires approximately one-third of the runtime needed for TDDFT calculations. It is important to note that diatomic molecules exhibit relatively short computational time even with TDDFT. However, as the system size increases, the computational cost differences become more pronounced. For example, the adenine radical cation required just over 1 hour to complete D_5 excited state optimization using TDDFT (with 5 optimization steps), while the TDDFT+TB method completed the same calculation in approximately 11 min with the same number of optimization steps. Notably, the emission energy difference between the two methods was only -0.02 eV. Therefore, these results clearly demonstrate that TDDFT+TB offers a substantial advantage for investigating larger molecular systems where conventional TDDFT calculations are computationally demanding.

Table 6.5. Computational runtime required for excited state geometry optimization of open-shell diatomic molecules using TDDFT and TDDFT+TB methods.

Molecule	State	Method	Runtime (hh:mm:ss)	Number of geometry steps
O_2	T_1	TDDFT	00:01:22	7
		TDDFT+TB	00:00:24	7
SO	T_1	TDDFT	00:02:24	7
		TDDFT+TB	00:00:38	7
S_2	T_1	TDDFT	00:01:48	6
		TDDFT+TB	00:00:32	6
NH (Imidogen)	T_1	TDDFT	00:01:00	5
		TDDFT+TB	00:00:17	5
NF	T_1	TDDFT	00:03:22	14
		TDDFT+TB	00:00:56	15
HHe	D_1	TDDFT	00:01:13	15
		TDDFT+TB	00:00:22	12
CN	D_1	TDDFT	00:01:34	5
		TDDFT+TB	00:00:28	5
BeH	D_1	TDDFT	00:00:38	3
		TDDFT+TB	00:00:11	3
BeF	D_1	TDDFT	00:01:04	5
		TDDFT+TB	00:00:21	5

Table 6.6. Computational runtime required for excited state geometry optimization of small open-shell organic radical and charged species using TDDFT and TDDFT+TB methods.

Molecule	State	Method	Runtime (hh:mm:ss)	Number of geometry steps
Acetyl free radical	D_3	TDDFT	00:09:09	6
		TDDFT+TB	00:02:10	7
Adenine radical cation	D_5	TDDFT	01:01:09	5
		TDDFT+TB	00:11:25	5
Benzyl free radical	D_2	TDDFT	00:57:06	6
		TDDFT+TB	00:11:15	6
p-Benzoquinone radical anion	D_1	TDDFT	00:25:19	5
		TDDFT+TB	00:05:23	5
cis-Butadiene radical cation	D_1	TDDFT	00:21:38	9
		TDDFT+TB	00:05:16	9
trans-Butadiene radical cation	D_1	TDDFT	00:21:28	9
		TDDFT+TB	00:04:28	8
Cyclopentadienyl cation	T_1	TDDFT	00:29:36	10
		TDDFT+TB	00:08:20	11
Cyclopentadienyl free radical*	D_2	TDDFT	00:11:07	2

		TDDFT+TB	00:08:08	10
Cyclopropene radical cation	D_3	TDDFT	00:09:31	8
		TDDFT+TB	00:02:24	8
2-Dehydroimidazolyl free radical	D_1	TDDFT	00:23:40	9
		TDDFT+TB	00:05:03	9
4-Dehydroimidazolyl free radical	D_1	TDDFT	00:22:04	7
		TDDFT+TB	00:03:19	6
5-Dehydroimidazolyl free radical	D_2	TDDFT	00:18:09	6
		TDDFT+TB	00:04:22	8
Ethene radical cation	D_2	TDDFT	00:04:53	6
		TDDFT+TB	00:01:10	6
1-Furanyl free radical	D_2	TDDFT	00:18:46	7
		TDDFT+TB	00:03:40	7
2-Furanyl free radical	D_2	TDDFT	00:15:34	6
		TDDFT+TB	00:03:09	6
Formyl free radical	D_2	TDDFT	00:01:57	5
		TDDFT+TB	00:00:39	5
Naphthalene radical cation	D_1	TDDFT	00:49:12	4

		TDDFT+TB	00:10:18	4
Pyrazine radical cation	D_1	TDDFT	00:13:07	4
		TDDFT+TB	00:03:07	4
Pyridazine radical cation	D_1	TDDFT	00:20:48	6
		TDDFT+TB	00:04:23	6
Pyridine radical cation	D_2	TDDFT	00:30:20	6
		TDDFT+TB	00:07:02	6
Pyrimidine radical cation	D_1	TDDFT	00:18:17	4
		TDDFT+TB	00:03:10	4
Pyrrole radical cation	D_1	TDDFT	00:30:41	8
		TDDFT+TB	00:07:16	8
Tetrazine radical cation	D_1	TDDFT	00:15:01	6
		TDDFT+TB	00:03:03	6

*TDDFT geometry optimization was started from the optimized TDDFT+TB D_2 state geometry.

6.5 Discussion

Despite the remarkable reduction of computational cost, it should be noted that TDDFT+TB excited-state gradients for open-shell systems represent an approximate treatment for TDDFT; consequently, these results are not expected to achieve the same level of accuracy as conventional TDDFT calculations. As discussed by Rüger et al.,[35] the TDDFT+TB method exhibits limitations in modeling local transitions due to atomic transition charges arising from the monopole approximation to the transition density. This is particularly notable for diatomics. It is worth noting that Domínguez et al.[22] have reported the same incorrect description of

transitions in TDDFTB method and further demonstrated that this can be overcome by applying on-site corrections, leading to extended TDDFTB formulations. At the current stage, the new implementation is able to reproduce emission energies with TDDFT level accuracy while significantly reducing the computational cost. More importantly, as the system size increases, the issues associated with modeling local transitions become less significant. Larger molecular systems typically exhibit lower symmetry, which reduces the impact of modeling local transitions, establishing TDDFT+TB to be more suitable for larger molecular systems.

6.6 Conclusion

Previous studies have demonstrated that TDDFT+TB excitation energies reproduce TDDFT results with significantly reduced computational cost. This was initially addressed by Havenridge et al.[36] through their implementation of restricted analytical excited state gradients in the TDDFT+TB method. Building upon the restricted formalism, we present the derivation and implementation of unrestricted analytical excited state gradients for TDDFT+TB in AMS, with key modifications to the coupling matrix and incorporation of spin indices in the gradient expression. We validated the method through calculations on various molecular systems, comparing the gradient accuracy, emission energies, and computational cost, to confirm that the method delivers reliable results for open-shell molecular excited states with improved efficiency compared to the standard TDDFT method. Overall, the analytical excited state gradient implementation for open-shell systems in TDDFT+TB demonstrates excellent agreement between numerical and analytical gradients, with MAD values below 5.00×10^{-4} Hartree/Å. The calculated emission energies are also well within 0.50 eV for open-shell diatomic molecules and 0.10 eV for small open-shell organic radicals and charged species relative to TDDFT values.

Additionally, the method reduces computational cost by approximately one-third compared to conventional TDDFT calculations. Importantly, the observed trends suggest that increasing system size results in more pronounced computational efficiency gains and improved relative accuracy of TDDFT+TB excited state geometry optimization. Therefore, these results establish TDDFT+TB as particularly well-suited for analyzing larger molecular systems where computational cost becomes prohibitive.

6.7 Appendix D – Supporting Information

See the Appendix D for a step-by-step derivation of the TDDFT+TB analytical excited state gradient, description of the numerical quality parameter in ADF, major changes related to the ADF input file, references for the small open-shell organic radicals and charged species, numerical vs. analytical excited state gradient comparison with different numerical displacements, effect of different parameters on the excited state geometry optimization, numerical vs. analytical excited state gradient comparison for closed-shell molecules, spin-contaminations for the excited states of open-shell molecules, comparison of spin-contaminations for the excited states of selected open-shell diatomic molecules with previously reported values, comparison of excitation energies of selected open-shell molecules with experimental and/or theoretical excitation energies, HHe molecule potential energy surface, and the equations for MAD and rms calculations.

6.8 Acknowledgments

D.S.N.D.S. would like to thank Erik van Lenthe and Robert Rüger for helpful discussions regarding the derivation and implementation of analytical excited state gradients for open-shell

systems in TDDFT+TB within the ADF engine. He would also like to thank Erik van Lenthe for merging the code into the AMS trunk and debugging during this process. D.S.N.D.S. and C.M.A. were supported by the National Science Foundation (NSF) of the United States (grant CHE-1955823). The computing for this work was performed on the Beocat Research Cluster at Kansas State University, which is funded in part by NSF grants CHE-1726332, CNS-1006860, EPS-1006860, and EPS-0919443.

6.9 References

1. Schlegel, H. B. Exploring Potential Energy Surfaces for Chemical Reactions: An Overview of Some Practical Methods. *J. Comput. Chem.* **2003**, *24* (12), 1514–1527.

2. Chen, Z.; Wang, J.; Hao, M.; Xie, Y.; Liu, X.; Yang, H.; Waterhouse, G. I. N.; Wang, X.; Ma, S. Tuning Excited State Electronic Structure and Charge Transport in Covalent Organic Frameworks for Enhanced Photocatalytic Performance. *Nat. Commun.* **2023**, *14* (1), 1106.

3. Juliá, F. Catalysis in the Excited State: Bringing Innate Transition Metal Photochemistry into Play. *ACS Catal.* **2025**, *15* (6), 4665–4680.

4. Schleper, A. L.; Goushi, K.; Bannwarth, C.; Haehnle, B.; Welscher, P. J.; Adachi, C.; Kuehne, A. J. C. Hot Exciplexes in U-Shaped TADF Molecules with Emission from Locally Excited States. *Nat. Commun.* **2021**, *12* (1), 6179.

5. Pal, A. K.; Bhattacharyya, K.; Datta, A. Remote Functionalization through Symmetric or Asymmetric Substitutions Control the Pathway of Intermolecular Singlet Fission. *J. Chem. Theory Comput.* **2019**, *15* (9), 5014–5023.

6. Shu, X.; Kallio, K.; Shi, X.; Abbyad, P.; Kanchanawong, P.; Childs, W.; Boxer, S. G.; Remington, S. J. Ultrafast Excited-State Dynamics in the Green Fluorescent Protein Variant S65T/H148D. 1. Mutagenesis and Structural Studies. *Biochemistry* **2007**, *46* (43), 12005–12013.

7. Mayer, D.; Lever, F.; Picconi, D.; Metje, J.; Alisauskas, S.; Calegari, F.; Düsterer, S.; Ehlert, C.; Feifel, R.; Niebuhr, M.; Manschwetus, B.; Kuhlmann, M.; Mazza, T.; Robinson, M. S.; Squibb, R. J.; Trabattoni, A.; Wallner, M.; Saalfrank, P.; Wolf, T. J. A.; Gühr, M. Following Excited-State Chemical Shifts in Molecular Ultrafast x-Ray Photoelectron Spectroscopy. *Nat. Commun.* **2022**, *13* (1), 198.

8. Ulenikov, O.; Bekhtereva, E.; Gromova, O.; Sidko, S.; Bauerecker, S. A Method for the Precise Determination of the Intramolecular Potential Energy Surface on the Basis of

Microwave and Submillimeter-Wave Spectra: Diatomic Molecules as a Relevant Illustration. *Int. J. Mol. Sci.* **2025**, *26*, 658.

9. Butz, K. W.; Krajnovich, D. J.; Parmenter, C. S. An experimental potential energy surface for internal rotation in glyoxal. *J. Chem. Phys.* **1990**, *93*, 1557–1567.

10. Havenridge, S.; Aikens, C. M. Deciphering the Dual Emission in the Photoluminescence of $Au_{14}Cd(SR)_{12}$: A Theoretical Study Using TDDFT and TDDFT + TB. *J. Chem. Phys.* **2021**, *155* (7).

11. Zeng, Y.; Havenridge, S.; Gharib, M.; Baksi, A.; Weerawardene, K. L. D. M.; Ziefuß, A. R.; Strelow, C.; Rehbock, C.; Mews, A.; Barcikowski, S.; Kappes, M. M.; Parak, W. J.; Aikens, C. M.; Chakraborty, I. Impact of Ligands on Structural and Optical Properties of Ag_{29} Nanoclusters. *J. Am. Chem. Soc.* **2021**, *143* (25), 9405–9414.

12. Alkan, F.; Aikens, C. M. Understanding Plasmon Coupling in Nanoparticle Dimers Using Molecular Orbitals and Configuration Interaction. *Phys. Chem. Chem. Phys.* **2019**, *21* (41), 23065–23075.

13. Zhang, K.; Zhang, H. Plasmon Coupling in Gold Nanotube Assemblies: Insight from a Time-Dependent Density Functional Theory (TDDFT) Calculation. *J. Phys. Chem. C* **2014**, *118* (1), 635–641.

14. Fernando, A.; Weerawardene, K. L. D. M.; Karimova, N. V.; Aikens, C. M. Quantum Mechanical Studies of Large Metal, Metal Oxide, and Metal Chalcogenide Nanoparticles and Clusters. *Chem. Rev.* **2015**, *115* (12), 6112–6216.

15. Muniz-Miranda, F.; Menziani, M. C.; Pedone, A. Influence of Silver Doping on the Photoluminescence of Protected Ag_nAu_{25-n} Nanoclusters: A Time-Dependent Density Functional Theory Investigation. *J. Phys. Chem. C* **2015**, *119* (19), 10766–10775.

16. Wang, Y.; Aikens, C. M. Effects of Field Strength and Silver Nanowire Size on Plasmon-Enhanced N_2 Dissociation. *J. Phys. Chem. A* **2023**, *127* (27), 5609–5619.

17. Van Stappen, C.; Decamps, L.; Cutsail, G. E.; Bjornsson, R.; Henthorn, J. T.; Birrell, J. A.; DeBeer, S. The Spectroscopy of Nitrogenases. *Chem. Rev.* **2020**, *120* (12), 5005–5081.

18. Samarasinghe, D. S. N. D.; Aikens, C. M. Effects of Static Electric Fields on the Excitations of Silver Nanowire Dimers. *J. Phys. Chem. A* **2024**, *128* (18), 3548–3556.

19. Shao, Y.; Mei, Y.; Sundholm, D.; Kaila, V. R. I. Benchmarking the Performance of Time-Dependent Density Functional Theory Methods on Biochromophores. *J. Chem. Theory Comput.* **2020**, *16*, 587−600.

20. Tussupbayev, S.; Govind, N.; Lopata, K.; Cramer, C. J. Comparison of Real-Time and Linear-Response Time-Dependent Density Functional Theories for Molecular Chromophores Ranging from Sparse to High Densities of States. *J. Chem. Theory Comput.* **2015**, *11*, 1102−1109.

21. Niehaus, T. A.; Suhai, S.; Della Sala, F.; Lugli, P.; Elstner, M.; Seifert, G.; Frauenheim, Th. Tight-Binding Approach to Time-Dependent Density-Functional Response Theory. *Phys. Rev. B* **2001**, *63* (8), 085108.

22. Domínguez, A.; Aradi, B.; Frauenheim, T.; Lutsker, V.; Niehaus, T. A. Extensions of the Time-Dependent Density Functional Based Tight-Binding Approach. *J. Chem. Theory Comput.* **2013**, *9* (11), 4901–4914.

23. Trani, F.; Scalmani, G.; Zheng, G.; Carnimeo, I.; Frisch, M. J.; Barone, V. Time-Dependent Density Functional Tight Binding: New Formulation and Benchmark of Excited States. *J. Chem. Theory Comput.* **2011**, *7* (10), 3304–3313.

24. Porezag, D.; Frauenheim, Th.; Köhler, Th.; Seifert, G.; Kaschner, R. Construction of Tight-Binding-like Potentials on the Basis of Density-Functional Theory: Application to Carbon. *Phys. Rev. B* **1995**, *51* (19), 12947–12957.

25. Seifert, G.; Porezag, D.; Frauenheim, Th. Calculations of Molecules, Clusters, and Solids with a Simplified LCAO-DFT-LDA Scheme. *Int. J. Quantum Chem.* **1996**, *58* (2), 185–192.

26. Niehaus, T. A. Approximate Time-Dependent Density Functional Theory. *J. Mol. Struct. THEOCHEM* **2009**, *914* (1–3), 38–49.

27. Spiegelman, F.; Tarrat, N.; Cuny, J.; Dontot, L.; Posenitskiy, E.; Martí, C.; Simon, A.; Rapacioli, M. Density-Functional Tight-Binding: Basic Concepts and Applications to Molecules and Clusters. *Adv. Phys. X* **2020**, *5* (1), 1710252.

28. Liu, Z.; Oviedo, M. B.; Wong, B. M.; Aikens, C. M. Plasmon-Induced Excitation Energy Transfer in Silver Nanoparticle Dimers: A Real-Time TDDFTB Investigation. *J. Chem. Phys.* **2022**, *156* (15).

29. Titov, E.; Humeniuk, A.; Mitrić, R. Exciton Localization in Excited-State Dynamics of a Tetracene Trimer: A Surface Hopping LC-TDDFTB Study. *Phys. Chem. Chem. Phys.* **2018**, *20* (40), 25995–26007.

30. Alkan, F.; Aikens, C. M. TD-DFT and TD-DFTB Investigation of the Optical Properties and Electronic Structure of Silver Nanorods and Nanorod Dimers. *J. Phys. Chem. C* **2018**, *122* (41), 23639–23650.

31. Asadi-Aghbolaghi, N.; Rüger, R.; Jamshidi, Z.; Visscher, L. TD-DFT+TB: An Efficient and Fast Approach for Quantum Plasmonic Excitations. *J. Phys. Chem. C* **2020**, *124* (14), 7946–7955.

32. Domínguez-Castro, A.; Frauenheim, T. Impact of Vibronic Coupling Effects on Light-Driven Charge Transfer in Pyrene-Functionalized Middle and Large-Sized Metalloid Gold Nanoclusters from Ehrenfest Dynamics. *Phys. Chem. Chem. Phys.* **2021**, *23* (32), 17129–17133.

33. Wu, X.; Liu, B.; Frauenheim, T.; Tretiak, S.; Yam, C.; Zhang, Y. Investigation of Plasmon Relaxation Mechanisms Using Nonadiabatic Molecular Dynamics. *J. Chem. Phys.* **2022**, *157* (21).

34. Kumawat, R. L.; Schatz, G. C. Efficient Modeling of Structural, Electronic, and Optical Properties of Silver and Gold Metal Nanoclusters and Alloys Using Optimized SCC-DFTB Parameters. *J. Phys. Chem. C* **2025**, *129*, 1348−1361.

35. Rüger, R.; van Lenthe, E.; Heine, T.; Visscher, L. Tight-Binding Approximations to Time-Dependent Density Functional Theory — A Fast Approach for the Calculation of Electronically Excited States. *J. Chem. Phys.* **2016**, *144* (18), 184103.

36. Havenridge, S.; Rüger, R.; Aikens, C. M. Analytical Excited State Gradients for Time-Dependent Density Functional Theory plus Tight Binding (TDDFT + TB). *J. Chem. Phys.* **2023**, *158* (22), 224103.

37. Grimme, S. A Simplified Tamm-Dancoff Density Functional Approach for the Electronic Excitation Spectra of Very Large Molecules. *J. Chem. Phys.* **2013**, *138* (24), 244104.

38. Risthaus, T.; Hansen, A.; Grimme, S. Excited States Using the Simplified Tamm–Dancoff-Approach for Range-Separated Hybrid Density Functionals: Development and Application. *Phys. Chem. Chem. Phys.* **2014**, *16* (28), 14408–14419.

39. Bannwarth, C.; Grimme, S. A Simplified Time-Dependent Density Functional Theory Approach for Electronic Ultraviolet and Circular Dichroism Spectra of Very Large Molecules. *Comput. Theor. Chem.* **2014**, *1040–1041*, 45–53.

40. Giannone, G.; Della Sala, F. Minimal Auxiliary Basis Set for Time-Dependent Density Functional Theory and Comparison with Tight-Binding Approximations: Application to Silver Nanoparticles. *J. Chem. Phys.* **2020**, *153* (8), 084110.

41. Zhou, Z.; Della Sala, F.; Parker, S. M. Minimal Auxiliary Basis Set Approach for the Electronic Excitation Spectra of Organic Molecules. *J. Phys. Chem. Lett.* **2023**, *14* (7), 1968–1976.

42. Pu, Z.; Wu, X.; Wang, Y.; Fan, C.; Yan, W.; Zhou, Z.; Gao, Y. Q.; Sun, Q. Analytical Excited-State Gradients and Derivative Couplings in TDDFT with Minimal Auxiliary Basis Set Approximation and GPU Acceleration. *J. Chem. Theory Comput.* **2026**, acs.jctc.5c01960.

43. te Velde, G.; Bickelhaupt, F. M.; Baerends, E. J.; Fonseca Guerra, C.; van Gisbergen, S. J. A.; Snijders, J. G.; Ziegler, T. Chemistry with ADF. *J. Comput. Chem.* **2001**, *22* (9), 931–967.

44. Furche, F.; Ahlrichs, R. Adiabatic Time-Dependent Density Functional Methods for Excited State Properties. *J. Chem. Phys.* **2002**, *117* (16), 7433–7447.

45. Furche, F. On the Density Matrix Based Approach to Time-Dependent Density Functional Response Theory. *J. Chem. Phys.* **2001**, *114* (14), 5982–5992.

46. Heringer, D.; Niehaus, T. A.; Wanko, M.; Frauenheim, TH. Analytical Excited State Forces for the Time-dependent Density-functional Tight-binding Method. *J. Comput. Chem.* **2007**, *28* (16), 2589–2601.

47. Wang, Y.; Havenridge, S.; Aikens, C. M. Implementation of Energy and Gradient for the TDDFT-Approximate Auxiliary Function (aas) Method. *J. Chem. Phys.* **2024**, *161* (2), 024101.

48. Spiegelman, F.; Tarrat, N.; Cuny, J.; Dontot, L.; Posenitskiy, E.; Martí, C.; Simon, A.; Rapacioli, M. Density-Functional Tight-Binding: Basic Concepts and Applications to Molecules and Clusters. *Adv. Phys. X.* **2020**, *5* (1), 1710252.

49. Schreiber, M.; Silva-Junior, M. R.; Sauer, S. P. A.; Thiel, W. Benchmarks for Electronically Excited States: CASPT2, CC2, CCSD, and CC3. *J. Chem. Phys.* **2008**, *128* (13).

50. Perdew, J. P.; Wang, Y. Accurate and Simple Analytic Representation of the Electron-Gas Correlation Energy. *Phys. Rev. B* **1992**, *45* (23), 13244–13249.

51. PLAMS, SCM, Theoretical Chemistry, Vrije Universiteit, Amsterdam, The Netherlands https://www.scm.com, https://github.com/SCM-NV/PLAMS (accessed 30 September 2025).

52. Ipatov, A.; Cordova, F.; Doriol, L. J.; Casida, M. E. Excited-State Spin-Contamination in Time-Dependent Density-Functional Theory for Molecules with Open-Shell Ground States. *J. Mol. Struct.: THEOCHEM.* **2009**, *914* (1–3), 60–73.

53. Li, Z.; Liu, W.; Zhang, Y.; Suo, B. Spin-Adapted Open-Shell Time-Dependent Density Functional Theory. II. Theory and Pilot Application. *J. Chem. Phys.* **2011**, *134* (13), 134101.

Chapter 7 - Conclusion and next steps

This dissertation presents a series of theoretical investigations into noble metal nanomaterial systems, motivated by their broad relevance across fields such as medicine, sensing, optoelectronics, and beyond. At its core, the work revolves around two central themes: understanding how external perturbations and environmental conditions shape the optical properties of nanowires and nanoclusters, and finding ways to overcome the computational limitations of conventional theoretical frameworks. To address these themes, four projects are presented, two chapters for each, together pushing forward both our physical understanding and the theoretical methods we use to get there.

In our chapter 3, we examined the effect of static electric fields on three distinct Ag_{10} dimer configurations: end-to-end, parallel, and 90° angled systems, using linear response TDDFT simulations. The results demonstrated that both the arrangement of the dimer and the direction of the applied field govern the shifts in molecular orbitals and excitation energies, with the end-to-end configuration under a z-directional field producing the most pronounced spectral changes. Overall, the static electric fields were found to induce blue shifts in longitudinal absorption peaks and red shifts in transverse absorption peaks, highlighting the sensitivity of nanowire optical properties to their geometric and field environment.

Moving from model silver nanowire systems to a real-world nanorod, Chapter 4 investigated the electronic structure and excitation characteristics of $Au_{42}(SCH_3)_{32}$ across solvent environments of varying polarity. In the gas phase, the NIR absorption peak revealed a dual-excitation character, arising from HOMO → LUMO and HOMO-1 → LUMO transitions. When solvent effects were introduced through an implicit solvation model, increasing polarity was found to systematically red-shift the HOMO → LUMO dominated excitation while the HOMO-1

→ LUMO dominated excitation remained nearly unchanged. This demonstrated that simply choosing the right solvent can serve as a practical tool for tuning NIR absorption wavelength with promising implications for photothermal applications.

Chapters 3 and 4 addressed the first objective of this dissertation, and we now turn toward the next two chapters which tackle the second. Chapter 5 takes on the challenge of computational efficiency by developing a machine learning force field (MLFF) for gold hydride nanoclusters, trained on the configurational space of $Au_{13}H_5$ and $Au_{18}H_{14}$ through a combined active and passive learning workflow. The final model achieved DFT-level accuracy in predicting relative potential energies across diverse cluster configurations and temperatures, with MAD values below 19.00 meV/atom for in-database structures and below 8.50 meV/atom for out-of-database structures. While absolute energy predictions still have room for improvement, the model lays a strong foundation for future development into a reactive force field for larger gold hydride systems.

Chapter 6 then took the TDDFT+TB framework a step further, extending it to explore the excited state potential energy surfaces of open-shell molecular systems by deriving and implementing the unrestricted analytical excited state gradients in AMS. The method was validated across a range of open-shell molecules confirming excellent agreement with numerical gradients, with emission energies falling within 0.50 eV for open-shell diatomic molecules and within 0.10 eV for small open-shell organic radicals and charged species relative to full TDDFT values, all while reducing computational cost by approximately one-third. What makes this especially promising is that the efficiency gains become more pronounced as system size grows, making TDDFT+TB a particularly powerful approach for studying the excited state properties of

larger noble metal nanomaterial systems where conventional TDDFT calculations would otherwise become prohibitively expensive.

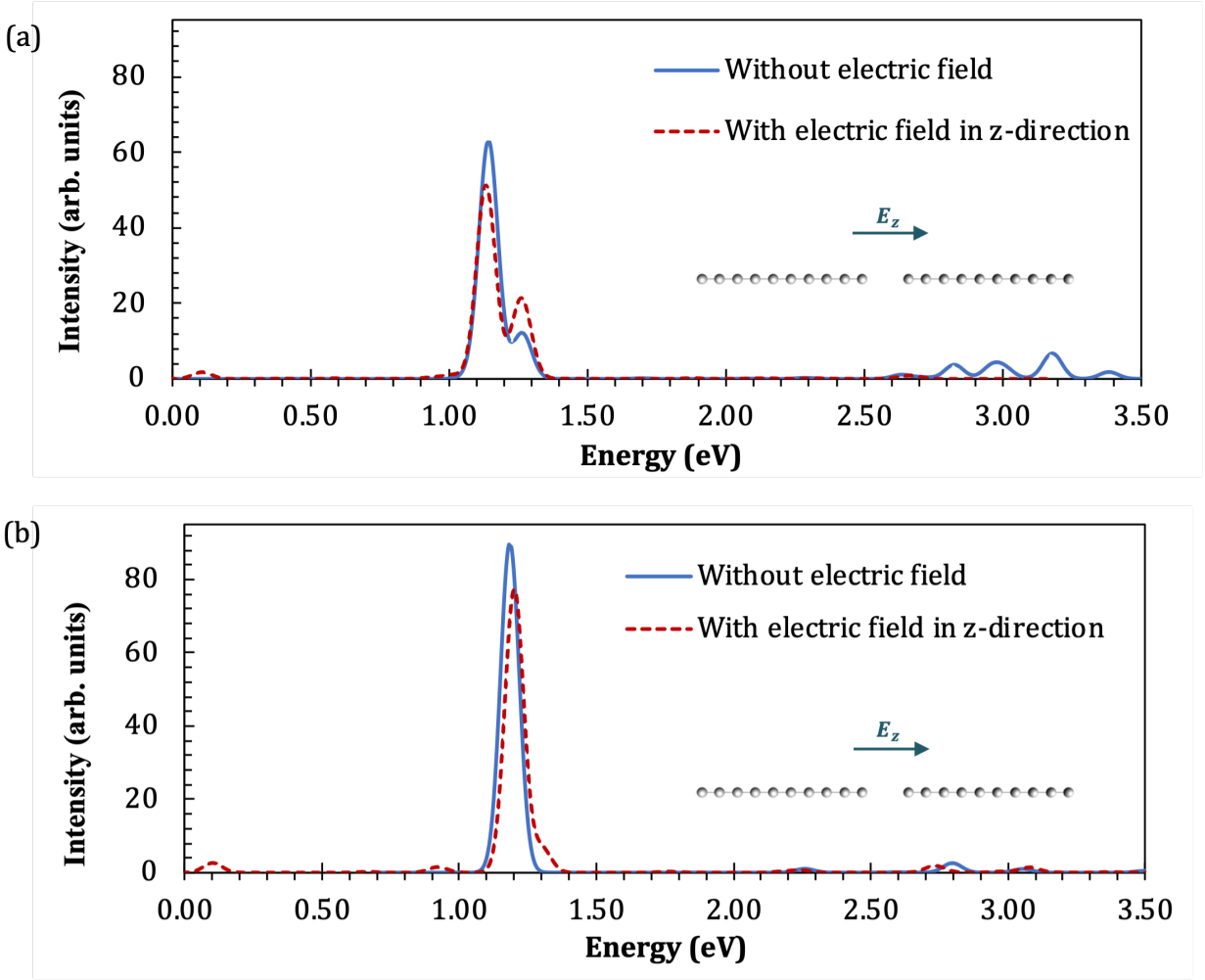
At the very heart of this dissertation lies a simple but profound question: how does light interact with matter, and what can theory tell us about it? As we walked through each chapter, two things became very clear: the surrounding environment and external perturbation play a decisive role in shaping light-matter interactions, and having efficient, accurate theoretical tools is just as important as the physics itself. Together, these threads weave into something bigger than any single result. But this is not the end of the road; if anything, it is a junction with many paths still ahead. The implicit solvation models used in Chapter 4, for instance, are just one piece of the picture; bringing in explicit solvation and molecular dynamics simulations would open up an entirely new dimension of research. Extending the study of external perturbations to larger nanorods and clusters holds equally exciting promise. The further development of the MLFF to include hydrogen bond dissociation and formation, along with extension of the model to predict not only hydrides but also other metal nanocluster protecting ligands, would elevate the applicability of this model to another level, deepening our understanding of these clusters. Additionally, the application of TDDFT+TB analytical excited state gradients for open-shell systems to probe the structural and electronic properties of open-shell gold nanocluster systems in their excited states (such as the neutral $Au_{25}(SH)_{18}$ nanocluster), represents a particularly promising avenue for future research. Furthermore, a deeper understanding of the computational bottlenecks of the current method would pave the way for introducing new approaches that further reduce computational cost while maintaining accuracy.

Appendix A - Supporting information for: Effects of static electric fields on the excitations of silver nanowire dimers

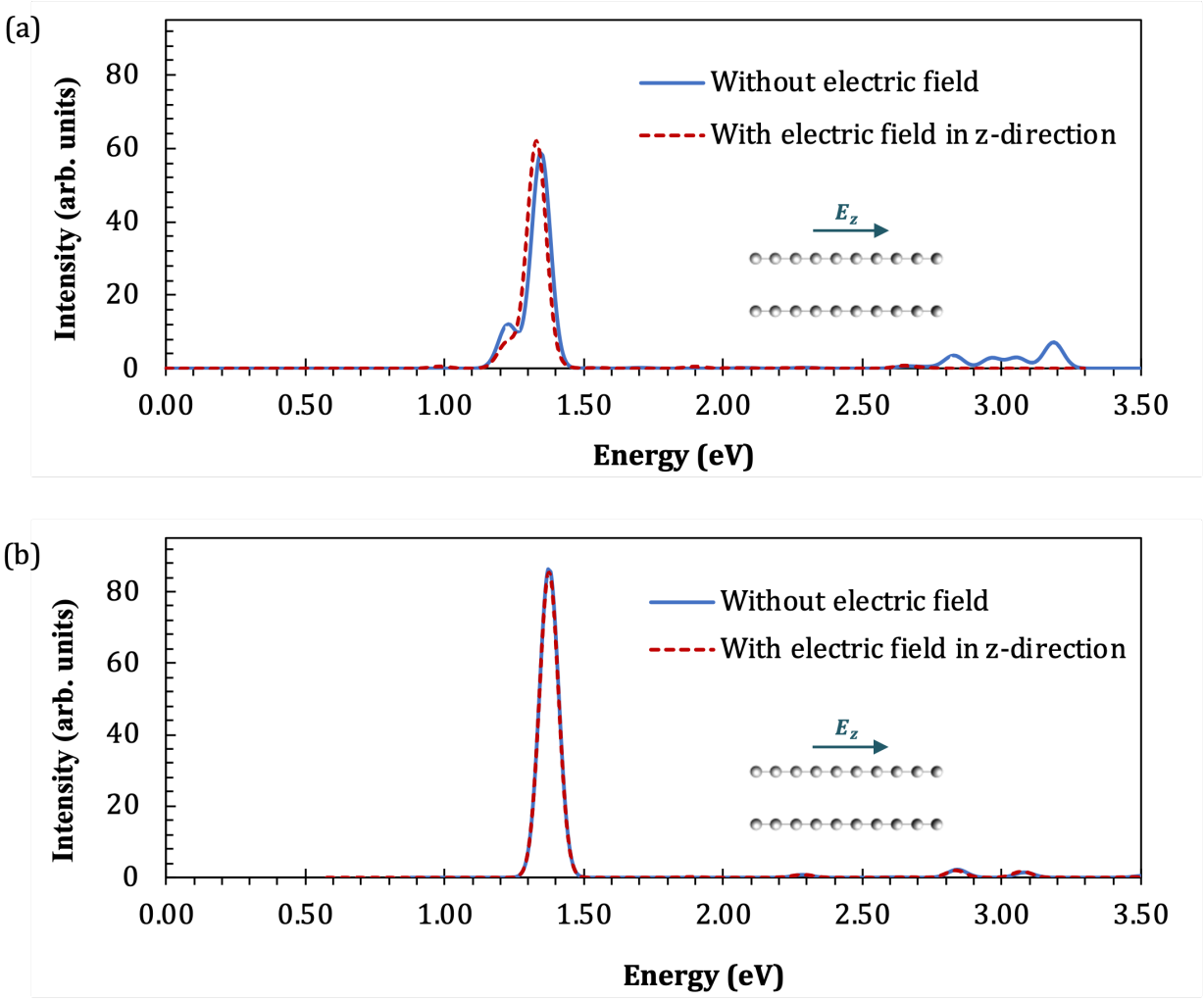
D. Sulalith N. D. Samarasinghe and Christine M. Aikens*

Department of Chemistry, Kansas State University, Manhattan, KS 66506, USA

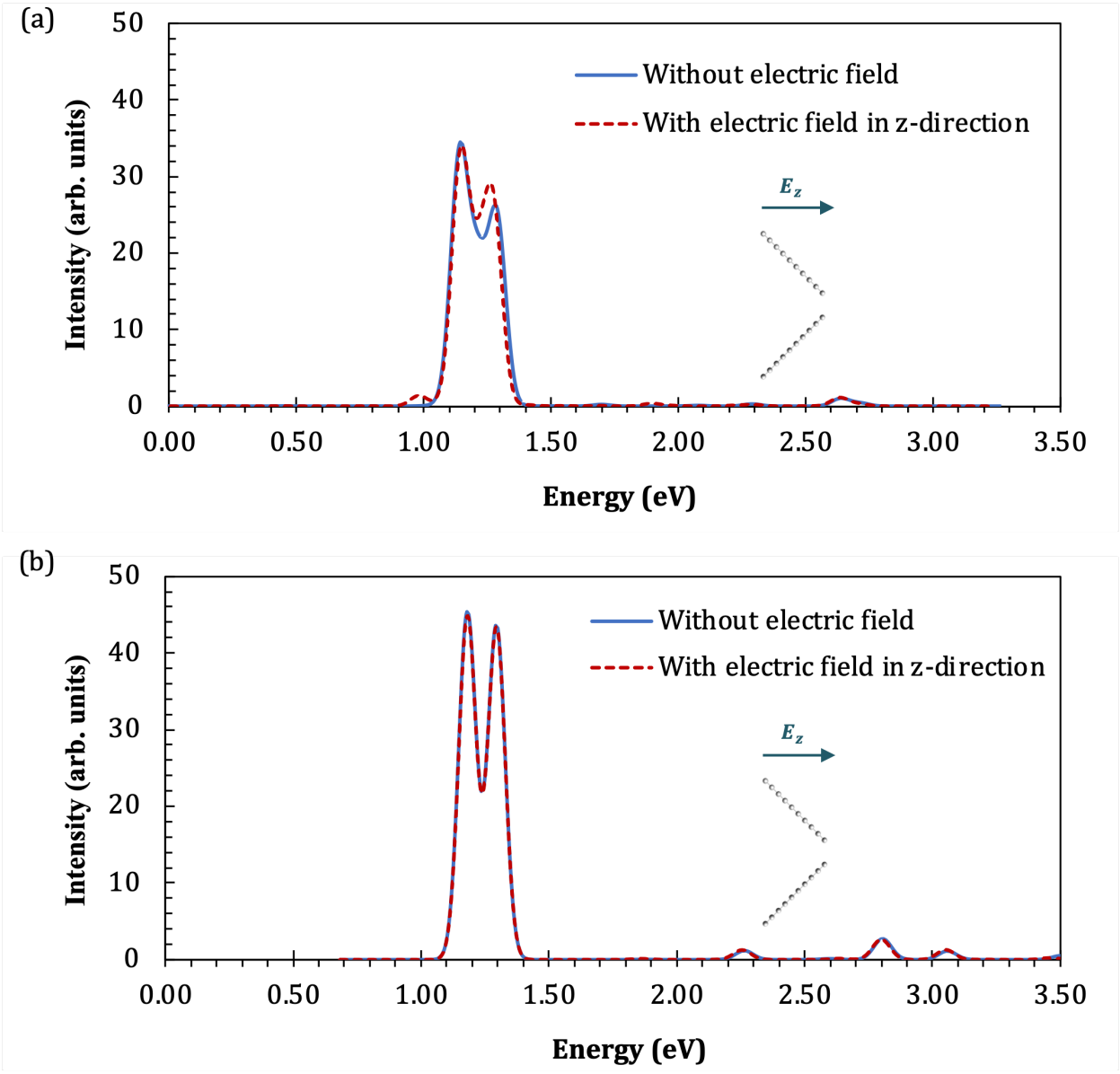
*Email: cmaikens@ksu.edu



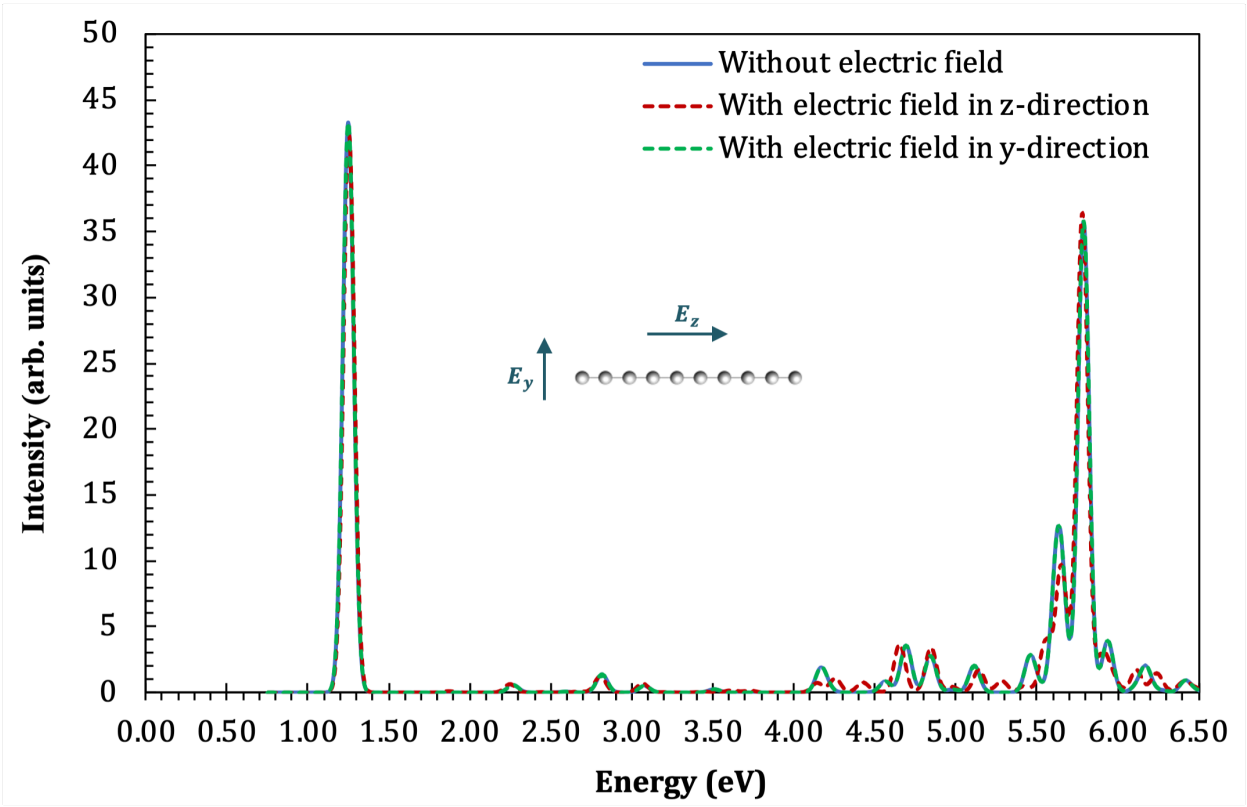
Appendix Figure A.1. Calculated absorption spectra for Ag_{10} end-to-end dimer system with and without the static electric field applied in z-direction using (a) BP86 and (b) long-range corrected (LC) CAMY-B3LYP functionals.



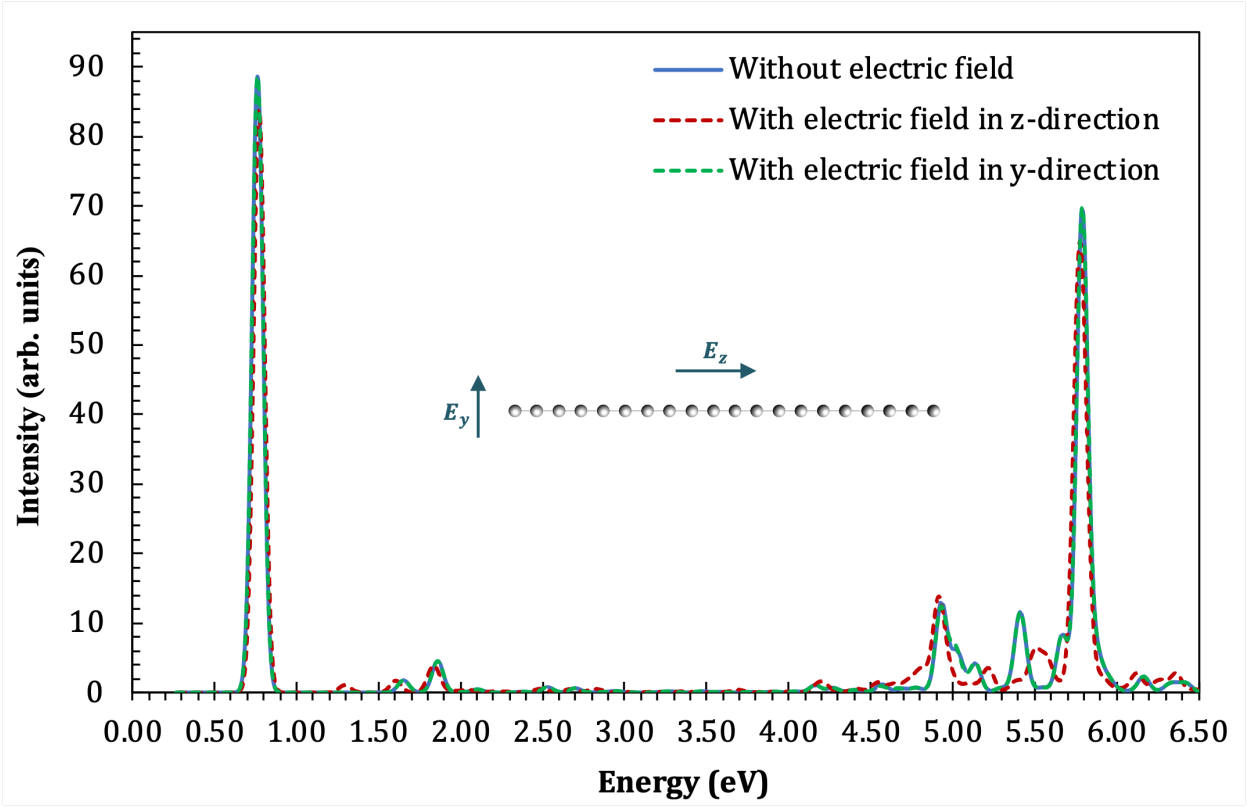
Appendix Figure A.2. Calculated absorption spectra for Ag_{10} parallel dimer system with and without the static electric field applied in z-direction using (a) BP86 and (b) long-range corrected (LC) CAMY-B3LYP functionals.



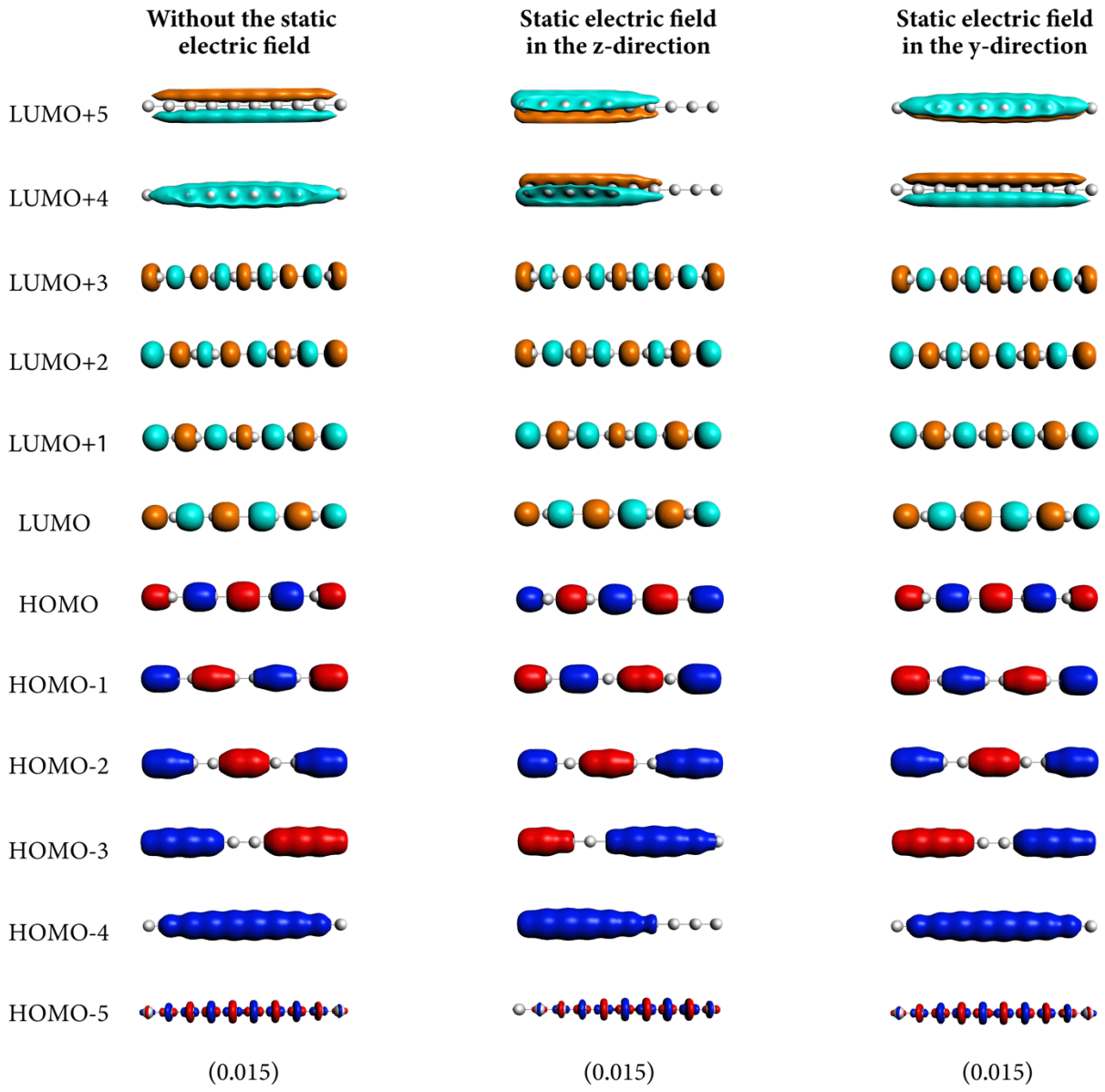
Appendix Figure A.3. Calculated absorption spectra for Ag_{10} 90° dimer system with and without the static electric field applied in z-direction using (a) BP86 and (b) long-range corrected (LC) CAMY-B3LYP functionals.



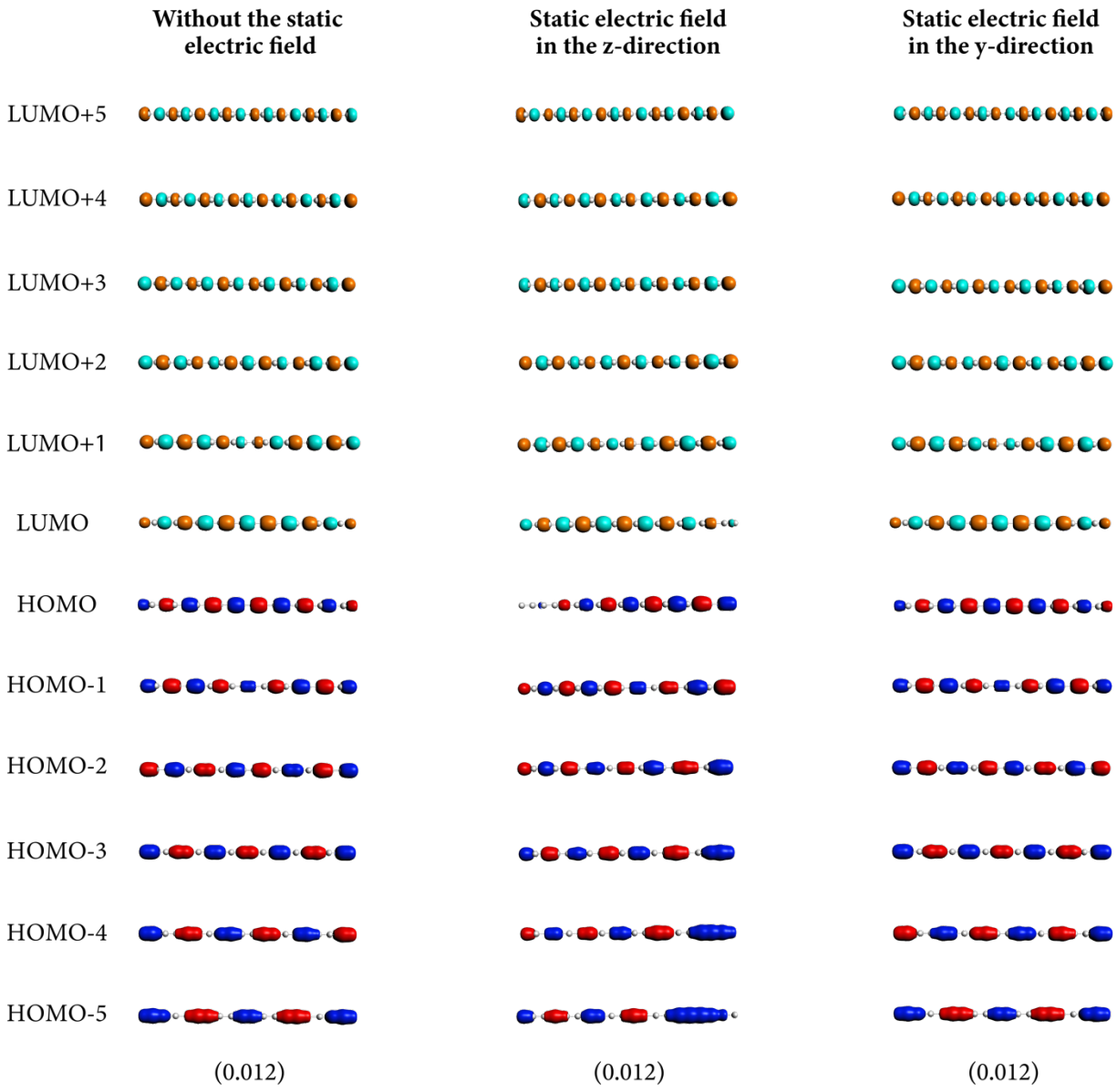
Appendix Figure A.4. Calculated absorption spectra for Ag_{10} monomer with and without the static electric field applied in the z-direction and y-direction.



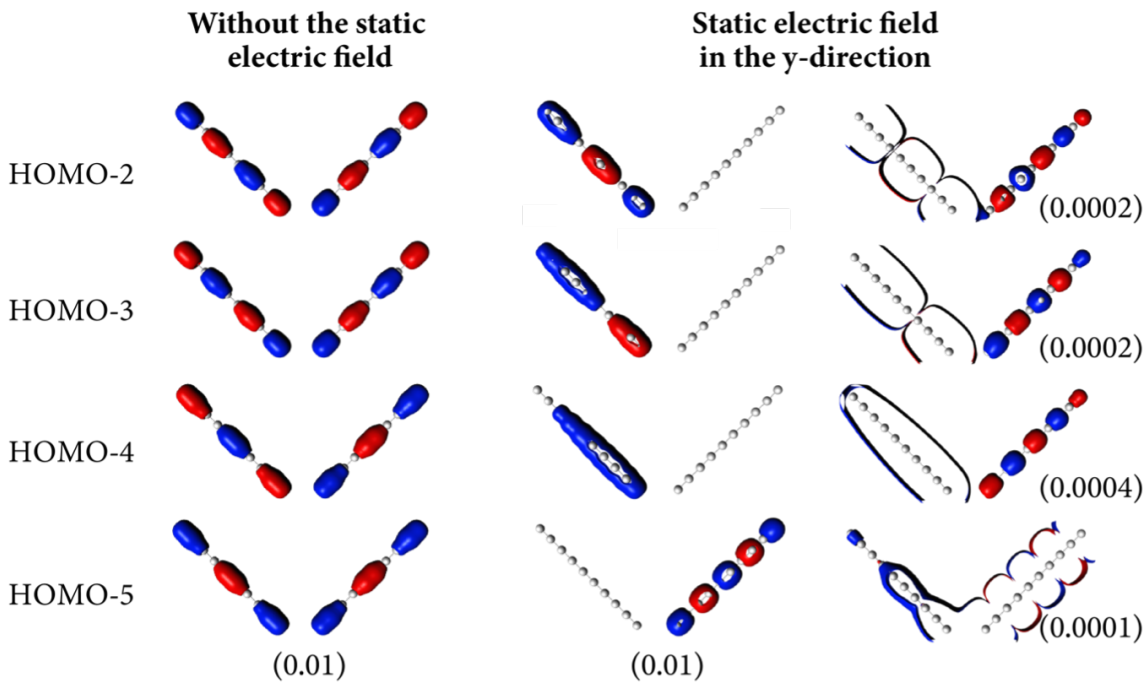
Appendix Figure A.5. Calculated absorption spectra for Ag_{20} monomer with and without the static electric field applied in the z-direction and y-direction.



Appendix Figure A.6. Illustrations of the molecular orbitals of Ag_{10} monomer, with and without the static electric field of 0.1 V/Å.



Appendix Figure A.7. Illustrations of the molecular orbitals of Ag_{20} monomer, with and without the static electric field of 0.1 V/Å.



Appendix Figure A.8. Illustrations of additional molecular orbitals of the Ag_{10} 90° dimer system, with and without the static electric field of 0.1 V/Å in the y-direction.

Appendix Table A.1. Longitudinal excitation energies for Ag_{10} end-to-end dimer system with and without the static electric field applied in z-direction using different functionals.

	Ag_{10} end-to-end dimer		
	Transitions		
	Orbital representation	Symmetry representation	Excitation energy (eV)
Using BP86 functional			
Without a static electric field	HOMO → LUMO	$\Sigma_u^+ \rightarrow \Sigma_g^+$	1.1434
	HOMO-1 → LUMO+1	$\Sigma_g^+ \rightarrow \Sigma_u^+$	
In z-directional static electric field	HOMO → LUMO+2	$\Sigma_u^+ \rightarrow \Sigma_g^+$	1.1339
	HOMO-4 → LUMO	$\Sigma_u^+ \rightarrow \Sigma_g^+$	

Using long-range corrected (LC) CAMY-B3LYP functional

Without a static electric field	HOMO → LUMO	$\Sigma_u^+ \rightarrow \Sigma_g^+$	1.1847
	HOMO-1 → LUMO+1	$\Sigma_g^+ \rightarrow \Sigma_u^+$	
In z-directional static electric field	HOMO → LUMO+2	$\Sigma_u^+ \rightarrow \Sigma_g^+$	1.2006
	HOMO-4 → LUMO	$\Sigma_u^+ \rightarrow \Sigma_g^+$	

Appendix Table A.2. . Longitudinal excitation energies for Ag_{10} parallel dimer system with and without the static electric field applied in z-direction using different functionals.

	Ag_{10} parallel dimer		
	Transitions		
	Orbital representation	Symmetry representation	Excitation energy (eV)
Using BP86 functional			
Without a static electric field	HOMO → LUMO+1	$B_{2u} \rightarrow B_{3g}$	1.3465
	HOMO-1 → LUMO	$A_g \rightarrow B_{1u}$	
In z-directional static electric field	HOMO → LUMO+1	$B_{2u} \rightarrow B_{3g}$	1.3305
	HOMO-1 → LUMO	$A_g \rightarrow B_{1u}$	
Using long-range corrected (LC) CAMY-B3LYP functional			
Without a static electric field	HOMO → LUMO+1	$B_{2u} \rightarrow B_{3g}$	1.3750
	HOMO-1 → LUMO	$A_g \rightarrow B_{1u}$	
	HOMO → LUMO+1	$B_{2u} \rightarrow B_{3g}$	1.3746

In z-directional static electric field	HOMO-1 → LUMO	$A_g \rightarrow B_{1u}$

Appendix Table A.3. Longitudinal excitation energies for Ag_{10} 90° dimer system with and without the static electric field applied in z-direction using different functionals.

	Ag_{10} 90° dimer		
	Transitions		
	Orbital representation	Symmetry representation	Excitation energy (eV)
Using BP86 functional			
Without a static electric field	HOMO → LUMO	$B_2 \rightarrow A_1$	1.1407
	HOMO-1 → LUMO+1	$A_1 \rightarrow B_2$	
	HOMO-1 → LUMO	$A_1 \rightarrow A_1$	1.2099
	HOMO → LUMO+1	$B_2 \rightarrow B_2$	
In z-directional static electric field	HOMO → LUMO	$B_2 \rightarrow A_1$	1.1442
	HOMO-1 → LUMO+1	$A_1 \rightarrow B_2$	
	HOMO-1 → LUMO	$A_1 \rightarrow A_1$	1.2117
	HOMO → LUMO+1	$B_2 \rightarrow B_2$	
Using long-range corrected (LC) CAMY-B3LYP functional			
Without a static electric field	HOMO → LUMO	$B_2 \rightarrow A_1$	1.1811
	HOMO-1 → LUMO+1	$A_1 \rightarrow B_2$	
	HOMO-1 → LUMO	$A_1 \rightarrow A_1$	1.2950
	HOMO → LUMO+1	$B_2 \rightarrow B_2$	
In z-directional static electric field	HOMO → LUMO	$B_2 \rightarrow A_1$	1.1813
	HOMO-1 → LUMO+1	$A_1 \rightarrow B_2$	
	HOMO-1 → LUMO	$A_1 \rightarrow A_1$	1.2951
	HOMO → LUMO+1	$B_2 \rightarrow B_2$	

I. Ag_{10} monomer within a static electric field

Appendix Table A.4. Excitation energies for Ag_{10} monomer with and without the static electric field (with LC BP86 functional).

	Ag_{10} monomer		
	Transitions		
	Orbital representation	Symmetry representation	Excitation energy (eV)
Longitudinal excitation			
Without a static electric field	HOMO → LUMO	$\Sigma_g^+ \rightarrow \Sigma_u^+$	1.2500
	HOMO-1 → LUMO+1	$\Sigma_u^+ \rightarrow \Sigma_g^+$	
In z-directional static electric field	HOMO → LUMO	$\Sigma_g^+ \rightarrow \Sigma_u^+$	1.2539
	HOMO-1 → LUMO+1	$\Sigma_u^+ \rightarrow \Sigma_g^+$	
In y-directional static electric field	HOMO → LUMO	$\Sigma_g^+ \rightarrow \Sigma_u^+$	1.2501
	HOMO-1 → LUMO+1	$\Sigma_u^+ \rightarrow \Sigma_g^+$	
Transverse excitation			
Without a static electric field	HOMO-4 → LUMO+4 and LUMO+5	$\Sigma_g^+ \rightarrow \Pi_u$	5.7888
	HOMO-1 → LUMO+12 and LUMO+13	$\Sigma_u^+ \rightarrow \Pi_g$	
In z-directional static electric field	HOMO-4 → LUMO+4 and LUMO+5	$\Sigma_g^+ \rightarrow \Pi_u$	5.7815
	HOMO-3 → LUMO+7 and LUMO+8	$\Sigma_u^+ \rightarrow \Pi_g$	
In y-directional static electric field	HOMO-4 → LUMO+4	$\Sigma_g^+ \rightarrow \Pi_u$	5.7890

HOMO-1 → LUMO+12	$\Sigma_u^+ \rightarrow \Pi_g$	

II. Ag_{20} monomer within a static electric field

Appendix Table A.5. Excitation energies for Ag_{20} monomer with and without the static electric field (with LC BP86 functional).

	Ag_{20} monomer		
	Transitions		
	Orbital representation	Symmetry representation	Excitation energy (eV)
Longitudinal excitation			
Without a static electric field	HOMO → LUMO	$\Sigma_u^+ \rightarrow \Sigma_g^+$	0.7622
	HOMO-1 → LUMO+1	$\Sigma_g^+ \rightarrow \Sigma_u^+$	
In z-directional static electric field	HOMO → LUMO	$\Sigma_u^+ \rightarrow \Sigma_g^+$	0.7718
	HOMO-1 → LUMO+1	$\Sigma_g^+ \rightarrow \Sigma_u^+$	
In y-directional static electric field	HOMO → LUMO	$\Sigma_u^+ \rightarrow \Sigma_g^+$	0.7623
	HOMO-1 → LUMO+1	$\Sigma_g^+ \rightarrow \Sigma_u^+$	
Transverse excitation			
Without a static electric field	HOMO-8 → LUMO+11 and LUMO+12	$\Sigma_u^+ \rightarrow \Pi_g$	5.7895
	HOMO-9 → LUMO+8 and LUMO+9	$\Sigma_g^+ \rightarrow \Pi_u$	
In z-directional static electric field	HOMO-9 → LUMO+8 and LUMO+9	$\Sigma_g^+ \rightarrow \Pi_u$	5.7616
	HOMO → LUMO+10 and LUMO+11	$\Sigma_u^+ \rightarrow \Pi_g$	

In y-directional static electric field	HOMO-8 → LUMO+11 HOMO-9 → LUMO+8	$\Sigma_u^+ \rightarrow \Pi_g$ $\Sigma_g^+ \rightarrow \Pi_u$	5.7897

III. Comparison of transverse excitations of different Ag_{10} dimer systems within static electric field

Appendix Table A.6. Comparison of the transverse excitations and their orbital representations for the dimer systems with and without the static electric field applied in the z- and y-directions.

	Transitions		Excitation energy (eV)
	Orbital representation	Symmetry representation	
Ag_{10} end-to-end dimer			
Without a static electric field	HOMO-9 → LUMO+10 and LUMO+11 HOMO-8 → LUMO+8 and LUMO+9	$\Sigma_u^+ \rightarrow \Pi_g$ $\Sigma_g^+ \rightarrow \Pi_u$	5.7914
In z-directional static electric field	HOMO-8 → LUMO+10 and LUMO+11 HOMO-9 → LUMO+7 and LUMO+8	$\Sigma_u^+ \rightarrow \Pi_g$ $\Sigma_g^+ \rightarrow \Pi_u$	5.7612
In y-directional static electric field	HOMO-9 → LUMO+10 HOMO-8 → LUMO+8	$\Sigma_u^+ \rightarrow \Pi_g$ $\Sigma_g^+ \rightarrow \Pi_u$	5.7916
Ag_{10} parallel dimer			
Without a static electric field	HOMO-8 → LUMO+10 HOMO-9 → LUMO+9	$B_{2u} \rightarrow B_{1g}$ $A_g \rightarrow B_{3u}$	5.8250

In z-directional static electric field	HOMO-8 → LUMO+10 HOMO-9 → LUMO+9	$B_{2u} \rightarrow B_{1g}$ $A_g \rightarrow B_{3u}$	5.8205
In y-directional static electric field	HOMO-6 → LUMO+16 HOMO-9 → LUMO+9	$B_{2u} \rightarrow B_{1g}$ $A_g \rightarrow B_{3u}$	5.8255

Ag_{10} 90° dimer

Without a static electric field	HOMO-9 → LUMO+10 HOMO-8 → LUMO+11	$B_2 \rightarrow A_2$ $A_1 \rightarrow B_1$	5.7927
In z-directional static electric field	HOMO-8 → LUMO+9 HOMO-9 → LUMO+8	$A_1 \rightarrow B_1$ $B_2 \rightarrow A_2$	5.7885
In y-directional static electric field	HOMO-9 → LUMO+7 HOMO-8 → LUMO+10	$A_1 \rightarrow B_1$ $B_2 \rightarrow A_2$	5.7795

IV. Dimer configurations and their coordinates

Appendix Table A.7. Ag_{10} end-to-end dimer coordinates.

Atom	x	y	z
Ag	0.000000	0.000000	-3.500000
Ag	0.000000	0.000000	-6.126165
Ag	0.000000	0.000000	-8.857695
Ag	0.000000	0.000000	-11.526395

Ag	0.000000	0.000000	-14.243255
Ag	0.000000	0.000000	-16.917419
Ag	0.000000	0.000000	-19.634279
Ag	0.000000	0.000000	-22.302980
Ag	0.000000	0.000000	-25.034506
Ag	0.000000	0.000000	-27.660675
Ag	0.000000	0.000000	27.660675
Ag	0.000000	0.000000	25.034506
Ag	0.000000	0.000000	22.302980
Ag	0.000000	0.000000	19.634279
Ag	0.000000	0.000000	16.917419
Ag	0.000000	0.000000	14.243255
Ag	0.000000	0.000000	11.526395
Ag	0.000000	0.000000	8.857695
Ag	0.000000	0.000000	6.126164
Ag	0.000000	0.000000	3.500000

Appendix Table A.8. Ag_{10} parallel dimer coordinates.

Atom	x	y	z
Ag	0.000000	-3.500000	-12.080340
Ag	0.000000	-3.500000	-9.454170
Ag	0.000000	-3.500000	-6.722640
Ag	0.000000	-3.500000	-4.053940

Ag	0.000000	-3.500000	-1.337080
Ag	0.000000	-3.500000	1.337080
Ag	0.000000	-3.500000	4.053940
Ag	0.000000	-3.500000	6.722640
Ag	0.000000	-3.500000	9.454170
Ag	0.000000	-3.500000	12.080340
Ag	0.000000	3.500000	-12.080340
Ag	0.000000	3.500000	-9.454170
Ag	0.000000	3.500000	-6.722640
Ag	0.000000	3.500000	-4.053940
Ag	0.000000	3.500000	-1.337080
Ag	0.000000	3.500000	1.337080
Ag	0.000000	3.500000	4.053940
Ag	0.000000	3.500000	6.722640
Ag	0.000000	3.500000	9.454170
Ag	0.000000	3.500000	12.080340

Appendix Table A.9. Ag_{10} 90° dimer coordinates.

Atom	x	y	z
Ag	0.000000	-20.584146	-8.542108
Ag	0.000000	-18.727167	-6.685121
Ag	0.000000	-16.795689	-4.753634
Ag	0.000000	-14.908636	-2.866574

Ag	0.000000	-12.987530	-0.945460
Ag	0.000000	-11.096617	0.945460
Ag	0.000000	-9.175510	2.866574
Ag	0.000000	-7.288458	4.753633
Ag	0.000000	-5.356979	6.685121
Ag	0.000000	-3.500000	8.542108
Ag	0.000000	20.584146	-8.542108
Ag	0.000000	18.727167	-6.685121
Ag	0.000000	16.795689	-4.753634
Ag	0.000000	14.908636	-2.866574
Ag	0.000000	12.987530	-0.945460
Ag	0.000000	11.096617	0.945460
Ag	0.000000	9.175510	2.866574
Ag	0.000000	7.288458	4.753633
Ag	0.000000	5.356979	6.685121
Ag	0.000000	3.500000	8.542108

Appendix B - Supporting information for: Theoretical insights into the excitation characteristics of the $Au_{42}(SCH_3)_{32}$ nanorod in the near-infrared region

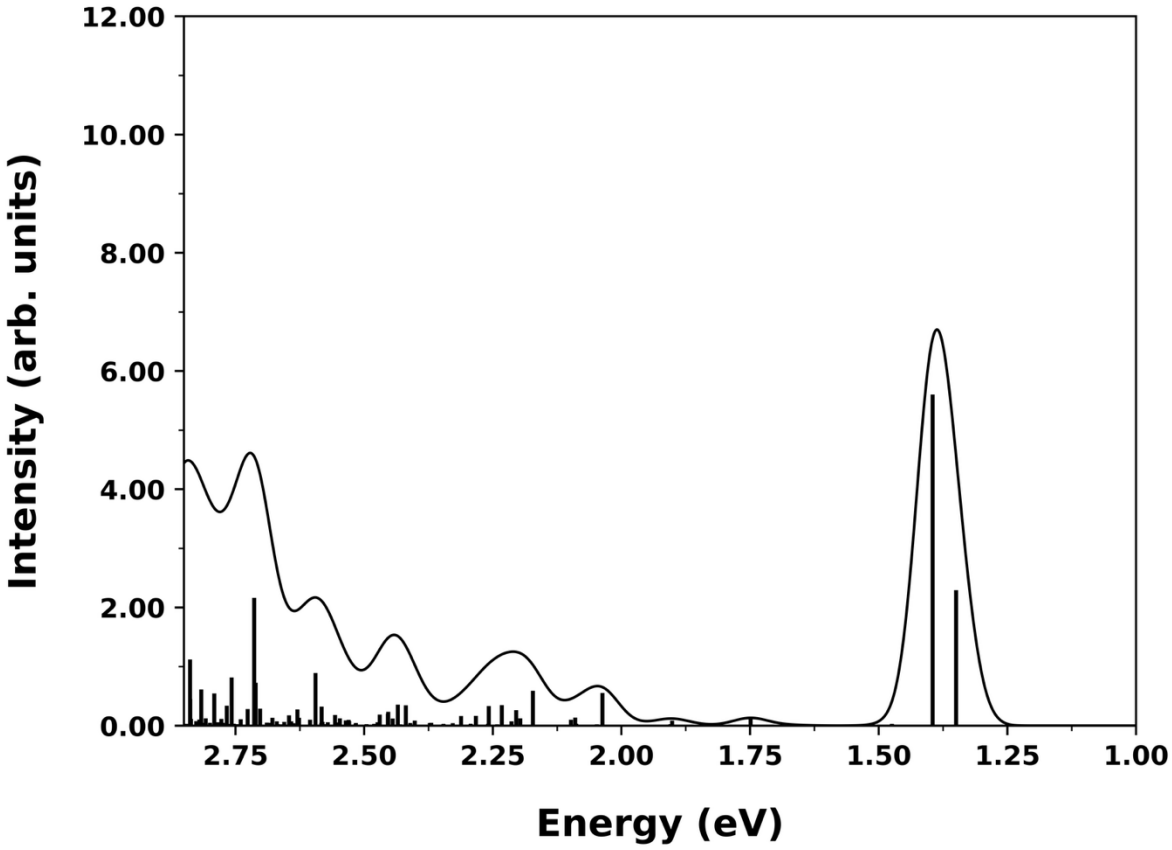
D. Sulalith N. D. Samarasinghe[†], Christine M. Aikens[†*]

[†] Department of Chemistry, Kansas State University, Manhattan, KS 66506, United States

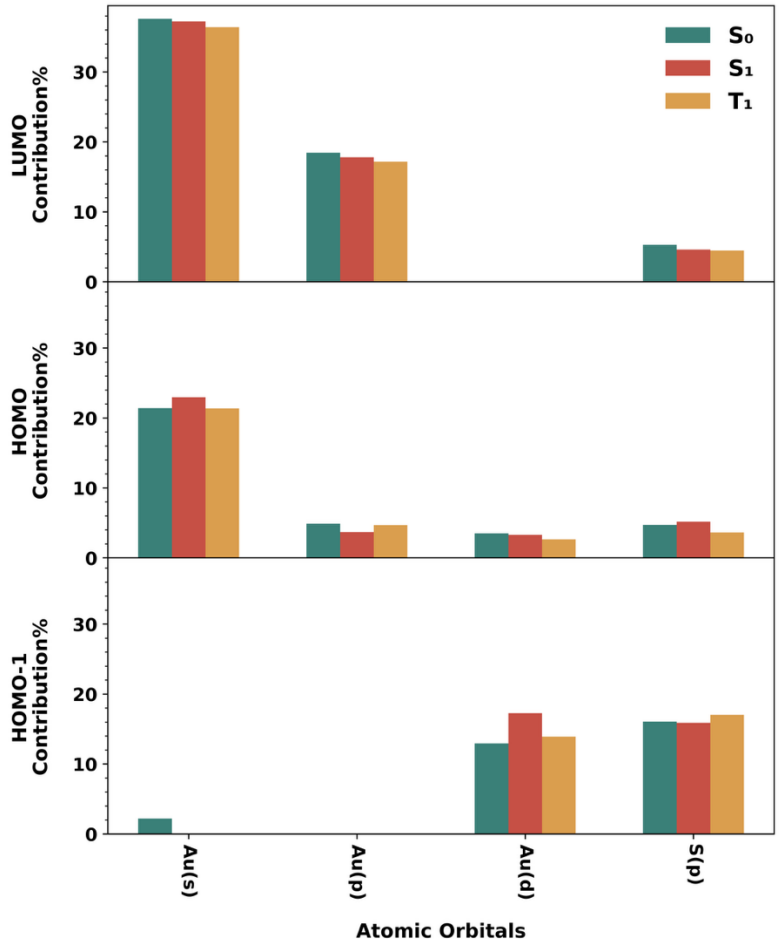
*Email: cmaikens@ksu.edu

I. The theoretical absorption spectrum

The theoretical absorption spectrum shown in Figure S1 successfully captures the absorption features observed experimentally by Li et al.[1] As discussed in the main text, the primary NIR absorption feature appears in the theoretical spectrum as two closely spaced features at approximately 1.35-1.40 eV. Additionally, the gradual onset and broadened absorption above 2.50 eV observed experimentally is well reproduced in the theoretical spectrum. This good agreement between theoretical and experimental spectra supports the validity of the present computational approach.



Appendix Figure B.1. The theoretical absorption spectrum at the BP86-D3/TZP level of theory (in gas phase) of the $Au_{42}(SCH_3)_{32}$ nanorod.



Appendix Figure B.2. Atomic orbital character for each molecular orbital for the respective electronic states at the BP86-D3/TZP level of theory (in gas phase).

Appendix Table B.1 Molecular orbital characteristics for $Au_{42}(SCH_3)_{32}$ at the BP86-D3/TZP level of theory (in gas phase).

Molecular orbital	Primary characteristics
LUMO	Individual s and p orbitals on Au atoms (s orbital contribution is > 35.0% and p orbital contribution is > 15.0%); p orbitals on S atoms (has a contribution < 10.0%) **Metal core centered molecular orbital, dominated by gold atomic orbital contributions**

HOMO	Individual d orbitals (with contributions < 5.0%), and s and p orbitals on Au atoms (s orbital contribution is > 20.0% and p orbital contribution is < 5.0%); p orbitals on S atoms (has a contribution < 10.0%) **Metal core centered molecular orbital, dominated by gold atomic orbital contributions**
HOMO-1	Individual d orbitals (have contributions > 10.0%), and s orbitals on Au atoms (has a contribution < 5.0%); p orbitals on S atoms (have contributions > 15.0 %) **Metal ligand shell centered molecular orbital, dominated by sulfur orbital contributions**

Appendix Table B.2. Excitation properties of the $Au_{42}(SCH_3)_{32}$ nanorod in DCM, acetone, DMBA, and DMFA solvation media obtained from TDDFT calculations at the BP86-D3/TZP level of theory, including excitation energies, oscillator strengths, and the corresponding electronic transitions with their orbital contribution weights.

Excitation energy	Oscillator strength (a.u.)	Transitions	Weight
DCM			
$\boldsymbol{\alpha}$: 1.290 eV (961 nm)	1.454	HOMO → LUMO	0.89
		HOMO-1 → LUMO	0.09
$\boldsymbol{\beta}$: 1.364 eV (909 nm)	0.238	HOMO-1 → LUMO	0.90
		HOMO → LUMO	0.09
acetone			
$\boldsymbol{\alpha}$: 1.277 eV (971 nm)	1.654	HOMO → LUMO	0.92
		HOMO-1 → LUMO	0.06
$\boldsymbol{\beta}$: 1.361 eV (911 nm)	0.200	HOMO-1 → LUMO	0.93
		HOMO → LUMO	0.06
DMBA			
$\boldsymbol{\alpha}$: 1.266 eV (979 nm)	1.756	HOMO → LUMO	0.94
		HOMO-1 → LUMO	0.05
$\boldsymbol{\beta}$: 1.358 eV (913 nm)	0.212	HOMO-1 → LUMO	0.94
		HOMO → LUMO	0.05
DMFA			
$\boldsymbol{\alpha}$: 1.275 eV (972 nm)	1.705	HOMO → LUMO	0.93
		HOMO-1 → LUMO	0.06

$\boldsymbol{\beta}$: 1.361 eV (911 nm)	0.198	HOMO-1 → LUMO	0.94
		HOMO → LUMO	0.05

Appendix Table B.3. Relative ground and excited state energies. Note: S_1/S_2 ordering reverses between gas phase and polar solvents due to differential stabilization. States are labeled E_α and E_β (E_α: excited state corresponding to $\boldsymbol{\alpha}$ excitation and E_β: excited state corresponding to $\boldsymbol{\beta}$ excitation) for consistency across all media (energies are reported in eV).

Medium	Relative ground state energy (S_0)	Relative E_α state energy	Relative E_β state energy
Gas phase	0.0242	1.4196	1.3740
Toluene	0.0118	1.3298	1.3834
DCM	0.0064	1.2970	1.3707
Acetone	0.0045	1.2819	1.3656
DMBA	0.0040	1.2792	1.3626
DMFA	0.0007	1.2670	1.3621
DMAc	0.0000	1.2620	1.3578

Appendix Table B.4. Total transition dipole moments (in *x*, *y*, and *z* directions) for each excitation in different solvation media.

Excitation energy	Oscillator strength (a.u.)	Total transition dipole moment (a.u.)		
		x	*y*	*z*
gas phase				
$\boldsymbol{\beta}$: 1.35 eV (918 nm)	0.194	-2.141	0.264	-1.101
$\boldsymbol{\alpha}$: 1.40 eV (885 nm)	0.475	-3.508	0.479	-1.160
toluene				
$\boldsymbol{\alpha}$: 1.32 eV (939 nm)	0.861	4.755	-0.604	1.922
$\boldsymbol{\beta}$: 1.37 eV (905 nm)	0.340	-3.079	0.445	-0.654
DCM				
$\boldsymbol{\alpha}$: 1.290 eV (961 nm)	1.454	6.323	-0.783	2.322
$\boldsymbol{\beta}$: 1.364 eV (909 nm)	0.238	2.631	-0.385	0.258
acetone				
$\boldsymbol{\alpha}$: 1.277 eV (971 nm)	1.654	-6.804	0.841	-2.419
$\boldsymbol{\beta}$: 1.361 eV (911 nm)	0.200	-2.417	0.372	-0.119
DMBA				
$\boldsymbol{\alpha}$: 1.266 eV (979 nm)	1.756	7.078	-0.886	2.394
$\boldsymbol{\beta}$: 1.358 eV (913 nm)	0.212	2.491	-0.384	0.0641

DMFA				
$\boldsymbol{\alpha}$: 1.275 eV (972 nm)	1.705	-6.919	0.855	-2.440
$\boldsymbol{\beta}$: 1.361 eV (911 nm)	0.198	-2.405	0.368	-0.0906
DMAc				
$\boldsymbol{\alpha}$: 1.26 eV (984 nm)	1.826	7.240	-0.902	2.416
$\boldsymbol{\beta}$: 1.36 eV (912 nm)	0.206	2.457	-0.380	0.0223

Appendix Table B.5. Transition dipole moment contributions (in *x*, *y*, and *z* direction) for each electronic transition, corresponding to the excitations in different solvation media.

Excitation energy	Transitions	Weight	Transition dipole moment contribution (a.u.)		
			x	*y*	*z*
gas phase					
$\boldsymbol{\beta}$: 1.35 eV (918 nm)	HOMO-1 → LUMO	0.70	0.538	-0.111	-0.705
	HOMO → LUMO	0.29	-4.689	0.588	-1.151
$\boldsymbol{\alpha}$: 1.40 eV (885 nm)	HOMO → LUMO	0.66	-7.009	0.880	-1.721
	HOMO-1 → LUMO	0.29	-0.341	0.0702	0.447
toluene					
$\boldsymbol{\alpha}$: 1.32 eV (939 nm)	HOMO → LUMO	0.74	7.625	-0.963	1.903
	HOMO-1 → LUMO	0.24	-0.451	0.0907	0.387
$\boldsymbol{\beta}$: 1.37 eV (905 nm)	HOMO-1 → LUMO	0.75	-0.785	0.158	0.673
	HOMO → LUMO	0.23	-4.154	0.524	-1.037
DCM					
$\boldsymbol{\alpha}$: 1.290 eV (961 nm)	HOMO → LUMO	0.89	8.434	-1.068	2.122
	HOMO-1 → LUMO	0.09	-0.322	0.0615	0.246
$\boldsymbol{\beta}$: 1.364 eV (909 nm)	HOMO-1 → LUMO	0.90	0.967	-0.185	-0.739
	HOMO → LUMO	0.09	2.611	-0.331	0.657
acetone					
$\boldsymbol{\alpha}$: 1.277 eV (971 nm)	HOMO → LUMO	0.92	-8.646	1.094	-2.204
	HOMO-1 → LUMO	0.06	0.269	-0.0566	-0.202
$\boldsymbol{\beta}$: 1.361 eV (911 nm)	HOMO-1 → LUMO	0.93	-0.994	0.209	0.746
	HOMO → LUMO	0.06	-2.157	0.273	-0.550
DMBA					

$\boldsymbol{\alpha}$: 1.266 eV (979 nm)	HOMO → LUMO	0.94	8.698	-1.108	2.210
	HOMO-1 → LUMO	0.05	-0.288	0.0539	0.172
$\boldsymbol{\beta}$: 1.358 eV (913 nm)	HOMO-1 → LUMO	0.94	1.170	-0.219	-0.700
	HOMO → LUMO	0.05	1.964	-0.250	0.499
DMFA					
$\boldsymbol{\alpha}$: 1.275 eV (972 nm)	HOMO → LUMO	0.93	-8.672	1.101	-2.208
	HOMO-1 → LUMO	0.06	0.265	-0.0535	-0.195
$\boldsymbol{\beta}$: 1.361 eV (911 nm)	HOMO-1 → LUMO	0.94	-1.017	0.206	0.748
	HOMO → LUMO	0.05	-2.076	0.264	-0.529
DMAc					
$\boldsymbol{\alpha}$: 1.26 eV (984 nm)	HOMO → LUMO	0.94	8.742	-1.113	2.225
	HOMO-1 → LUMO	0.05	-0.275	0.0513	0.162
$\boldsymbol{\beta}$: 1.36 eV (912 nm)	HOMO-1 → LUMO	0.95	1.191	-0.222	-0.699
	HOMO → LUMO	0.04	1.848	-0.235	0.470

References

1. Li, Y.; Song, Y.; Zhang, X.; Liu, T.; Xu, T.; Wang, H.; Jiang, D.; Jin, R. Atomically Precise Au_{42} Nanorods with Longitudinal Excitons for an Intense Photothermal Effect. *J. Am. Chem. Soc.* **2022**, *144* (27), 12381–12389.

Appendix C - Supporting information for: Development of a machine learning force field for gold hydride nanoclusters that predicts potential energy with quantum-level precision

D. Sulalith N. D. Samarasinghe[†], Yuchen Wang [†], Christine M. Aikens[†*]

[†] Department of Chemistry, Kansas State University, Manhattan, KS 66506, United States

*Email: cmaikens@ksu.edu

I. Incorporating hyperparameters

In Eq. 5.1, the training coefficient (α) depends on a diagonal matrix of noise values that capture the expected error related to training label, incorporating the corresponding noise hyperparameters for energy, force and stress. These values were drawn from the standard noise parameters recommended by the FLARE++ module. Within the training process, total Gaussian process uncertainty ($\sqrt{\sigma_n^2 + \sigma_{i\alpha}^2}$) can be separated into two distinct terms: the epistemic uncertainty ($\sigma_{i\alpha}$), which emerges from the limitations of the training data and evolves through the training process, and the noise term (σ_n), which accounts for the inherent variability present in the training data that lies beyond the capacity of the model to reproduce, a characteristic behavior commonly associated with Gaussian process models. It is worth noting that all hyperparameters are continuously optimized as new local environments and their respective components are incorporated into the training set, enabling the error threshold to dynamically adapt to novel environments encountered throughout the simulation.[1-3] A more through description of the hyperparameter evaluation and optimization can be found in Vandermause et al.[1,2]

II. Conformers of the $Au_{13}H_5$ nanocluster

Multiple conformers of the $Au_{13}H_5$ nanocluster can be formed from different arrangements of hydride ligands within the cluster structure. The relative energies of three are presented in Table C.1. Note that the $Au_{13}H_5$ bridge I conformer is energetically more favorable than the other two, and therefore the relative energies are represented with respect to the $Au_{13}H_5$ bridge I conformer. The bridge I structure is not necessarily the global minimum for this nanocluster, but the global minimum is not required for MLFF training.

Appendix Table C.1. Relative energies of the three $Au_{13}H_5$ nanocluster conformers considered in this work at the BP86/TZP level of theory.

Conformer	Relative energy (eV)
Edge	1.04
Bridge I	0.00
Bridge II	0.37

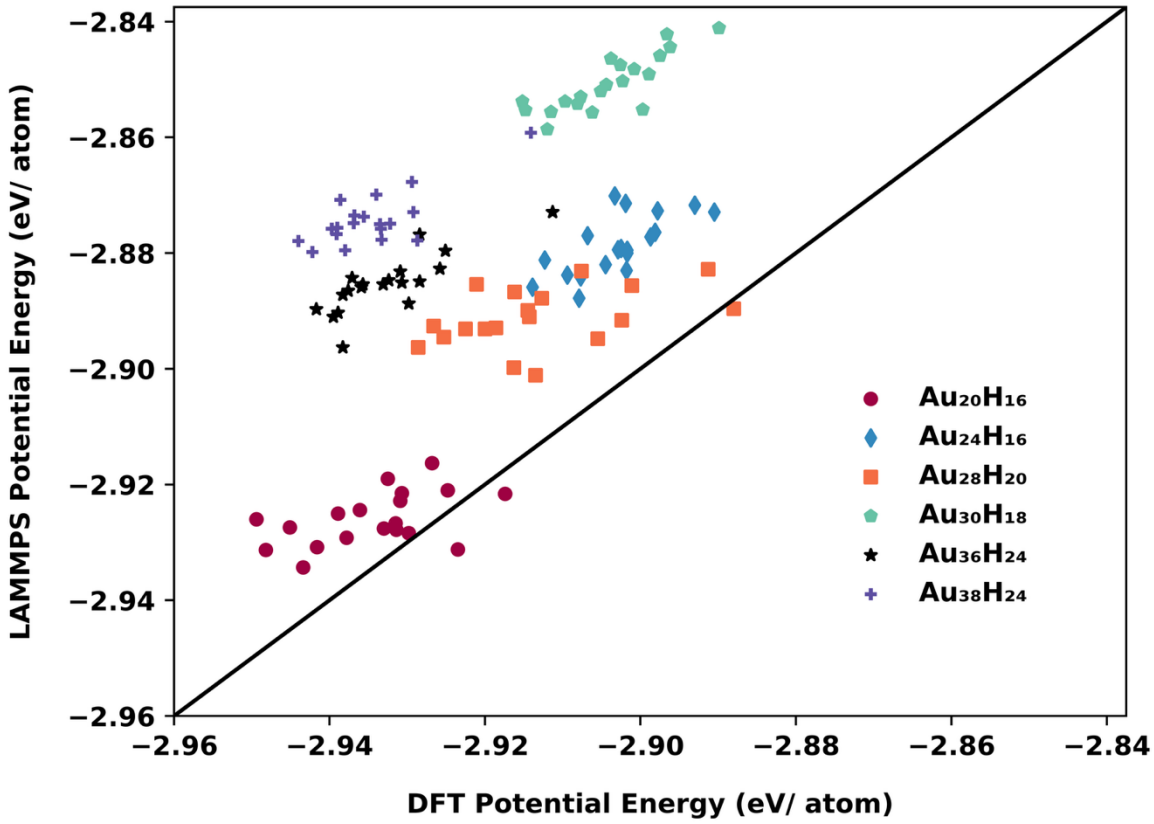
III. Mean absolute deviation (MAD) and root mean square error (RMSE) values

Mean absolute deviation (MAD, Eq. C.1) and root mean square error (RMSE, Eq. C.2) were calculated as follows. For comparison between MLFF predicted potential energies (from LAMMPS, E_{MLFF}) and DFT reference energies (E_{DFT}), $\bar{x}$ represents the average difference for all predictions, while x_i is the potential energy difference for a single frame ($E_{MLFF} - E_{DFT}$). n denotes the total number of frames considered for the test set. Dividing the resulting MAD and RMSE values by the number of atoms in each system yields the per-atom error metrics used throughout this study.

$$MAD = \frac{\sum_i |x_i - \bar{x}|}{n} \quad \text{(C. 1)}$$

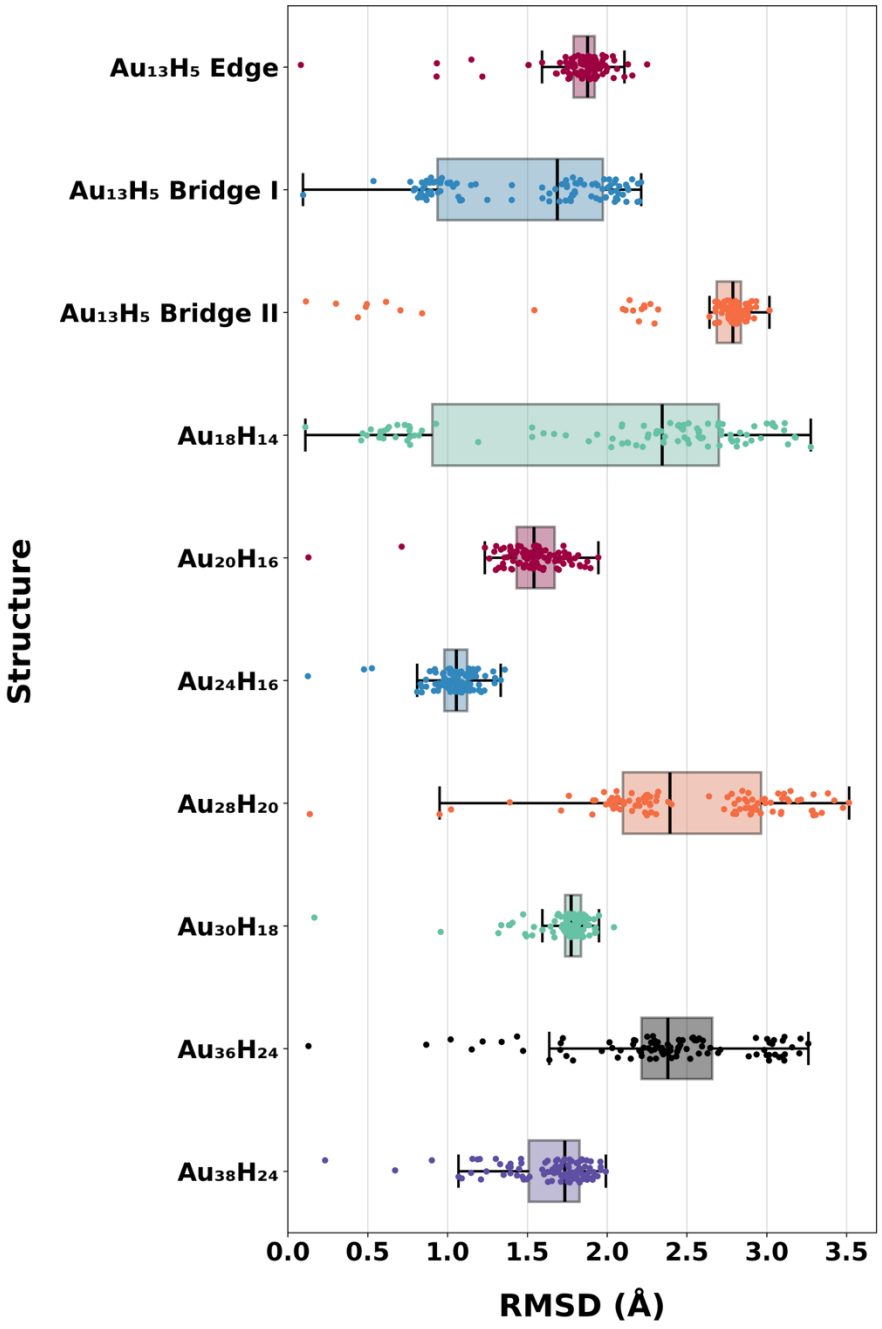
$$RMSE = \sqrt{\frac{1}{n}\sum_{i}^{n} x_i^2} \qquad (C.2)$$

IV. Prediction accuracy per atom for structures outside the training set

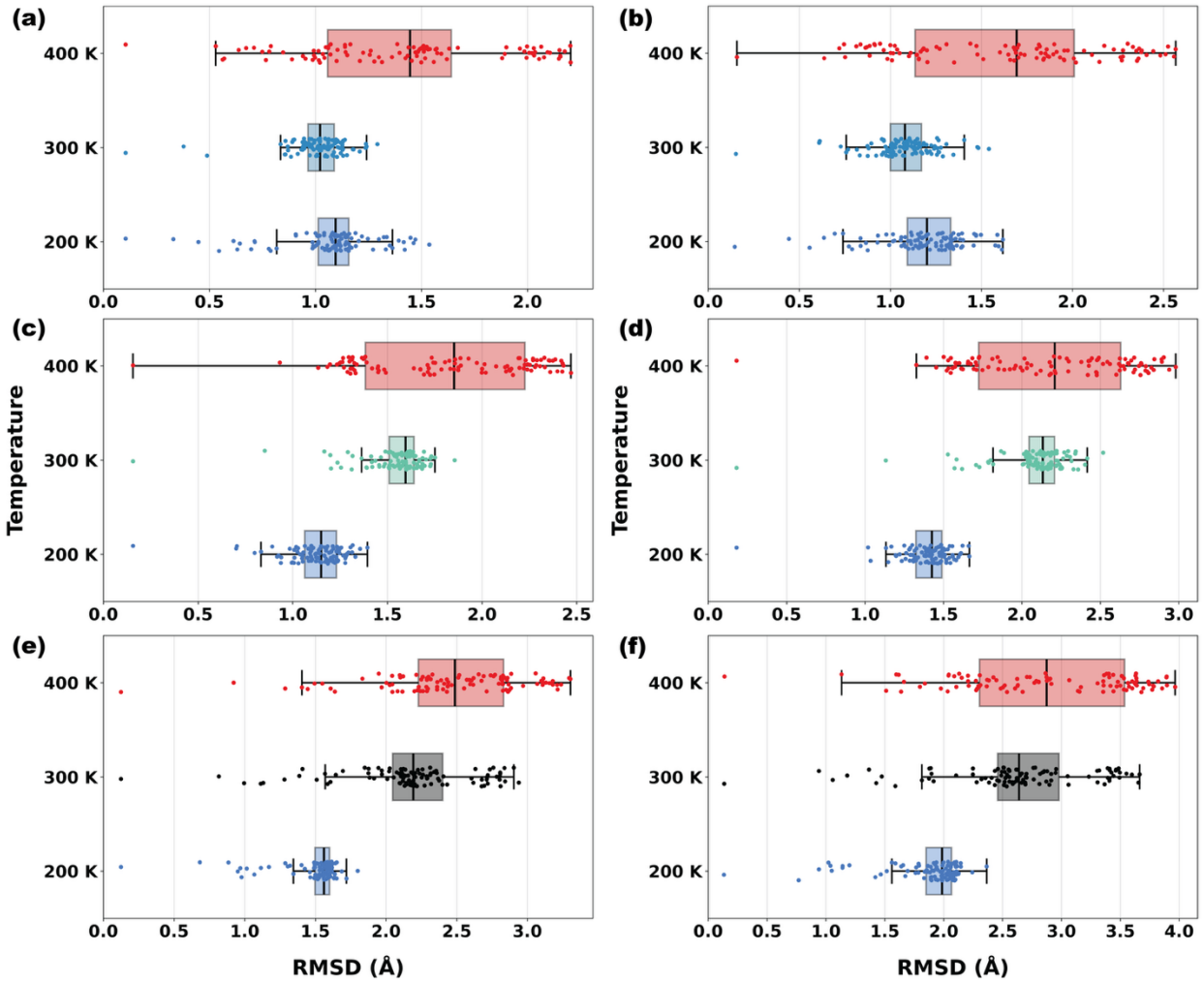


Appendix Figure C.1. Prediction accuracy per atom for structures outside the training set before offset corrections.

V. Structural landscape analysis



Appendix Figure C.2. Box plots showing total RMSDs across all tested systems during 300 K MD simulations.



Appendix Figure C.3. Box plots showing RMSDs at different temperatures for (a,c,e) gold atoms and (b,d,f) hydrogen atoms in $Au_{24}H_{16}$, $Au_{30}H_{18}$, and $Au_{36}H_{24}$, respectively.

References

1. Vandermause, J.; Xie, Y.; Lim, J. S.; Owen, C. J.; Kozinsky, B. Active Learning of Reactive Bayesian Force Fields Applied to Heterogeneous Catalysis Dynamics of H/Pt. *Nat Commun* **2022**, *13* (1), 5183.

2. Vandermause, J.; Torrisi, S. B.; Batzner, S.; Xie, Y.; Sun, L.; Kolpak, A. M.; Kozinsky, B. On-the-Fly Active Learning of Interpretable Bayesian Force Fields for Atomistic Rare Events. *npj Comput. Mater.* **2020**, *6* (1), 20.

3. Wang, Y.; Samarasinghe, D. S. N. D.; Deng, H.; Liu, B.; Aikens, C. M. Gaussian Process Approach to Constructing Transferable Force Fields for Thiolate-Protected Gold Nanoclusters. *J. Chem. Inf. Model.* **2025**.

Appendix D - Supporting information for: Implementation of analytical excited state gradients for open-shell systems in time-dependent density functional theory plus tight binding (TDDFT+TB) method

D. Sulalith N. D. Samarasinghe[†], Shana Havenridge[†], Christine M. Aikens[†*]

[†] Department of Chemistry, Kansas State University, Manhattan, KS 66506, United States

*Email: cmaikens@ksu.edu

I. From TDDFT to TDDFT+TB

The Casida approach [Eq. (D.1)] within the time-dependent density functional theory (TDDFT) is used to solve the eigenvalue problem and obtain the excitation energies.[1]

$$\begin{pmatrix} A & B \\ B^* & A^* \end{pmatrix}\begin{pmatrix} X \\ Y \end{pmatrix} = \omega \begin{pmatrix} 1 & 0 \\ 0 & -1 \end{pmatrix}\begin{pmatrix} X \\ Y \end{pmatrix} \quad (D.1)$$

where ω denotes the excitation energy. It is important to note that the Casida equation can be transformed into the form shown in Eq. (D.2),[2,3]

$$\Omega F = \omega^2 F \quad (D.2)$$

where,

$$F = (A-B)^{-\frac{1}{2}}(X+Y) \quad (D.3)$$

$$\Omega = (A-B)^{\frac{1}{2}}(A+B)(A-B)^{\frac{1}{2}} \quad (D.4)$$

In TDDFT, $(A+B)$ and $(A-B)$ have the following forms,[4]

$$(A+B)_{ia\sigma,jb\sigma'} = (\epsilon_{a\sigma}-\epsilon_{j\sigma})\delta_{ij}\delta_{ab}\delta_{\sigma\sigma'} + 2(ia\sigma|jb\sigma') + 2\left(ia|f^{xc}_{\sigma\sigma'}|jb\right) - c_x\delta_{\sigma\sigma'}[(ja\sigma|ib\sigma) + (ab\sigma|ij\sigma)] \quad (D.5)$$

$$(A-B)_{ia\sigma,jb\sigma'} = (\epsilon_{a\sigma}-\epsilon_{j\sigma})\delta_{ij}\delta_{ab}\delta_{\sigma\sigma'} + c_x\delta_{\sigma\sigma'}[(ja\sigma|ib\sigma) - (ab\sigma|ij\sigma)] \quad (D.6)$$

The hybrid mixing parameter is denoted as c_x while the Coulomb-exchange-correlation kernel in the adiabatic approximation is given by $f_{\sigma\sigma'}^{uxc}$.[4] It is important to note that

$$c_x = \begin{cases} 1\,; \text{TDHF theory}, E^{xc} = 0 \\ 0\,; \text{pure density functional} \end{cases}$$

and the TDDFT+TB method can only employ pure exchange-correlation functionals ($c_x = 0$). Therefore Eq. (D.5) and Eq. (D.6) can be rewritten as follows,

$$(A+B)_{ia\sigma,jb\sigma'} = \left(\epsilon_{a\sigma} - \epsilon_{j\sigma}\right)\delta_{ij}\delta_{ab}\delta_{\sigma\sigma'} + 2(ia\sigma|jb\sigma') + 2\left(ia|f_{\sigma\sigma'}^{xc}|jb\right) \quad (D.7)$$

$$(A-B)_{ia\sigma,jb\sigma'} = \left(\epsilon_{a\sigma} - \epsilon_{j\sigma}\right)\delta_{ij}\delta_{ab}\delta_{\sigma\sigma'} \quad (D.8)$$

The Coulomb-exchange-correlation kernel ($f_{\sigma\sigma'}^{uxc}$) has the following form,[4-6]

$$f_{\sigma\sigma'}^{uxc} = \left(\frac{1}{|\boldsymbol{r}-\boldsymbol{r}'|} + \frac{\delta^2 E^{xc}}{\delta\rho_\sigma(\boldsymbol{r})\delta\rho_{\sigma'}(\boldsymbol{r}')}\right) \quad (D.9)$$

where the static exchange-correlation energy functional is denoted by E^{xc}, and the charge-density fluctuations are denoted as $\delta\rho$ with respect to their spin. $1/|\boldsymbol{r}-\boldsymbol{r}'|$ is the Coulomb term. Therefore, the full integral, $f_{ia\sigma,jb\sigma'}^{uxc} = \left(ia|f_{\sigma\sigma'}^{uxc}|jb\right)$, can be written as,[2,7]

$$f_{ia\sigma,jb\sigma'}^{uxc} = \iint \phi_{i\sigma}(\boldsymbol{r})\phi_{a\sigma}(\boldsymbol{r}) \times \left(\frac{1}{|\boldsymbol{r}-\boldsymbol{r}'|} + \frac{\delta^2 E^{xc}}{\delta\rho_\sigma(\boldsymbol{r})\delta\rho_{\sigma'}(\boldsymbol{r}')}\right) \times \phi_{j\sigma'}(\boldsymbol{r})\phi_{b\sigma'}(\boldsymbol{r}) \quad (D.10)$$

and

$$\frac{\delta^2 E^{xc}}{\delta\rho_\sigma(\boldsymbol{r})\delta\rho_{\sigma'}(\boldsymbol{r}')} = \frac{\delta^2 E^{xc}}{\delta\rho(\boldsymbol{r})\delta\rho(\boldsymbol{r}')} + \delta_\sigma \frac{\delta^2 E^{xc}}{\delta m(\boldsymbol{r})\delta\rho(\boldsymbol{r}')} + \delta_{\sigma'} \frac{\delta^2 E^{xc}}{\delta\rho(\boldsymbol{r})\delta m(\boldsymbol{r}')} + \delta_\sigma\delta_{\sigma'} \frac{\delta^2 E^{xc}}{\delta m(\boldsymbol{r})\delta m(\boldsymbol{r}')} \quad (D.11)$$

where m denotes the magnetization, and $\delta_\sigma = 2\delta_{\uparrow\sigma} - 1$, where,

$$\delta_\sigma = \begin{cases} 1; \text{when } \delta_{\uparrow\sigma} = 1, \text{if } \sigma \text{ is spin} - \text{up} \\ -1; \text{when } \delta_{\uparrow\sigma} = 0, \text{if } \sigma \text{ is spin} - \text{down} \end{cases}.$$

It is important to note that the key change in TDDFT+TB arises from the application of a first-order monopole approximation to the TDDFT formalism. This approximation addresses the

computationally expensive two-electron integrals ($(ia\sigma|jb\sigma')$ and $f^{xc}_{ia\sigma,jb\sigma'}$) in the TDDFT approach by applying a DFTB-like approximations. Therefore, the two electron integrals are not calculated; instead, the transition densities are approximated as,[7-9]

$$\phi_{i\sigma}(\boldsymbol{r})\phi_{a\sigma}(\boldsymbol{r}) \approx \sum_{Al} q_{ia\sigma,Al}\zeta_{Al}(\boldsymbol{r}) \tag{D.12}$$

$$q_{ia\sigma,Al} = \sum_{\mu\in A,l} C'_{\mu i\sigma}C'_{\mu a\sigma} \tag{D.13}$$

$$C' = S^{1/2}C \tag{D.14}$$

where the atomic transition charges are denoted by $q_{ia\sigma,Al}$. $\zeta_{Al}(\boldsymbol{r})$ is a spherically symmetric function, which is centered on atom A. Notably, $q_{ia\sigma,Al}$ is calculated from the Kohn-Sham molecular orbital coefficient matrix (C) and the overlap matrix (S). Additionally, the atomic transition charges in TDDFT+TB employ Löwdin population analysis instead of Mulliken analysis.[8] Therefore, the new coupling matrix ($K_{ia\sigma,jb\sigma'}$) takes the following form,[2,7,10]

$$K_{ia\sigma,jb\sigma'} = \sum_{ABll'} q_{ia\sigma,Al}\left[\gamma_{Al,Bl'} + \delta_\sigma\delta_{\sigma'}\delta_{AB}W_{Al,l'} + 2\delta_\sigma\delta_{\sigma\sigma'}D_{Al,Bl'}\right]q_{jb\sigma',Bl'} \tag{D.15}$$

$$\gamma_{Al,Bl'} = \left(\zeta_{Al}(\boldsymbol{r})\left|\frac{1}{|\boldsymbol{r}-\boldsymbol{r}'|} + \frac{\delta^2E^{xc}}{\delta\rho(\boldsymbol{r})\delta\rho(\boldsymbol{r}')}\right|_\rho\right|\zeta_{Bl'}(\boldsymbol{r}')\right) \tag{D.16}$$

$$W_{Al,l'} = \left(\zeta_{Al}(\boldsymbol{r})\left|\frac{\delta^2E^{xc}}{\delta m(\boldsymbol{r})\delta m(\boldsymbol{r}')}\right|_\rho\right|\zeta_{Bl'}(\boldsymbol{r}')\right) \tag{D.17}$$

$$D_{Al,Bl'} = \left(\zeta_{Al}(\boldsymbol{r})\left|\frac{\delta^2E^{xc}}{\delta m(\boldsymbol{r})\delta\rho(\boldsymbol{r}')}\right|_\rho\right|\zeta_{Bl'}(\boldsymbol{r}')\right) \tag{D.18}$$

Parameter $D_{Al,Bl'}$ has the mixed derivative components with respect to ρ and m. When spin-orbit interactions are neglected, $D_{Al,Bl'} = 0$.[7] Then, Eq. (D.15) becomes,

$$K_{ia\sigma,jb\sigma'} = \sum_{ABll'} \left[q_{ia\sigma,Al} \gamma_{Al,Bl'} q_{jb\sigma',Bl'} + q_{ia\sigma,Al} \delta_{\sigma} \delta_{\sigma'} \delta_{AB} W_{Al,l'} q_{jb\sigma',Bl'} \right] \quad \text{(D. 19)}$$

$$K_{ia\sigma,jb\sigma'} = K^{S}_{ia\sigma,jb\sigma'} + K^{T}_{ia\sigma,jb\sigma'} \quad \text{(D. 19)}$$

Both on-site terms are approximated by Hubbard terms: (1) the gamma function ($\gamma_{Al,Bl'}$) and (2) the magnetic Hubbard parameter, $W_{Al,l'} = \frac{1}{2}\left(\partial \varepsilon_{l\uparrow}^{HOMO} / \partial n_{l'\uparrow} - \partial \varepsilon_{l\uparrow}^{HOMO} / \partial n_{l'\downarrow}\right)$.[2,10] It is important to note that both chemical hardness and magnetic Hubbard parameters can be calculated via atomic DFT calculations.[2,8] The superscripts *S* and *T* in the coupling matrix term (Eq. D.19) indicate singlet and triplet excitations, where $K^{S}_{ia\sigma,jb\sigma'}$ will be applicable for closed-shell systems, and $K^{T}_{ia\sigma,jb\sigma'}$ will also be required for open-shell systems. Though "S" and "T" are used here, these equations are applicable for all open-shell cases.

Therefore using Eq. (D.19), the $(A+B)_{ia\sigma,jb\sigma'}$ term in Eq. (D.7) can be expressed according to the TDDFT+TB formalism as,

$$(A+B)_{ia\sigma,jb\sigma'} = \left(\epsilon_{a\sigma} - \epsilon_{j\sigma}\right)\delta_{ij}\delta_{ab}\delta_{\sigma\sigma'} + 4K_{ia\sigma,jb\sigma'} \quad (D.20)$$

II. Derivation of the excitation energy

The expanded form of Eq. (6.11) is given by:

$$Q_{pq\sigma} = \sum_{\mu} \frac{1}{2} \begin{pmatrix} X+Y \\ X-Y \end{pmatrix} \begin{pmatrix} \dfrac{\partial (A+B)_{ia\sigma,jb\sigma'}}{\partial C_{\mu p\sigma}} C_{\mu q\sigma} & 0 \\ 0 & \dfrac{\partial (A-B)_{ia\sigma,jb\sigma'}}{\partial C_{\mu p\sigma}} C_{\mu q\sigma} \end{pmatrix} \begin{pmatrix} X+Y \\ X-Y \end{pmatrix}$$

$$= \frac{1}{2} \sum_{ia\sigma} \sum_{jb\sigma'} (X+Y)_{ia\sigma} \sum_{\mu} \frac{\partial (A+B)_{ia\sigma,jb\sigma'}}{\partial C_{\mu p\sigma}} C_{\mu q\sigma} \, (X+Y)_{jb\sigma'}$$

$$+ \frac{1}{2} \sum_{ia\sigma} \sum_{jb\sigma'} (X-Y)_{ia\sigma} \sum_{\mu} \frac{\partial (A-B)_{ia\sigma,jb\sigma'}}{\partial C_{\mu p\sigma}} C_{\mu q\sigma} \, (X-Y)_{jb\sigma'} \quad (D.21)$$

Substituting Eq. (6.5) and Eq. (6.6) into Eq. (D.21),

$$= \frac{1}{2}\sum_{ia\sigma}\sum_{jb\sigma'}(X+Y)_{ia\sigma}\sum_{\mu}\frac{\partial\left(F_{ab\sigma}\delta_{ij}-F_{ij\sigma}\delta_{ab}\right)\delta_{\sigma\sigma'}}{\partial C_{\mu p\sigma}}C_{\mu q\sigma}\,(X+Y)_{jb\sigma'}$$

$$+\frac{1}{2}\sum_{ia\sigma}\sum_{jb\sigma'}(X+Y)_{ia\sigma}\sum_{\mu}4\frac{\partial K_{ia\sigma,jb\sigma'}}{\partial C_{\mu p\sigma}}C_{\mu q\sigma}\,(X+Y)_{jb\sigma'}$$

$$+\frac{1}{2}\sum_{ia\sigma}\sum_{jb\sigma'}(X-Y)_{ia\sigma}\sum_{\mu}\frac{\partial\left(F_{ab\sigma}\delta_{ij}-F_{ij\sigma}\delta_{ab}\right)\delta_{\sigma\sigma'}}{\partial C_{\mu p\sigma}}C_{\mu q\sigma}\,(X-Y)_{jb\sigma'} \qquad (D.22)$$

Following Furche et al.,[4] we define the unrelaxed difference density matrix T,

$$T_{ab\sigma} = \frac{1}{2}\sum_{i}((X+Y)_{ia\sigma}(X+Y)_{ib\sigma}+(X-Y)_{ia\sigma}(X-Y)_{ib\sigma}) \qquad (D.23)$$

$$T_{ij\sigma} = -\frac{1}{2}\sum_{a}\left((X+Y)_{ia\sigma}(X+Y)_{ja\sigma}+(X-Y)_{ia\sigma}(X-Y)_{ja\sigma}\right) \qquad (D.24)$$

$$T_{ia\sigma} = T_{ai\sigma} = 0$$

and linear transformations,

$$H^{+}_{pq\sigma}[T] = \sum_{rs\sigma'}\left[2(pq\sigma|rs\sigma')+2f^{xc}_{pq\sigma,rs\sigma'}\right]T_{rs\sigma} \qquad (D.25)$$

It should be noted that in TDDFT, two linear transformations called $H^{+}_{pq\sigma}[T]$ and $H^{-}_{pq\sigma}[T]$ include terms involving c_x.[4] These terms are excluded in TDDFT+TB since we consider only pure functionals; this leads to $H^{-}_{pq\sigma}[T] = 0$.

The following equations show the four distinct conditions that emerge from the molecular orbital constraints for Z and W once the unrelaxed difference density matrix T and linear transformation definitions from TDDFT are applied. We begin with the TDDFT formulation and then demonstrate how it is modified for the TDDFT+TB framework:

For p and q both occupied,

$$Q_{ij\sigma} = \Omega \sum_{a} \left\{ (X+Y)_{ia\sigma}(X-Y)_{ja\sigma} + (X-Y)_{ia\sigma}(X+Y)_{ja\sigma} \right\}$$

$$- \sum_{a} \varepsilon_{a\sigma} \left\{ (X+Y)_{ia\sigma}(X+Y)_{ja\sigma} + (X-Y)_{ia\sigma}(X-Y)_{ja\sigma} \right\} + H^{+}_{ij\sigma}[T]$$

$$+2 \sum_{kc\sigma',ld\sigma''} g^{xc}_{ij\sigma,kc\sigma',ld\sigma''} (X+Y)_{kc\sigma'}(X+Y)_{ld\sigma''}$$

where, $g^{xc}_{ij\sigma,kc\sigma',ld\sigma''} = 0$ for TDDFT+TB,

$$Q_{ij\sigma} = \Omega \sum_{a} \left\{ (X+Y)_{ia\sigma}(X-Y)_{ja\sigma} + (X-Y)_{ia\sigma}(X+Y)_{ja\sigma} \right\}$$

$$- \sum_{a} \varepsilon_{a\sigma} \left\{ (X+Y)_{ia\sigma}(X+Y)_{ja\sigma} + (X-Y)_{ia\sigma}(X-Y)_{ja\sigma} \right\} + H^{+}_{ij\sigma}[T] \qquad (D.26)$$

For p and q both virtual,

$$Q_{ab\sigma} = \Omega \sum_{i} \{ (X+Y)_{ia\sigma}(X-Y)_{ib\sigma} + (X-Y)_{ia\sigma}(X+Y)_{ib\sigma} \}$$

$$+ \sum_{i} \varepsilon_{i\sigma} \{ (X+Y)_{ia\sigma}(X+Y)_{ib\sigma} + (X-Y)_{ia\sigma}(X-Y)_{ib\sigma} \} \qquad (D.27)$$

When p is occupied and q is virtual,

$$Q_{ia\sigma} = \sum_{b} \{ (X+Y)_{ib\sigma} H^{+}_{ab\sigma}[X+Y] + (X-Y)_{ib\sigma} H^{-}_{ab\sigma}[X-Y] \} + H^{+}_{ia\sigma}[T]$$

$$+2 \sum_{jb\sigma',kc\sigma''} g^{xc}_{ia\sigma,jb\sigma',kc\sigma''} (X+Y)_{jb\sigma'}(X+Y)_{kc\sigma''}$$

where, $g^{xc}_{ia\sigma,jb\sigma',kc\sigma''} = 0$, and $H^{-}_{ab\sigma}[X-Y] = 0$,

$$H^{+}_{ab\sigma}[X+Y] = \sum_{jc\sigma'} \left[2(ab\sigma|jc\sigma') + 2f^{xc}_{ab\sigma,jc\sigma'} \right] (X+Y)_{jc\sigma}$$

$$H^{+}_{ab\sigma}[X+Y] = 2 \sum_{jc\sigma'} K_{ab\sigma,jc\sigma'} (X+Y)_{jc\sigma}$$

$$Q_{ia\sigma} = 2\sum_{b}(X+Y)_{ib\sigma}\sum_{jc\sigma'}K_{ab\sigma,jc\sigma'}\,(X+Y)_{jc\sigma} + H^{+}_{ia\sigma}[T] \qquad (D.28)$$

For p virtual and q occupied,

$$Q_{ai\sigma} = \sum_{j}\left\{(X+Y)_{ja\sigma}H^{+}_{ji\sigma}[X+Y] + (X-Y)_{ia\sigma}H^{-}_{ji\sigma}[X-Y]\right\}$$

where, $H^{+}_{ji\sigma}[X+Y] = \sum_{kb\sigma'}\left[2(ji\sigma|kb\sigma') + 2f^{xc}_{ji\sigma,kb\sigma'}\right](X+Y)_{kb\sigma} = 2\sum_{kb\sigma'}K_{ji\sigma,kb\sigma'}(X+Y)_{kb\sigma}$ and $H^{-}_{ji\sigma}[X-Y] = 0$,

Thus,

$$Q_{ai\sigma} = 2\sum_{j}(X+Y)_{ja\sigma}\sum_{kb\sigma'}K_{ji\sigma,kb\sigma'}\,(X+Y)_{kb\sigma} \qquad (D.29)$$

An important consideration is that Eq. (6.10) transforms to Eq. (6.12), (6.14), (6.16), and (6.18) within the TDDFT+TB approach. The resulting relation of $W_{ia\sigma} = W_{ai\sigma}$ can be expressed as follows, by subtracting Eq. (6.18) − Eq. (6.16):

$$Q_{ai\sigma} + \varepsilon_{i\sigma}Z_{ia\sigma} - Q_{ia\sigma} - \varepsilon_{a\sigma}Z_{ia\sigma} - H^{+}_{ia\sigma}[Z] = 0$$

$$Q_{ai\sigma} - Q_{ia\sigma} = -(Q_{ia\sigma} - Q_{ai\sigma}) = (\varepsilon_{a\sigma} - \varepsilon_{i\sigma})Z_{ia\sigma} + H^{+}_{ia\sigma}[Z] \qquad (D.30)$$

From the Z vector equation,

$$-R_{ia\sigma} = \sum_{jb\sigma'}(A+B)^{TDDFT}_{ia\sigma,jb\sigma'}Z_{jb\sigma'} \qquad (D.31)$$

$$-R_{ia\sigma} = -(Q_{ia\sigma} - Q_{ai\sigma}) \qquad (D.32)$$

$$R_{ia\sigma} = 2\sum_{b}(X+Y)_{ib\sigma}\sum_{jc\sigma'}K_{ab\sigma,jc\sigma'}\,(X+Y)_{jc\sigma} + H^{+}_{ia\sigma}[T] - 2\sum_{j}(X+Y)_{ja\sigma}\sum_{kb\sigma'}K_{ji\sigma,kb\sigma'}\,(X+Y)_{kb\sigma} \qquad (D.33)$$

$$\sum_{jb\sigma'}(A+B)^{TDDFT}_{ia\sigma,jb\sigma'} = \left(\epsilon_{a\sigma} - \epsilon_{j\sigma}\right)\delta_{ij}\delta_{ab}\delta_{\sigma\sigma'} + 4K_{ia\sigma,jb\sigma'} \qquad (D.34)$$

Therefore, next step is to solve the Lagrange multiplier, W, where p and q are both occupied [Eq. (6.12)],

$$W_{ij\sigma} = \frac{1}{1+\delta_{ij}}\left(Q_{ij\sigma} + H^{+}_{ij\sigma}[Z]\right)$$

$$W_{ij\sigma} = \frac{1}{1+\delta_{ij}}\Bigg(\Omega\sum_{a}\left\{(X+Y)_{ia\sigma}(X-Y)_{ja\sigma} + (X-Y)_{ia\sigma}(X+Y)_{ja\sigma}\right\}$$

$$-\sum_{a}\varepsilon_{a\sigma}\left\{(X+Y)_{ia\sigma}(X+Y)_{ja\sigma} + (X-Y)_{ia\sigma}(X-Y)_{ja\sigma}\right\} + H^{+}_{ij\sigma}[T] + H^{+}_{ij\sigma}[Z]\Bigg)$$

where, the relaxed one-particle difference density matrix is $P = T + Z$.

$$W_{ij\sigma} = \frac{1}{1+\delta_{ij}}\Bigg(\Omega\sum_{a}\left\{(X+Y)_{ia\sigma}(X-Y)_{ja\sigma} + (X-Y)_{ia\sigma}(X+Y)_{ja\sigma}\right\}$$

$$-\sum_{a}\varepsilon_{a\sigma}\left\{(X+Y)_{ia\sigma}(X+Y)_{ja\sigma} + (X-Y)_{ia\sigma}(X-Y)_{ja\sigma}\right\} + H^{+}_{ij\sigma}[P]\Bigg) \qquad (D.35)$$

For p and q both virtual [Eq. (6.14)],

$$W_{ab\sigma} = \frac{1}{1+\delta_{ab}}Q_{ab\sigma}$$

$$W_{ab\sigma} = \frac{1}{1+\delta_{ab}}\Bigg(\Omega\sum_{i}\{(X+Y)_{ia\sigma}(X-Y)_{ib\sigma} + (X-Y)_{ia\sigma}(X+Y)_{ib\sigma}\}$$

$$+\sum_{i}\varepsilon_{i\sigma}\{(X+Y)_{ia\sigma}(X+Y)_{ib\sigma} + (X-Y)_{ia\sigma}(X-Y)_{ib\sigma}\}\Bigg) \qquad (D.36)$$

Where p is occupied and q is virtual [Eq. (6.16)] and where p is virtual and q is occupied [Eq. (6.18)],

$$W_{ia\sigma} = W_{ai\sigma} = 2\sum_{j}(X+Y)_{ja\sigma}\sum_{kb\sigma'}K_{ji\sigma,kb\sigma'}\,(X+Y)_{kb\sigma} + \varepsilon_{i\sigma}Z_{ia\sigma} \qquad (D.37)$$

$$W_{ia\sigma} = W_{ai\sigma} = 2\sum_{b}(X+Y)_{ib\sigma}\sum_{jc\sigma'}K_{ab\sigma,jc\sigma'}\,(X+Y)_{jc\sigma} + H^{+}_{ia\sigma}[T] + H^{+}_{ia\sigma}[Z] + \varepsilon_{a\sigma}Z_{ia\sigma} \quad (D.38)$$

$$W_{ia\sigma} = W_{ai\sigma} = 2\sum_{b}(X+Y)_{ib\sigma}\sum_{jc\sigma'}K_{ab\sigma,jc\sigma'}\,(X+Y)_{jc\sigma} + H^{+}_{ia\sigma}[P] + \varepsilon_{a\sigma}Z_{ia\sigma} \quad (D.39)$$

The full derivative of the auxiliary functional (L) with respect to the nuclear coordinates (R_A) can be derived as follows.

$$L^{\xi}[X,Y,\Omega,C,Z,W] = G^{\xi}[X,Y,\Omega] + \sum_{ia\sigma} Z_{ia\sigma}\,F^{\xi}_{ia\sigma} - \sum_{pq\sigma,p\leq q} W_{pq\sigma}\,S^{\xi}_{pq\sigma} \quad (D.40)$$

where,

$$G^{\xi}[X,Y,\Omega] = \frac{1}{2}\begin{pmatrix}X+Y\\X-Y\end{pmatrix}\begin{pmatrix}(A+B)^{\xi}_{ia\sigma,jb\sigma'} & 0\\ 0 & (A-B)^{\xi}_{ia\sigma,jb\sigma'}\end{pmatrix}\begin{pmatrix}X+Y\\X-Y\end{pmatrix}$$

$$= \frac{1}{2}\sum_{ia\sigma}\sum_{jb\sigma'}(X+Y)_{ia\sigma}\,(A+B)^{\xi}_{ia\sigma,jb\sigma'}(X+Y)_{jb\sigma'}$$
$$+\frac{1}{2}\sum_{ia\sigma}\sum_{jb\sigma'}(X-Y)_{ia\sigma}\,(A-B)^{\xi}_{ia\sigma,jb\sigma'}(X-Y)_{jb\sigma'} \quad (D.41)$$

Substituting Eq. (D.40) with Eq. (D.41) leads to:

$$L^{\xi}[X,Y,\Omega,C,Z,W] = \frac{1}{2}\sum_{ia\sigma}\sum_{jb\sigma'}(X+Y)_{ia\sigma}\,(A+B)^{\xi}_{ia\sigma,jb\sigma'}(X+Y)_{jb\sigma'}$$

$$+\frac{1}{2}\sum_{ia\sigma}\sum_{jb\sigma'}(X-Y)_{ia\sigma}\,(A-B)^{\xi}_{ia\sigma,jb\sigma'}(X-Y)_{jb\sigma'} + \sum_{ia\sigma} Z_{ia\sigma}\,F^{\xi}_{ia\sigma} - \sum_{pq\sigma,p\leq q} W_{pq\sigma}\,S^{\xi}_{pq\sigma} \quad (D.42)$$

Substituting Eq. (6.5) and Eq. (6.6) into Eq. (D.42) leads to:

$$L^{\xi}[X,Y,\Omega,C,Z,W] = \frac{1}{2}\sum_{ia\sigma}\sum_{jb\sigma'}(X+Y)_{ia\sigma}\left[\left(F^{\xi}_{ab\sigma}\delta_{ij} - F^{\xi}_{ij\sigma}\delta_{ab}\right)\delta_{\sigma\sigma'} + 4K^{\xi}_{ia\sigma,jb\sigma'}\right](X+Y)_{jb\sigma'}$$

$$+\frac{1}{2}\sum_{ia\sigma}\sum_{jb\sigma'}(X-Y)_{ia\sigma}\left(F^{\xi}_{ab\sigma}\delta_{ij} - F^{\xi}_{ij\sigma}\delta_{ab}\right)\delta_{\sigma\sigma'}(X-Y)_{jb\sigma'} + \sum_{ia\sigma} Z_{ia\sigma}\,F^{\xi}_{ia\sigma} - \sum_{pq\sigma,p\leq q} W_{pq\sigma}\,S^{\xi}_{pq\sigma}$$

$$= \frac{1}{2}\sum_{ia\sigma}\sum_{jb\sigma'}\left(F^{\xi}_{ab\sigma}\delta_{ij} - F^{\xi}_{ij\sigma}\delta_{ab}\right)\delta_{\sigma\sigma'}\left\{(X+Y)_{ia\sigma}(X+Y)_{jb\sigma'} + (X-Y)_{ia\sigma}(X-Y)_{jb\sigma'}\right\}$$

$$+2\sum_{ia\sigma}\sum_{jb\sigma'}(X+Y)_{ia\sigma}\,K^{\xi}_{ia\sigma,jb\sigma'}(X+Y)_{jb\sigma'} + \sum_{ia\sigma}Z_{ia\sigma}\,F^{\xi}_{ia\sigma} - \sum_{pq\sigma,p\leq q}W_{pq\sigma}\,S^{\xi}_{pq\sigma}$$

The relaxed difference density matrix T is then substituted into the above equation:

$$L^{\xi}[X,Y,\Omega,C,Z,W] = \sum_{ab\sigma}F^{\xi}_{ab\sigma}\,T_{ab\sigma} + \sum_{ij\sigma}F^{\xi}_{ij\sigma}\,T_{ij\sigma} + 2\sum_{ia\sigma}\sum_{jb\sigma'}(X+Y)_{ia\sigma}\,K^{\xi}_{ia\sigma,jb\sigma'}(X+Y)_{jb\sigma'}$$

$$+\sum_{ia\sigma}F^{\xi}_{ia\sigma}\,Z_{ia\sigma} - \sum_{pq\sigma,p\leq q}W_{pq\sigma}\,S^{\xi}_{pq\sigma} \qquad (D.43)$$

Eq. (D.43) can be further simplified using the relaxed one-particle difference density matrix relation:

$$L^{\xi}[X,Y,\Omega,C,Z,W] = \sum_{pq\sigma}F^{\xi}_{pq\sigma}\,P_{pq\sigma} + 2\sum_{ia\sigma}\sum_{jb\sigma'}(X+Y)_{ia\sigma}\,K^{\xi}_{ia\sigma,jb\sigma'}(X+Y)_{jb\sigma'}$$

$$-\sum_{pq\sigma,p\leq q}W_{pq\sigma}\,S^{\xi}_{pq\sigma} \qquad (D.44)$$

Substituting Eq. (6.7) into Eq. (D.44) leads to:

$$L^{\xi}[X,Y,\Omega,C,Z,W] = \sum_{pq\sigma}\left\{h_{pq\sigma} + \sum_{i\sigma'}(pq\sigma|ii\sigma') + V^{xc}_{pq\sigma}\right\}^{\xi}P_{pq\sigma}$$

$$+2\sum_{ia\sigma}\sum_{jb\sigma'}(X+Y)_{ia\sigma}\,K^{\xi}_{ia\sigma,jb\sigma'}(X+Y)_{jb\sigma'} - \sum_{pq\sigma,p\leq q}W_{pq\sigma}\,S^{\xi}_{pq\sigma}$$

$$L^{\xi}[X,Y,\Omega,C,Z,W] = \sum_{pq\sigma}h^{\xi}_{pq\sigma}\,P_{pq\sigma} + \sum_{pq\sigma}\sum_{i\sigma'}(pq\sigma|ii\sigma')^{\xi}\,P_{pq\sigma} + \sum_{pq\sigma}V^{xc\,\xi}_{pq\sigma}\,P_{pq\sigma}$$

$$+2\sum_{ia\sigma}\sum_{jb\sigma'}(X+Y)_{ia\sigma}\,K^{\xi}_{ia\sigma,jb\sigma'}(X+Y)_{jb\sigma'} - \sum_{pq\sigma,p\leq q}W_{pq\sigma}\,S^{\xi}_{pq\sigma} \qquad (D.45)$$

Expanding the $2\sum_{ia\sigma}\sum_{jb\sigma'}(X+Y)_{ia\sigma}\,K^{\xi}_{ia\sigma,jb\sigma'}(X+Y)_{jb\sigma'}$ term by substituting Eq. (D.19) leads to:

$$2\sum_{ia\sigma}\sum_{jb\sigma'}(X+Y)_{ia\sigma}\sum_{ABll'}\Big[q_{ia\sigma,Al}\gamma_{Al,Bl'}q_{jb\sigma',Bl'}$$

$$+q_{ia\sigma,Al}\delta_{\sigma}\delta_{\sigma'}\delta_{AB}W_{Al,l'}q_{jb\sigma',Bl'}\Big]^{\xi}(X+Y)_{jb\sigma'} \qquad (D.46)$$

Therefore, the derivative of the term involving the gamma function is given by,

$$2\sum_{\mu\in A,\nu\notin A,\sigma}S_{\mu\nu\sigma}^{1/2}\left[S_{\mu\nu\sigma}^{1/2}\right]^{\xi}(\Xi_A+\Xi_B)U_{\mu\nu\sigma}+4\sum_{\mu\in A,\nu\notin A,\sigma}\gamma_{Al,Bl'}^{\xi}\,U_AU_B \qquad (D.47)$$

where,

$$U_{\mu\nu\sigma}=(X+Y)_{\mu\nu\sigma} \qquad (D.48)$$

$$U_A=\sum_{ia\sigma}(X+Y)_{ia\sigma}q_{ia\sigma,Al} \qquad (D.49)$$

$$\Xi_A=\sum_{B}\gamma_{Al,Bl'}U_B \qquad (D.50)$$

The derivative of the term involving magnetic Hubbard parameter is given by,

$$\delta_{\sigma}\delta_{\sigma'}\delta_{AB}\left\{2\sum_{\mu\in A}S_{\mu\nu\sigma}^{1/2}\left[S_{\mu\nu\sigma}^{1/2}\right]^{\xi}\Theta_AU_{\mu\nu\sigma}+4\sum_{\mu\in A}W_{Al,l'}^{\xi}\,U_AU_B\right\} \qquad (D.51)$$

where,

$$\Theta_A=\sum_{A}W_{Al,l'}U_A \qquad (D.52)$$

It is worth noting that the magnetic Hubbard parameter derivative ($W_{Al,l'}^{\xi}$) does not depend on atomic coordinates, so the second term in Eq. (D.51) is zero.[10,11] Therefore, the final form of the gradient is given by:

$$L^{\xi}[X,Y,\Omega,C,Z,W]$$

$$=\sum_{\mu\in A,\nu\notin A,\sigma}h_{\mu\nu\sigma}^{\xi}\,P_{\mu\nu\sigma}+\sum_{\mu\nu\sigma}\sum_{\kappa\in A,\lambda\notin A,\sigma'}(\mu\nu\sigma|\kappa\lambda\sigma')^{\xi}\,P_{\mu\nu\sigma}+\sum_{\mu\in A,\nu\notin A,\sigma}V_{\mu\nu\sigma}^{xc\,\xi}\,P_{\mu\nu\sigma}$$

$$+2\sum_{\mu\in A,\nu\notin A,\sigma} S_{\mu\nu\sigma}^{1/2}\left[S_{\mu\nu\sigma}^{1/2}\right]^{\xi}(\Xi_A+\Xi_B)U_{\mu\nu\sigma}+4\sum_{\mu\in A,\nu\notin A,\sigma}\gamma_{Al,Bl'}^{\xi}\,U_A U_B+$$

$$+2\delta_\sigma\delta_{\sigma'}\sum_{\mu\in A} S_{\mu\nu\sigma}^{1/2}\left[S_{\mu\nu\sigma}^{1/2}\right]^{\xi}\Theta_A U_{\mu\nu\sigma}-\sum_{\mu\in A,\nu\notin A,\sigma} W_{\mu\nu\sigma}\,S_{\mu\nu\sigma}^{\xi} \qquad (D.53)$$

The underlying theory, derivation, and derivative component of the $\gamma_{Al,Bl'}$ can be found in the works of Frauenheim et al.[10], Köhler,[11] and Gaus et al.[12]

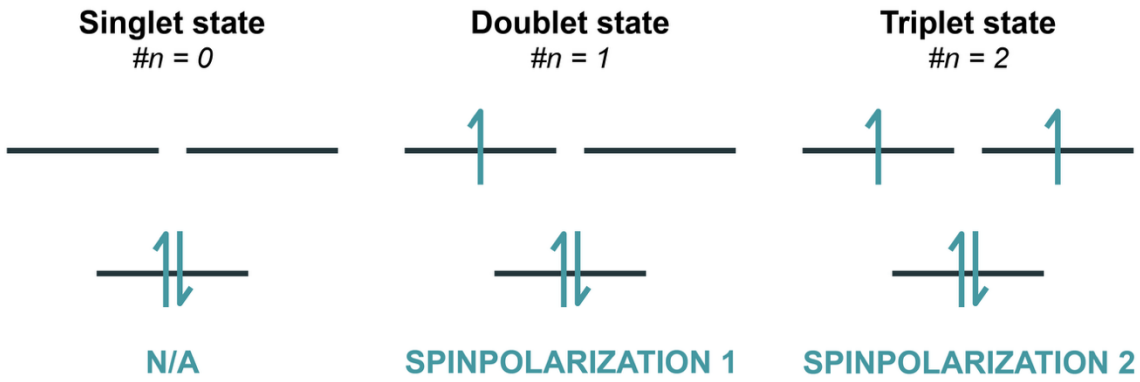
III. Detailed description of the numerical quality parameter in ADF

According to the ADF manual, there are several key features that determine the precision of a calculation: (1) level of theory applied, (2) convergence parameters, (3) density fitting quality, and (4) numerical integration quality.[13] While we have elaborated on the first two features in the main text, this section will focus on the latter two aspects. It is important to note the significance of the density fitting procedure's accuracy. The basic concept involves splitting the total electron density into atomic densities, which are then approximated by a combination of radial spline functions and real spherical harmonics. The algorithm for incorporating this approach in ADF was proposed by Becke and Delley.[14,15] In the input file, this parameter is specified using the "ZLMFIT" block with the quality level defined by "QUALITY *#level*", where *#level* can be basic, normal, good, very good, or excellent. The second aspect is the numerical integration quality, where ADF employs numerical integration via an integration grid that can significantly affect the accuracy of the calculated results and the efficiency (the effect of the grid quality on the calculated results is shown in the section on excited state geometry optimization with different parameters).[16] The default numerical integration grid used by ADF is known as the fuzzy cells integration grid, which was developed by Becke.[16,17] This is specified in the input file using the "BECKEGRID" keyword block with the grid quality defined by

"QUALITY *#level*", using the same quality types as the "ZLMFIT" block. However, in our computations, we did not incorporate these individual keywords. Instead, we employed the "NUMERICALQUALITY *#level*" keyword, which simultaneously sets both the density fitting quality and numerical integration quality with a single command, applying the same quality level to both parameters.[18]

IV. Transition from restricted to unrestricted calculation in ADF

Since this study involves testing the new implementation, it is necessary to specify that this is an unrestricted calculation by incorporating "UNRESTRICTED YES" keyword in the engine block. For open-shell molecular systems, an additional keyword, "SPINPOLARIZATION *#n*" must be added, where *#n* corresponds to the number of unpaired electrons in the system. For example, the O_2 molecule exists in a triplet state with two unpaired electrons, which requires *#n* = 2. For closed-shell molecules, this keyword is omitted since all electrons are paired (Figure D.1).



Appendix Figure D.1. Different valence electronic configurations and how the "SPINPOLARIZATION" keyword is used based on the number of unpaired electrons.

V. Small open-shell organic radical and charged species

Appendix Table D.1. Literature sources for the molecules used in this study.

Molecule	References
NF (Nitrosyl fluoride radical)	**[1]** Yamamoto, S.; Saito, S. The Microwave Spectrum of the NF Radical in the Metastable Electronic State ($a\ ^1\Delta$). *J. Chem. Phys.* **1987**, *86* (1), 102–105. https://doi.org/10.1063/1.452600. **[2]** Kobayashi, K.; Saito, S. The Microwave Spectrum of the NF Radical in the Second Electronically Excited ($b\ ^1\Sigma^+$) State: Potentials of Three Low-Lying States ($X\ ^3\Sigma^-$,$a\ ^1\Delta$,$b\ ^1\Sigma^+$). *J. Chem. Phys.* **1998**, *108* (16), 6606–6610. https://doi.org/10.1063/1.476075.
Acetyl free radical	**[1]** Jacox, M. E. The reaction of F atoms with acetaldehyde and ethylene oxide. Vibrational spectra of the CH_3CO and CH_2CHO free radicals trapped in solid argon. *Chem. Phys.* **1982**, *69*(3), 407-422. https://doi.org/10.1016/0301-0104(82)88079-8 **[2]** Ruscis, B.; Boggs, J. E.; Burcat, A.; Császár, A. G.; Demaison, J,; Janoschek, R.; Martin, J. M. L.; Morton, M. L.; Rossi, M. J.; Stanton, J. F.; Szalay, P. G.; Westmoreland, P. R.; Zabel, F.; Bérces, T. IUPAC Critical Evaluation of Thermochemical Properties of Selected Radicals. Part I. *J. Phys. Chem. Ref. Data* **2005**, *34*, 573-656. https://doi.org/10.1063/1.1724828.
Adenine radical cation	**[1]** Baptista, F. A.; Krizsan, D.; Stitch, M.; Sazanovich, I. V.; Clark, I. P.; Towrie, M.; Long, C.; Martinez-Fernandez, L.; Improta, R.; Kane-Maguire, N. A. P.; Kelly, J. M.; Quinn, S. J. Adenine Radical Cation Formation by a Ligand-Centered Excited State of an Intercalated Chromium Polypyridyl Complex Leads to Enhanced DNA Photo-Oxidation. *J. Am. Chem. Soc.* **2021**, *143* (36), 14766–14779. https://doi.org/10.1021/jacs.1c06658.
Benzyl free radical	**[1]** Ishiguro, K.; Nakano, T.; Shibata, H.; Sawaki, Y. Redox Reaction of Benzyl Radicals with Aromatic Radical Ions Photogenerated. The Marcus Inverted Region and the Selective Formation of Carbocations or Carbanions. *J. Am. Chem. Soc.* **1996**, *118* (31), 7255–7264. https://doi.org/10.1021/ja953689u.
p-benzoquinone radical anion	**[1]** Piech, K.; Bally, T.; Ichino, T.; Stanton, J. Vibronic Spectra of the P-Benzoquinone Radical Anion and Cation: A Matrix Isolation and Computational Study. *Phys. Chem. Chem. Phys.* **2014**, *16* (5), 2011–2019. https://doi.org/10.1039/C3CP53960A.

cis-Butadiene radical cation and trans-Butadiene radical cation	**[1]** Sastry, G. N.; Bally, T.; Hrouda, V.; Cársky, P. The $C_4H_6^{\bullet+}$ Potential Energy Surface. 1. The Ring-Opening Reaction of Cyclobutene Radical Cation and Related Rearrangements. *J. Am. Chem. Soc.* **1998**, *120* (36), 9323–9334. https://doi.org/10.1021/ja981651m. **[2]** Oxgaard, J.; Wiest, O. Rehybridized 1,3-Butadiene Radical Cations: How Far Will a Radical Cation Go To Maintain Conjugation? *J. Phys. Chem. A* **2002**, *106* (15), 3967–3974. https://doi.org/10.1021/jp020041c.
Cyclopentadienyl cation	**[1]** Ranasinghe, S.; Martin, C. D.; Dutton, J. L. Cyclopentadienyl Cations. *Chem. Sci.* **2025**, *16* (5), 2083–2088. https://doi.org/10.1039/D4SC07024K.
Cyclopentadienyl free radical	**[1]** Applegate, B. E.; Bezant, A. J.; Miller, T. A. The Jahn–Teller and Related Effects in the Cyclopentadienyl Radical. II. Vibrational Analysis of the $\tilde{A}^2A_2''$–$\tilde{X}^2E_1''$ Electronic Transition. *J. Chem. Phys.* **2001**, *114* (11), 4869–4882. https://doi.org/10.1063/1.1348276.
Cyclopropene radical cation	**[1]** Vasilatou, K.; Michaud, J. M.; Baykusheva, D.; Grassi, G.; Merkt, F. The Cyclopropene Radical Cation: Rovibrational Level Structure at Low Energies from High-Resolution Photoelectron Spectra. *J. Chem. Phys.* **2014**, *141* (6). https://doi.org/10.1063/1.4890744.
2-dehydroimidazolyl free radical, 4-dehydroimidazolyl free radical, and 5-dehydroimidazolyl free radical	**[1]** Safaei, Z.; Shiroudi, A.; Zahedi, E.; Sillanpää, M. Atmospheric Oxidation Reactions of Imidazole Initiated by Hydroxyl Radicals: Kinetics and Mechanism of Reactions and Atmospheric Implications. *Phys. Chem. Chem. Phys.* **2019**, *21* (16), 8445–8456. https://doi.org/10.1039/C9CP00632J.
Ethene radical cation	**[1]** Mohr, M.; Zipse, H. Does the Cationic or the Radical Character Dominate the Reactivity of Alkene Radical Cations towards Solvent Molecules? *Phys. Chem. Chem. Phys.* **2001**, *3* (7), 1246–1252. https://doi.org/10.1039/b007990l.
1-furanyl free radical and 2-furanyl free radical	**[1]** Nascimento, J. L.; Queiroz, M. H.; Rivelino, R.; Alves, T. V. Predicting Pressure-Dependent Rate Constants for the Furan + OH Reactions and Their Impact under Tropospheric Conditions. *J. Chem. Phys.* **2024**, *160* (11). https://doi.org/10.1063/5.0193553.
Formyl free radical	**[1]** Liu, D.; Yang, K.; Fang, D.; Li, S.; Lan, Y.; Chen, Y. Formyl Radical Generation from A-Chloro *N* -Methoxyphthalimides

	Enables Selective Aldehyde Synthesis. *Angew. Chem. Int. Ed.* **2023**, *62* (1). https://doi.org/10.1002/anie.202213686. **[2]** Butscher, T.; Duvernay, F.; Rimola, A.; Segado-Centellas, M.; Chiavassa, T. Radical Recombination in Interstellar Ices, a Not so Simple Mechanism. *Phys. Chem. Chem. Phys.* **2017**, *19* (4), 2857–2866. https://doi.org/10.1039/C6CP07024H.
Naphthalene radical cation	**[1]** Erickson, R.; Benetis, N. P.; Lund, A.; Lindgren, M. Radical Cation of Naphthalene on H−ZSM-5 Zeolite and in $CFCl_3$ Matrix. A Theoretical and Experimental EPR, ENDOR, and ESEEM Study. *J. Phys. Chem. A* **1997**, *101* (13), 2390–2396. https://doi.org/10.1021/jp9631994. **[2]** West, B.; Joblin, C.; Blanchet, V.; Bodi, A.; Sztáray, B.; Mayer, P. M. On the Dissociation of the Naphthalene Radical Cation: New IPEPICO and Tandem Mass Spectrometry Results. *J. Phys. Chem. A* **2012**, *116* (45), 10999–11007. https://doi.org/10.1021/jp3091705.
Pyrazine radical cation	**[1]** Eiermann, U.; Neugebauer, F. A.; Chandra, H.; Symons, M. C. R.; Wyatt, J. L. Radical Cations and Anions of Pyrazines: An Electron Paramagnetic Resonance Study. *J. Chem. Soc., Perkin Trans. 2* **1992**, No. 1, 85–89. https://doi.org/10.1039/p29920000085. **[2]** Rao, D. N. R.; Eastland, G. W.; Symons, M. C. R. Structures of Diazabenzene Cations Formed by Radiolysis. An Electron Spin Resonance Study. *J. Chem. Soc., Faraday Trans. 1: Physical Chemistry in Condensed Phases* **1985**, *81* (3), 727. https://doi.org/10.1039/f19858100727.
Pyridazine radical cation	**[1]** Kato, T.; Shida, T. Electronic Structures of Ion Radicals of Nitrogen-Heteroaromatic Hydrocarbons as Studied by ESR and Optical Spectroscopy. *J. Am. Chem. Soc.* **1979**, *101* (23), 6869–6876. https://doi.org/10.1021/ja00517a014. **[2]** Rao, D. N. R.; Eastland, G. W.; Symons, M. C. R. Structures of Diazabenzene Cations Formed by Radiolysis. An Electron Spin Resonance Study. *J. Chem. Soc., Faraday Trans. 1: Physical Chemistry in Condensed Phases* **1985**, *81* (3), 727. https://doi.org/10.1039/f19858100727.

Pyridine radical cation	**[1]** Widjaja, F.; Jin, Z.; Nash, J. J.; Kenttämaa, H. I. Comparison of the Reactivity of the Three Distonic Isomers of the Pyridine Radical Cation Toward Tetrahydrofuran in Solution and in the Gas Phase. *J. Am. Soc. Mass Spectrom.* **2013**, *24* (4), 469–480. https://doi.org/10.1007/s13361-012-0543-3.
Pyrimidine radical cation	**[1]** Hamid, A. M.; Bera, P. P.; Lee, T. J.; Aziz, S. G.; Alyoubi, A. O.; El-Shall, M. S. Evidence for the Formation of Pyrimidine Cations from the Sequential Reactions of Hydrogen Cyanide with the Acetylene Radical Cation. *J. Phys. Chem. Lett.* **2014,** *5* (19), 3392–3398. https://doi.org/10.1021/jz501648q. **[2]** Lomoth, R.; Naumov, S.; Brede, O. Genuine Pyrimidine Radical Cations Generated by Radiation-Induced Electron Transfer to Butyl Chloride or Acetone Parent Ions. *J. Phys. Chem. A* **1999**, *103* (15), 2641–2648. https://doi.org/10.1021/jp9829804.
Pyrrole radical cation	**[1]** Jatratkar, A. A.; Yadav, J. B.; Kamat, S. V.; Patil, V. S.; Mahadik, D. B.; Barshilia, H. C.; Puri, V.; Puri, R. K. Consequence of Oxidant to Monomer Ratio on Optical and Structural Properties of Polypyrrole Thin Film Deposited by Oxidation Polymerization Technique. *J. Phys. Chem. Sol.* **2015**, *80*, 78–83. https://doi.org/10.1016/j.jpcs.2015.01.004. **[2]** Yadav, P. K.; Kumar, S.; Maiti, P. Conjugated Polymers for Solar Cell Applications. In *Conjugated Polymers for Next-Generation Applications*; Elsevier, **2022**; pp 367–401. https://doi.org/10.1016/B978-0-12-824094-6.00004-2.
Tetrazine radical cation	**[1]** Fischer, H.; Müller, T.; Umminger, I.; Neugebauer, F. A.; Chandra, H.; Symons, M. C. R. Radical Cations and Anions of 1,2,4,5-Tetrazines: An Electron Spin Resonance and Cyclic Voltammetric Study. *J. Chem. Soc., Perkin Trans. 2* **1988**, No. 3, 413–421. https://doi.org/10.1039/P29880000413.

VI. Numerical vs. analytical excited state gradient comparison using different numerical displacement values

Appendix Table D.2. Numerical vs. analytical gradient differences for excited state (D_1/T_1) of open-shell molecules at different numerical displacement values (at the PW92/DZP level of theory with "Very Good" numerical quality). MAD values are in Hartree/Å.

Molecule	State	Method	Numerical displacement values

			0.00005 Å	0.0001 Å	0.0005 Å	0.001 Å
O_2	T_1	TDDFT	3.22×10^{-4}	9.56×10^{-4}	1.72×10^{-5}	1.51×10^{-5}
		TDDFT+TB	2.92×10^{-5}	2.92×10^{-5}	2.91×10^{-5}	2.89×10^{-5}
SO	T_1	TDDFT	2.04×10^{-5}	2.07×10^{-5}	2.02×10^{-5}	2.01×10^{-5}
		TDDFT+TB	1.65×10^{-5}	1.70×10^{-5}	1.66×10^{-5}	1.64×10^{-5}
HHe	D_1	TDDFT	3.60×10^{-6}	3.29×10^{-6}	1.75×10^{-6}	1.74×10^{-6}
		TDDFT+TB	3.18×10^{-6}	3.10×10^{-6}	1.83×10^{-6}	1.64×10^{-6}
CN	D_1	TDDFT	9.75×10^{-5}	1.05×10^{-4}	1.04×10^{-4}	1.04×10^{-4}
		TDDFT+TB	1.07×10^{-4}	1.10×10^{-4}	1.08×10^{-4}	1.07×10^{-4}
BeH	D_1	TDDFT	9.36×10^{-7}	9.32×10^{-7}	9.74×10^{-7}	1.07×10^{-6}
		TDDFT+TB	1.37×10^{-7}	1.32×10^{-7}	1.61×10^{-7}	2.58×10^{-7}

VII. Excited state geometry optimization with different parameters

In this section, we investigated how different exchange-correlation functionals, basis sets, numerical quality levels, and numbers of compute cores affect the overall results obtained from the new implementation. We examine these parameters using O_2 and the pyrazine radical cation as test systems, with Table D.3 and Table D.4 focusing on O_2 and Table D.5 and Table D.6 presenting results for the pyrazine radical cation. All calculations in this section employed energy and gradient convergence criteria of 1×10^{-4} Hartree and 1×10^{-3} Hartree/Å, respectively. It is important to note that the individual emission energies were affected in both systems by the variations in exchange-correlation functionals, basis set, and numerical quality parameters for both TDDFT and TDDFT+TB methods, which is expected. However, the overall deviations (TDDFT vs. TDDFT+TB) for the emission energies in these two systems exhibited similar trends. Regarding the computational efficiency, the number of cores primarily affected the calculation speed, while the emission energies remained unchanged for both methods.

Appendix Table D.3. Excited state geometry optimization for the T_1 state of O_2 using various exchange-correlation functionals (XC), basis set, and numerical quality.

XC	Basis set	Numerical quality	Method	Runtime (hh:mm:ss)	Emission energy (eV)	Number of geometry steps
XC functional						
PW92 (LDA)	DZP	Very good	TDDFT	00:06:10	3.46	6
			TDDFT+TB	00:01:21	3.51	6
Xalpha (LDA)	DZP	Very good	TDDFT	00:05:02	3.48	6
			TDDFT+TB	00:01:23	3.53	6
RPBE (GGA)	DZP	Very good	TDDFT	00:06:15	3.10	7
			TDDFT+TB	00:02:08	3.15	7
PBE (GGA)	DZP	Very good	TDDFT	00:06:47	3.19	7
			TDDFT+TB	00:02:08	3.24	7
BP86 (GGA)	DZP	Very good	TDDFT	00:06:35	3.18	7
			TDDFT+TB	00:01:54	3.23	7
OLYP (GGA)	DZP	Very good	TDDFT	00:06:36	3.22	7
			TDDFT+TB	00:01:55	3.27	7
BLYP (GGA)	DZP	Very good	TDDFT	00:06:37	3.01	7
			TDDFT+TB	00:02:03	3.06	7
Basis set						
PW92 (LDA)	SZ	Very good	TDDFT	00:02:44	3.48	6
			TDDFT+TB	00:00:48	3.48	6
PW92 (LDA)	DZ	Very good	TDDFT	00:05:47	2.78	7
			TDDFT+TB	00:01:06	2.79	7
PW92 (LDA)	DZP	Very good	TDDFT	00:04:29	3.46	6
			TDDFT+TB	00:01:17	3.51	6
PW92 (LDA)	TZP	Very good	TDDFT	00:05:08	3.53	6
			TDDFT+TB	00:01:26	3.59	6
Numerical quality						

PW92 (LDA)	DZP	Basic	TDDFT	00:00:35	3.46	6
			TDDFT+TB	00:00:07	3.51	6
PW92 (LDA)	DZP	Normal	TDDFT	00:01:02	3.46	6
			TDDFT+TB	00:00:12	3.51	6
PW92 (LDA)	DZP	Good	TDDFT	00:02:02	3.46	6
			TDDFT+TB	00:00:27	3.51	6
PW92 (LDA)	DZP	Very good	TDDFT	00:05:15	3.46	6
			TDDFT+TB	00:01:29	3.51	6
PW92 (LDA)	DZP	Excellent	TDDFT	00:17:28	3.46	6
			TDDFT+TB	00:05:05	3.51	6

*These computations were performed using a single core.

Appendix Table D.4. Excited state geometry optimization for the T_1 state of O_2 using different numbers of compute cores. It should be noted that the O_2 molecule is a very small test case, and thus very little gain in speedup is achieved for more than 4 cores.

# Cores	Method	Runtime (hh:mm:ss)	Emission energy (eV)	Number of geometry steps
1	TDDFT	00:04:57	3.46	6
	TDDFT+TB	00:01:11	3.51	6
2	TDDFT	00:02:57	3.46	6
	TDDFT+TB	00:00:45	3.51	6
3	TDDFT	00:01:49	3.46	6
	TDDFT+TB	00:00:30	3.51	6
4	TDDFT	00:01:45	3.46	6
	TDDFT+TB	00:00:30	3.51	6
5	TDDFT	00:01:19	3.46	6
	TDDFT+TB	00:00:23	3.51	6
6	TDDFT	00:01:11	3.46	6
	TDDFT+TB	00:00:22	3.51	6

Appendix Table D.5. Excited state geometry optimization for the D_1 state of pyrazine radical cation using various exchange-correlation functionals (XC), basis set, and numerical quality.

XC	Basis set	Numerical quality	Method	Runtime (hh:mm:ss)	Emission energy (eV)	Number of geometry steps
XC functional						
PW92 (LDA)	DZP	Very good	TDDFT	00:12:22	0.86	4
			TDDFT+TB	00:02:55	0.86	4
Xalpha (LDA)	DZP	Very good	TDDFT	00:12:44	1.01	4
			TDDFT+TB	00:02:55	1.02	4
RPBE (GGA)	DZP	Very good	TDDFT	00:13:54	0.66	4
			TDDFT+TB	00:04:23	0.66	4
PBE (GGA)	DZP	Very good	TDDFT	00:14:04	0.73	4
			TDDFT+TB	00:04:23	0.74	4
BP86 (GGA)	DZP	Very good	TDDFT	00:14:00	0.72	4
			TDDFT+TB	00:04:21	0.73	4
OLYP (GGA)	DZP	Very good	TDDFT	00:13:52	0.66	4
			TDDFT+TB	00:04:29	0.67	4
BLYP (GGA)	DZP	Very good	TDDFT	00:13:56	0.65	4
			TDDFT+TB	00:04:20	0.66	4
Basis set						
PW92 (LDA)	SZ	Very good	TDDFT	00:09:09	0.76	5
			TDDFT+TB	00:01:37	0.76	5
PW92 (LDA)	DZ	Very good	TDDFT	00:10:01	1.17	5
			TDDFT+TB	00:02:12	1.17	5
PW92 (LDA)	DZP	Very good	TDDFT	00:12:26	0.86	4
			TDDFT+TB	00:02:57	0.86	4
PW92 (LDA)	TZP	Very good	TDDFT	00:14:37	0.82	4
			TDDFT+TB	00:03:26	0.83	4
Numerical quality						

PW92 (LDA)	DZP	Basic	TDDFT	00:01:13	0.88	4
			TDDFT+TB	00:00:14	0.88	4
PW92 (LDA)	DZP	Normal	TDDFT	00:02:41	0.86	4
			TDDFT+TB	00:00:26	0.86	4
PW92 (LDA)	DZP	Good	TDDFT	00:06:54	0.86	4
			TDDFT+TB	00:01:02	0.86	4
PW92 (LDA)	DZP	Very good	TDDFT	00:12:21	0.86	4
			TDDFT+TB	00:02:55	0.86	4
PW92 (LDA)	DZP	Excellent	TDDFT	00:38:20	0.85	4
			TDDFT+TB	00:10:07	0.86	4

Appendix Table D.6. Excited state geometry optimization for the D_1 state of pyrazine radical cation using different number of compute cores.

# Cores	Method	Runtime (hh:mm:ss)	Emission energy (eV)	Number of geometry steps
1	TDDFT	00:55:27	0.86	4
	TDDFT+TB	00:15:33	0.86	4
2	TDDFT	00:35:20	0.86	4
	TDDFT+TB	00:08:36	0.86	4
3	TDDFT	00:25:33	0.86	4
	TDDFT+TB	00:05:50	0.86	4
4	TDDFT	00:16:27	0.86	4
	TDDFT+TB	00:04:20	0.86	4
5	TDDFT	00:13:49	0.86	4
	TDDFT+TB	00:03:16	0.86	4
6	TDDFT	00:12:24	0.86	4
	TDDFT+TB	00:02:56	0.86	4

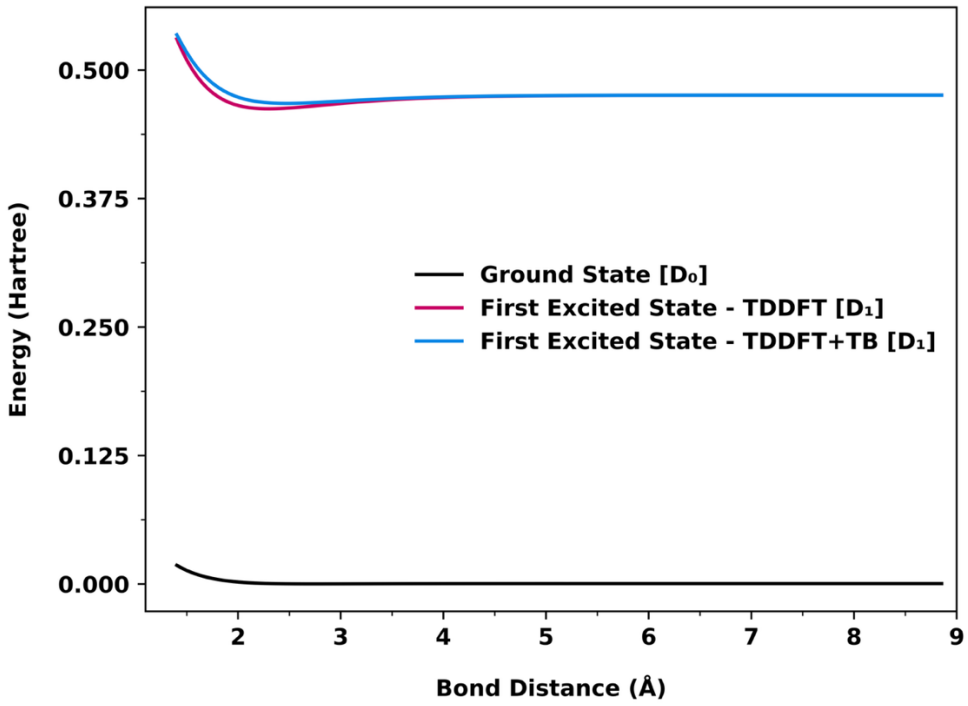
VIII. Numerical vs. analytical excited state gradient comparison for closed-shell molecules

As shown in Table D.7, a similar analysis can be performed for the closed-shell molecules. The observed results indicate MAD values below 5.00×10^{-4} Hartree/Å, demonstrating good performance for closed-shell systems as well. It is important to note that for closed-shell molecules, the first excited state analyzed using the unrestricted TDDFT+TB can be either: (1) singlet or (2) triplet. Therefore, singlet states are denoted as S_1 and triplet states are denoted as ST_1, as the transitions originate from a singlet ground state.

Appendix Table D.7. Numerical vs. analytical gradient differences for excited states of closed-shell diatomic molecules (Hartree/Å).

Molecule	State	MAD	rms
H_2	ST_1	1.58×10^{-6}	2.74×10^{-6}
N_2	ST_1	1.23×10^{-4}	2.13×10^{-4}
Li_2	ST_1	7.20×10^{-7}	1.25×10^{-6}
LiH	ST_1	2.53×10^{-4}	4.38×10^{-4}
Cl_2	S_1	1.14×10^{-9}	1.74×10^{-9}
HCl	S_1	3.22×10^{-6}	5.57×10^{-6}

IX. HHe molecule ground and excited state potential energy surfaces



Appendix Figure D.2. Relative energy of the HHe molecule in ground and excited states respect to the H-He bond length (at the PW92/DZP level of theory). The excited state potential energy surface represents the energy difference between D_1 and D_0 depending on the computational method used: TDDFT or TDDFT+TB.

X. Excited state spin-contaminations

Spin-contamination is a well-known issue in unrestricted TDDFT calculations, as documented in several studies.[7,19,20] Since DFT is a one-particle method, the $\hat{S}$ operator for the n-particle system must be expressed in terms of single particle operators. As TDDFT+TB is built upon the TDDFT formalism, this limitation naturally carries over to the new implementation. The extent of spin-contamination across all test cases is reported in Tables D.8 and D.9. For doublets and triplets, the $\langle S^2 \rangle_{\text{exact}}$ values are 0.75 and 2.00, respectively, where the $\langle S^2 \rangle_{\text{computed}}$

for each state in ADF is evaluated following the expressions given by Szabo and Ostlund.[13,21] The spin-contamination is then determined as $\langle S^2 \rangle_{\text{computed}}$-$\langle S^2 \rangle_{\text{exact}}$.

Appendix Table D.8. Spin-contaminations for excited states (D_1/T_1) of open-shell diatomic molecules using TDDFT and TDDFT+TB.

Molecule	State	Method	Spin-contamination
O_2	T_1	TDDFT	3.33×10^{-3}
		TDDFT+TB	3.33×10^{-3}
SO	T_1	TDDFT	2.94×10^{-3}
		TDDFT+TB	2.95×10^{-3}
S_2	T_1	TDDFT	1.72×10^{-3}
		TDDFT+TB	1.72×10^{-3}
NH	T_1	TDDFT	4.66×10^{-3}
		TDDFT+TB	4.59×10^{-3}
NF	T_1	TDDFT	2.40×10^{-1}
		TDDFT+TB	2.39×10^{-1}
HHe	D_1	TDDFT	1.00×10^{-5}
		TDDFT+TB	1.00×10^{-5}
CN	D_1	TDDFT	3.85×10^{-3}
		TDDFT+TB	3.85×10^{-3}
BeH	D_1	TDDFT	3.70×10^{-4}
		TDDFT+TB	3.60×10^{-4}
BeF	D_1	TDDFT	1.41×10^{-3}
		TDDFT+TB	1.40×10^{-3}

Appendix Table D.9. Spin-contaminations for excited states (D_1/T_1) of small open-shell organic radical and charged species using TDDFT and TDDFT+TB methods.

Molecule	State	Method	Spin contamination
Acetyl free radical	D_3	TDDFT	1.37×10^{-3}
		TDDFT+TB	1.39×10^{-3}
Adenine radical cation	D_5	TDDFT	1.51×10^{-3}
		TDDFT+TB	1.51×10^{-3}
Benzyl free radical	D_2	TDDFT	6.34×10^{-3}
		TDDFT+TB	5.53×10^{-3}

p-Benzoquinone radical anion	D_1	TDDFT	2.19×10^{-3}
		TDDFT+TB	2.19×10^{-3}
cis-Butadiene radical cation	D_1	TDDFT	2.00×10^{-3}
		TDDFT+TB	2.00×10^{-3}
trans-Butadiene radical cation	D_1	TDDFT	2.71×10^{-3}
		TDDFT+TB	2.72×10^{-3}
Cyclopentadienyl cation	T_1	TDDFT	1.82×10^{-3}
		TDDFT+TB	1.81×10^{-3}
Cyclopentadienyl free radical*	D_2	TDDFT	5.05×10^{-3}
		TDDFT+TB	5.05×10^{-3}
Cyclopropene radical cation	D_3	TDDFT	1.03×10^{-3}
		TDDFT+TB	1.03×10^{-3}
2-Dehydroimidazolyl free radical	D_1	TDDFT	7.43×10^{-3}
		TDDFT+TB	6.94×10^{-3}
4-Dehydroimidazolyl free radical	D_1	TDDFT	5.89×10^{-3}
		TDDFT+TB	5.73×10^{-3}
5-Dehydroimidazolyl free radical	D_2	TDDFT	5.94×10^{-3}
		TDDFT+TB	5.48×10^{-3}
Ethene radical cation	D_2	TDDFT	1.21×10^{-3}
		TDDFT+TB	1.21×10^{-3}
1-Furanyl free radical	D_2	TDDFT	8.89×10^{-3}
		TDDFT+TB	8.87×10^{-3}
2-Furanyl free radical	D_2	TDDFT	7.19×10^{-3}
		TDDFT+TB	7.22×10^{-3}
Formyl free radical	D_2	TDDFT	1.15×10^{-3}
		TDDFT+TB	1.15×10^{-3}
Naphthalene radical cation	D_1	TDDFT	1.90×10^{-3}
		TDDFT+TB	1.90×10^{-3}
Pyrazine radical cation	D_1	TDDFT	1.61×10^{-3}
		TDDFT+TB	1.61×10^{-3}
Pyridazine radical cation	D_1	TDDFT	3.18×10^{-3}
		TDDFT+TB	3.19×10^{-3}
Pyridine radical cation	D_2	TDDFT	4.26×10^{-3}
		TDDFT+TB	4.24×10^{-3}
Pyrimidine radical cation	D_1	TDDFT	3.32×10^{-3}
		TDDFT+TB	3.32×10^{-3}
Pyrrole radical cation	D_1	TDDFT	1.76×10^{-2}

		TDDFT+TB	1.76×10^{-2}
Tetrazine radical cation	D_1	TDDFT	1.13×10^{-3}
		TDDFT+TB	1.13×10^{-3}

Ipatov et al.[19] investigated excited-state spin-contamination in open-shell molecules, providing a useful benchmark for the present work. Table D.10 presents a comparison of spin-contamination values between their study and the current results, including a comparison against Tamm-Dancoff approximation (TDA) results reported therein. Notably, the TDDFT+TB results obtained here show good agreement with the previously reported data.

Appendix Table D.10. Comparison of spin-contaminations for the excited states (D_1) of selected open-shell diatomic molecules with previously reported values by Ipatov et al.[19] Spin-contamination values are reported with respect to the method employed.

Molecule	TDDFT+TB	TDDFT*[19]	TDDFT**[19]	TDA**[19]
CN	3.85×10^{-3}	2.90×10^{-3}	1.60×10^{-2}	8.40×10^{-3}
BeH	3.60×10^{-4}	4.27×10^{-2}	6.00×10^{-3}	1.10×10^{-3}
BeF	1.40×10^{-3}	1.69×10^{-1}	0.00	5.00×10^{-4}

* Computed using GAUSSIAN software package (LDA functional and the Sadlej basis set).[19]

** Computed using DEMON2K software package (LDA functional and the GenA3* auxiliary basis set).[19]

XI. Comparative analysis of electronic excitation energies with experimental and higher-level theoretical studies

Appendix Table D.11. Comparison of excitation energies ($E_{TDDFT+TB}$) of selected open-shell diatomic molecules and small open-shell organic radical and charged species with experimental and/or theoretical excitation energies ($E_{Reference}$). Excitation energies are provided in eV.

Molecule	State	$E_{TDDFT+TB}$	$E_{Reference}$	Reference	Notes
O_2	T_1	7.14	6.00-6.20	7,22,23	Experimental.
CN	D_1	1.39	1.36	19	TDDFT calculations carried out with the LDA functional and the Sadlej basis set using the GAUSSIAN software package.
			1.21	19	TDDFT calculations carried out with the LDA functional and the GenA3* auxiliary basis set using the DEMON2K software package.
			1.20	19	TDA calculations carried out with the LDA functional and the GenA3* auxiliary basis set using the DEMON2K software package.
BeH	D_1	2.39	2.36	19	TDDFT calculations carried out with the LDA functional and the Sadlej basis set using the GAUSSIAN software package.
			2.25	19	TDDFT calculations carried out with the LDA functional and the GenA3* auxiliary basis set using the DEMON2K software package.
			2.29	19	TDA calculations carried out with the LDA functional and the GenA3* auxiliary basis set using the DEMON2K software package.
BeF	D_1	4.06	4.07	19	TDDFT calculations carried out with the LDA functional and the Sadlej basis set using the GAUSSIAN software package.

			3.98	19	TDDFT calculations carried out with the LDA functional and the GenA3* auxiliary basis set using the DEMON2K software package.
			4.02	19	TDA calculations carried out with the LDA functional and the GenA3* auxiliary basis set using the DEMON2K software package.
Naphthalene radical cation	D_1	0.79	1.01	20	TDDFT calculations carried out with VWN functional and ATZ2P basis set using BDF package.
			1.09	20	TDDFT calculations carried out with BLYP functional and ATZ2P basis set using BDF package.
			0.73	20,24	Experimental value for neutral geometry.
			0.99	20,24	Calculated via CASSCF/CASPT2 method using the MOLCAS package.
			~1.25	25	Experimental.
Pyridazine radical cation	D_3	3.43	2.80	25	Experimental.
Pyrimidine radical cation	D_2	2.17	3.10	26	Experimental.

XII. Mean absolute deviation (MAD) and root mean square (rms) values.

The following equations show how the MAD and rms values were calculated throughout this study. For the numerical vs. analytical excited state gradient comparison, $\bar{x}$ represents the average numerical vs. analytical gradient difference for all atoms in all directions, while x_i is the individual numerical vs. analytical gradient difference for a single atom in one direction. In this case, $n = 3N$, where N represents the total number of atoms in the system. For the emission energy calculations, $\bar{x}$ is the average emission energy difference (TDDFT vs. TDDFT+TB) for a

test set (diatomic molecules or small organic radicals and charged species), and x_i is the individual emission energy difference between the two methods. For this calculation, *n* corresponds to the total number of molecular systems in the test set.

$$\frac{\sum_i |x_i - \bar{x}|}{n} \tag{D.54}$$

$$\sqrt{\frac{1}{n}\sum_i^n x_i^2} \tag{D.55}$$

References

1. Casida, A. E.; Huix-Rotllant, M. Progress in Time-Dependent Density-Functional Theory. *Annu. Rev. Phys. Chem.* **2012**, *63*, 287–323.

2. Niehaus, T. A.; Suhai, S.; Della Sala, F.; Lugli, P.; Elstner, M.; Seifert, G.; Frauenheim, Th. Tight-Binding Approach to Time-Dependent Density-Functional Response Theory. *Phys. Rev. B* **2001**, *63* (8), 085108.

3. Wang, Y.; Havenridge, S.; Aikens, C. M. Implementation of Energy and Gradient for the TDDFT-Approximate Auxiliary Function (aas) Method. *J. Chem. Phys.* **2024**, *161* (2), 024101.

4. Furche, F.; Ahlrichs, R. Adiabatic Time-Dependent Density Functional Methods for Excited State Properties. *J. Chem. Phys.* **2002**, *117* (16), 7433–7447.

5. Furche, F. On the Density Matrix Based Approach to Time-Dependent Density Functional Response Theory. *J. Chem. Phys.* **2001**, *114* (14), 5982–5992.

6. Heringer, D.; Niehaus, T. A.; Wanko, M.; Frauenheim, TH. Analytical Excited State Forces for the Time-dependent Density-functional Tight-binding Method. *J. Comput. Chem.* **2007**, *28* (16), 2589–2601.

7. Domínguez, A.; Aradi, B.; Frauenheim, T.; Lutsker, V.; Niehaus, T. A. Extensions of the Time-Dependent Density Functional Based Tight-Binding Approach. *J. Chem. Theory Comput.* **2013**, *9* (11), 4901–4914.

8. Rüger, R.; van Lenthe, E.; Heine, T.; Visscher, L. Tight-Binding Approximations to Time-Dependent Density Functional Theory — A Fast Approach for the Calculation of Electronically Excited States. *J. Chem. Phys.* **2016**, *144* (18), 184103.

9. Havenridge, S.; Rüger, R.; Aikens, C. M. Analytical Excited State Gradients for Time-Dependent Density Functional Theory plus Tight Binding (TDDFT + TB). *J. Chem. Phys.* **2023**, *158* (22), 224103.

10. Frauenheim, T.; Seifert, G.; Elstner, M.; Niehaus, T.; Köhler, C.; Amkreutz, M.; Sternberg, M.; Hajnal, Z.; Di Carlo, A.; Suhai, S. Atomistic simulations of complex materials: ground-state and excited-state properties. *J. Phys.: Condens. Matter* **2002**, *14* (11), 3015–3047.

11. Köhler, C. Berücksichtigung von Spinpolarisationseffekten in einem dichtefunktionalbasierten Ansatz, Paderborn, Univ., Diss., 2003.

12. Gaus, M.; Cui, Q.; Elstner, M. DFTB3: Extension of the Self-Consistent-Charge Density-Functional Tight-Binding Method (SCC-DFTB). *J. Chem. Theory Comput.* **2011**, *7* (4), 931–948.

13. te Velde, G.; Bickelhaupt, F. M.; Baerends, E. J.; Fonseca Guerra, C.; van Gisbergen, S. J. A.; Snijders, J. G.; Ziegler, T. Chemistry with ADF. *J. Comput. Chem.* **2001**, *22* (9), 931–967.

14. Becke, A. D.; Dickson, R. M. Numerical Solution of Poisson's Equation in Polyatomic Molecules. *J. Chem. Phys.* **1988**, *89* (5), 2993–2997.

15. Delley, B. An All-Electron Numerical Method for Solving the Local Density Functional for Polyatomic Molecules. *J. Chem. Phys.* **1990**, *92* (1), 508–517.

16. Franchini, M.; Philipsen, P. H. T.; Visscher, L. The Becke Fuzzy Cells Integration Scheme in the Amsterdam Density Functional Program Suite. *J. Comput. Chem.* **2013**, *34* (21), 1819–1827.

17. Becke, A. D. A Multicenter Numerical Integration Scheme for Polyatomic Molecules. *J. Chem. Phys.* **1988**, *88* (4), 2547–2553.

18. Seth, M.; Mazur, G.; Ziegler, T. Time-Dependent Density Functional Theory Gradients in the Amsterdam Density Functional Package: Geometry Optimizations of Spin-Flip Excitations. *Theor. Chem. Acc.* **2011**, *129* (3–5), 331–342.

19. Ipatov, A.; Cordova, F.; Doriol, L. J.; Casida, M. E. Excited-State Spin-Contamination in Time-Dependent Density-Functional Theory for Molecules with Open-Shell Ground States. *J. Mol. Struct.: THEOCHEM.* **2009**, *914* (1–3), 60–73.

20. Li, Z.; Liu, W.; Zhang, Y.; Suo, B. Spin-Adapted Open-Shell Time-Dependent Density Functional Theory. II. Theory and Pilot Application. *J. Chem. Phys.* **2011**, *134* (13), 134101.

21. Szabo, A.; Ostlund, N. S. *Modern Quantum Chemistry: Introduction to Advanced Electronic Structure Theory*; Dover Publications, Inc: Mineola, New York, 2012.

22. Oddershede, J.; Grūner, N. E.; Diercksen, G. H. F. Comparison between Equation of Motion and Polarization Propagator Calculations. *Chem. Phys.* **1985**, *97* (2–3), 303–310.

23. Krupenie, P. H. The Spectrum of Molecular Oxygen. *J. Phys. Chem. Ref. Data* **1972**, *1* (2), 423–534.

24. Bally, T.; Carra, C.; Fülscher, M. P.; Zhu, Z. Electronic Structure of the Naphthalene Radical Cation and Some Simple Alkylated Derivatives. *J. Chem. Soc., Perkin Trans. 2* **1998**, No. 8, 1759–1766.

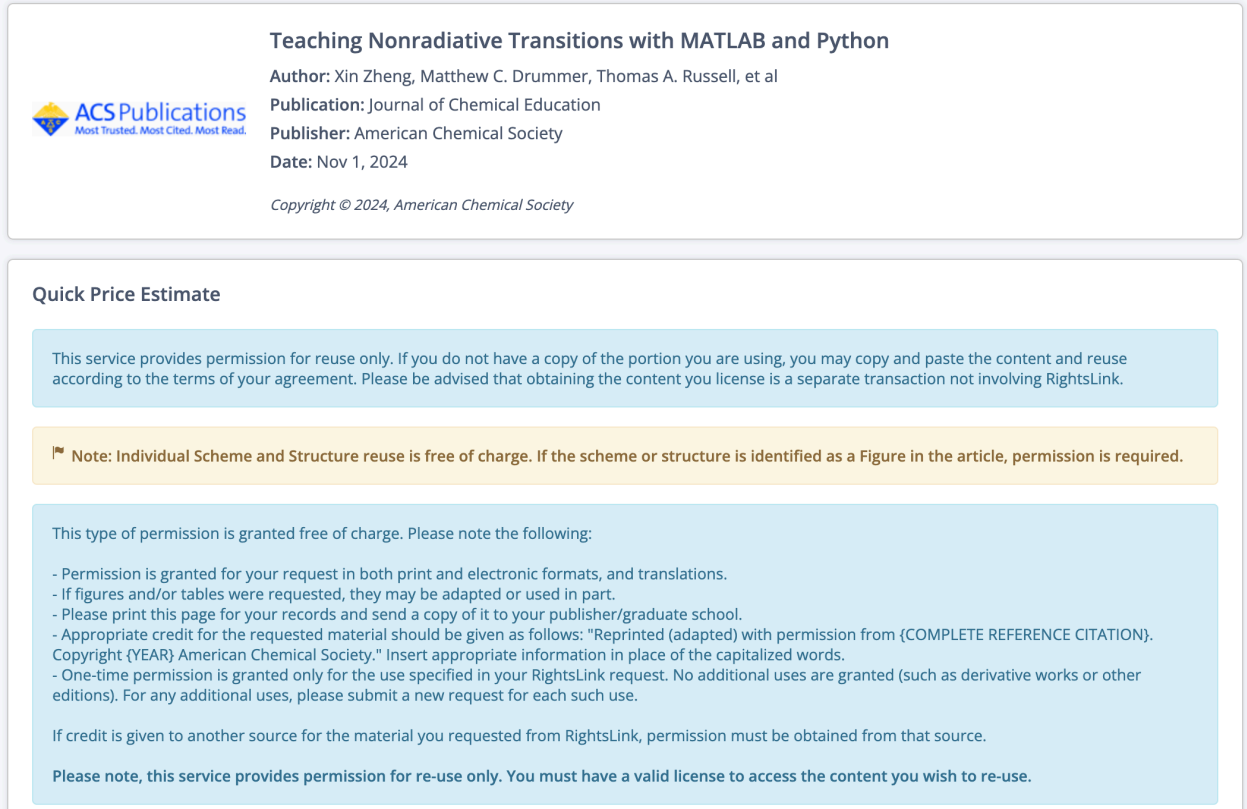
25. Kato, T.; Shida, T. Electronic Structures of Ion Radicals of Nitrogen-Heteroaromatic Hydrocarbons as Studied by ESR and Optical Spectroscopy. *J. Am. Chem. Soc.* **1979**, *101* (23), 6869–6876.

26. Lomoth, R.; Naumov, S.; Brede, O. Genuine Pyrimidine Radical Cations Generated by Radiation-Induced Electron Transfer to Butyl Chloride or Acetone Parent Ions. *J. Phys. Chem. A* **1999**, *103* (15), 2641–2648.

Appendix E - Copyright Permissions

Chapter 1 References

Figure 1.1:



Teaching Nonradiative Transitions with MATLAB and Python

Author: Xin Zheng, Matthew C. Drummer, Thomas A. Russell, et al
Publication: Journal of Chemical Education
Publisher: American Chemical Society
Date: Nov 1, 2024

Copyright © 2024, American Chemical Society

Quick Price Estimate

This service provides permission for reuse only. If you do not have a copy of the portion you are using, you may copy and paste the content and reuse according to the terms of your agreement. Please be advised that obtaining the content you license is a separate transaction not involving RightsLink.

Note: Individual Scheme and Structure reuse is free of charge. If the scheme or structure is identified as a Figure in the article, permission is required.

This type of permission is granted free of charge. Please note the following:

- Permission is granted for your request in both print and electronic formats, and translations.
- If figures and/or tables were requested, they may be adapted or used in part.
- Please print this page for your records and send a copy of it to your publisher/graduate school.
- Appropriate credit for the requested material should be given as follows: "Reprinted (adapted) with permission from {COMPLETE REFERENCE CITATION}. Copyright {YEAR} American Chemical Society." Insert appropriate information in place of the capitalized words.
- One-time permission is granted only for the use specified in your RightsLink request. No additional uses are granted (such as derivative works or other editions). For any additional uses, please submit a new request for each such use.

If credit is given to another source for the material you requested from RightsLink, permission must be obtained from that source.

Please note, this service provides permission for re-use only. You must have a valid license to access the content you wish to re-use.

Figure 1.2:



Visible to NIR-II Photoluminescence of Atomically Precise Gold Nanoclusters

Author: Zhongyu Liu, Lianshun Luo, Rongchao Jin

Publication: Advanced Materials

Publisher: John Wiley and Sons

Date: Dec 3, 2023

© 2023 The Authors. Advanced Materials published by Wiley-VCH GmbH

Open Access Article

This is an open access article distributed under the terms of the Creative Commons CC BY license, which permits unrestricted use, distribution, and reproduction in any medium, provided the original work is properly cited.

You are not required to obtain permission to reuse this article.

For an understanding of what is meant by the terms of the Creative Commons License, please refer to Wiley's Open Access Terms and Conditions.

Permission is not required for this type of reuse.

Wiley offers a professional reprint service for high quality reproduction of articles from over 1400 scientific and medical journals. Wiley's reprint service offers:

- Peer reviewed research or reviews
- Tailored collections of articles
- A professional high quality finish
- Glossy journal style color covers
- Company or brand customisation
- Language translations
- Prompt turnaround times and delivery directly to your office, warehouse or congress.

Please contact our Reprints department for a quotation. Email corporatesaleseurope@wiley.com or corporatesalesusa@wiley.com or corporatesalesDE@wiley.com.

Figure 1.3:

Nanoscale

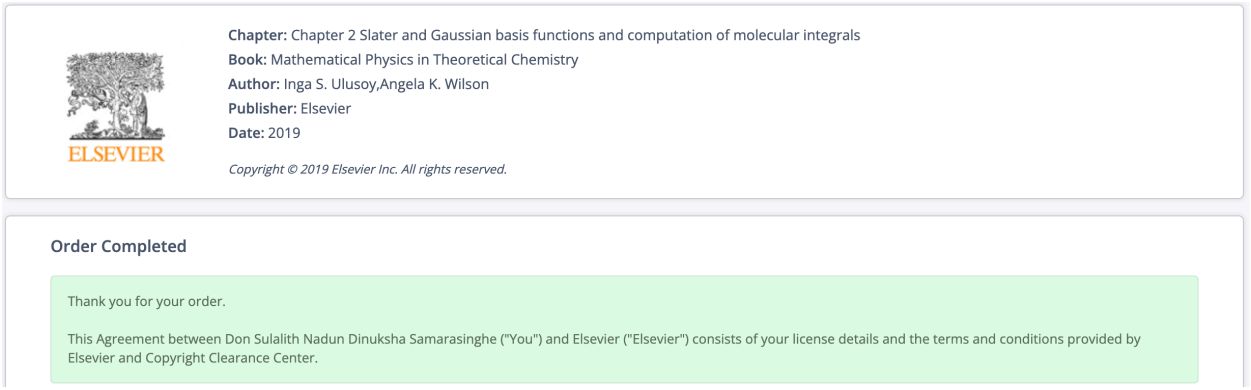
Publication type: e-Journal
Article: A First Glance into Mixed Phosphine-Stibine Moieties as Protecting Ligands for Gold Clusters

ISSN: 2040-3372
DOI: 10.1039/D2NR05497C
Publication Year: 2009 - Present
Publisher: RSC Pub
Language: English
View less details

Rightsholder: Royal Society of Chemistry
Country: United Kingdom of Great Britain and Northern Ireland
URL: http://www.rsc.org/Publishing/Journals/NR/index.asp
Authors: Royal Society of Chemistry (Great Britain); National Center for Nanoscience and Technology.

Chapter 2 References

Figure 2.1:



Chapter: Chapter 2 Slater and Gaussian basis functions and computation of molecular integrals
Book: Mathematical Physics in Theoretical Chemistry
Author: Inga S. Ulusoy,Angela K. Wilson
Publisher: Elsevier
Date: 2019

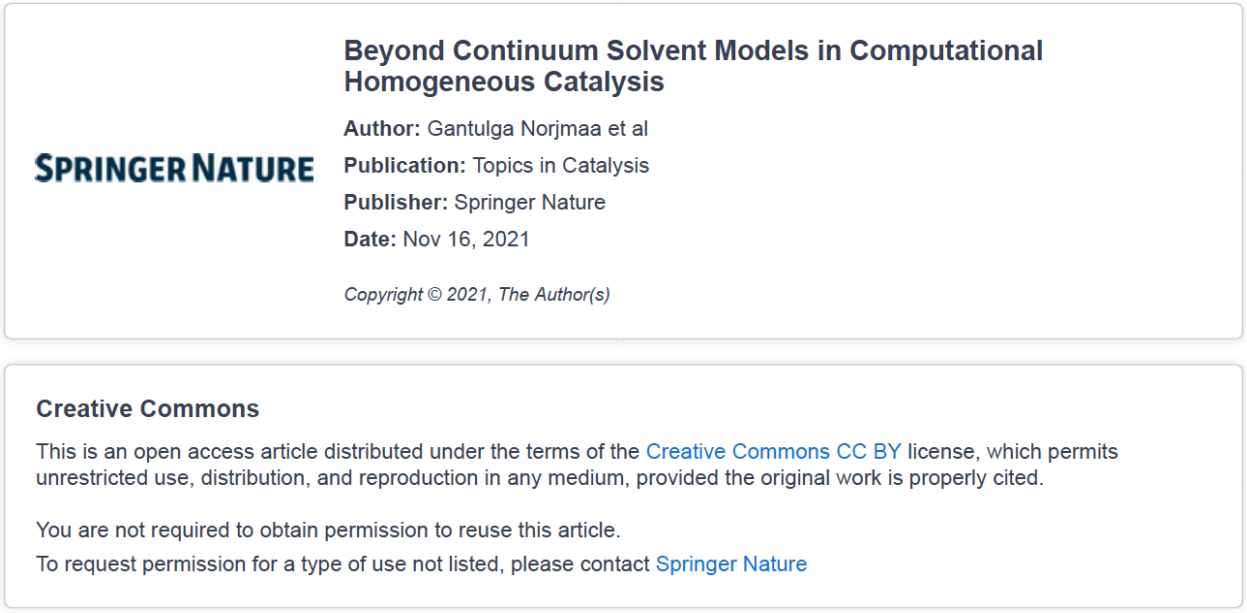
Copyright © 2019 Elsevier Inc. All rights reserved.

Order Completed

Thank you for your order.

This Agreement between Don Sulalith Nadun Dinuksha Samarasinghe ("You") and Elsevier ("Elsevier") consists of your license details and the terms and conditions provided by Elsevier and Copyright Clearance Center.

Figure 2.2:



Beyond Continuum Solvent Models in Computational Homogeneous Catalysis

Author: Gantulga Norjmaa et al
Publication: Topics in Catalysis
Publisher: Springer Nature
Date: Nov 16, 2021

Copyright © 2021, The Author(s)

Creative Commons

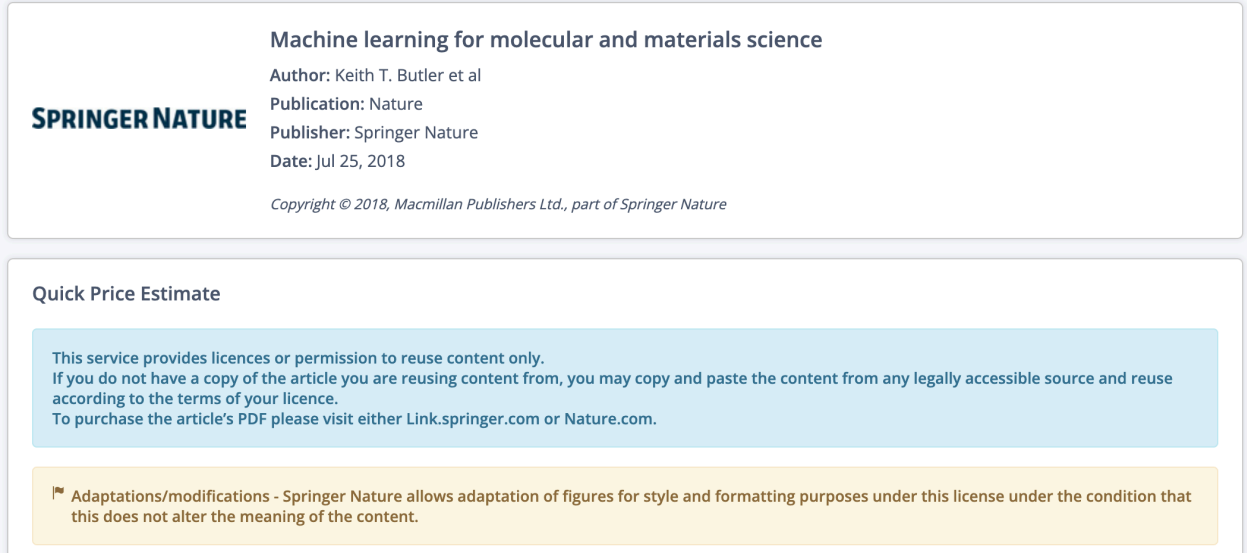
This is an open access article distributed under the terms of the Creative Commons CC BY license, which permits unrestricted use, distribution, and reproduction in any medium, provided the original work is properly cited.

You are not required to obtain permission to reuse this article.

To request permission for a type of use not listed, please contact Springer Nature

© 2026 Copyright - All Rights Reserved | Copyright Clearance Center, Inc. | Privacy statement | Data Security and Privacy | For California Residents | Terms and ConditionsComments? We would like to hear from you. E-mail us at customercare@copyright.com

Figure 2.3:



SPRINGER NATURE

Machine learning for molecular and materials science

Author: Keith T. Butler et al
Publication: Nature
Publisher: Springer Nature
Date: Jul 25, 2018

Copyright © 2018, Macmillan Publishers Ltd., part of Springer Nature

Quick Price Estimate

This service provides licences or permission to reuse content only.
If you do not have a copy of the article you are reusing content from, you may copy and paste the content from any legally accessible source and reuse according to the terms of your licence.
To purchase the article's PDF please visit either Link.springer.com or Nature.com.

Adaptations/modifications - Springer Nature allows adaptation of figures for style and formatting purposes under this license under the condition that this does not alter the meaning of the content.

Chapter 3 References

Samarasinghe, D. S. N. D.; Aikens, C. M. Effects of Static Electric Fields on the Excitations of Silver Nanowire Dimers. *J. Phys. Chem. A* **2024**, *128* (18), 3548–3556.

American Chemical Society's Policy on Thesis and Dissertations

If your university requires you to obtain permission, you must use the RightsLink permission system.

See RightsLink instructions at http://pubs.acs.org/page/copyright/permissions.html.

This is regarding request for permission to include **your** paper(s) or portions of text from **your** paper(s) in your thesis.
Permission is now automatically granted; please pay special attention to the **implications** paragraph below. The Copyright Subcommittee of the Joint Board/Council Committees on Publications approved the following:

> Copyright permission for published and submitted material from thesis and dissertations
> ACS extends blanket permission to students to include in their thesis and dissertations their own articles, or portions thereof, that have been published in ACS journals or submitted to ACS journals for publication, provided that the ACS copyright credit line is noted on the appropriate page(s).
>
> Publishing implications of electronic publication of thesis and dissertation material
> Students and their mentors should be aware that posting of thesis and dissertation material on the Web prior to submission of material from that thesis or dissertation to an ACS journal may affect publication in that journal. Whether Web posting is considered prior publication may be evaluated on a case-by-case basis by the journal's editor. If an ACS journal editor considers Web posting to be "prior publication", the paper will not be accepted for publication in that journal. If you intend to submit your unpublished paper to ACS for publication, check with the appropriate editor prior to posting your manuscript electronically.

Reuse/Republication of the Entire Work in Thesis or Collections: Authors may reuse all or part of the Submitted, Accepted or Published Work in a thesis or dissertation that the author writes and is required to submit to satisfy the criteria of degree-granting institutions. Such reuse is permitted subject to the ACS' "Ethical Guidelines to Publication of Chemical Research" (http://pubs.acs.org/page/policy/ethics/index.htmlb); the author should secure written confirmation (via letter or email) from the respective ACS journal editor(s) to avoid potential conflicts with journal prior publication*/embargo policies. Appropriate citation of the Published Work must be made. If the thesis or dissertation to be published is in electronic format, a direct link to the Published Work must also be included using the ACS Articles on Request author-directed link - see http://pubs.acs.org/page/policy/articlesonrequest/index.html

* Prior publication policies of ACS journals are posted on the ACS website at http://pubs.acs.org/page/policy/prior/index.html

If your paper has not yet been published by ACS, please print the following credit line on the first page of your article: "Reproduced (or 'Reproduced in part') with permission from [JOURNAL NAME], in press (or 'submitted for publication'). Unpublished work copyright [CURRENT YEAR] American Chemical Society." Include appropriate information.

If your paper has already been published by ACS and you want to include the text or portions of the text in your thesis/dissertation, please print the ACS copyright credit line on the first page of your article: "Reproduced (or 'Reproduced in part') with permission from [FULL REFERENCE CITATION.] Copyright [YEAR] American Chemical Society." Include appropriate information.

Submission to a Dissertation Distributor: If you plan to submit your thesis to UMI or to another dissertation distributor, you should not include the unpublished ACS paper in your thesis if the thesis will be disseminated electronically, until ACS has published your paper. After publication of the paper by ACS, you may release the entire thesis (**not the individual ACS article by itself**) for electronic dissemination through the distributor; ACS's copyright credit line should be printed on the first page of the ACS paper.

v1.4

Questions? customercare@copyright.com.